

ResearchOnline@JCU

This file is part of the following reference:

Lovisa, Amy (2015) *Characterising the fatigue response of corrugated roof cladding*. PhD thesis, James Cook University.

Access to this file is available from:

<http://researchonline.jcu.edu.au/44647/>

The author has certified to JCU that they have made a reasonable effort to gain permission and acknowledge the owner of any third party copyright material included in this document. If you believe that this is not the case, please contact

*ResearchOnline@jcu.edu.au and quote
<http://researchonline.jcu.edu.au/44647/>*

JAMES COOK UNIVERSITY

COLLEGE OF SCIENCE, TECHNOLOGY & ENGINEERING

Civil Engineering

Characterising the fatigue response of corrugated roof cladding

Amy Lovisa

DOCTORAL THESIS

Thesis submitted to the College of Science, Technology and Engineering in partial fulfilment
of the requirements for the degree of

**Doctor of Philosophy
(Civil Engineering)**

September, 30th 2015

STATEMENT OF ACCESS

I, the undersigned, the author of this thesis, understand that James Cook University will make it available for use within the University Library and via the Australian Digital Theses network for use elsewhere.

I understand that as an unpublished work a thesis has significant protection under the Copyright act and I do not wish to place restrictions on access to this work.

Amy Lovisa

Date

DECLARATION OF SOURCES

I declare that this thesis is my work and has not been submitted for another degree or diploma at any university or other institution of tertiary education. Information derived from published or unpublished work of others has been acknowledged in the text and a list of references given.

Amy Lovisa

Date

STATEMENT ON THE CONTRIBUTION OF OTHERS

This thesis included the following contributions of others:

Supervision: A/Prof J. D. Ginger (JCU), Dr. D. J. Henderson and Dr. V. Wang were the principal supervisors of this work.

Editorial Assistance: Principal editorial assistance was provided by A/Prof J. D. Ginger (JCU), Dr. D. J. Henderson and Dr. V. Wang. Additional assistance was provided by Adjunct Professor G. Walker and Dr. J. Lovisa.

Experimental Infrastructure: The apparatus used in the experiment was manufactured by Mr. C. Arrowsmith, and designed in coordination with undergraduate students Christian Walsh and Randil Samarasuriya. Tensile test data of the cladding steel was obtained by Dr. D. J. Henderson and Bluescope Steel.

ACKNOWLEDGEMENT

I would like to express appreciation and thanks to my thesis supervisors, Associate Professor John Ginger, Dr. David Henderson and Dr. Vincent Wang, for their constructive advice and encouragement; their guidance ensured that I survived this investigation.

I would also like to thank Adjunct Professor George Walker for his careful and detailed review of my journal papers. As a result, I am proud of every paper I have produced and will be for the remainder of my professional career.

On a more personal note I would like to express my deepest love and thanks to my family; my husband for still agreeing to marry me even after my PhD had driven me insane, my sister for continually reminding me that everyone goes insane and for guiding me when I felt most lost, and my parents for the unwavering confidence in my ability and time spent listening to my ideas.

ABSTRACT

Current fatigue design of roof cladding is entirely reliant on complex and repetitive prototype testing. Standardised cladding fatigue design has successfully minimized the occurrence of fatigue failure during severe wind storms such as cyclones, but the prototype tests required in fatigue design are costly and time consuming. All variations of the cladding assembly, including the various profiles, manufacturers, fasteners and fastener arrangements, must be tested multiple times. A greater understanding of the mechanism underlying fatigue of roof cladding in combination with a numerical model capable of simulating cladding fatigue could reduce the total reliance on prototype testing in fatigue design. Such a numerical model would employ fracture mechanics to simulate crack initiation in the cladding and could to some extent replace aspects of the prototype test or enable a semi-empirical approach to fatigue design.

This thesis investigates the mechanism of fatigue crack initiation in corrugated roof cladding in a bid to develop a model capable of simulating this phenomenon numerically. Characterising fatigue crack initiation required the development of a specialized testing arrangement which isolated a single cladding-fastener connection. The test, known as the isolated fastener connection (IFC) test, restrained all four edges of a 720 mm × 150 mm section of corrugated cladding with a fastener located at the centre displacing to induce load. The IFC test successfully recreated the response of the cladding that was observed in full scale testing when subject to both monotonic and cyclic loads. In particular, the IFC test reproduced the two common crack formations observed in cladding fatigue, the ‘star’ type crack and ‘H’ type crack, and produced the cracks after a comparable number of cycles.

A unique and inexpensive photogrammetric method was developed to measure the displacement of the cladding sample within the IFC test when subject to monotonic loads. The photogrammetric method involved texturizing the cladding surface and taking 70 photographs of the cladding at distinct angles. These photographs were passed through commercial photogrammetry software to produce a 3D digital reconstruction of the cladding surface. The displacement of the cladding was then calculated by comparing the digital reconstruction of the deformed cladding with a digital reconstruction of the cladding under no applied load. The digital surface models produced using the photogrammetric method was also used to extend numerical model validation studies. The digital reconstructions were compared directly with the deformed mesh of a numerical model to provide a full-field comparison of the displacement of the cladding sheet.

The IFC test was employed to study the mechanism underlying crack initiation. Corrugated cladding samples were cycled under constant amplitude loading to form a ‘star’ type crack. The fastener hole edge was monitored by both digital microscopes and strain gauge rosettes. The longitudinal arm of the ‘star’ type crack opened in the underside of the cladding in regions of tensile strain. The crack proceeded to propagate through the thickness of the cladding along the plane of maximum shear. Once the thickness of the cladding had been entirely bisected, the crack then rapidly opened into the plane of the cladding. A similar mechanism was observed for the transverse leg of the crack. Crack initiation was then defined as the point in which the crack had entirely bisected the thickness of the cladding and had begun to open into the plane of the cladding. Under a number of load amplitudes this point of crack initiation occurred at a crack length of 0.9 mm and 0.5 mm for the longitudinal and transverse cracks

respectively. Based on this definition of crack initiation, the strain field at the crack tip at crack initiation was monitored to produce a strain based crack initiation criterion. A crack initiation criterion based on the principal surface strains and distinct to the longitudinal and transverse directions was found.

Attempts were also made to identify the kinematic material properties of the cladding steel. Anti-buckling fixtures were developed to enable tension-compression testing of the thin steel sheet but the cladding softened too much and continued to buckle under compressive loads. Preliminary results suggest the cladding is prone to significant cyclic softening and the nonlinear combined kinematic and isotropic hardening model is required to accurately describe the kinematic material properties of the steel in a numerical simulation.

A numerical model of the cladding subject to monotonic loads in an IFC test was also developed. The model accurately predicted the fastener reaction, strain surrounding the fastener hole and the displacement of the cladding sheet. Under a maximum applied load the cladding predicted the displacement of the cladding to within 89% of that documented experimentally. Development of the model involved a mesh convergence study, in depth analysis of the boundary conditions and compression studies of the EPDM (ethylene propylene diene monomer) seal. The boundary conditions of the model were simplified to reduce the simulation run time making the model more appropriate for a fatigue study. These simplifications significantly reduced the computation cost of the simulation but performing a fatigue simulation was still too costly. Furthermore, a fatigue model requires the kinematic material properties of the steel which remain unknown.

This study identified the mechanism underlying crack initiation in corrugated cladding and characterised the phenomenon using a strain based crack initiation criterion. This investigation also successfully developed a numerical model capable of simulating the response of the cladding subject to monotonic loads. This crack initiation criterion and validated numerical model provide a strong foundation for future development of a numerical model capable of simulating cladding fatigue. Development of such a numerical model is likely to be an iterative process combining both experiments and numerical simulations. A model capable of simulating cladding fatigue could directly reduce the total reliance on prototype testing in cladding fatigue design by either replacing components of the prototype test or enabling a fracture mechanics based analysis of cladding fatigue.

TABLE OF CONTENTS

Statement of Access	i
Declaration of Sources	ii
Statement on the Contribution of Others	iii
Acknowledgement	iv
Abstract	v
Table of Contents	vii
List of Figures	x
List of Tables	xvii
List of Publications	xviii
1. Introduction.....	1
1.1 Objectives.....	4
1.2 Scope and Focus.....	4
1.3 Outline of Thesis.....	5
2. Literature Review.....	6
2.1 Cladding.....	6
2.2 Wind-loading on Low Rise Buildings.....	7
2.3 Cladding Fatigue	11
2.4 Cladding Testing Arrangements	14
2.5 Cladding Behaviour	17
2.5.1 Response of Cladding Subject to Monotonic Loads	17
2.5.2 Response to Cyclic Loading.....	23
2.5.3 Cyclonic Wind Loading Studies	28
2.6 Potential Cladding Fatigue Modelling Methods	29
2.7 Mechanics of Materials.....	30
2.7.1 Fatigue Crack Initiation.....	33

2.7.2	Monotonic Crack Initiation	39
3.	Developing an Appropriate Testing Method.....	43
3.1	Developing and Validating an Isolated Cladding-Fastener Connection Test	43
3.1.1	Background	43
3.1.2	Designing a Test Apparatus	45
3.1.3	Cladding Specimens Specifications	49
3.1.4	Validating the IFC test	50
3.1.5	Summary	53
3.2	Measuring Deflection Using Photogrammetry	54
3.2.1	Sample Preparation and Photoshooting.....	56
3.2.2	Using Agisoft PhotoScan to Create DSM.....	58
3.2.3	Scaling and Post Processing.....	59
3.2.4	Accuracy of Photogrammetric Method.....	59
3.2.5	Inferring Displacement of the Cladding Sample.....	61
3.2.6	Summary	68
4.	Fatigue Response of Cladding	68
4.1	Cyclic Material Properties.....	68
4.1.1	Background	68
4.1.2	Cladding Samples.....	72
4.1.3	Test Apparatus	74
4.1.4	Tension-Compression Cyclic Testing.....	76
4.1.5	Summary and Recommendations.....	79
4.2	Characterising Fatigue Macrocrack Initiation.....	81
4.2.1	Background	81
4.2.2	Experimental Set-up.....	82
4.2.3	Defining Crack Initiation	82

4.2.4	Creating a Strain Based Crack Initiation Criterion	86
4.2.5	Limitations	92
4.2.6	Summary	94
4.3	General Observations	94
5.	Finite Element Simulations	100
5.1	Constitutive Description.....	100
5.2	Explicit Analysis Methods	102
5.3	Mesh Geometry	109
5.4	Mesh Sensitivity For Numerical Model.....	111
5.5	Boundary Condition Simulations	123
5.6	Washer Compression Study	132
5.7	Model Validation	140
5.8	Fatigue Model	152
6.	Conclusion And Recommendations	153
6.1	Conclusion	153
6.2	Recommendations	155
6.3	Summary	156
Appendix	A.....	157
	Crack orientation for constant amplitude loading	157
Appendix	B	168
	Model revision index	168
Appendix	C	175
	Wind loading tributaries.....	175
References	182

LIST OF FIGURES

Figure 1.1: Corrugated cladding	1
Figure 1.2: Static pull-through failure (credited to: Mahaarachchi, 2003)	1
Figure 1.3: Fatigue crack formation types (a) “star”, (b) “T” and (c) “H” (credited to: Henderson, 2010)	2
Figure 2.1: (a) Corrugated (b) Rib-pan and (c) Trapezoidal Cladding.....	6
Figure 2.2: Cladding fastener through corrugated cladding crest.....	6
Figure 2.3: Roof schematic for a typical house.....	7
Figure 2.4: Wind Flow Around a low-rise building.....	8
Figure 2.5: Cyclone anemograph for a tropical cyclone (credited to: Holmes, 2001)...	8
Figure 2.6: Design cyclone pressure trace (credited to: Henderson, 2010).....	10
Figure 2.7: Simplified code distributions and external pressure distributions at three different time instances (credited to: Holmes, 2001).....	11
Figure 2.8: Loading Sequences for Cladding Fatigue Testing.....	14
Figure 2.9: Mid-span line load method (a) prototype and (b) equivalent test set up.....	15
Figure 2.10: Plot of PLA achieved pressure response in comparison to requested time pressure trace (credited to: Henderson, 2010).....	16
Figure 2.11: (a) Small scale experiment and (b) load-deflection curve for small scale experiment (Mahendran, 1992).....	17
Figure 2.12: Corrugated cladding profile undeformed and following LPD.....	17
Figure 2.13: Static load-deflection curve for corrugated cladding (credited to: Mahendran, 1990a).....	18
Figure 2.14: Static load-deflection curves for all three cladding types (credited to: Xu and Reardon, 1993).....	18
Figure 2.15: Comparison of FEA and experimental results (credited to: Xu, 1993)...	19
Figure 2.16: Single rib Profile for FEM (credited to: Xu, 1993).....	20
Figure 2.17: Comparison of experimental and numerical deformed shape for (a) LDP and (b) residual permanent deformation (credited to Lovisa <i>et al.</i> 2012).....	22
Figure 2.18: Comparison of experimental and numerical (a) Load-deflection data and (b) Stress-load data (credited to Lovisa <i>et al.</i> 2012).....	23
Figure 2.19: Load cycles for constant amplitude loading.....	24

Figure 2.20: Crack formations observed by Morgan and Beck (1977).....	24
Figure 2.21: (a) Mahendran (1990b) and (b) Xu (1995) fatigue life curves.....	25
Figure 2.22: Crack Formations (credited to: Mahendran, 1990b).....	26
Figure 2.23: Crack initiation and formation for various Peak loads (credited to: Henderson, 2010).....	27
Figure 2.24: Effects of varying load ratio on cycles to failure (credited to: Henderson and Ginger, 2005).....	28
Figure 2.25: (a) Stress-strain diagram highlighting the Bauschinger effect and (b) Equivalent absolute stress-strain diagram (credited to: Suresh, 1991).....	30
Figure 2.26: Cyclic stress-strain curve under constant strain amplitude (Credited to: Liu, 2005).....	31
Figure 2.27: (a) change of strain amplitude during constant stress amplitude cycling and (b) change in stress amplitude during constant strain amplitude cycling (Credited to: Hosford, 2009).....	32
Figure 2.28: Several stabilized hysteresis loops for SAE 4340 steel which appears to have cyclically softened. (Credited to: Liu, 2005).....	32
Figure 2.29: Types of loading based on Von Mises strain where (a) is proportional loading, (b) is 90° out-of-phase nonproportional loading and (c) pseudorandom nonproportional loading.....	33
Figure 2.30: Plot of total fatigue life of an annealed 4340 steel (credited to: Hosford, 2009).....	35
Figure 2.31: Crack growth with increasing number of cycles (credited to: Smith, 1991).....	38
Figure 2.32: Generic FFLD and FLD for a metallic sheet.....	41
Figure 2.33: Fracture plane through the thickness of sheet metal subject to out-of-plane biaxial stretching (credited to: Jain et al, 1999).....	41
Figure 3.1: Photograph of the apparatus installed within a United STM-50kN.....	45
Figure 3.2: Full schematic of IFC test apparatus.....	46
Figure 3.3: Cladding and fastener arrangement for IFC test.....	47
Figure 3.4: (a) Cladding crest clamped along longitudinal edge and (b) schematic of cladding apparatus.....	48
Figure 3.5: Stress-strain curve for G550 steel in longitudinal direction.....	49
Figure 3.6: Comparison of cladding deflections observed in airbox and IFC studies...	51
Figure 3.7: Crack formations observed during airbox and IFC studies.....	53

Figure 3.8: Number of cycles until failure documented during IFC and airbox studies.	53
Figure 3.9: Texturized cladding sample.....	57
Figure 3.10: Photoshooting method (a) Phase 1 and (b) Phase 2.....	58
Figure 3.11: Definition of “true distance”.....	60
Figure 3.12: Surface deviation between DSMs from laser scanning and photogrammetric method for (a) 350 mm × 142 mm section and (b) 70 mm × 70 mm section.....	61
Figure 3.13: Fastener displacement-reaction curve for photogrammetry trials.....	62
Figure 3.14: Out-of-plane deflection of cladding sample subject to differing magnitudes of loading for Trial 1.....	64
Figure 3.15: Out-of-plane deflection of cladding sample subject to differing magnitudes of loading for Trial 2.....	65
Figure 3.16: Out-of-plane deflection of cladding sample subject to differing magnitudes of loading for Trial 3.....	66
Figure 3.17: Cross sectional view of the cladding installed within the apparatus.....	67
Figure 4.1: Example of isotropic hardening for an isotropic material (credited to Milne et al, 2003).....	69
Figure 4.2: Small strain anti-buckling fixture implemented by Eggertsen and Mattiasson (2011).....	71
Figure 4.3: Anti-buckling fixture created by (a) Dietrich et al (2014) and (b) Magargee et al. (2011).....	71
Figure 4.4: Dog bone sample as shown in AS 1391-2007.....	73
Figure 4.5: Strain contour for tensile sample with (a) AS 1391 recommended dimensions and (b) modified geometry.....	73
Figure 4.6: Anti-buckling fixture using sliding Perspex plates.....	74
Figure 4.7: Anti-buckling fixture using steel plates.....	75
Figure 4.8: (a) stress-strain cycle for unsymmetric cycling and (b) mean stress of each load cycle.....	77
Figure 4.9: Symmetric tension-compression tests for a strain range of (a) 0.001 and (b) 0.0005.....	78
Figure 4.10: Strain range and mean strain based on attached strain gauge, resulting from stress controlled cycling.....	79
Figure 4.11: Strain range and mean strain based on cross head position, resulting from stress controlled cycling.....	79

Figure 4.12: Three point bend test used to inversely estimate material properties of sheet metal (credited to: Zao and Lee, (2004)).....	80
Figure 4.13: (a) IFC test for fatigue of cladding and (b) view of cladding from digital microscope.....	82
Figure 4.14: ariel view of strain gauges.....	82
Figure 4.15: Crack growth curves for differing load amplitudes in the (a) transverse and (b) longitudinal direction.....	84
Figure 4.16: Stylized crack growth curves, strain profiles and fractographic analysis..	84
Figure 4.17: Changing state of strain at transverse hole edge under constant amplitude loading.....	86
Figure 4.18: Original and inferred strain data for two differing trials.....	90
Figure 4.19: Crack opening modes.....	90
Figure 4.20: (a) Principal strains at crack initiation as distinguished by peak load and (b) Crack initiation criteria for corrugated cladding.....	91
Figure 4.21: Anomalous strain path.....	92
Figure 4.22: Transverse strain history at longitudinal hole edge for (a) entire history, (b) first 200 cycles and (c) last 200 cycles.....	95
Figure 4.23: Longitudinal strain history at transverse hole edge for (a) entire history, (b) first 200 cycles and (c) last 200 cycles.....	96
Figure 4.24: Changing mean principal strain with number of cycles at (a) the transverse and (b) longitudinal hole edge.....	97
Figure 4.25: Changing principal strain with number of cycles at (a) the transverse and (b) longitudinal hole edge.....	97
Figure 4.26: Principal strain with in-plane shear at (a) longitudinal and (b) transverse hole edge.....	98
Figure 4.27: Principal strain with in-plane shear at longitudinal hole edge under a peak load of 500 N.....	99
Figure 5.1: Strain data layout on cladding model for load rate trials.....	106
Figure 5.2: Effect of load rate on strain along the surface of the cladding.....	107
Figure 5.3: (a) load amplitude curves and (b) load-displacement curve for differing load amplitudes.....	108
Figure 5.4: Cladding profile provided by manufacturers.....	109
Figure 5.5: Comparison of cladding profiles taken from manufacturer and photogrammetry.....	109

Figure 5.6: Effect of cladding profile on the static response of cladding	110
Figure 5.7: Discretized cladding model.....	111
Figure 5.8: Strain variable locations surrounding fastener hole.....	112
Figure 5.9: Strain comparison for differing aspect ratios of the elements in Region 1..	112
Figure 5.10: Strain comparison for different transverse dimensions of elements in Region 2.....	114
Figure 5.11: Strain comparison for different transverse dimensions of elements in Region 2 with a refined mesh in Region 3.....	114
Figure 5.12: Strain sensitivity to changes in mesh density in Regions 3 and 2.....	115
Figure 5.13: Fastener reaction for differing transverse element dimensions.....	117
Figure 5.14: Out-of-plane translation and rotation at the border to Region 3 for differing transverse element dimensions.....	117
Figure 5.15: (a) Variation in node height at the crest of the cladding between local and global model and (b) an example of strain free adjustment of two contacting surfaces.....	118
Figure 5.16: Comparison of strain for various mesh densities of the submodel and full model.....	119
Figure 5.17: Overlay plot of submodel and global model deformed shape.....	120
Figure 5.18: Comparing element geometries at the point of extraction for the submodels with an element size of 0.2 mm and 0.3 mm.....	120
Figure 5.19: Strain comparison for different transverse dimension of elements in Region 2.....	121
Figure 5.20: Basic sliding test used to calculate coefficient of friction.....	122
Figure 5.21: Coefficient of friction for contact between EPDM seal and exposed steel of cladding.....	122
Figure 5.22: Discretised EPDM seal.....	123
Figure 5.23: Examples of boundary conditions used during numerical trials.....	123
Figure 5.24: Cross sectional view of DSM created during Photogrammetry Trial 3....	124
Figure 5.25: ABAQUS simulation of apparatus lid and equivalent simplification used in cladding model.....	126
Figure 5.26: Translation of screw head documented during Photogrammetry Trial 3..	127
Figure 5.27: Experimental set up of fastener, detailed simulation of fastener in ABAQUS and the spring and rigid surface system used in the cladding model.....	127

Figure 5.28: Strain gauge locations for investigating the boundary conditions.....	128
Figure 5.29: Numerical and experimental fastener reaction – fastener displacement curve.....	129
Figure 5.30: Numerical and experimental strain data at the cladding boundary.....	130
Figure 5.31: (a) Transverse boundary and (b) Longitudinal boundary of simplified model.....	131
Figure 5.32: Numerical and experimental fastener reaction – fastener displacement curve using both the working model and simplified model.....	131
Figure 5.33: Numerical and experimental strain data at the cladding boundary using the simplified model.....	132
Figure 5.34: (a) average dimensions of EPDM seal and (b) shortening and expansion of EPDM seal under compressive load.....	133
Figure 5.35: EPDM seal compression study test.....	133
Figure 5.36: Shortening and expansion of EPDM seals under compressive load.....	134
Figure 5.37: Numerical model of washer compression.....	134
Figure 5.38: Model sensitivity to changes in material definition.....	136
Figure 5.39: Cross section of the deformed washer using the different material definitions.....	136
Figure 5.40: Model geometries used for mesh convergence study.....	136
Figure 5.41: Force-shortening response of EPDM seal for different mesh densities and geometries.....	137
Figure 5.42: Friction coefficient for EPDM seal and smooth lubricated steel.....	138
Figure 5.43: Sensitivity of washer compression to friction between washer and platens.....	139
Figure 5.44: Comparison of final working model with experimental data.....	140
Figure 5.45: Location of strain gauge rosettes.....	142
Figure 5.46: Comparison of numerical and experimental transverse strain data.....	143
Figure 5.47: Comparison of numerical and experimental longitudinal strain data.....	144
Figure 5.48: Comparison of numerical and experimental transverse strain data for simplified model and working model.....	145
Figure 5.49: Comparison of numerical and experimental longitudinal strain data.....	146

Figure 5.50: Surface deviation (or absolute distance) between numerical and experimental DSMs for Photogrammetry Trial 1.....	149
Figure 5.51: Surface deviation (or absolute distance) between numerical and experimental DSMs for Photogrammetry Trial 2.....	149
Figure 5.52: Surface deviation (or absolute distance) between numerical and experimental DSMs for Photogrammetry Trial 3.....	150
Figure 5.53: Surface deviation (or absolute distance) between numerical and experimental DSMs for earlier version of numerical model.....	150

LIST OF TABLES

Table 2.1: Corrugated cladding fatigue subject to varying peak loads (credited to: Mahendran, 1989)	25
Table 3.1: Cladding material properties (credited to: Henderson, 2010)	47
Table 3.2: Local plastic deformation for static trials in IFC test.....	50
Table 3.3: “Star” type crack initiation documented in IFC and five samples taken from the airbox tests	52
Table 5.1: Cladding material properties (credited to: Henderson, 2010)	97
Table 5.2: Load rate simulations and required simulation run times.....	103
Table 5.3: Geometry of cladding boundary in the transverse direction.....	122
Table 5.4: Washer mesh convergence study – simulation run time comparison.....	135

LIST OF PUBLICATIONS

Journal Publications

- Lovisa A. C., Henderson D. J. and Ginger J. D. (2014) “An Inexpensive Method for Measuring Deformation of Corrugated Cladding Using Close Range Photogrammetry.” *Experimental Mechanics*, DOI 10.1007/s11340-014-9977-9.
- Lovisa A. C., Wang V. Z., Henderson D.J. and Ginger J. D. (2013) “Development and validation of a numerical model for steel roof cladding subject to static uplift loads.” *Wind and Structures*, 17(5). pp. 495-513.
- Lovisa A. C., Henderson D. J. and Ginger J. D. (2014) “Characterising fatigue macrocrack initiation in profiled steel roof cladding” - Submitted to *Engineering Structures* 15/09/2015.

Conference Publications

- Lovisa A., Henderson, D., Wang V., Ginger J. (2013) *Wind loading tributaries for pierced fixed metal roof cladding*, Proceedings of the 8th Asia-Pacific Conference on Wind Engineering, Chennai (India), December 2013
- Lovisa A., Henderson, D., Wang V., Ginger J. (2013) *Wind loading tributaries for pierced fixed metal roof cladding*, Proceedings of the 16th Australasian Wind Engineering Society Workshop, Brisbane (Australia), July 2013. Access at: <http://www.awes.org/archives/workshop-proceedings/awes-16>.
- Lovisa, A., Wang, V., Henderson, D. and Ginger, J. (2012) *A finite element model for pierced-fixed, corrugated metal roof cladding subject to uplift wind loads*. Proceedings of the 12th Australasian Structural Engineering Conference, Perth (Australia), July 2012.

1. INTRODUCTION

During severe wind events such as tropical cyclones, low rise buildings are subjected to extreme wind loads. At the roof edge in particular, roofing is subject to intense and highly fluctuating surface pressures. Consequently, the roofing itself and its fixings are subjected to the largest loads and are at greater risk of failure. The propensity for failure of the roof envelope was emphasized during the damage investigations that followed Tropical Cyclone Tracy in 1974. Cyclone Tracy devastated Darwin with over 90% of houses and 70% of other structures suffering significant loss of their roof envelope. Profiled steel roof cladding showed the greatest incidence of failure with fatigue of the cladding-fastener connection being the root cause of the failure (Walker, 1975).

Profiled steel cladding is made from thin, high strength steel which is fixed to the underlying battens using a self-tapping screw at each alternate crest of the cladding. There are a number of different profiles of steel roof cladding manufactured in Australia, with the corrugated profile most commonly used in residential housing. Corrugated cladding is characterized by its unique wave-form profile which is presented in Figure 1.1. During severe wind events the cladding-fastener connection can fail by either the fastener pulling through the cladding in a quasi-static manner or with the fastener pulling through the cladding following significant fatigue cracking. Figure 1.2 shows the cladding following static pull-through failure; clearly exhibiting the gross deformation that precedes failure of this type.

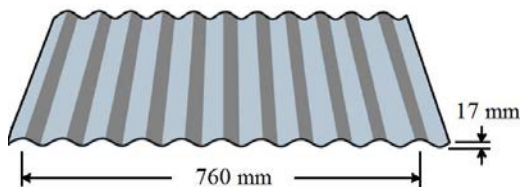


Figure 1.1: Corrugated cladding



Figure 1.2: Static pull-through failure (credited to: Mahaarachchi, 2003)

Fatigue of the cladding occurs due to the repeated loading generated by the fluctuating surface pressures. Fatigue cracks initiate within the cladding in the vicinity of the fastener and propagate as the fluctuating loads continue. The cracks can propagate to form a sizeable hole that allows the fastener to pull through the cladding, overloading the neighboring fasteners and expediting the failure of those connections (Morgan and Beck, 1977). Entire sheets of roof cladding can be dislodged, leading to water ingress into the house, hazardous wind-borne debris and in extreme circumstances total structural collapse (Walker, 1975). Figure 1.3 describes the various fatigue crack formations that can result in pull-through failure of the corrugated cladding-fastener connection. Each crack formation presents at differing load ranges with the 'star' type crack shown in Figure 1.3 (a) commonly occurring at low load ranges.

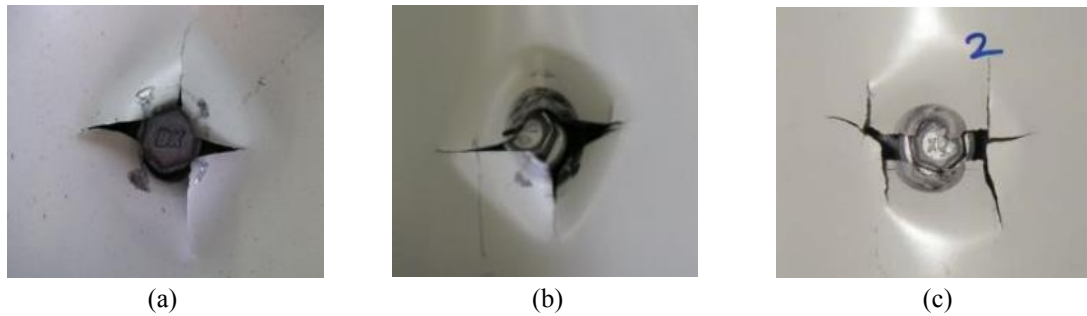


Figure 1.3: Fatigue crack formation types (a) “star”, (b) “T” and (c) “H” (credited to: Henderson, 2010)

Following Cyclone Tracy extensive research was undertaken in order to further understand the fatigue response of cladding. These predominantly experimental investigations led to the development of the Low-High-Low cyclic test which is used to experimentally establish the fatigue strength of various roof cladding systems. The design of roof cladding is entirely based on repetitive prototype testing using the Low-High-Low cyclic test. Morgan and Beck (1977), Mahendran (1990b) and Xu (1995) attempted to apply a total fatigue life approach to cladding design in order to reduce the reliance on prototype testing. The total fatigue life approach is a semi-empirical approach that interpolates simplified prototype tests using a variety of analytical models. Morgan and Beck (1977), Mahendran (1990b) and Xu (1995) successfully established the fatigue life curves for various roof cladding profiles but found the analytical models typically used in combination with the fatigue life curves to account for complex load spectra did not accurately predict the life of the cladding in a cyclone. These theoretical models do not account for the sequence of the applied loads and the fatigue response of the cladding is strongly dependent on the time history of the applied load (Jancauskas *et al.* 1994; Mahendran 1993; 1995; Xu, 1995; Suresh Kumar and Stathopoulos, 1998; Henderson, 2010). The importance of the loading sequence is emphasized by the Low-High-Low cyclic test which involves the application of load cycles at a range of low, high, followed by low amplitudes in a bid to mimic the changing magnitude of applied pressures caused by the passage of a cyclone.

Implementing the Low-High-Low cyclic test in the design of roof cladding has minimized the occurrence of fatigue failure during more recent cyclone events. Damage investigations following Tropical Cyclone Yasi, which devastated North Queensland in 2011, found only a few instances of cladding fatigue failure and for all observed cases the fasteners were spaced greater than the specifications provided by the manufacturer which increased the applied load to each connection (Boughton, et al, 2011). However, the Low-High-Low test requires that all prototype assemblies be tested, meaning every combination of fastener type and arrangement, support, cladding profile and cladding manufacturer must be tested. Although the Low-High-Low test is effective, the ensuing cost of the test is significant.

Investigations into cladding fatigue have primarily focused on the simplifying the load spectra applied to the cladding during a cyclone, or investigating the fatigue life of the cladding under differing loading conditions. These investigations were concurrent and together yielded the Low-High-Low test. Fewer attempts have been made to study the fracture mechanics underlying cladding fatigue as a detailed description of the stress state within the cladding is required. Determining the stress state within the cladding is challenging experimentally given the large plastic straining that occurs during loading. Consequently Mahendran (1990a) and

Xu and Teng (1994) relied on Finite Element Analysis to investigate the stress state in cladding under monotonic loads. These numerical models could be evolved to simulate cladding fatigue directly. Fracture mechanics, in combination with an appropriate crack initiation criterion, could be implemented in a numerical model to simulate cladding fatigue. Such a numerical model would be robust, capable of simulating cladding fatigue for a variety of loading conditions, including realistic cyclonic load spectra. Fatigue design of roof cladding is totally reliant on prototype testing but a numerical model capable of simulating cladding fatigue could directly reduce this reliance by either replacing some components of prototype testing or at the least provide a much needed analytical tool.

1.1 OBJECTIVES

The aim of this thesis was to identify and characterise the mechanism of fatigue crack initiation in corrugated steel cladding specifically for the ‘star’ type crack formation, and to recreate the phenomenon numerically. A numerical model that can recreate cladding fatigue would be the first of its kind, providing a much needed analytical tool in the pursuit of understanding fatigue failure. A greater understanding of cladding fatigue could potentially evolve cladding design to minimize fatigue damage during severe wind events.

This thesis successfully characterised the mechanism of fatigue crack initiation in corrugated cladding using a strain-based criterion. A numerical model that could accurately simulate the static response of the cladding was also developed, however, extending this model in order to simulate the fatigue response of the cladding proved difficult. The intent to create a numerical model capable of simulating crack initiation cannot be downplayed as it drove this thesis, with each specific objective of this thesis crafted in order to achieve this aim.

The specific objectives of this thesis, listed in chronological order, were:

- To develop an isolated cladding-fastener connection test that produces similar fatigue damage to that observed in the field following a wind event and in full scale airbox studies.
- To develop a numerical model that can simulate the response of the cladding in an isolated cladding-fastener connection test subject to increasing monotonic loads. An accurate numerical model was considered to be a model capable of simulating the deformation, strain and local plastic collapse of the corrugated cladding under monotonic loads.
- To validate the static numerical model by comparing the numerical results with corresponding experimental data, specifically fastener reaction, deformation and strain at critical locations.
- To develop an appropriate strain based criterion for fatigue crack initiation that is independent to applied load and semi-dependent on the system geometry.
- To determine the kinematic material properties of profiled steel cladding through specialized coupon testing of the corrugated sheet metal.
- To implement the crack initiation criterion and kinematic material properties in the validated static numerical model to form a functioning fatigue model.

1.2 SCOPE AND FOCUS

This thesis was focused on the following:

- Corrugated cladding produced by a single manufacturer. The cladding used in all laboratory testing originated from the same coil.
- The “star” type crack formation. All other crack formations, which occur at higher load levels, were considered to be beyond the scope of this investigation.
- Crack initiation only. Crack propagation and the final pull-through failure of the fastener were considered to be beyond the scope of this investigation.

1.3 OUTLINE OF THESIS

This thesis is divided into several chapters. Each chapter contains the following:

- Chapter 1** An introduction to the thesis that defines the motives and the underlying objectives.
- Chapter 2** Details the relevant literature relating to roof cladding fatigue, fracture mechanics and the mechanics of low cycle fatigue. This chapter highlights the lack of analytical or theoretical data relating to cladding fatigue and the need for a numerical result to compensate.
- Chapter 3** This chapter details the development of the isolated cladding-fastener connection test that was utilized for all testing of the corrugated cladding. This chapter also describes a unique means of measuring the cladding deformation using photogrammetry.
- Chapter 4** The fatigue response of corrugated cladding subject to constant amplitude loading is included in this chapter as well as the strain based fatigue crack initiation criterion that was developed using the results of the cyclic tests. Finally, this chapter includes the kinematic material properties of the corrugated cladding based on individual coupon tests.
- Chapter 5** Presents the development of a numerical model of the isolated cladding-fastener connection test. This chapter validates the accuracy of the model in simulating the static response of the corrugated cladding.
- Chapter 6** Highlights the conclusions drawn from this investigation and details recommendations for future research that would further evolve a numerical model that simulates cladding fatigue.

2. LITERATURE REVIEW

2.1 CLADDING

Metal roof cladding, used in low-rise buildings in Australia, is manufactured from “G550” high tensile steel with specified minimum yield strength of 550 MPa. Three common cladding profiles are corrugated, rib-pan and trapezoidal, and are shown in Figure 2.1.

Cladding is produced by rolling sheets to 0.42 mm or 0.48 mm base metal thickness (bmt). Cladding is fastened to the purlins or battens with self-drilling screws with a hexagonal washer head and an EPDM rubber seal as shown in Figure 2.2 (Strammit, 2009). Roof cladding is crest fixed to purlins or battens, which typically span 900 mm but can vary from 450 mm to 1800 mm depending on the design wind load. Purlins and battens are made from either timber or light gauge metal. The battens are then connected in turn to the rafters or trusses beneath. Figure 2.3 details the various roofing components and connections that form the roof system.

G550 cladding is anisotropic due to the rolling process (BHP, 1992). Coupon tests performed by Xu (1993) and Rogers and Hancock (1997) on samples of G550 coil, described the longitudinal (rolling) direction as possessing a smaller ultimate tensile strength and Young’s modulus than the transverse direction. Rogers and Hancock (1997) also documented a significant variance (a range of 290 MPa) in the longitudinal tensile strength between samples of G550 coil. Mahaarachchi and Mahendran (2004) have shown that this variability in material properties can affect the fatigue performance of roof cladding.

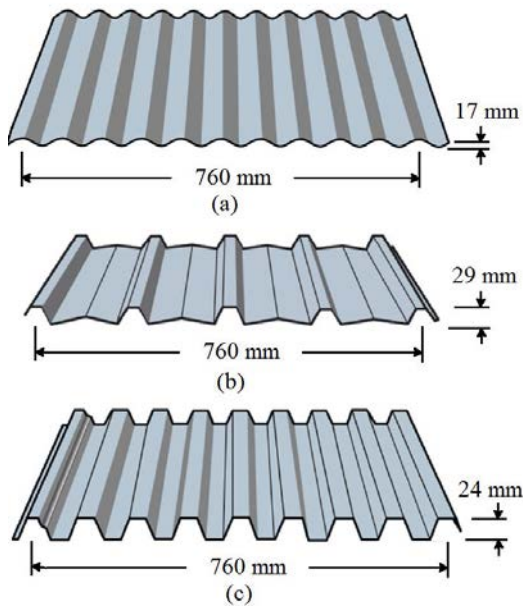


Figure 2.1: (a) Corrugated (b) Rib-pan and (c) Trapezoidal Cladding

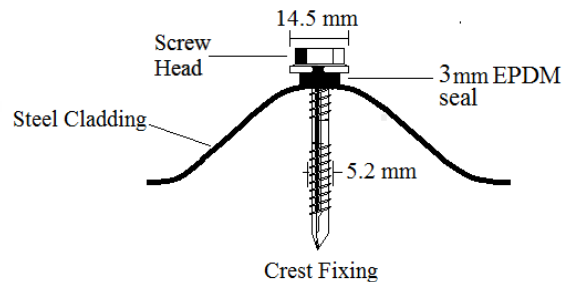


Figure 2.2: Cladding fastener through corrugated cladding crest

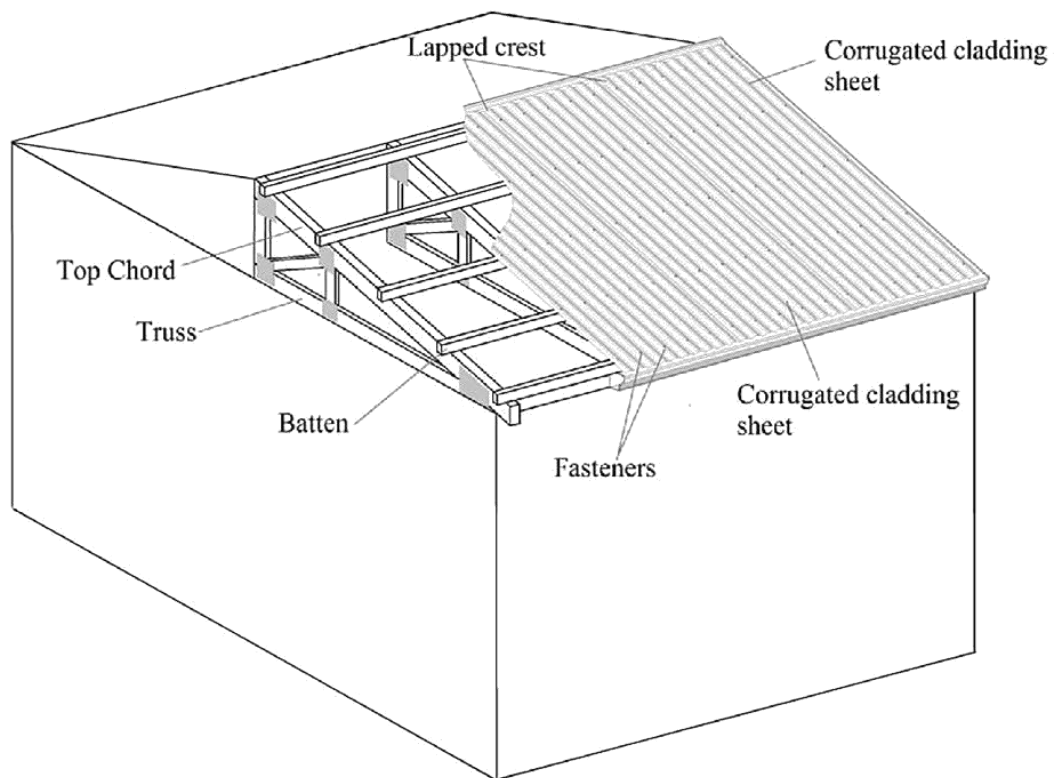


Figure 2.3: Roof schematic for a typical house

2.2 WIND-LOADING ON LOW RISE BUILDINGS

The approach wind flow and its interaction with the building generate fluctuating pressures on the roof. In regions of flow separation, such as the roof edges, cladding experiences highly fluctuating peak suction pressures due to the formation of vortices (Stathopoulos, 1984, Holmes, 2001). These regions of flow separation are dependent on the roof geometry including the roof type and the roof pitch (slope) (Xu and Reardon, 1998; Holmes, 2001). Meecham *et al.* (1991) compared the two most common roof types, gable and hip, and found that generally a gable roof experiences local peak suction pressures that are larger than those corresponding to the hip roof. Figure 2.4 shows the process of flow separation for a typical low rise building.

The fluctuations in wind pressure caused by flow separation add to the fluctuations in the approach wind speed during a cyclone, resulting in highly fluctuating suction pressures at the roof edge. A cyclone (referred to as a hurricane or typhoon in other parts of the world) is characterised by a vortex structure of circulating wind surrounding a calm eye. The maximum wind speeds occur at the eye wall and decrease radially from the eye (Holmes, 2001). As a result, a structure will experience a general change in wind speed and direction during the passage of a cyclone in addition to the fluctuations in wind speed. Consequently, the wind pressures on the roof envelope vary both spatially and temporally making recreating these conditions in experimental studies difficult (Ginger *et al.* 2000). Figure 2.5 is an anemograph describing the fluctuations of wind speed and the changing direction for a tropical cyclone.

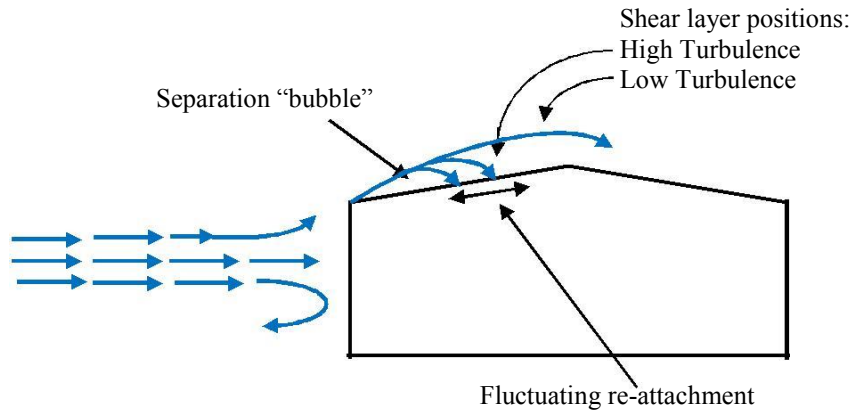


Figure 2.4: Wind Flow Around a low-rise building

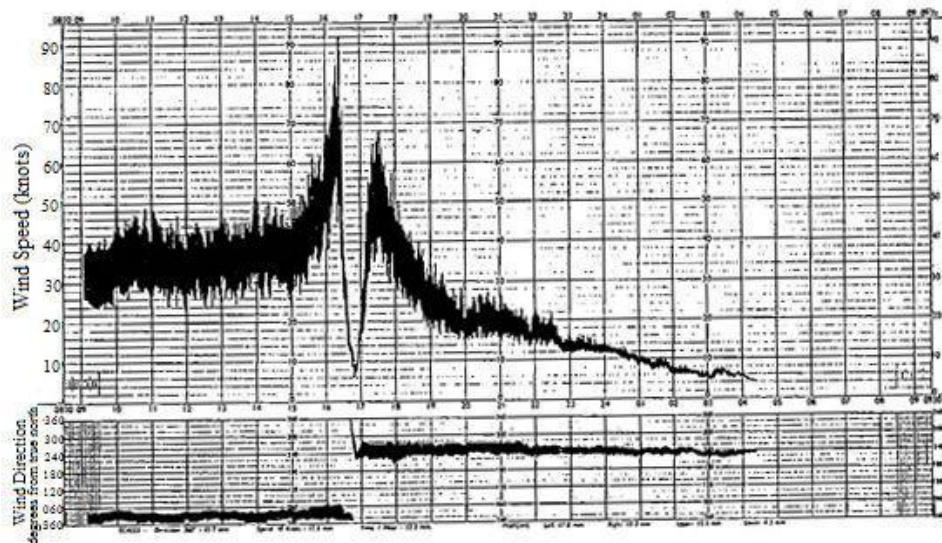


Figure 2.5: Cyclone anemograph for a tropical cyclone (credited to: Holmes, 2001)

The fluctuating response of a structure can be described using two components: a background component and a resonant component. The background component follows the applied wind pressures whilst the resonant component is the amplification of the applied loading effects which occurs when the frequency of the fluctuating wind load exceeds the natural frequency of the building (Uematsu and Isyumov, 1999; Ginger *et al.* 2000). However, the resonant response can be neglected since the frequency of the wind fluctuations (less than 1 Hz) is generally less than the frequency of low-rise buildings and its components (Holmes, 2001).

The fluctuations in the applied pressure follow a non-Gaussian process for roof cladding when considering the probability density function, which measures the variations in amplitude of the pressure fluctuations at a given location (Homes, 2001). This is crucial for cladding design given that over a large area the pressure fluctuations tend towards a Gaussian process whilst small tributary areas, such as those associated with cladding fasteners, are dominated by non-Gaussian pressure fluctuations (Suresh Kumar, 1999). In addition, it was reported that non-Gaussian wind loads tend to induce greater fatigue damage than Gaussian wind loads (Suresh Kumar and Stathopoulos, 1999).

Internal pressures are also produced by the air either through building porosity or a dominant opening in the building envelope. Should the airflow pass through a dominant opening in a wall, such as a broken window or failed door, the internal pressure may be equal to the external pressure acting on the wall containing the opening. Should the building remain sealed, only a low internal pressure results. As the windward wall experiences the largest positive external pressure, then a dominant opening here would generate the largest positive uplift internal pressures. These large internal uplift pressures, in conjunction with the large external suction pressures at the roof edge, produce critical net uplift loads on the roof (Ginger *et al.* 1997).

The pressure histories applied to roof cladding can vary significantly depending on the roof geometry, the terrain, the applied cyclone's characteristics and even the cladding's location on the roof. Xu (1996) found that the differing roof types alone greatly affect the nature of the pressure fluctuations in terms of the number of cycles and the cycle distributions. This variability and the dependence of fatigue on the time history of the pressure trace require a "design" cyclone rather than simply specifying a single design wind speed, which is custom. Jancauskas *et al.* (1994) developed a 'design' cyclone specifically for fatigue related applications. The design cyclone pressure history also accounts for the change in wind speed and direction of a cyclone over its duration which is assumed to be five hours. Jancauskas *et al.* (1994) also assumed that the low-rise building in question was positioned adjacent to the eye of the cyclone half way through the duration so that the maximum wind speed was then a superposition of the cyclone's forward movement and rotational wind. This maximum wind speed was taken to be the ultimate wind speed of 70 m/s to correspond with wind load standards AS/NZS 1170.2. The remaining characteristics of the cyclone were based on Cyclone Winifred which devastated Innisfail in 1986. Cyclone Winifred was a severe cyclone of the same category as Cyclone Tracy.

Henderson (2010) used the wind speeds and directions of the design cyclone defined by Jancauskas *et al.* (1994) in conjunction with pressure coefficient time histories from the United States' National Institute of Standards and Technology (NIST) database to create a design cyclone pressure trace. The pressure trace was for the corner region of a roof with a pitch of 5° and a 5 m eaves height, with a dominant opening in the windward wall occurring midway through the duration. The dominant opening was deliberately introduced simultaneously with the peak passage of the cyclone, where the building is positioned close to the eye and the wind speeds are compounded by the forward movement of the cyclone. The resulting pressure trace is shown in Figure 2.6 and highlights the significant fluctuations in the net uplift pressures.

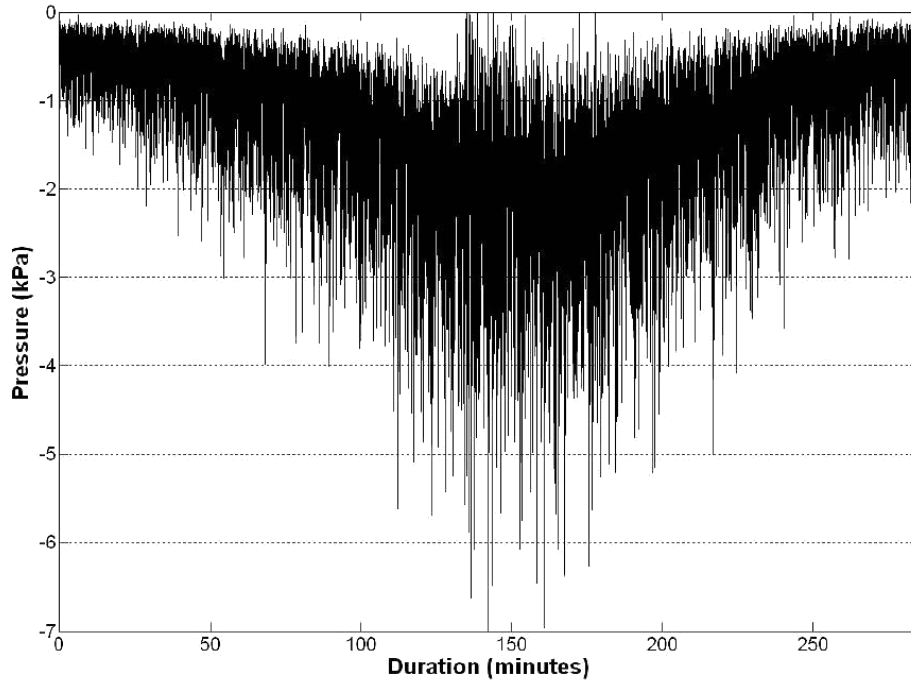


Figure 2.6: Design cyclone pressure trace (credited to: Henderson, 2010)

Wind load standards, AS/NZS1170.2 (AS/NZS, 2011), describe a process for determining design wind loads for both the ultimate and serviceability limit states. Wind load standards consider the loading to be quasi-static (Uematsu and Isyumov, 1999; Ginger and Letchford, 1999).

The peak design wind pressure (p_{design}) is given by:

$$p_{design} = \frac{1}{2} \rho_{air} V^2 C_{fig} C_{dyn} \quad (2.1)$$

Where ρ_{air} is the density of air, V is the design gust velocity, C_{dyn} is the dynamic factor and C_{fig} is the aerodynamic shape factor (AS/NZS, 2011).

The aerodynamic shape factor (C_{fig}) is a factored quasi-static pressure coefficient. For external pressures, the external pressure coefficient is specified for regions of the building envelope for various building dimensions and roof shapes (AS/NZS, 2011). The effect of simplifying the external pressure coefficient to discrete regions can be seen in Figure 2.7. A number of factors are then applied to the design pressure coefficient to account for the considerable variation in applied pressures. These factors include an area reduction factor that accounts for the significant variation in pressure across a large tributary area and a local pressure factor that accounts for increased pressures at areas of flow separation (Sharma and Richards, 1999; Ginger and Holmes, 2003).

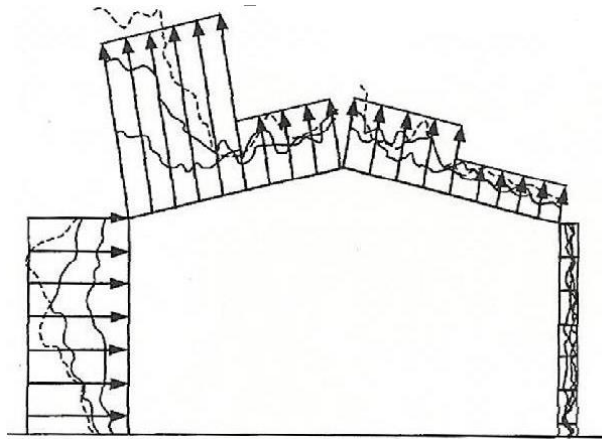


Figure 2.7: Simplified code distributions and external pressure distributions at three different time instances (credited to: Holmes, 2001)

2.3 CLADDING FATIGUE

Fatigue is defined as the failure of a material or structure due to repeated loading (Madayag, 1969). For metal roof cladding, the repeated loading that causes fatigue is the fluctuating suction pressures applied to the roof envelope during a severe wind event (Morgan and Beck, 1977). Fatigue failure of metal roof cladding was first documented during the damage investigations that followed Cyclone Tracy in 1974 (Walker et al, 1975). Prior to Cyclone Tracy, cladding was assessed for strength using only a static pull-through test (Walker, 1980).

Static pull-through failure occurs when the loads applied are large enough to form a deep draw down of the fastener with radial splitting of the fastener hole, allowing the fastener to pull through the cladding sheet (Morgan and Beck, 1977). Static pull-through failure is sudden and requires a single monotonic load of sufficient magnitude rather than repeated loading. Fatigue failure is also a mode of pull through failure, and occurs at much smaller loads than that of static pull-through. The prolonged and fluctuating loads applied to the cladding generate fatigue cracks in the vicinity of the fastener. These cracks then propagate to a sizeable hole that allows the fastener head to pull through the cladding sheet.

Morgan and Beck (1977) inspected the roof cladding damage and failure caused by Cyclone Tracy and compared the observed crack formations to the various crack formations recreated in laboratory testing. Through this comparison a step wise progression of sheeting failure was identified. Fatigue cracks initiated surrounding the first internal fasteners at the roof edge (in high suction pressure zones). The cracks propagated under continual loading and allowed the fasteners to pull through the cladding, shedding their load to the adjoining edge fasteners. This increased load was then large enough to cause a static pull-through failure of the edge fasteners, dislodging the entire cladding sheet.

Extensive experimental studies were conducted to develop appropriate fatigue testing methods which have produced systems that are unlikely to fail in fatigue during a cyclone. The Darwin Area Building Manual (DABM) was the first standardized cladding fatigue test instigated in Australia following the devastation caused by Cyclone Tracy. Prior to the DABM, cladding strength was determined by applying static loads. The DABM applied 10,000 cycles with a load range of 0 to 100% of the design load with a final overload cycle to 180% of the design

load. The DABM was limited as it did not accurately represent cyclonic loading and was considered too severe, although it successfully served as an interim method (Mahendran, 1994a; 1995).

Melbourne (1977) and Beck and Stevens (1979) presented revised low-high loading sequences that each used a form of the up-crossing analysis method to equate cyclonic pressure trace data to cyclic loads of varying load ranges. During the development of these loading sequences, it was also found that the DABM test was too conservative. However, the loading sequences created by Melbourne (1977) and Beck and Stevens (1979) were considered too complicated and were simplified to the TR440 test that was then adopted in all cyclone regions excluding the Northern Territory (EBS, 1978).

The use of two different test methods depending on the region created discontent for manufacturers and designers who were required to satisfy two different criteria for the same roofing (Mahendran, 1994a; 1995). Further studies also showed that the TR440 test was conservative for trapezoidal cladding whilst unconservative for corrugated cladding, with some roofing systems that failed during Cyclone Tracy passing the test (Xu, 1993; Mahendran, 1994a; 1995). Consequently, Mahendran (1994a) developed the Random Block Load test (RBL) to describe the fatigue loading of cladding during a cyclone which even included the effects of changing wind speed and direction.

Mahendran (1994a) used a loading matrix developed by Jancauskas *et al.* (1994) as the basis of the RBL test. In addition to generating the “design” cyclone pressure trace, Jancauskas *et al.* (1994) created a loading matrix for the design cyclone by equating the pressure trace to a discrete number of cycles at various mean pressures and ranges. Jancauskas *et al.* (1994) used the rain-flow cycle counting method to determine the equivalent number of cycles from the pressure trace. This method had been found by Dowling (1972) to be most appropriate for distinguishing load cycles in wide-band, non-Gaussian processes such as roof pressures.

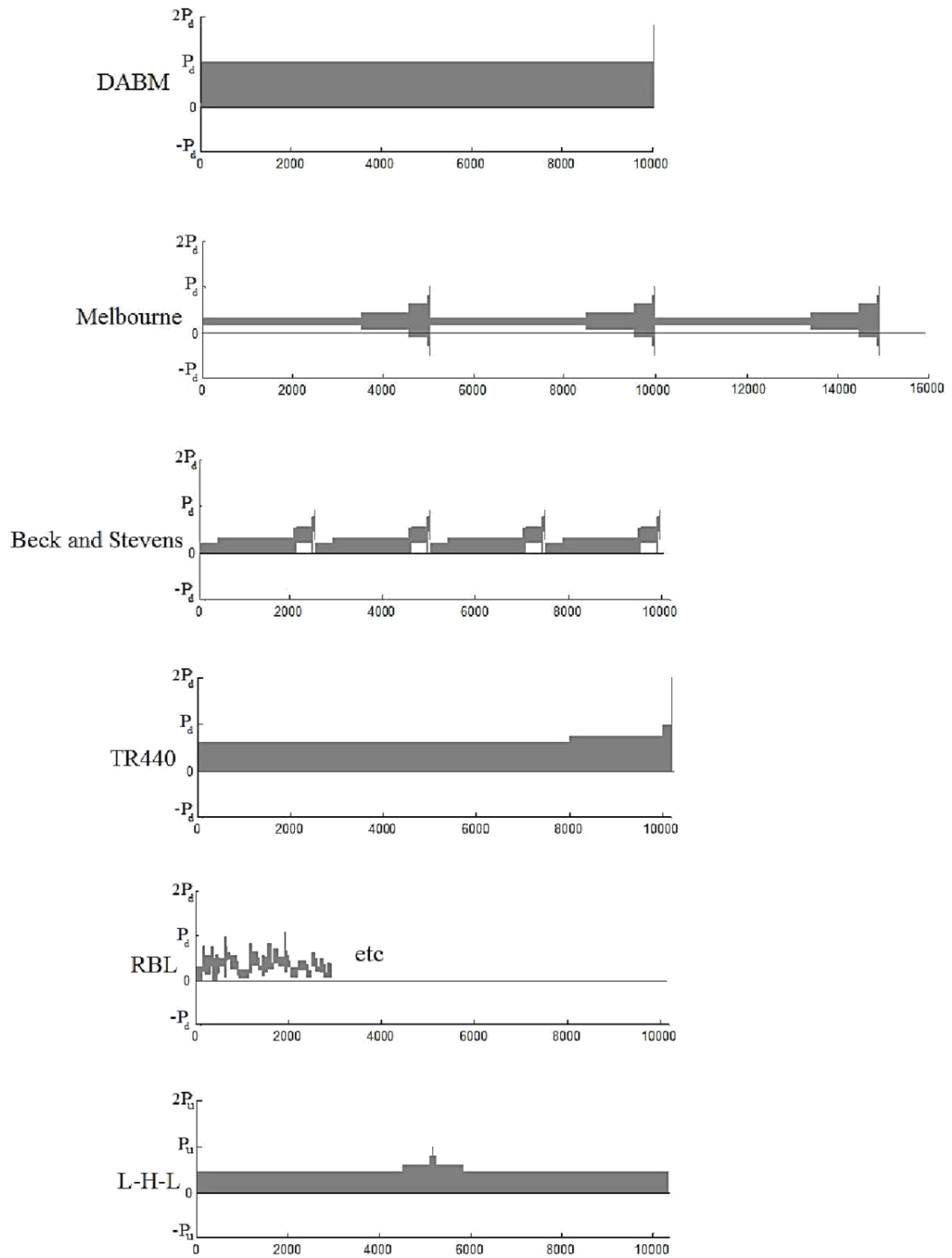
Mahendran (1994a) discretized the design cyclone loading matrix by dividing the load blocks with more than 200 cycles into multiple smaller blocks that did not exceed 200 cycles. This ensured that when a block was selected at random and applied to the cladding sheet, it would more accurately simulate the fluctuations in pressure caused by a cyclone. The RBL sequence was then determined by a computer which selected a load block at random one after the other.

For widespread implementation, Mahendran (1994a; 1995) simplified the RBL test into an equivalent Low-High-Low load sequence that mimicked the passage of a cyclone. Mahendran (1994a; 1995) sorted the loading blocks of design cyclone loading matrix based on their maximum load having found that the fatigue mechanisms for all types of cladding were more sensitive to the maximum load applied. The grouped load blocks were then equated to 5 groups with ranges from 0 to 0.2, 0.4, 0.6, 0.8 and 1 times the ultimate design load using experimental fatigue life equations and Palmgren-Miner law. These load blocks were then halved and arranged to form a Low-High-Low sequence to mimic the design cyclone where the building experiences the maximum wind speed midway through the duration.

Currently, cladding fatigue endurance is tested using a modified Low-High-Low loading sequence that was adopted by the Building Code of Australia in 2007 (Australian Building Codes Board, 2007). The Low-High-Low loading sequence is scaled based on the ultimate

design pressure (P_u) applied to the cladding during a cyclone as determined using AS/NZ1170.2. The strength of the cladding, or endurance limit, is the design pressure that causes failure of the cladding system during the applied Low-High-Low test where failure is considered to be when a fastener pulls through the cladding sheet. No consideration is made to multiple cyclonic events accumulating damage typically because the cladding is replaced following such an extreme event. Should cladding experience an extreme cyclonic event similar to that of the ultimate limit state design, although failure is unlikely, the cladding will experience damage with cracking and deformation at the fastener. This cracking requires that the cladding be replaced to avoid rust or rain to penetrate the building envelope.

Figure 2.8 describes each loading sequence in graph form to highlight the differences between each.



*Where P_d is the working stress design load and P_u is the ultimate limit state design load where $P_u = 1.5P_d$

Figure 2.8: Loading Sequences for Cladding Fatigue Testing

2.4 CLADDING TESTING ARRANGEMENTS

The line load method was utilized by Beck and Stevens (1979), Mahendran (1990a; 1990b), Xu and Reardon (1993) and Xu (1993; 1995) to test the fatigue response of cladding. The mid-span line load method applied line loads to the cladding, rather than a surface pressure. The basis of the line load method was to recreate the same fastener reaction and bending moments

at the central fastener that would occur if a uniform surface pressure was applied. Linear beam theory was used to determine the equivalent span and line load necessary to simulate the uniform uplift load. Figure 2.9 compares the two equivalent systems.

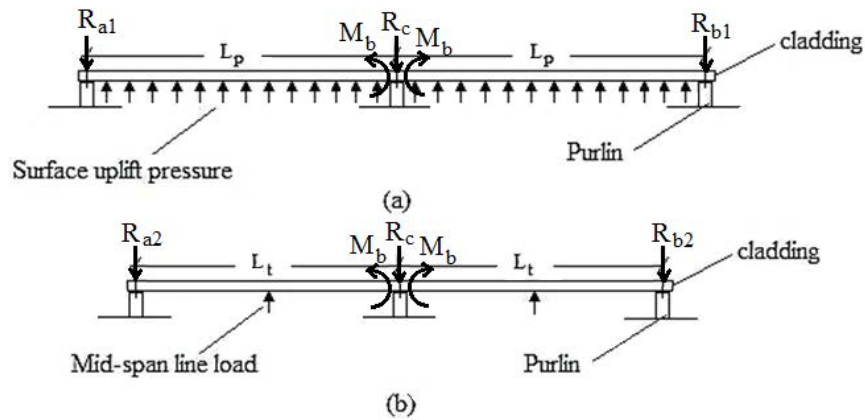


Figure 2.9: Mid-span line load method (a) prototype and (b) equivalent test set up

Mahendran (1990a; 1990b), Xu and Reardon (1993) and Xu (1993; 1995) were limited by the available technology which prevented the application of surface pressures, necessitating the need to develop equivalent methods such as the line load method. However, current technology has the ability to apply a uniform surface air pressures for roof cladding testing. This technology includes the airbox, which is currently implemented in cladding fatigue testing at the Cyclone Testing Station at James Cook University in Townsville, and the pressure load actuator (PLA) which can apply complex pressure traces to cladding sheets.

The airbox has the ability to apply a uniform positive pressure to the underside of a cladding specimen. The airbox is limited as the pressure applied can either be on or off, that is, applying pressure or applying zero pressure which produces the desired cyclic loading sequence (James Cook University, 2010). In contrast, the pressure load actuator has the ability to apply both suction and uplift pressures in a variety of traces. The PLA was developed by the University of Western Ontario and uses a blower to generate the required air flow rate and pressure rise in conjunction with a rotating disk inside the valve to regulate the pressure applied to the specimen. A computer interface is used to control the pressure output. Figure 2.10 demonstrates the ability of the PLA to accurately mimic requested pressure traces, comparing a one second portion of requested trace with the achieved trace of the PLA (Henderson, 2010).

The airbox volume and leakage affect the output pressure capabilities of the PLA. Henderson (2010) performed a number of trials and determined that an airbox size of 2000 mm x 890 mm x 300 mm was optimum whilst accommodating a double-span, single-width cladding specimen.

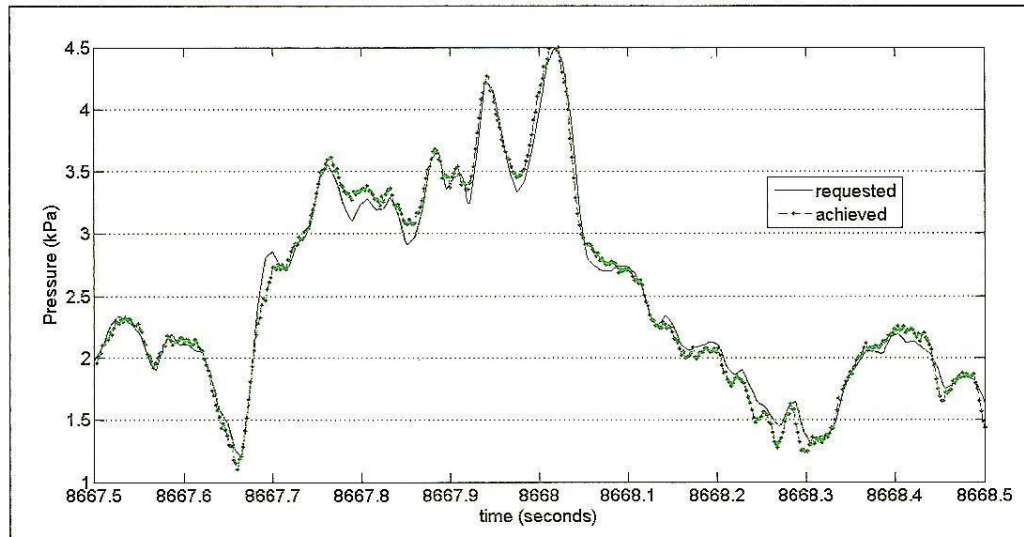


Figure 2.10: Plot of PLA achieved pressure response in comparison to requested time pressure trace (credited to: Henderson, 2010)

In addition to full scale testing such as the line load method and airbox studies, some researchers have also used small isolated cladding-fastener tests – referred to as small scale testing by authors – to primarily study static pull-through failure of cladding. Mahendran (1992) successfully extended small scale testing to study the fatigue response of roof cladding. Mahendran (1992) suggested that since fatigue failure was localized to a small region surrounding the fastener head then ideally both static and fatigue studies could be simplified by focusing on a small area around one critical fastener rather than the full two-span cladding sheet. After trialing a number of arrangements, Mahendran (1992) suggested a 240 mm x 240 mm section of cladding as pictured in Figure 2.11 (a), fastened at each quadrant to fixed supports and with a central fastener free to deflect, produced results most similar to full scale tests. In reality, wind uplift attempts to lift the cladding over a stationary screw, whilst in the small scale study this process was reversed, with the central fastener deflected to induce loading.

Mahendran (1992) compared both the static and fatigue response of the cladding to validate this testing arrangement which he referred to as small scale tests. For the static response, this required checking that the small scale test provided similar dimpling and plastic deformation surrounding the fastener. Figure 2.11 (b) compares the load-deflection curves for the full scale and small scale tests and shows that both methods undergo a sudden loss of stiffness at similar loads. For the fatigue studies Mahendran (1992) validated the small scale arrangement by confirming that prior overload cycles reduced the fatigue strength of the cladding as was previously observed in full scale studies (Mahendran, 1990b). No information is provided with respect to the types of crack formations that were produced using the small scale arrangement.

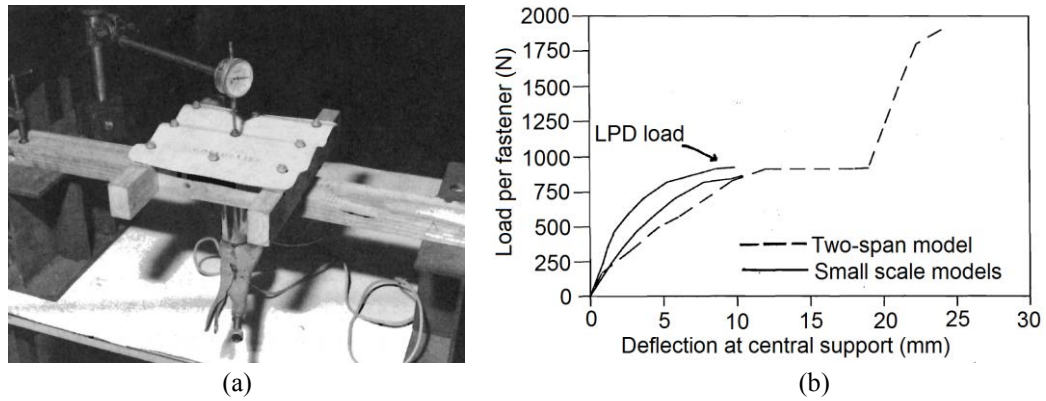


Figure 2.11: (a) Small scale experiment and (b) load-deflection curve for small scale experiment (Mahendran, 1992).

2.5 CLADDING BEHAVIOUR

2.5.1 Response of Cladding Subject to Monotonic Loads

Morgan and Beck (1977) were possibly the first to identify that fatigue cracks initiated in zones of high deformation surrounding the cladding fasteners. Beck and Stevens (1979) then found that the fatigue response of cladding was directly related to the load at which cladding undergoes local plastic deformation (LPD). LPD, also referred to as local plastic collapse, is characterised by the buckling and flattening of the fixed crests at the central span with the bulging of the unfixed crests for corrugated cladding, as shown in Figure 2.12. Given these findings, a large proportion of the experimental investigations involving fatigue have studied the response of cladding subject to a static uplift load. Mahendran (1990a) investigated the static behavior of corrugated cladding using the mid-span line load method and found that LPD load was between 550 and 650 N per fastener, regardless of the span of the cladding when the cladding was fastened at each alternate crest.

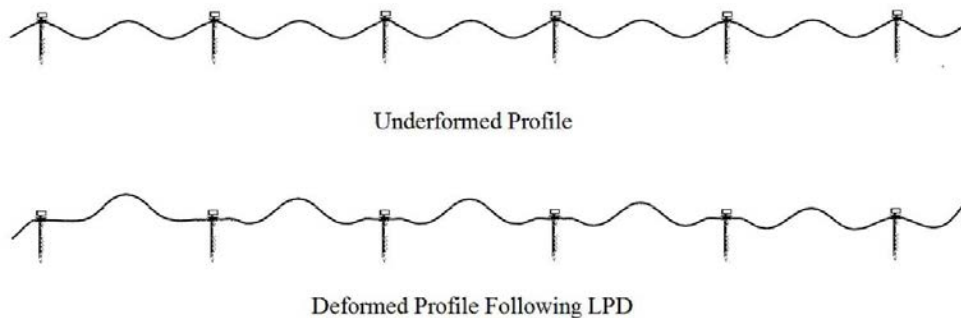


Figure 2.12: Corrugated cladding profile undeformed and following LPD

The static response of cladding can be categorized into four stages which are shown in Figure 2.13. The first stage is characterised by unscrewed crests deflecting many times more than the adjacent screwed crests. Stage 2 is then the local plastic deformation stage which is followed by geometric stiffening of the cladding, shown as Stage 3. The geometric stiffening of the cladding is due to the gross change in the sectional properties caused by the plastic collapse. Finally, the cladding fasteners pulled through cladding which is considered as ultimate failure and is shown as Stage 4.

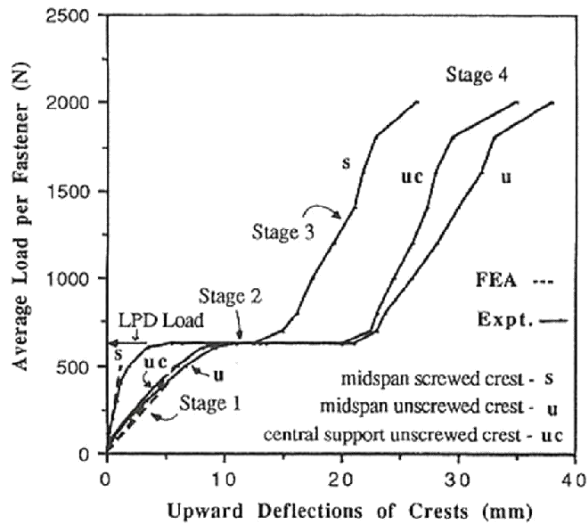


Figure 2.13: Static load-deflection curve for corrugated cladding (credited to: Mahendran, 1990a)

Xu and Reardon (1993) also investigated the response of the various cladding types subject to static loads using the mid-span line load method. The behavior of the cladding was found to be dependent on the cladding profile, with the three different cladding types exhibiting very different responses. Figure 2.14 presents the load-deflection curves for three cladding types at the mid-span of an unfixed crest (labelled as Point D).

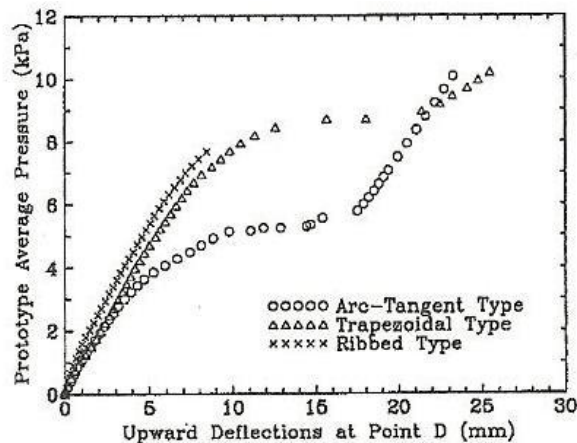


Figure 2.14: Static load-deflection curves for all three cladding types (credited to: Xu and Reardon, 1993)

Corrugated cladding (arc-tangent type) described a similar load-deflection curve to that documented by Mahendran (1990a) with an LPD load of approximately 600 N per fastener. The trapezoidal type cladding responded in a similar manner to the corrugated cladding but at larger loads and with a deeper snap-through buckling. The LPD load for trapezoidal type cladding ranged between 1000 and 1160 N per fastener. The rib pan cladding was the most dissimilar of the cladding types and did not exhibit any significant local plastic collapse or geometric stiffening. The rib pan cladding would split under the screw head upon local plastic collapse, resulting in ultimate failure. The corresponding reaction force at failure was 1350 N per fastener. The large local plastic collapse and resulting geometric stiffening of the other two profiles were considered a result of the unfastened crests. These unfastened crests allowed for large deformations and subsequently generated a differing stress distribution. The rib pan

profile possessed the flat pan rather than an unfastened crest so the large deformations were restricted. Xu and Reardon (1993) also concluded that the buckling of roof cladding under wind uplift is mostly due to the fastener reaction force given that the differing spans created only small variations in the LPD fastener reaction load.

Xu (1993) later classified the static response of corrugated or trapezoidal type cladding into four stages which are shown in Figure 2.15. The stages of response as documented by Xu (1993) are similar to that documented by Mahendran (1990a) although Xu (1993) considered Stage 1 to be the elastic deformation stage where the load-deformation curve is generally linear. Stage 2 then describing the softening of the cladding as it begins to yield and Stage 3 is the local plastic collapse stage followed by the geometric stiffening stage (Stage 4).

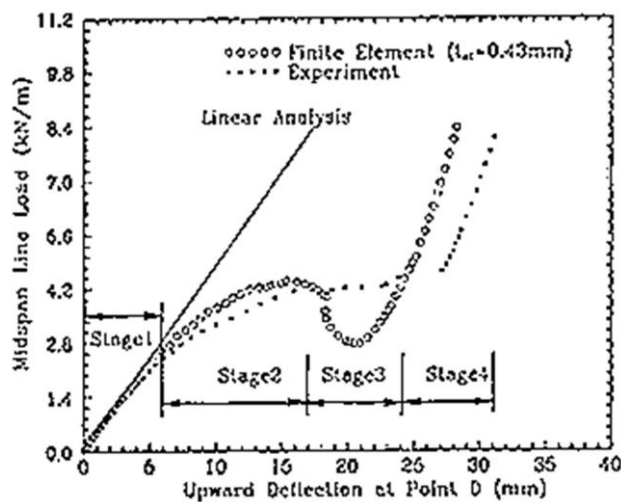


Figure 2.15: Comparison of FEA and experimental results (credited to: Xu, 1993)

Henderson (2010) and Henderson and Ginger (2011) also applied static loads to corrugated cladding using the PLA and found the results to be similar to those found using the mid-span line load method. In particular, Henderson (2010) and Henderson and Ginger (2011) studied the response of corrugated cladding subject to static uplift pressure and found that LDP occurred at a fastener reaction load of 600 to 650 N. A three axis load cell was used to measure the fastener reaction during loading and it recorded a lateral reaction force at the screw following LPD, with a magnitude of approximately 15% of the normal reaction force.

Henderson (2010) and Henderson and Ginger (2011) utilized static point load tests to determine the effective tributary area for a cladding screw using influence coefficients. Australian Standards describe the tributary area as half the distance between neighboring fasteners longitudinally and laterally. Henderson (2010) and Henderson and Ginger (2011) showed that typically the load was transferred along the stiff fixed crest with approximately 5% of the load shed to adjacent fasteners. This suggests that the tributary area of a cladding fastener is slightly elongated along the fastened crest with an area of 0.14 m² for corrugated cladding with a 900 mm span.

Considerable efforts were also made to study the static response of cladding numerically. Mahendran (1990b;1994b), Xu (1993), Xu and Teng (1994), Mahaarachchi and Mahendran (2004; 2009) and Lovisa *et al.* (2012) have all developed various numerical models using finite element analysis (FEA) that can successfully predict the static response of cladding. Validated

crest-fixed rib-pan cladding and discretized the model using four-node quadrilateral shell elements. Both the splitting characteristics of the material and the effects of the neoprene washer were included in the model, although the anisotropic qualities of the cladding sheet were assumed to be negligible and subsequently isotropic material properties were used. In addition, the model included geometric imperfections and residual stresses.

The splitting characteristics of the material were found by Mahaarachchi and Mahendran (2009a). To develop a strain criterion for splitting, rib-pan cladding was statically loaded until pull-through failure occurred, while the strains in the sheeting of the cladding surrounding a fastener were measured. The strains at the initiation of splitting indicate that when transverse splitting occurs the membrane tensile strain is 60% of the maximum tensile strain where the maximum tensile strain is equal to the measured failure strain from coupon tests.

Modelling the buckling of the cladding is difficult given that local buckling generates an unstable numerical solution within a static analysis. The stiffness matrix of the affected elements can become singular, resulting in excess strain energy and subsequently moving the solution out of equilibrium (Crisfield, 1991; Hibbit et al. 2009). In reality, this excess strain energy is dissipated in the form of kinetic energy as the material buckles, and a static analysis cannot account for the inertial effects. Consequently, Mahaarachchi and Mahendran (2004) utilized a modified form of the static analysis by implementing the Riks method. The Riks method is a form of the arc-length method that maintains equilibrium in unstable analyses by factoring the applied load. This method was also implemented by Xu (1993) and Xu and Teng (1994).

A static analysis with the Riks method is computationally efficient but does not realistically describe the changes in strain within the buckling region (Hibbit et al. 2009). Regardless, comparison of the FEA results with those found experimentally by Mahaarachchi and Mahendran (2000) showed the numerical model accurately predicted the pull-through failure loads. This validated model was then used in a parametric study that resulted in a design strength formula for the rib-pan cladding (Mahaarachchi and Mahendran, 2004).

A numerical model was similarly constructed for trapezoidal cladding by Mahaarachchi and Mahendran (2009b). The model was once again validated by comparison with experimental data and utilized in a parametric study. A design static strength formula was developed and it was assumed that the formula could then be adapted to fatigue design using a reduction factor since the static uplift strength of the cladding is related to the fatigue strength of the cladding.

Lovisa *et al.* (2012) developed a numerical model of corrugated cladding that accounted for the anisotropic material properties and some strain hardening characteristics of the cladding. The model was also discretized using four node quadrilateral shell elements, similar to those used by Mahaarachchi and Mahendran (2004; 2009b). Careful consideration was taken when selecting the element size in the transverse direction (x direction) to ensure the curved profile, and the subsequent deformation, was minimally effected by the planar elements. Consequently, 14 elements were used to discretize a single corrugation width, which is similar to the 12 elements chosen by Mahendran (1990a).

The model developed by Lovisa *et al.* (2012) is unlike previous models as it utilized a dynamic analysis to simulate the buckling and post buckling behavior of the cladding, rather than the

Riks method. A nonlinear dynamic analysis was favored over the modified static analysis as it simulates the transformation of excess strain energy into kinetic energy and can therefore provide a more accurate prediction of the change in strain surrounding the fasteners, which is necessary for future fatigue studies.

The model also simplified the fasteners as two rings of partially restrained nodes, similar to Xu (1993) and Xu and Teng (1994). The first ring of nodes was located at the fastener hole edge whilst the second ring of nodes was located where the outer edge of the EPDM seal would hypothetically be located. The second ring of nodes was included to mimic the load dispersal effect of the EPDM seal.

The numerical model developed by Lovisa *et al.* (2012) successfully simulated the deformed shape of the cladding for all the applied loads as described in Figure 2.17. The study showed good agreement between numerical and experimental results for the load-deflection data and the stress-load data as shown in Figure 2.18.

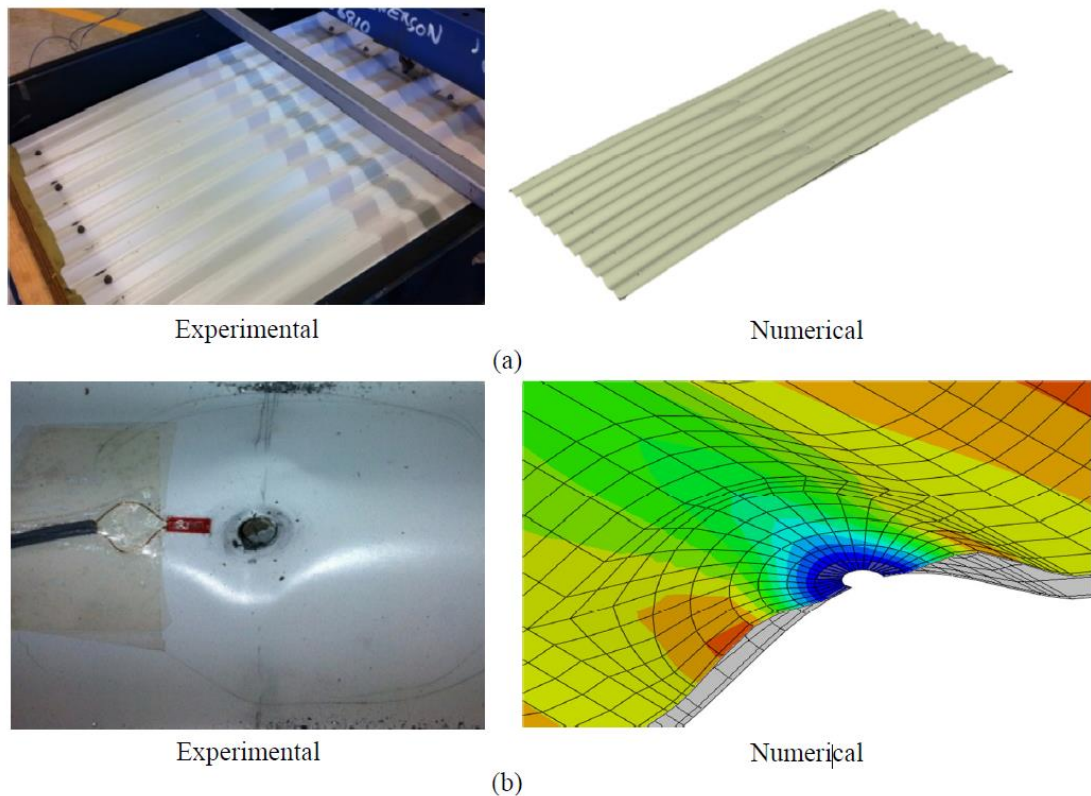


Figure 2.17: Comparison of experimental and numerical deformed shape for (a) LDP and (b) residual permanent deformation (credited to Lovisa *et al.* 2012)

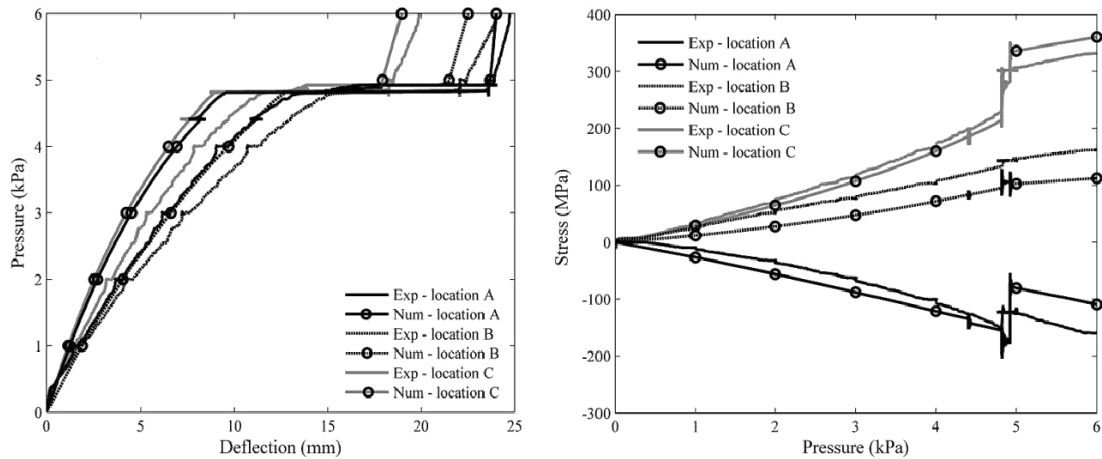


Figure 2.18: Comparison of experimental and numerical (a) Load-deflection data and (b) Stress-load data (credited to Lovisa *et al.* 2012)

Most experimental and numerical studies of roof cladding typically neglect the effects of the batten or purlin supporting the cladding in order to simplify the problem and focus on the cladding-fastener connection directly. However, Lucas *et al.* (1997a; 1997b) created a numerical model of the purlin-cladding system in a bid to study the failure of cold-formed steel purlins and found that the behavior of the purlins was strongly influenced by the behavior of the cladding and likely vice versa. In situ, the cladding sheet provides rotational and shear stiffness to the purlin and including the cladding sheet in the model was necessary to obtain an accurate solution. The effects of the purlin-cladding connection are somewhat minimized through use of timber battens rather than cold-formed steel purlins as the battens themselves resist rotation. However, cold-formed steel purlins are becoming increasingly more popular and future studies on cladding fatigue will need to incorporate the effects of the purlin-cladding connection.

2.5.2 Response to Cyclic Loading

Cyclic loading has often been employed to study the mechanisms of crack propagation in roof cladding without considering the much more complex nature of fluctuating wind loading. Cyclic loading, also known as constant amplitude loading or repeated loading, describes the repeated application of the same load cycle which is usually sinusoidal in appearance, as shown by Figure 2.19. The load cycles can have differing ranges (ΔS) which are determined by $\Delta S = S_{\max} - S_{\min}$, or they can be described by their load ratio (R) which is given by $R = S_{\min} / S_{\max}$. A load cycle is also characterised by the peak load (S_{\max}) or the mean load (S_{mean}) which is calculated by $S_{\text{mean}} = (S_{\max} - S_{\min}) / 2$.

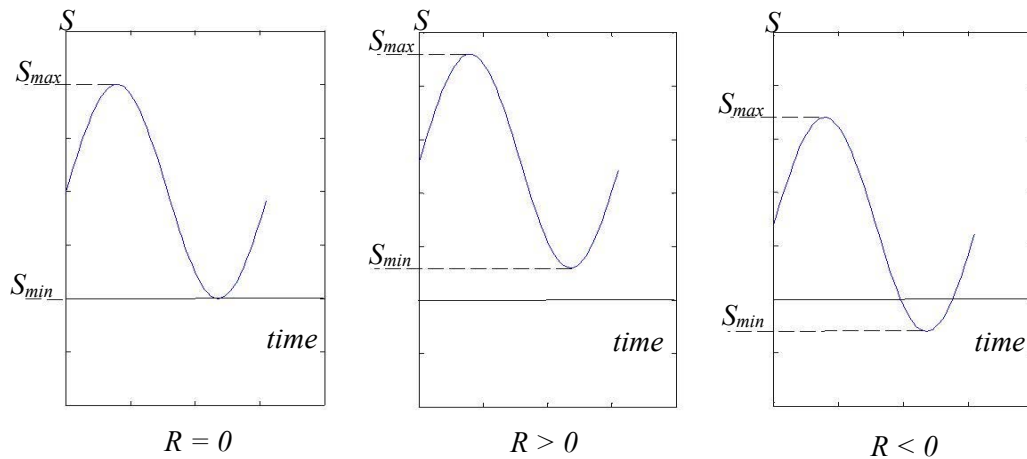


Figure 2.19: Load cycles for constant amplitude loading

Morgan and Beck (1977) were among the first to apply cyclic loading to corrugated cladding to investigate fatigue. Corrugated cladding was the focus of the investigation as it was popular in Darwin and had experienced widespread failure during Cyclone Tracy (Walker, 1975; Morgan and Beck, 1977). At that time, realistic cyclonic wind loading could not be replicated nor were the specific characteristics of the cyclonic loading known so repeated load tests were conducted as an alternative. The load cycles applied had a minimum load of zero and therefore a load ratio of zero.

Morgan and Beck (1977) investigated differing fastener systems and found that the strength of cladding reduced as the number of cycles applied increased. It was also found that for the same load per fastener, an increase in the number of fasteners used reduced the fatigue strength of the cladding and resulted in differing crack formations. Morgan and Beck (1977) observed three distinct crack formations as shown in Figure 2.20. These crack formations would occur depending on the magnitude of the applied load and the number of fasteners and are characterised as:

- Type A: commonly found following static pull through failure, where the cladding sheet splits.
- Type B: cracks initiated away from the fastener hole in regions of plastic deformation with the cracks then propagating primarily in the longitudinal direction.
- Type C: similar to Type B, cracks initiated in regions of plastic deformation but propagated primarily in the transverse direction.

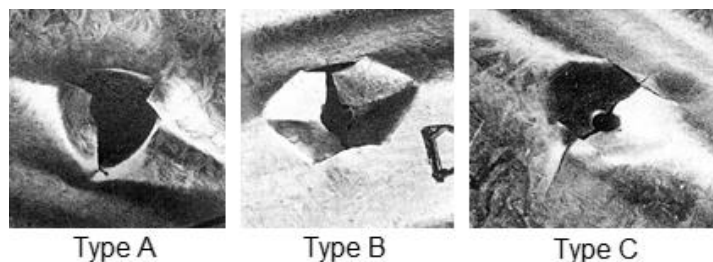


Figure 2.20: Crack formations observed by Morgan and Beck (1977)

Beck and Stevens (1979) used cyclic load tests with a load ratio of zero to develop fatigue life curves for corrugated cladding. The cladding was fastened at each alternate crest with varying magnitudes of tension introduced into the fasteners. The fatigue life curve, which describes the number of cycles until failure required for a variety of load cycle amplitudes, revealed a distinct bi-linear trend with a transition zone correlating to the LPD load. Beck and Stevens (1979) also found that at loads less than LPD, a larger initial fastener tension required a larger number of cycles to failure. It was hypothesized that the reduced load range caused by the initial fastener tension improved the fatigue strength of the cladding.

Mahendran (1989; 1990b) and Xu (1995) later investigated cladding fatigue under cyclic loading using the mid-span line load method. The resulting fatigue life curves for corrugated cladding, presented in Figure 2.21, show a bilinear trend with the transition point coinciding with LPD which is consistent with that documented by Beck and Stevens (1979). Xu (1995) also applied cyclic loading to trapezoidal and rib-pan cladding and found that the fatigue response of both differed to that of corrugated cladding. Trapezoidal and rib-pan cladding both demonstrated linear fatigue life curves, as pictured in Figure 2.21 (b), rather than bilinear. All of the fatigue life curves were based on cyclic loading with a load ratio of zero.

Both Mahendran (1989; 1990b) and Xu (1995) observed multiple unique crack formations during the cyclic load tests which are shown in Figure 2.22. The various crack formations were dependent on the peak load applied to the cladding. At loads well below LPD, crack formation Type B was observed where the crack initiated at the edge of the fastener hole in line with the centre of the hole.

Crack Type A-B was observed at loads nearing the LPD load when local bending moments increased, with cracks initiating at the hole edge and propagating in the longitudinal and transverse direction. Loads larger than the LPD load created crack Type A where the cracks initiated away from the hole in regions of plastic deformation.

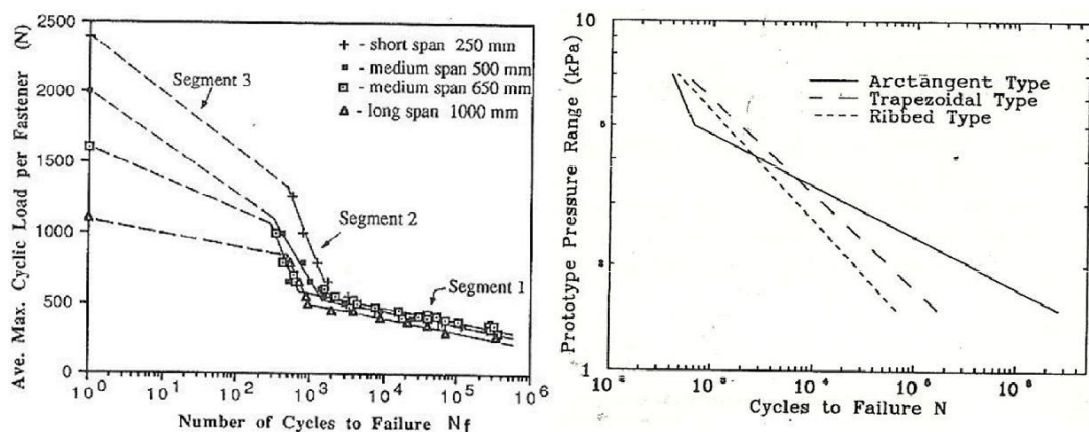


Figure 2.21: (a) Mahendran (1990b) and (b) Xu (1995) fatigue life curves

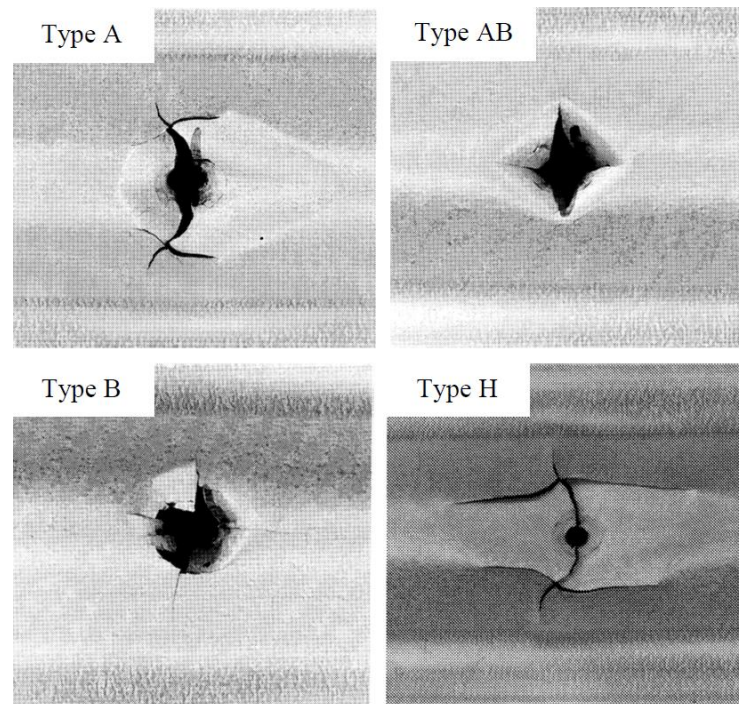


Figure 2.22: Crack Formations (credited to: Mahendran, 1990b)

Mahendran's (1990b) investigation into cladding fatigue also included a study of the effects of varying the mean and range of the applied load cycles. For a given mean, increasing the range decreased the number of cycles to failure as expected. Increasing the mean load for a fixed range generally decreased the number of cycles to failure. However, when the minimum load was greater the LPD load, the number of cycles to failure increased and a new crack formation was observed, Type H. This unusual increase in fatigue strength was attributed to the load cycling beyond LPD rather than through LPD.

Henderson (2010) and Henderson and Ginger (2011) investigated the response of the cladding under cyclic loading using the PLA and found the number of cycles to failure for a given peak load compared favorably to the results presented by Mahendran (1989; 1990b) and Xu (1995). Henderson (2010) and Henderson and Ginger (2011) also observed similar crack formations to those described by Mahendran (1989) and Xu (1995). In particular, Henderson (2010) and Henderson and Ginger (2011) categorized the various crack formations into two groups, the crease crack group and the star crack group. The crease crack group consisted of any cracks that initiated away from the fastener in regions of plastic deformation and the star crack group comprised the cracks that initiated at the hole edge. The crease crack group consisted primarily of 'H' cracks, known as Type A by Mahendran (1990b), and 'T' cracks. Henderson (2010) and Henderson and Ginger (2011) recorded the number of cycles at various peak loads required to initiate cracking and to form various types of cracks, as presented in Figure 2.23. The peak load in this instance is the largest magnitude load being applied where all pressures being applied are suction, and therefore negative, pressures. Figure 2.23 also shows no 'Star' cracks, known as Type A-B by Mahendran (1990b), occurring above the LPD load which is consistent with previous investigations (Beck and Stevens, 1979; Mahendran, 1989; 1990b; Xu, 1995).

Figure 2.23 also highlights the variability of crack propagation due to factors such as material properties and alignment, tightness and position of the screws (Henderson, 2010; Mahendran,

1989). Mahendran (1989), Henderson (2010) and Henderson and Ginger (2011) studied the variability associated with cladding fatigue and found that for cyclic loading the number of cycles to failure can vary by 30% to 40%. The location of the most severe crack can also vary as shown in Table 2.1. Table 2.1 details the cycles to failure, crack formation types and locations of the most severe crack for various load ranges and highlights the random variability of the crack locations. The variability and random nature of crack initiation and propagation considerably complicates the cladding fatigue problem.

Reliability of fatigue results in standard uniaxial fatigue tests of smooth specimens, let alone in complex roof cladding fatigue studies, is an issue. Consequently a great deal of research has explored fatigue reliability in experimental testing suggesting that all fatigue testing must be performed on a sufficient sample size (Osgood, 1970). Standardized fatigue testing of roof cladding under the L-H-L sequence somewhat accommodates this reliability issue by routinely testing a proportion of the cladding produced by multiple manufacturers. Should fewer tests be performed for a particular manufacturer and cladding system, a variation factor must be applied to the ultimate design pressure being applied to the cladding during the L-H-L test to account for possible variation in fatigue results (BCA, 2007).

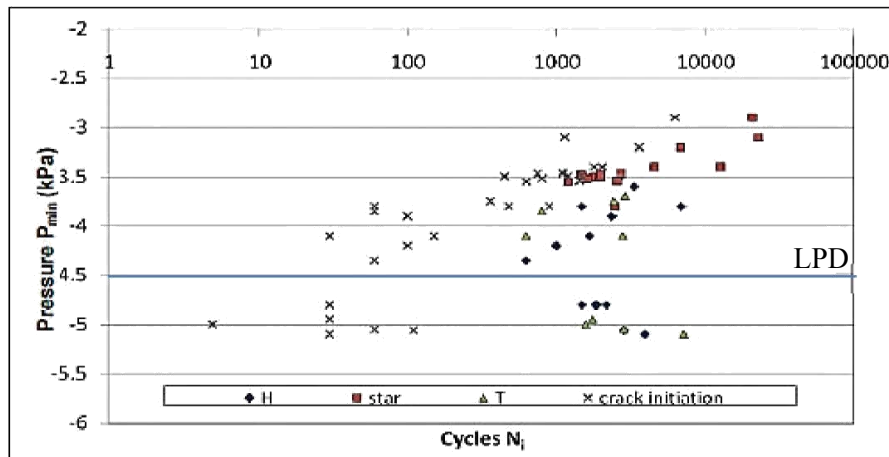
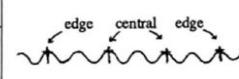


Figure 2.23: Crack initiation and formation for various Peak loads (credited to: Henderson, 2010)

Table 2.1: Corrugated cladding fatigue subject to varying peak loads (credited to: Mahendran, 1989)

Test span = 650 mm (medium span) Loading Frequency = 1.0 Hz

Cyclic Load Range (N/f)	Number of Cycles to		Type of Crack	Pull Through at
	Crack Initiation N_i	Failure N_f		
(1) 0 - 300	n.o.	362,200	B	Edge Hole
(2) 0 - 325	110,000	290,140	B	Edge & Central Holes
(3) 0 - 344	n.o.	274,150	B	Edge Hole
(4) 0 - 350	22,000	62,750	B	Central Hole
(5) 0 - 350	n.o.	320,450	B	Edge Hole
(6) 0 - 375	n.o.	102,200	B	Central Hole
(7) 0 - 387	n.o.	68,650	B	Edge Hole
(8) 0 - 400	n.o.	18,160	A-B	Central Hole
(9) 0 - 400	n.o.	38,710	B	Central Hole
(10) 0 - 413	n.o.	30,210	B	Central Hole
(11) 0 - 413	n.o.	52,150	B	Edge Hole
(12) 0 - 425	n.o.	38,580	B	Edge Hole
(13) 0 - 450	7,000	15,600	B	Edge Hole
(14) 0 - 475	n.o.	7,780	Almost B	Central Hole
(15) 0 - 500	n.o.	4,420	A-B	Central Hole
(16) 0 - 525	n.o.	3,840	A-B	Edge Hole
(17) 0 - 550	700	2,250	A-B	Central Hole
(18) 0 - 600	500	1,560	A-B	Central Hole
(19) 0 - 650	120	650	A	Edge Hole
(20) 0 - 700	80	610	A	Central Hole
(21) 0 - 800	60	430	A	Central Hole
(22) 0 - 1000	60	340	A	Both Central Holes



Henderson and Ginger (2005) investigated the effects of the cycle load ratio (R) on cladding fatigue and found that an increase in the load ratio resulted in an increase in the number of cycles till failure, as shown in Figure 2.24. This is likely due to the reduced flexure per load cycle and the smaller changes in stress at the crack tip (Henderson and Ginger, 2011). The increase in fatigue life for large load ratios suggests that current fatigue testing methods are conservative as cyclones typically contain numerous cycles with load ratios greater than zero (Xu, 1993; Henderson, 2010; Henderson and Ginger, 2011).

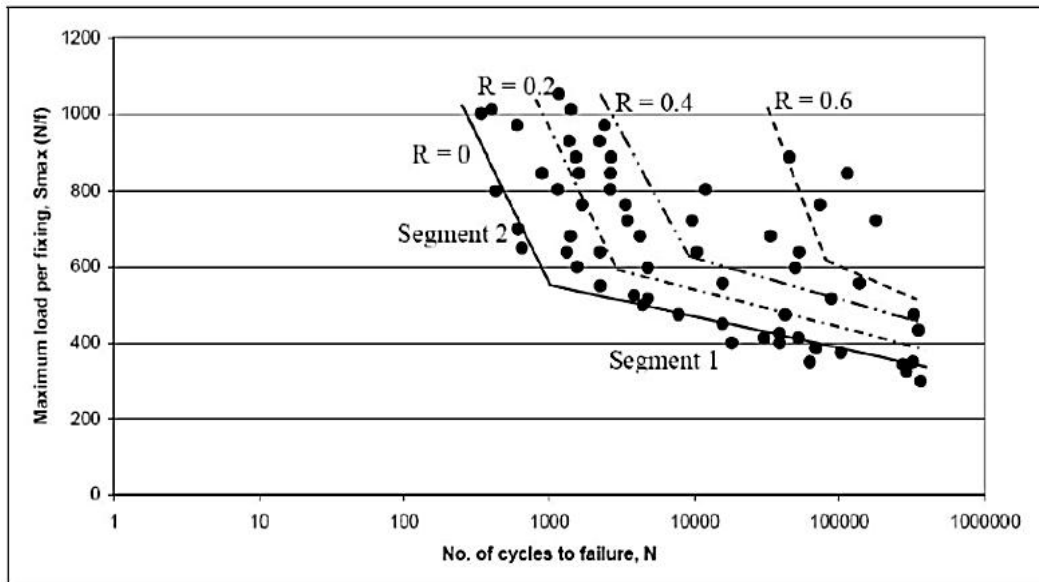


Figure 2.24: Effects of varying load ratio on cycles to failure (credited to: Henderson and Ginger, 2005)

2.5.3 Cyclonic Wind Loading Studies

Henderson (2010) applied realistic fluctuating wind pressure traces to cladding using a PLA to determine the response of the cladding to dynamic pressures and compare these results with cyclic load tests. Henderson (2010) documented the similarity in damage to the cladding, with respect to crack initiation and resulting formations caused by the dynamic pressure trace to that observed during cyclic loading. In addition, cladding deformed and collapsed at loads similar in magnitude to those in the cyclic load tests.

Under dynamic pressure loads, the cladding responded in a quasi-static manner as no resonance of the cladding occurred. The dynamic pressure trace also produced crack patterns that closely resembled those observed during damage surveys that were conducted following cyclonic events. Henderson (2010) and Henderson and Ginger (2011) also highlighted that cladding fatigue strongly depended on the time history of the applied loads, not just the peak load. A severe cyclone pressure trace, based on a gust wind speed of 50 m/s at a height of 10 m, was applied to the cladding to further emphasize the dependence on time history. The cladding experienced the peak pressure of 8.3 kPa nine minutes prior to failure. The peak pressure severely buckled the cladding but the additional nine minutes of loading was required to cause fatigue failure, which occurred at a significantly lower pressure of 6.6 kPa.

2.6 POTENTIAL CLADDING FATIGUE MODELLING METHODS

To the author's knowledge, there are no numerical models that can simulate the fatigue response of cladding with reasonable accuracy. This is largely due to the limitations associated with modelling fatigue cracking in finite element analysis. However, extended finite element analysis (XFEA) has been widely used since it was first introduced in 1999 by Belytschko and Black (Belytschko and Black, 1999) to model cracking. XFEA expands the FEA nodal displacement definition to include additional degrees of freedom (DOF) for nodes in the interior of the crack and at the crack tip. Elements containing additional DOF's are termed enriched elements. In addition, XFEA can model cracking independent of the mesh definition and can propagate a crack through elements rather than being constrained to follow an element's edge (Mohammadi, 2008; Giner *et al.* 2009).

Although XFEA appears to be more suitable than FEA for modelling fatigue cracking, the method is still limited as it is largely based on current fracture mechanics. Crack propagation is determined through either linear elastic fracture mechanics (LEFM) or a cohesive segments approach. Regardless of the limitations inherent in current fracture mechanics theory, both of these methods ensure that the crack propagation follows an arbitrary, solution-dependent path, rather than along a predefined set of paths (Dassault Systems, 2010; Giner *et al.* 2009). Crack initiation is also follows a user defined damage initiation criterion, similar to the splitting criterion created by Mahaarachchi and Mahendran (2009a) (Dassault Systems, 2010). This criterion is generally developed through experimental testing which introduces further limitations.

The cohesive segments approach introduces a series of phantom nodes to represent the discontinuity of the cracked elements. An element dissected by a crack is split into two parts, with each part containing real and phantom nodes depending on the orientation of the crack. Each phantom node corresponds to a real node and when the element is intact the phantom node is constrained to the real node. Once the element is dissected by the crack, the nodes can move apart. The magnitude by which the nodes separate is determined by a cohesive law which is governed by a cohesive strength and once that strength reaches zero the phantom and real nodes can move apart independently. This approach is suitable for both ductile and brittle materials (Dassault Systems, 2010).

The LEFM crack propagation criterion is more appropriate for a brittle material given that it assumes a singular elastic region surrounding the crack tip. Similar to the cohesive segments approach, the LEFM approach also uses phantom and real nodes. The phantom and real nodes separate once the calculated strain energy release rate exceeds the critical strain energy release rate at the crack tip. The strain energy release rate is calculated using a modified virtual crack closure technique (Dassault Systems, 2010).

Although the extended finite element method is limited, it offers the possibility of creating the first numerical model that can predict the initiation and propagation of fatigue cracks for metal roof cladding subject to wind loads.

2.7 MECHANICS OF MATERIALS

The fatigue strength of a material can often be a fraction of the static yield strength of that material. This large discrepancy between strengths is due to the changing mechanical properties of the material subject to repeated loading. This discrepancy is made clear when comparing the stress-strain curve for a material subject to monotonic loads with that subject to cyclic loads. J. Bauschinger in 1886 documented a reduction in yield strength after applying a load of the opposite sign that caused inelastic deformation (Liu, 2005). Consequently, this phenomenon is known as the Bauschinger effect and is illustrated in Figure 2.25. Figure 2.25 (a) shows the resulting stress strain curve for a material being loaded in tension along load path ABC, unloaded to D and reloaded in compression along DEF. Figure 2.25 (b) shows the same load path but in terms of absolute stress and strain to highlight the reduction in strength ($\Delta\sigma_b$) caused by a reverse cycle. The monotonic stress-strain curve is shown using a dashed line with C' being the equivalent monotonic strength of the material at the end of the load cycle (Suresh, 1991).

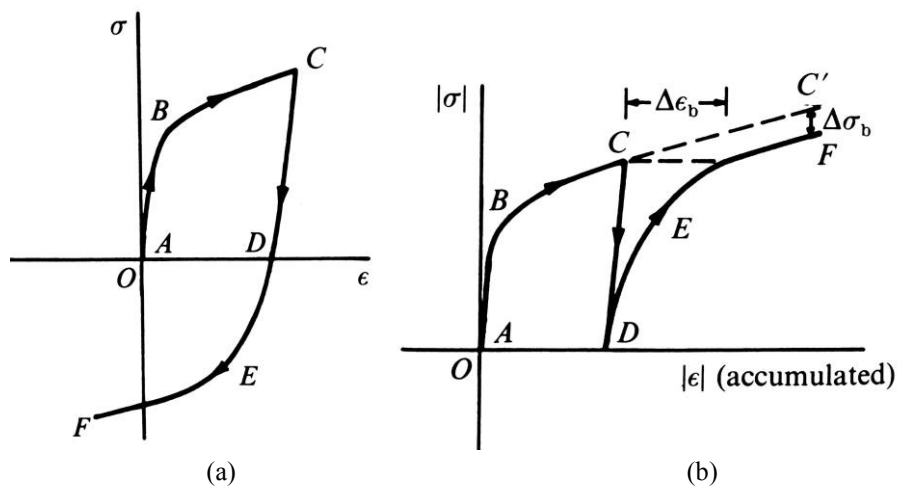


Figure 2.25: (a) Stress-strain diagram highlighting the Bauschinger effect and (b) Equivalent absolute stress-strain diagram (credited to: Suresh, 1991).

Following J. Bauschinger's revelation, numerous studies were undertaken to identify specific characteristics of materials subject to cyclic loads, such as cyclic strain hardening and softening. Figure 2.26 describes the stress-strain diagram for a material subject to fully reversible strain cycles with a peak strain of 0.048 and a minimum strain of -0.048. The material is initially loaded in tension past the elastic limit A_0 to an arbitrarily selected strain of 0.048 (B_0) and unloaded through to a compressive strain of -0.048 (B_1). The portion of the stress-strain cycle from B_0 - B_1 - B_2 is known as a hysteresis loop. Figure 2.26 describes two full hysteresis loops with the terminus of the second loop being B_4 (Liu, 2005).

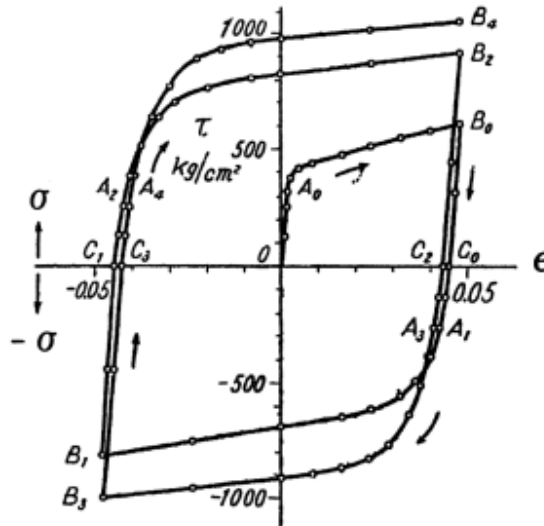


Figure 2.26: Cyclic stress-strain curve under constant strain amplitude (Credited to: Liu, 2005)

Figure 2.26 shows that with each cycle greater stress is applied to reach the target strain; this phenomenon is known as cyclic hardening (Liu, 2005). Some materials also demonstrate cyclic softening where less stress is required to produce the same strain with each cycle. Most heat treated or annealed metals that demonstrate significant strain hardening when monotonically loaded will typically cyclically harden during reversed plastic straining. Metals that have been cold worked, such as the rolling process used to produce corrugated cladding, will demonstrate little to no strain hardening during monotonic loading and will likely cyclically soften during reversed plastic straining (Anand and Parks, 2004). The monotonic stress-strain properties can be used to predict whether cyclic hardening or softening will occur; should the ultimate tensile strength to yield strength ratio be greater than 1.4, hardening will occur and if the ratio is less than 1.2, softening will occur. When the ratio of the ultimate tensile strength to yield strength is between 1.2 and 1.4, the material is typically stable during cyclic loading (Liu, 2005).

Quantifying the material characteristics under cyclic loading typically requires fully reversible tension-compression tests. Strain controlled tests are favorable as plastic strain is required to produce either cyclic softening or hardening. When a material is loaded cyclically in tension and compression the rate of hardening or softening between cycles will gradually decrease until the cyclic hardening or softening has stabilized. Figure 2.27 describes the eventual stabilization of cyclic hardening/softening for a material. Figure 2.27 is presented in terms of the resulting strain amplitude for constant stress amplitude cycling and the resulting stress amplitude for constant strain amplitude cycling. By performing a number of tension-compression tests at various strain amplitudes, the stabilized hysteresis loop for each respective test can be found. When these stabilized hysteresis loops are overlaid on a single stress-strain diagram, the tip or terminus of each loop forms a cyclic stress-strain curve with quantifiable hardening characteristics that follow a power law. An example is provided in Figure 2.28 which describes several stabilized hysteresis loops for SAE 4340 steel. The steel cyclically softened given the cyclic stress strain curve sits below the monotonic stress strain curve (Liu, 2005).

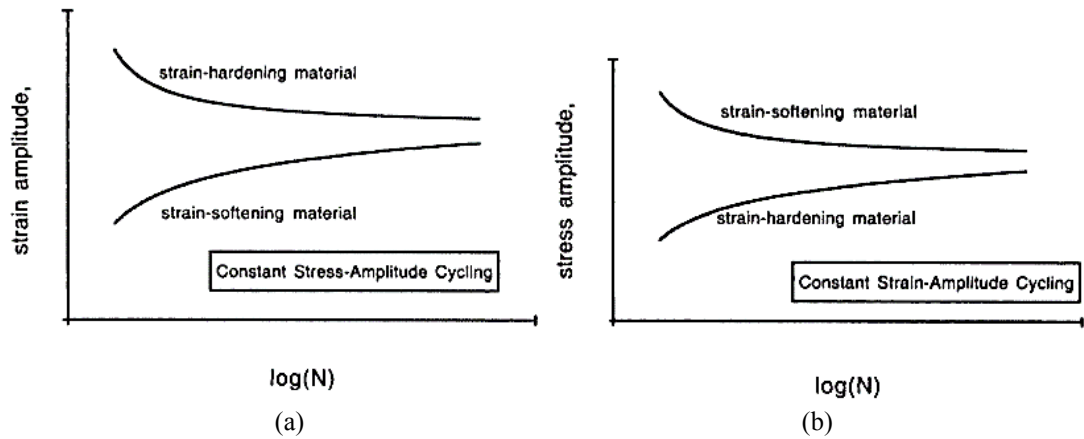


Figure 2.27: (a) change of strain amplitude during constant stress amplitude cycling and (b) change in stress amplitude during constant strain amplitude cycling (Credited to: Hosford, 2009)

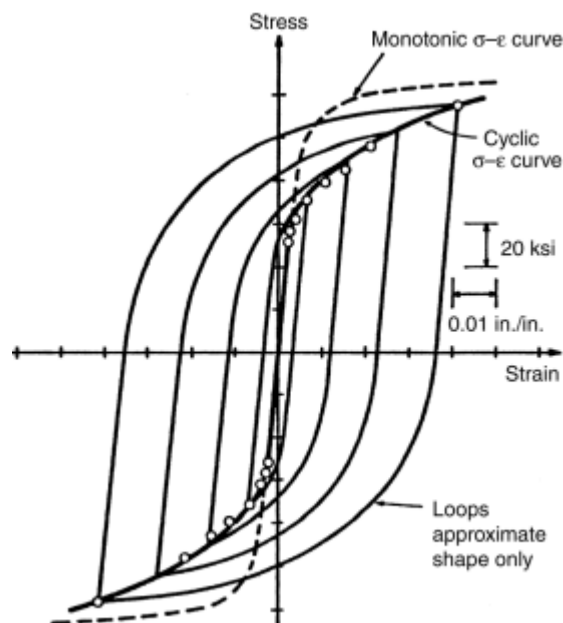


Figure 2.28: Several stabilized hysteresis loops for SAE 4340 steel which appears to have cyclically softened. (Credited to: Liu, 2005)

Some additional cyclic hardening can occur due to nonproportional loading. Nonproportional loading is any type of loading in which the principal strain axes rotates in time. A simple example of nonproportional loading is a bar subject to alternating cycles of tension and torsion loading. Moving between tension and torsion loading results in the principal strain axes varying by 45° between cycles. Technically all low cycle fatigue tests are subject to nonproportional loading given the difference between the elastic and plastic Poisson's ratio (typically 0.5 for metals) although the greatest hardening occurs when the material is directly subject to nonproportional loads. A common type of nonproportional loading is known as out-of-phase loading where the cyclic loading histories are sinusoidal and the two load types, such as tension and torsion, are out of phase. Figure 2.29 details the various types of loading as they appear on the Von Mises strain space. Figure 2.29 (b) describes the strain space for 90° out-of-phase loading which typically produces the largest degree of nonproportional loading. Nonproportional loading can be characterised by a proportionality factor ' f ' which can be

found by drawing an ellipse that circumscribes the entire strain path and taking the ratio of the minor to major axis as shown in Figure 2.29 (c). Nonproportional loading also introduces difficulties with cycle counting for variable amplitude loading and therefore challenges fatigue damage accumulation models (Milne et al, 2003).

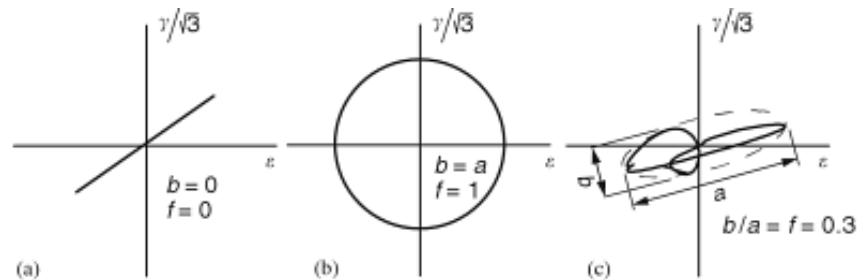


Figure 2.29: Types of loading based on Von Mises strain where (a) is proportional loading, (b) is 90° out-of-phase nonproportional loading and (c) pseudorandom nonproportional loading

2.7.1 Fatigue Crack Initiation

The fatigue life of a structure has two distinct periods, crack initiation period and crack growth period. Crack initiation begins with the development of cyclic slip bands in the material lattice structure on a free surface where one side of the grain structure is unrestrained and weaker. These slip bands are created by concentrated cyclic shear stresses which occur at inclusions in the material or irregularities in the microstructure of the material, making crack initiation a material surface phenomenon (Schijve, 2009). The slip bands deepen along the line of maximum shear stress with each cycle eventually dissecting grain boundaries, this growth is known as nucleation and microcrack growth. Microcrack growth is dependent on the grain size of the material and plasticity of the crack tip (Stephens et al, 2001). Following microcrack growth the second period of fatigue life commences, that is, crack growth. The transition point between crack initiation and crack growth is difficult to define but in qualitative terms it is considered to be the point in which crack growth no longer depends on the material surface conditions. Crack growth now depends on the bulk material properties such as yield strength and stiffness (Schijve, 2009). Crack growth is governed by the maximum tensile stress which opens the crack, propagating the crack normal to the maximum principle stress.

The mechanism of fatigue crack initiation and propagation in materials containing notches, such as fastener holes, differs to pure fatigue behavior given the large concentration of stress occurring at the notch tip. Stress concentration of that magnitude overcome the smaller stress concentrations created by surface roughness ensuring that fatigue cracks initiate at a free edge of the notch where the maximum shear stress is located. A common means of calculating the resulting stress at a notch tip is using a stress concentration factor (K_t). A stress concentration factor describes the ratio between the actual stress occurring at the notch to the nominal stress that would be present should the notch not exist, thereby suggesting that the maximum and nominal stress are proportional. The stress concentration factor is dimensionless and depends on the type of loading, geometry of the sample and the geometry of the notch itself. However, stress concentration factors are not suitable in low cycle fatigue studies given the larger applied stresses characteristic of low cycle fatigue result in plasticity in the vicinity of the notch. The yielding at the notch causes the maximum stress and nominal stress to no longer be proportional and also causes the geometry of the notch to change which provides the basis for

the calculation of stress concentration factors (Yao and Munse, 1961). Consequently, an alternative to the stress concentration factor for fatigue problems has been developed, known as the fatigue notch factor which is simply the ratio of the fatigue life of an unnotched specimen to the fatigue life of a notched specimen (Suresh, 1991).

There are a number of different approaches to predicting the fatigue life of structures which vary greatly depending on the scale of observation. A practicing engineer will often define crack nucleation based on the resolution of the crack detection technique whilst a materials scientist focuses on the microscopic mechanism of crack nucleation. The two observable differences result in a vastly different apparent failure mechanisms with some mechanisms based on macroscopic stress concentrations whilst others are based on microscopic flaws at grain boundaries.

Predicting the fatigue life of a structure in practical situations is challenging and often involves either a semi-empirical approach or is entirely reliant on prototype testing. Most theoretical fatigue concepts involve fixed amplitudes of either stress or strain which contrast with the complex load spectra involved in most practical situations. The semi-empirical approach to the fatigue design of structures typically involves simplified prototype testing to which a theoretical fatigue model is then applied to accommodate realistic load spectra. The semi-empirical approach to the fatigue design can be further characterised into two distinct approaches known as the fatigue life approach and the defect-tolerant approach.

The fatigue life approach predicts the life of a structure based only on the known applied loads. One of the earliest instances of a fatigue life model was that documented by Wöhler (1860) who investigated fatigue of railroad axles subject to bending, torsion and axial loads. Wöhler (1860) was the first to present a fatigue life curve which he referred to as the stress amplitude-life curve, or more simply the S-N curve, which describes the required number of cycles (N) needed to initiate a crack under constant and controlled amplitudes of cyclic stress (ΔS). Both ΔS and N are plotted in log scale (Wirsching and Light, 1980) with the resulting ΔS - N curve often being linear. For linear ΔS - N curves, the fatigue life of a structure can then be expressed as:

$$N_f (\Delta S)^m = C \quad (2.2)$$

Where N_f is the number of cycles until crack initiation, and C and m are constants that depend on the material (Smith, 1991).

Coffin (1954) and Manson (1954) independently proposed an alternative fatigue life curve based on plastic strain rather than stress, which they considered to be responsible for cyclic damage. The result is what is known as the Coffin-Manson law and is widely used in low cycle fatigue problems where the applied stress is large, approaching the limiting design loads in magnitude. Current fatigue design of pressure vessels, as recommended by ASME standards, relies on fatigue life curves which are similar to the Coffin-Manson law as the curves are based on constant strain amplitude testing of smooth uniaxial bars. The Coffin-Manson law describes the number of cycles until crack initiation (N_f) in terms of the strain amplitude with only the plastic strain amplitude ($\Delta \epsilon_p$) being considered. The relationship between number of cycles until failure and the plastic strain amplitude is described as:

$$\Delta \varepsilon_p / 2 = \varepsilon_f' (2N_f)^{-c} \quad (2.3)$$

Where ε_f' is the true strain at fracture during a uniaxial tensile test and $-c$ is the slope of the strain line formed when plotting number of cycles until failure with the plastic strain amplitude on a log-log plot as shown in Figure 2.30.

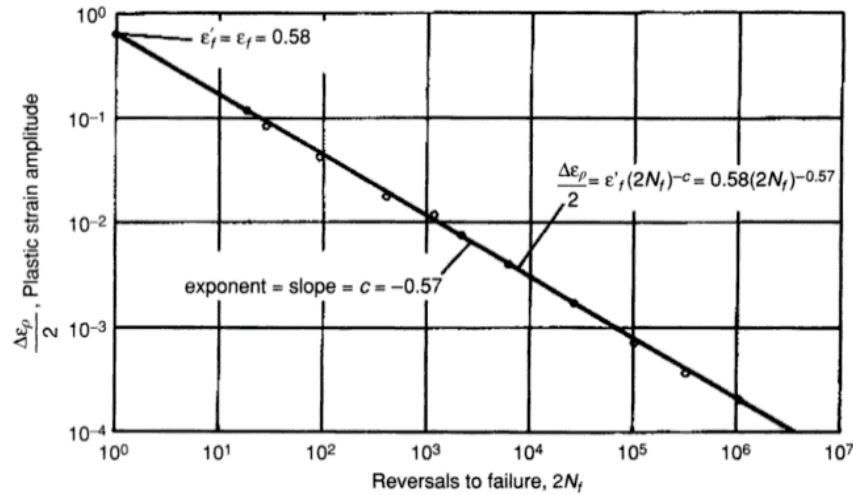


Figure 2.30: Plot of total fatigue life of an annealed 4340 steel (credited to: Hosford, 2009)

The fatigue life curves described by Mahendran (1990b) and Xu (1995) are similar to the ΔS - N curve and Coffin-Mason Law but rather than the controlling variable being stress or strain, the fastener reaction or applied surface pressure was used. By applying a constant fastener reaction or surface pressure, the stress and strain within the cladding vary with each cycle. Regardless a bi-linear fatigue life curve was achieved and provides a suitable alternative to the S-N curve and Coffin-Mason Law.

The fatigue life curves can then be modified for different fatigue conditions such as multiaxial fatigue or variable amplitude fatigue using theoretical fatigue models. Multiaxial fatigue is incorporated by replacing the relevant strain variable with either the maximum principal strain, von Mises equivalent strain or the Tresca strain. The simplest modification for variable amplitude fatigue is through the application of the Palmgren-Miner's Rule. Palmgren (1924) and eventually Miner (1945) were able to accommodate for variable amplitude loading by creating a damage accumulation model. However, Palmgren-Miner's Rule does not account for the sequence in which the load cycles are applied, making it most suitable for lower stress amplitudes where crack closure is unlikely. The principle of Palmgren-Miner's rule is to collate the incremental damage caused by loading at various amplitudes, as:

$$DI = \sum \frac{n_i}{N_i} \leq 1 \quad (2.4)$$

Where n_i is the number of stress cycles at an amplitude, N_i is the number of cycles to cause failure at that amplitude and DI is the damage index (Dowling, 1999).

The use of computational tools such as Palmgren-Miner's Principle, does not take into account the time history of loading (The Committee on Fatigue and Fracture Reliability, 1982). For

example, roof cladding that experiences a peak load during the initial stages of loading, generally requires fewer cycles to cause failure than cladding that experiences the peak load at a later stage (Jancauskas *et al.* 1994). In addition, Miner's rule relies on constant material properties and cannot account for nonlinear effects such as changes in strength, stiffness and sectional properties (Beck and Stevens, 1979; Mahendran, 1993; Xu, 1993). Jancauskas *et al.* (1994), Mahendran (1993; 1995), Xu (1995), Suresh Kumar and Stathopoulos (1998), Henderson (2010) and Henderson and Ginger (2011) all utilized Palmgren-Miner's rule to quantify the extent of fatigue damage. In comparison to experimental data, both Xu (1995) and Suresh Kumar and Stathopoulos (1998) found that Palmgren-Miner's Rule significantly underestimated cladding fatigue failure. Furthermore, cyclonic pressure traces contain various load ranges and amplitudes and as Henderson and Ginger (2005) have described, the fatigue life curves vary with load ratio complicating the interpolation of the fatigue life data with Palmgren-Miner's Principle.

Madayag (1969) modified Miner's Principle to accommodate more complex loading histories. Rather than characterising failure by a damage index (DI) of 1, Madayag (1969) introduced an empirical constant M , described as:

$$DI = \sum \frac{n_i}{N_i} \leq M \quad (2.5)$$

Xu (1995) suggested a M value of 0.25 for corrugated cladding based on cyclic load tests. Henderson (2010) utilized S-N data and wind tunnel pressure trace data to determine the equivalent damage indexes for various building sizes and cyclonic loads. Henderson (2010) considered a damage index greater than 0.25 to be a highly likely failure criterion. Madayag's (1969) modified Miner's Principle is still limited by its inability to account for the loading sequence or nonproportional loading. Given these theoretical models could not be confidently applied to roof cladding fatigue, the total fatigue life approach for cladding fatigue design was abandoned. With no other alternative, cladding fatigue design resorted to full prototype testing under the Low-High-Low test method.

No researchers have, to date, attempted to apply a nonlinear fatigue accumulation model to cladding fatigue based on continuum damage mechanics. Miner's Principal is a linear damage model and since it is unable to account for load history, load sequence effects or the effects of load interaction, a number of nonlinear damage models have been suggested. These damage models account for the reduction in stiffness of a material due to damage itself. In its most basic form – for a unitary reference volume element - the damage of that element is also denoted by a scalar D and depends on the area of the effective resisting section (A_{eff}) and the area of the nominal section (A_0) as shown (Bonora and Newaz, 1998):

$$D = 1 - \frac{A_{eff}}{A_0} \quad (2.6)$$

Quantifying the effective section area and the nominal section area is challenging and the subject of significant research. Kachanov (1986), for example, proposed a continuum damage model that quantified a reduction in stiffness through comparing an effective Young's modulus (E_{eff}) with that of the initial Young's modulus (E_0) as presented in the following equation:

$$D = 1 - \frac{E_{eff}}{E_0} \quad (2.7)$$

Typically the Young's modulus during fatigue loading is determined by measuring stress and strain in the sample. More complex models have been proposed to accommodate complex load cases that result in multiaxial stress states or mean stresses for example. However, most of these models require some knowledge of the stress or strain state within the material during loading, both of which are difficult to predict or measure within in the case of cladding fatigue.

A more complex form of the total fatigue life approach, known as the critical plane approach, can be used to more accurately predict the fatigue life of a structure for material subject to multiaxial stresses or strains and nonproportional loading. A critical plane model relates fatigue damage to the stresses and/or strains occurring on the specific plane in which cracks nucleate. Depending on the material and the loading conditions, the critical plane is either the maximum shear plane or the maximum tensile plane. The critical plane approach is often favored as it not only predicts the fatigue life but also the orientation of the crack. An example of a critical plane model is the Fatemi and Socie criteria which assume that cracks nucleate on the shear plane and is described as:

$$\frac{\Delta\gamma_{max}}{2} \left(1 + k \frac{\sigma_{n,max}}{\sigma_y} \right) = \frac{\tau_f'}{G} (2N_f)^b + \gamma_f' (2N_f)^c \quad (2.8)$$

Where $\Delta\gamma_{max}$ is the maximum shear strain amplitude being applied, $\sigma_{n,max}$ is the maximum normal stress acting on the critical plane, σ_y is the yield stress, τ_f' is a shear fatigue strength coefficient, γ_f' is the shear fatigue ductility coefficient, b is the shear fatigue strength exponent, c is the shear fatigue ductility exponent, G is the shear modulus and N_f is the number of cycles until failure. The normal stress parameter is included to account for the normal stress opening the crack and overcoming the interlocking frictional forces that resist the shear stress along the crack face. The coefficient k can be determined through comparison of uniaxial tensile fatigue tests and torsion fatigue tests. The coefficients on the right side of the equation can also be approximated from uniaxial strain-life properties (i.e. Coffin-Mason law). The Fatemi and Socie criterion is more suitable for low cycle fatigue as the driving variable, $\Delta\gamma_{max}$, is strain based (Goswami, 2004).

The second approach commonly used in fatigue life design is the defect-tolerant approach. The defect-tolerant approach uses fracture mechanics in combination with the assumption that all engineering components are inherently flawed. The fatigue life of the structure is then defined as the number of cycles or time required to propagate the flaw to a critical dimension. Predicting the fatigue life of the structure is based on the empirical crack growth laws developed using fracture mechanics. However, this method is strongly based on linear elastic fracture mechanics (LEFM) which assumes that the plastic zone at the crack tip is small in comparison to the characteristic dimensions of the cracked structure and the crack itself, and that the crack is positioned far away from the plastic strain field of any stress concentrators (Suresh, 1991). The rate at which a crack grows as the number of cycles is increased can be described by plotting the rate of change of amplitude with the number of cycles (da/dN) and the respective change in the stress intensity factor (ΔK_i). Stress intensity factors are similar to stress concentration factors but describe the stress state at the tip of a crack. Stress intensity

factors are also dependent on the applied load, rather than just the geometry of the crack. Recall that stress intensity factors are applicable within the elastic response. Figure 2.31 defines three regions of crack growth: I, II and III. Region I suggests a crack will not propagate until ΔK_i reaches a critical value, region II describes an almost linear rate of crack growth and region III suggests the plastic region is so large it dominates the elasticity of the material (Smith, 1991).

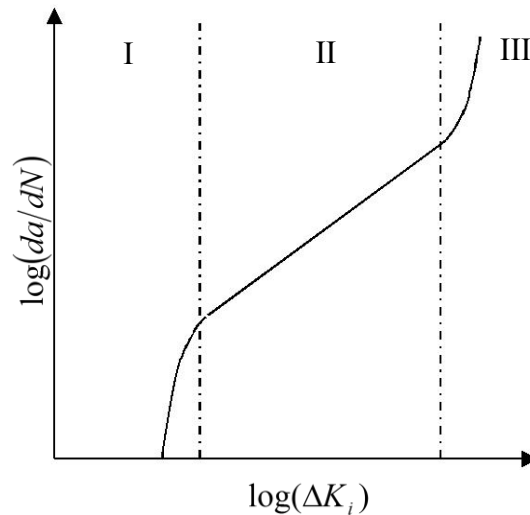


Figure 2.31: Crack growth with increasing number of cycles (credited to: Smith, 1991)

Region II is considerably larger than both Regions I and II and as a result is often the only stage of crack growth considered when estimating the fatigue life of a structure using the defect-tolerant approach. Given the linear nature of Stage II crack growth, the propagation of the crack can be approximated using Paris's Law:

$$\frac{da}{dN} = C(\Delta K_i)^m \quad (2.9)$$

Where N is the number of cycles, a is half the crack length and C and m are empirical constants unique to the material (Smith, 1991). Through integration of Paris's Law in combination with a target or limiting crack length, the total fatigue life of a structure can be determined.

Figure 2.31 suggests there are fatigue thresholds, a point at which cracks are unable to propagate as insufficient stress is applied per cycle to open a crack with dimensions larger than that of the material grain structure. Consequently this region of loading is considered to be microstructurally sensitive. McClintock (1963) suggested that the fatigue threshold is reached when the value of local strain at a particular distance ahead of the crack reaches a critical value.

The defect tolerant approach, being based predominantly on linear elastic fracture mechanics, means it is most suitable for when the loading conditions are predominantly elastic. Consequently the defect tolerant approach is often adopted in high cycle fatigue problems. This approach is also used to conservatively design components such as turbine blades and gas circulators for an infinite fatigue life (Moavenzadeh, 1990). Few investigations have attempted to apply the defect tolerant approach to roof cladding design as determining an appropriate

stress intensity factor for the numerous crack formations observed in cladding fatigue studies is challenging experimentally. Determining the stress intensity factor for a particular loading condition, specimen geometry and crack formation requires the bulk applied stress surrounding the crack to be known. Even at low loads the cladding is subject to large stresses that cannot be directly inferred from the applied load or strain gauges.

2.7.2 Monotonic Crack Initiation

Fracture models for monotonic loading are material dependent and do not rely on the applied load or the geometry of the structure (Lee, 2005). These types of fracture models are known as phenomenological as they typically assume fracture occurs once a critical strain or stress is exceeded (Mattiasson et al, 2014). In contrast, fatigue crack initiation models require either the strain range or the number of applied cycles until initiation which are specific to the specimen geometry and nature of the applied load. Fracture models that are solely dependent on material properties have become more popular over the last five years as most finite element analysis programs, such as ABAQUS, LS-DYNA and PAM-CRASH, have enabled different fracture criteria to be implemented in certain analyses. In crack free bodies, material separation and therefore crack nucleation are a result of complex micromechanical mechanisms, similar to the nucleation of fatigue cracks. However, on a macro scale the surface components of stress and strain govern crack nucleation, and these variables are readily available as the output of most numerical models (Wierzbicki et al, 2005).

There is considerable difference between ductile and brittle fracture of materials and the strain criteria used for each mode of failure reflects their vast differences. Ductile fracture is characterised by significant plastic deformation with crack nucleation, growth and coalescence occurring over a period of time. Brittle fracture occurs suddenly with little to no plastic deformation. A generalization between the two states suggests ductile fracture is due to maximum shear stress whilst brittle fracture is caused by the principal tensile stress (Hibbeler, 2013). Consequently, ABAQUS offers a simple crack initiation criterion for brittle materials known as the maximum principal stress (or strain) criterion where the simulation will introduce a crack perpendicular to the principal stress/strain when the maximum tensile stress/strain in the region exceeds the specified maximum principal stress/strain. For ductile materials the shear component that initiates a crack can be incorporated in the maximum nominal stress (or strain) criteria provided by ABAQUS. The maximum nominal stress/strain criteria describes a crack initiating when the stress/strain normal to the crack direction exceeds a limiting value or when the shear stress/strain along the crack direction exceeds a limiting value. The maximum nominal stress/strain criterion is more suitable for delamination problems (Dassault Systemes, 2013).

Ductile fracture in sheet metal, such as corrugated cladding, is a complex mechanism and as a result numerous crack initiation criteria have been developed with differencing strengths and limitations. These crack initiation criteria can be either dependent on strain, stress or both. Ductile fracture is also heavily dependent on the stress state of the material during multiaxial loading which can be characterised by the stress triaxiality parameter, η , given by the following equation:

$$\eta = \frac{\sigma_m}{\bar{\sigma}} \quad (2.10)$$

Where σ_m is the mean or hydrostatic stress and $\bar{\sigma}$ is the equivalent stress, typically the von Mises stress. This section details a sample of the macro scale criteria available in a number of FEA programs (Wierzbicki et al, 2005; Hiermaier, 2007).

Option 1: Constant equivalent strain criterion

The constant equivalent strain criterion is somewhat similar to the limited maximum principal strain criteria provided by ABAQUS. This criterion is favored for its simplicity and validity for all possible stress states. The criteria states that a crack will initiate should the equivalent plastic strain ($\bar{\varepsilon}_p$) reach a critical value ($\bar{\varepsilon}_f$). The equivalent plastic strain for an incompressible and therefore plastic material is as follows:

$$\bar{\varepsilon}_p = \sqrt{\frac{2}{3}} \sqrt{\varepsilon_1^2 + \varepsilon_2^2 + \varepsilon_3^2} \quad (2.11)$$

Where ε_1 , ε_2 and ε_3 are the principal strains (Wierzbicki et al, 2005).

Option 2: Fracture Forming Limit Diagram (FFLD)

The Fracture Forming Limit Diagram (FFLD) is useful for predicting when sheet metal will neck or split during forming. A FFLD depends on the principal strains present in the surface of a material and the stress state ranging from uniaxial tension to equibiaxial tension. Originally the FFLD was developed to identify when a material would neck (forming limit diagram or FLD) but evolved to incorporate fracture. A generic example of a FFLD and a FLD are presented in Figure 2.32. The locus of a material in a FFLD (shown as a bold line in Figure 2.32) varies with the strain hardening characteristics of the material; typically an increase in strain hardening will raise the locus by increasing in the limiting maximum principal strain (Lee, 2005; Wierzbicki et al, 2005). Figure 2.32 also shows an example of the strain paths in the material prior to fracture for monotonic loading with the strain path prior to necking being linear. The FFLD is consequently less accurate for materials subject to nonlinear strain paths (Mattiasson et al, 2014).

There exists an alternative to the FLD known as the Forming Limit Stress Diagram (FLSD) where the diagram is constructed from the principal stresses rather than principal strains. The FLSD is less sensitive to the strain path and can consequently be used in more complicated loading scenarios such as crumpling of car bodies. The FLSD was first introduced in 1982 by Arrieux et al (1982) but has not achieved wide-spread use. The lack of interest in the FLSD likely stems from the inability to directly measure stress and the greater inaccuracy in predicted stress rather than strain in numerical modelling (Mattiasson et al, 2014).

Mahaarachchi and Mahendran (2009a) investigated the splitting characteristics of trapezoidal cladding under monotonic loads and created a FFLD to characterise crack initiation. A typical FFLD did not yield a definitive criterion for crack initiation as the samples that did split were not distinguished from those that did not. Mahaarachchi and Mahendran (2009a) postulated that the FFLD was incapable of accommodating combined membrane and flexural action. A

modified version of the FFLD was then created which depended on the flexural component of the principal strain and the maximum tensile strain. The final resulting strain criterion states that the flexural component of the principal strain must exceed 60% of the maximum tensile strain (based on the modified FFLD) while the maximum tensile strain must also be equal to the fracture strain from coupon tests of the cladding material.

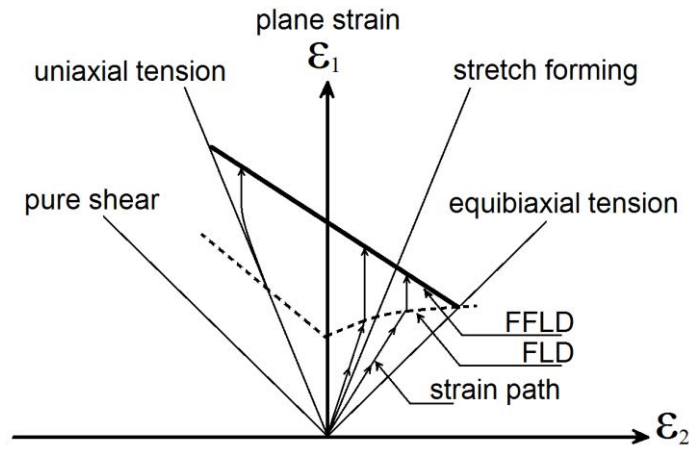


Figure 2.32: Generic FFLD and FLD for a metallic sheet

Option 3: Maximum shear stress criterion (Tresca criterion)

Ductile fracture typically occurs due to the maximum shear stress within the material. The maximum shear stress criterion states that a crack initiates when the maximum shear stress in a material reaches a limiting value. This condition is widely used in soil and rock mechanics (Wierzbicki et al, 2005). Inspecting the crack direction typically identifies whether the maximum shear stress or principal tensile stress are the controlling factor. For thin metal sheets subject to stretching by a hemispherical punch, shear fracture initiated through the thickness of sheet metal rather than within the plane of the sheet (Jain et al, 1999). Figure 2.33 shows the fracture plane through the thickness of the sheet.



Figure 2.33: Fracture plane through the thickness of sheet metal subject to out-of-plane biaxial stretching (credited to: Jain et al, 1999)

Option 4: Johnston-Cook fracture model (J-C)

The Johnson and Cook (J-C) fracture model suggests that the equivalent fracture strain ($\bar{\epsilon}_f$) is a function of the stress triaxiality (η) as given by the following equation:

$$\bar{\epsilon}_f = C_1 + C_2 e^{C_3 \eta} \quad (2.12)$$

Where C_1 , C_2 and C_3 are material constants.

The J-C model is limited when the stress triaxiality is small or negative as the model was calibrated at a specific range. The J-C model also cannot account for the variation in strain rate or the changes in stress triaxiality that can occur during monotonic loading (Wierzbicki et al, 2005). The model does however highlight the dependence of crack initiation on stress triaxiality. By incorporating stress triaxiality the fracture model becomes strain path independent (Mattiasson et al, 2014).

Option 5: Xu-Wierzbicki model (X-W)

The Xu-Wierzbicki model postulates that crack initiation will occur “when the accumulated equivalent plastic strain ($\bar{\epsilon}$), modified by the function of stress triaxiality (η) and the deviatoric state parameter (ξ), reaches a limiting value equal to one” (Wierzbicki et al, 2005, p723). The Xu-Wierzbicki model is given by the following equation:

$$\int_0^{\bar{\epsilon}_f} \frac{d\bar{\epsilon}}{F(\eta, \xi)} = 1 \quad (2.13)$$

Where the function ‘F’ is defined by Equation 2.12 and the deviatoric state parameter ‘ ξ ’ is defined by Equation 2.13.

$$F(\eta, \xi) = C_1 e^{-C_2 \eta} - (C_1 e^{-C_2 \eta} - C_3 e^{-C_4 \eta})(1 - \xi^{1/\eta})^\eta \quad (2.14)$$

$$\xi = \frac{J_3}{\bar{\sigma}^3} \quad (2.15)$$

In Equation 2.13, J_3 is the third invariant of the stress deviators and $\bar{\sigma}$ is the equivalent stress.

The suitability of each option to a particular problem is dependent on the material type and load condition. Some scenarios may even be described by a number of crack initiation criterion with each model achieving similar accuracy. The appropriate selection of a criterion is a simple process of applying numerous options and verifying the resulting accuracy. Some researchers even chose to sacrifice the accuracy of the solution in order to use a simplified crack initiation criterion (Wierzbicki et al, 2005).

3. DEVELOPING AN APPROPRIATE TESTING METHOD

3.1 DEVELOPING AND VALIDATING AN ISOLATED CLADDING-FASTENER CONNECTION TEST

3.1.1 Background

An objective of this thesis is to develop a crack initiation criterion that could be implemented in a numerical model in order to simulate cladding fatigue. However, the tests commonly used to study cladding fatigue – namely the airbox test – must be simplified in order to study crack initiation in corrugated cladding. A simplified test would minimize the significant number of factors that can cause the fatigue response of cladding to vary and potentially obscure the underlying mechanics of crack initiation. Such a test should ideally recreate the same fatigue response observed in airbox studies and in-situ, to ensure the underlying mechanics of crack initiation are the same whilst providing greater control of other external variables.

The past four decades of cladding fatigue studies have identified a vast number of variables that affect the mechanism of cladding fatigue. Morgan and Beck (1977) identified that fastener spacing affected fatigue with an increasing number of fasteners relating to a reduction in fatigue strength, even producing differing crack formations. Beck and Stevens (1979) investigated fatigue under differing pre-tension in the fasteners. Mahendran (1990b) looked at the effect of differing load ranges and mean loads on the fatigue response of cladding and documented four distinct crack formations that occurred under certain loading sequences. The two most distinct crack formations were the ‘star’ type crack which formed when the cladding was loaded below the transition point on the bi-linear fatigue life curve, and the ‘H’ type crack which occurred when the cladding was loaded above the transition point. Henderson and Ginger (2011) also observed large variation in fatigue results which they attributed to the alignment, tightness and position of the screws. Cladding fatigue is further complicated by the large variations inherent in the material properties of cladding.

Both the number of cycles until failure and the location of the connection that fails first vary between trials in airbox fatigue studies. Henderson (2010) and Mahendran (1989) both observed a 30%-50% variation in cycles until failure for full scale testing of corrugated roof cladding. Both Henderson (2010) and Mahendran (1989) also needed to document where failure first occurred for each trial as the relevant fastener location would vary. Disregarding the large number of resources required to monitor crack initiation at multiple fasteners, the full scale testing methods are not ideal for fatigue testing as the applied loading history changes once a neighboring cladding-fastener connection begins to crack. As a fatigue crack grows the load applied to the fastener is shed to adjacent fasteners which may not be exhibiting cracking yet, thereby varying the loading history between trials. Ideally fatigue testing of cladding should isolate a cladding-fastener connection to ensure the same loading history is recreated between trials. An additional benefit of reducing the test to a single fastener connection is fewer resources are required to monitor for crack initiation. Although the variability in the fatigue life of the cladding cannot be entirely reduced given the number of variables in effect, such as screw alignment and tightness, the load history and location of the cracks specific to the fastener can at least be controlled.

The following design criteria were used in the development of a testing apparatus for both static and fatigue studies of corrugated cladding.

Primary design objectives:

- Apparatus should feature a single cladding-fastener connection
- Apparatus should accommodate the corrugated cladding profile
- The resulting fatigue damage must mimic the damage observed in full scale testing
- The test should be repeatable
- The complexity of the corresponding numerical model must be minimized, for example, avoid two deformable surfaces making contact.

Secondary design criteria:

- The underside of the cladding beneath the EPDM seal must be visible throughout loading in order to monitor crack initiation
- The surface of the cladding must be in view without obstruction for possible photogrammetry applications
- The span of the cladding sample must be adjustable to study the effect of biaxiality on crack initiation.

Mahendran (1992) developed what he referred to as a small scale testing arrangement for cladding which isolated a single fastener. The arrangement featured a section of cladding, 240 mm × 240 mm, fixed to a timber frame using eight Type 17 screws. A ninth screw was placed at the centre which was free to displace, thereby inducing load. This arrangement is the reverse of the uplift process that occurs during a wind event, where the applied suction lifts the cladding over a fixed screw. This testing arrangement was successfully used to study the static pull-through strength of the cladding. Mahendran (1992) also used this test arrangement to investigate the fatigue response of cladding and suggested that the small scale test was suitable for fatigue investigations as an initial overload cycle caused the fatigue behavior of two differing cladding profiles to vary in a similar manner to that observed in full scale tests. In particular, the fatigue life of corrugated cladding was significantly reduced by an initial overload cycle while the reverse was true for trapezoidal cladding. Mahendran (1992) does not mention what crack formations were produced using the small scale testing arrangement.

The small scale testing arrangement documented by Mahendran (1992) inspired the testing arrangement developed specifically for this investigation, known as the Isolated Fastener Connection test or IFC test. The small scale test arrangement satisfies the design criteria and most of the primary objectives; however, a corresponding numerical model of the test arrangement would be highly complex. Mahendran (1992) used eight Type 17 screws to fix the edges of the cladding sample to the timber. As the restraining fasteners are in close proximity to the central fastener, then the effects of those fasteners are more apparent on the local response of the cladding meaning the fasteners must be accurately recreated in the numerical model. Eight screws with deformable washers contacting the surface of the cladding would be extremely costly to model numerically. Complete restraint of the cladding edge or rigid clamps restraining the cladding edge would more favorably translate in a numerical model. The flexibility of the timber frame that Mahendran (1992) used to support the cladding

sample would also need to be included in the numerical model as the stiffness of timber is comparable to the stiffness of the cladding. Consequently the small scale test arrangement was simplified to reduce the complexity of a corresponding numerical model and modified further to accommodate a United STM-50kN table mounted testing machine.

3.1.2 Designing a Test Apparatus

The IFC test apparatus involved a rigid steel frame fixed directly to the United STM. A cladding sample $720\text{ mm} \times 150\text{ mm}$ was then compressed between a removable lid and the fixed base of the apparatus, making the cladding sample interchangeable between trails while the restraints remained constant. The longitudinal edge of the cladding was restrained by two 6 mm wide steel plates which would clamp the cladding crest under a compressive force. The transverse boundary was similarly clamped by two removable high density polyethylene (HDPE) blocks that were laser cut to match the profile of the cladding. Compressive force was applied to the clamps using six high-tensile steel bolts which fixed the lid to the base of the apparatus. At the centre of the cladding sample, in line with the central crest, was a single fastener. Like the small scale tests created by Mahendran (1992) the central fastener was then displaced to induce a load. Figure 3.1 shows the apparatus installed within the United STM and Figure 3.2 presents a detailed schematic of the IFC test apparatus.

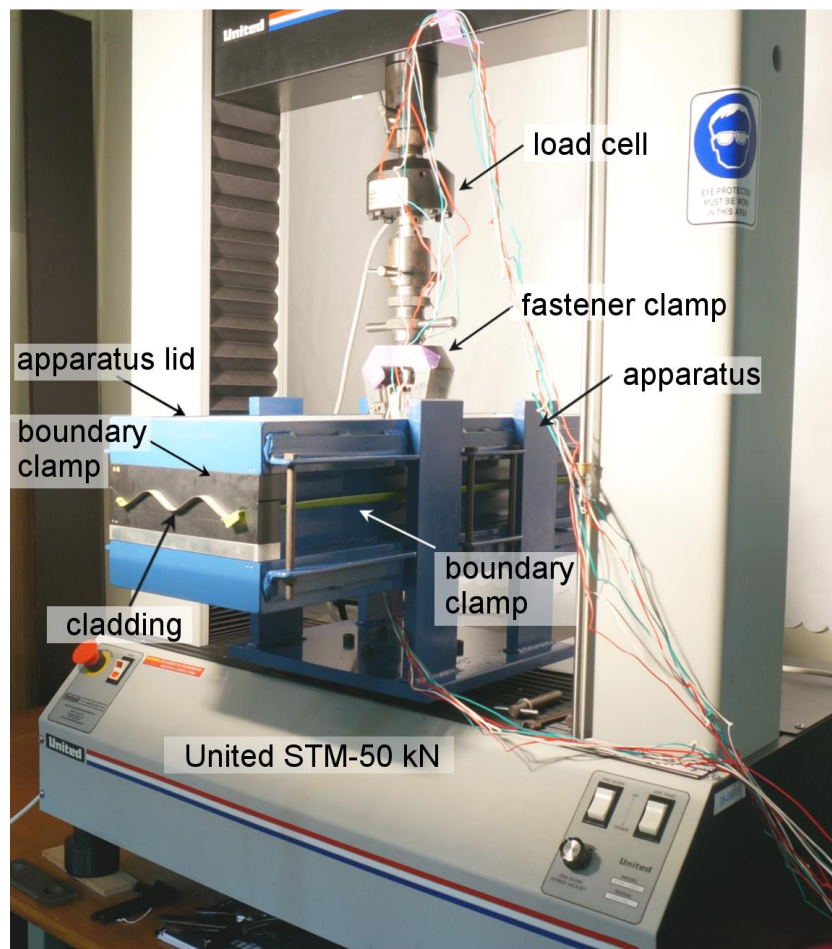
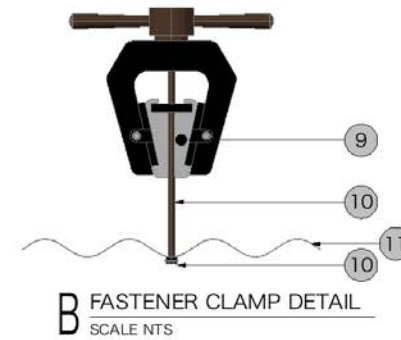
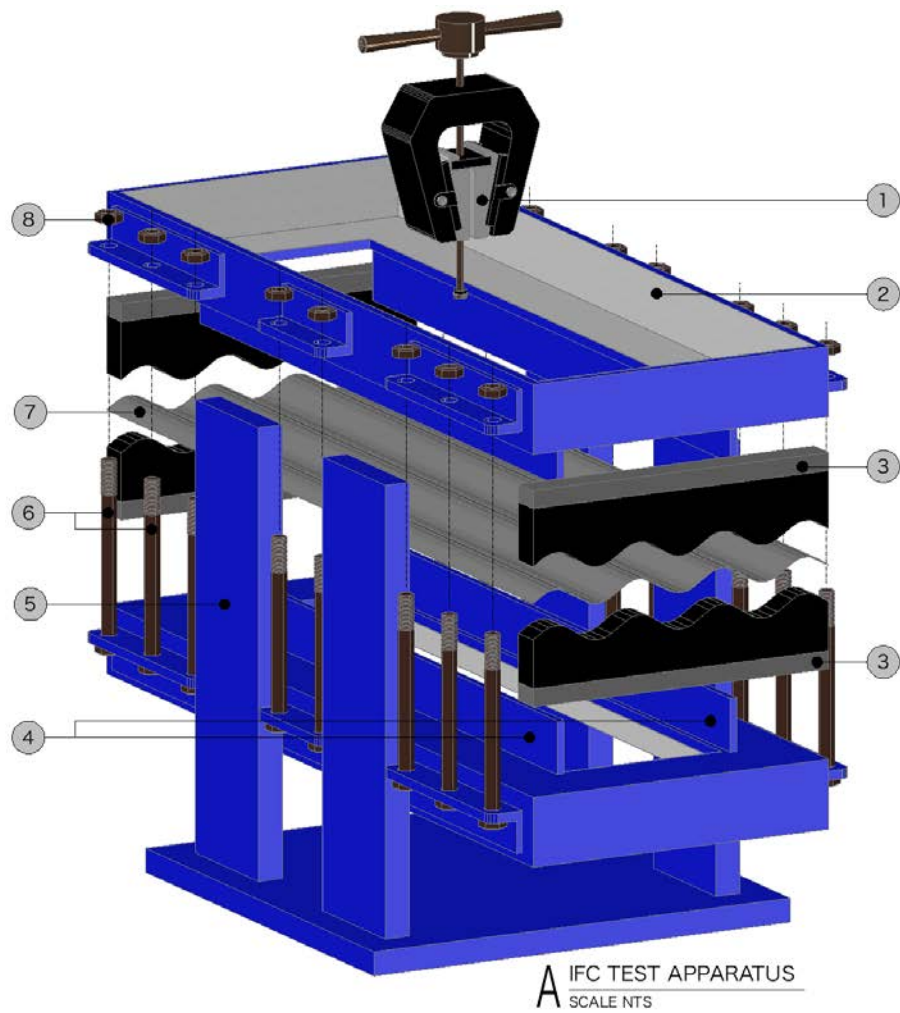


Figure 3.1: Photograph of the apparatus installed within a United STM-50kN



	DESCRIPTION
A1	FASTENER CLAMP
A2	APPARATUS LID
A3	HDPE BLOCKS
A4	LONGITUDINAL CLAMPS
A5	FIXED APPARATUS BASE
A6	HIGH TENSILE STEEL BOLTS
A7	CLADDING SAMPLE
A8	HIGH TENSILE STEEL NUTS
B9	FASTENER CLAMP
B10	FASTENER
B11	CLADDING SAMPLE

Figure 3.2: Full schematic of IFC test apparatus

The rigid steel frame of the apparatus was favored as it is less challenging to model numerically than timber given that the frame is significantly stiffer than the cladding and can be simplified as rigid. An added benefit of the rigid frame is that it remained fixed within the United STM, central to the load cell, so the cladding sample needed to be aligned at the beginning of each trial. Presumably this arrangement made each trial more repeatable as the boundary conditions remained the same between trials. The rigid steel frame was made using a combination of mild steel plates, 6 mm thick, and 5 mm thick equal angle sections.

As the cladding was loaded by deflecting the central fastener, the choice then became whether the cladding should be mounted right side up with the United STM deflecting the screw downwards, or deflecting the screw upwards with the cladding mounted upside down. Having the cladding mounted upside down was preferred as it more easily accommodated the cameras required to monitor crack initiation and propagation. The cameras were then able to be mounted directly to the fastener clamp where they then moved with the cladding surface, keeping the cladding surface within the focal distance of the camera. Viewing the underside of the cladding sheet was favorable as it provided an unobstructed view of crack initiation at the fastener hole edge. Figure 3.3 describes the preferred cladding arrangement for the IFC test with the fastener displaced upwards.

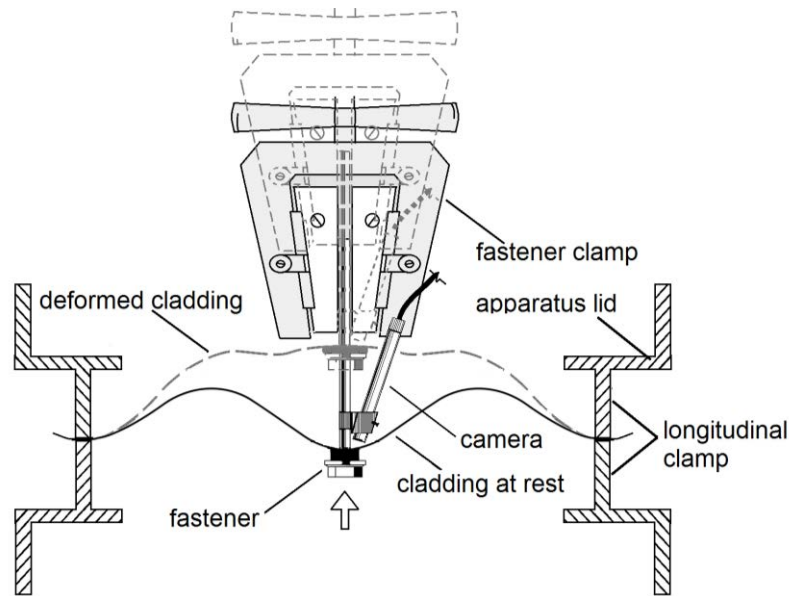


Figure 3.3: Cladding and fastener arrangement for IFC test

A design criteria of the IFC test was the ability to vary the span of the cladding so the longitudinal dimensions of the frame was taken to be the maximum length the United STM could accommodate. The transverse dimensions of the frame was then selected based on the known tributary area of a cladding fastener which Henderson (2010) and Lovisa et al (2013) described as elongated in the longitudinal direction, and extending between the centrelines of the unfixed crests either side of the fastener in the transverse direction. Consequently the centre line of the unfixed crests either side of the fastener was taken as the extents of the frame in the transverse direction.

The longitudinal and transverse edges of the cladding were restrained by clamping the cladding edge using steel plates and HDPE blocks. However, restraining the cladding in this way, with the longitudinal and transverse edges remaining level, caused the biaxiality ratio of the stress through the cladding to vary to that experienced by the cladding in airbox studies. Subject to a surface pressure in an airbox the unfixed crests either side of the fastener in the transverse direction typically deflect more than the unrestrained span in the longitudinal direction. During airbox studies the unfixed crest either side of the fastener displaced up to 30% more than the mid-span which undergoes the largest deflection in the longitudinal direction. Ideally, the transverse boundary in the IFC test should be supported by a vertical roller that allows the transverse edges to displace vertically as the central fastener is displaced, allowing the fully restrained longitudinal edges to remain fixed. This would ensure that the longitudinal edge would undergo greater displacement than the transverse edge relative to the central fastener. However, implementing a roller support along the transverse edge is logistically a challenge, particularly as the roller must also restrain the rotation about the transverse axis. As the biaxiality ratio was going to be purposely varied in this investigation to study the effects on the fatigue response of the cladding, then the resulting change in biaxiality ratio was excused.

A 6 mm wide steel plate was used to clamp the longitudinal edge of the cladding in order to restrain both the rotation and displacement of the cladding edge. The longitudinal edge should not undergo rotation given that this point corresponds to the point of maximum deflection when the cladding is subject to surface pressures. However, restraining both the translation and rotation of the cladding was difficult given the curved profile. A number of different sections were trialed and the simplest and most effective was found to be a 6 mm thick steel plate, as it could comfortably be seated into the curved crest of the cladding without causing excess deformation. When firmly clamped by tightening a series of bolts, the 6 mm wide plate flattened the crest of the cladding up to 0.2 mm as shown in Figure 3.4 (a). Any section narrower than 6 mm would deform the cladding crest less but it would also reduce the relative stiffness of the rail, and simplifying the apparatus boundary conditions numerically requires the stiffness of the boundary to be sufficiently greater than the stiffness of the cladding. Figure 3.4 (b) describes a schematic of the apparatus highlighting the longitudinal and transverse clamps.

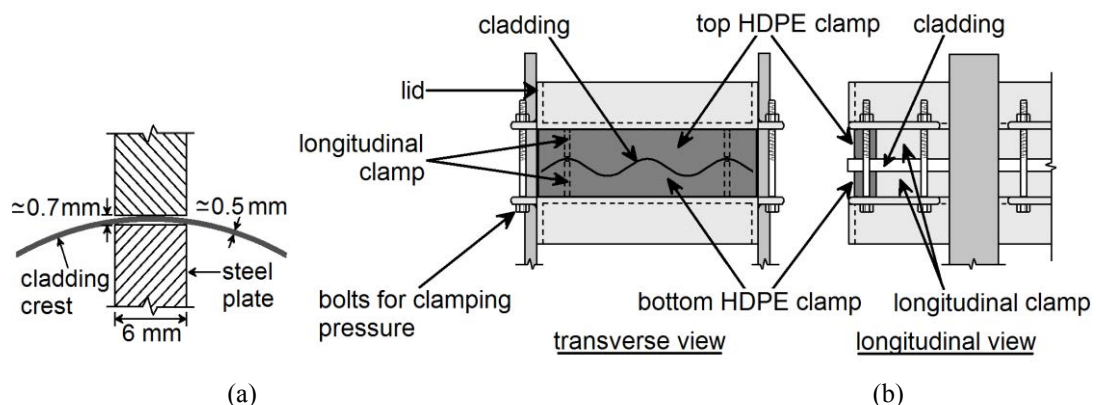


Figure 3.4: (a) Cladding crest clamped along longitudinal edge and (b) schematic of cladding apparatus.

For the transverse boundary the cladding was clamped by two removable sections of high density polyethylene (HDPE). HDPE is a stiff plastic that can be precision cut using a laser to

match the profile of the corrugated cladding. The laser cut was based on the standard profile provided by cladding manufacturers and did not precisely match the cladding section being tested. A compressive force was then applied when clamping the transverse edge, similar to longitudinal clamp, to form the cladding snug with the HDPE profiles. The HDPE sections were 30 mm wide to provide a stronger grip on the cladding sample. A benefit to using the removable HDPE clamps is that the cladding can be installed both right side up and upside down. Furthermore, the HDPE clamps can be moved to reduce the span of the cladding for when studying the effects of biaxiality ratio on the fatigue response of the cladding.

3.1.3 Cladding Specimens Specifications

Following development of an appropriate test apparatus, the design had to be validated by studying the static and fatigue response of cladding samples installed within the apparatus. All cladding samples used throughout the investigation were Custom Orb (corrugated) Colorbond cladding manufactured from a single coil produced by Bluescope Steel. Using samples taken from a single coil reduced the variability in material properties given the tensile strength of the cladding can vary from 580 MPa to 870 MPa between coils (Rogers and Hancock, 1997). The coil was rolled to produce both the corrugated cladding and flat sheets of a similar thickness (0.42 mm). Coupons were cut from the flat sheets by Henderson (2010) to establish the material properties of the cladding after cold working. Table 3.1 describes the resulting material properties of the cladding samples based on standardized tensile testing of the coupons. Figure 3.5 presents an example of the stress-strain curve for the longitudinal direction of the cladding, highlighting the brittle nature of the steel.

Table 3.1: Cladding material properties (credited to: Henderson, 2010)

	Number of Samples Tested	Average Young's Modulus (GPa)	Average Yield Strain (%)	Average Yield Stress (MPa)	Maximum Yield Stress (MPa)	Minimum Yield Stress (MPa)
Longitudinal	14	210	0.38	796	799	774
Transverse	9	221	0.40	877	886	845

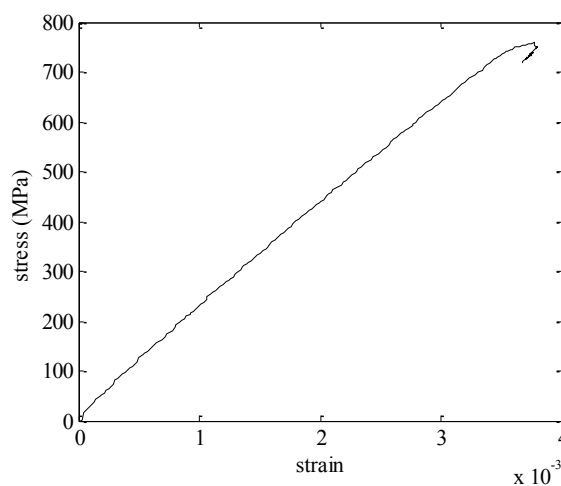


Figure 3.5: Stress-strain curve for G550 steel in longitudinal direction

3.1.4 Validating the IFC test

The effectiveness of the IFC test for studying the fatigue response of cladding can be quantitatively established by comparing the results of an IFC test with that of airbox studies. The fatigue behaviour of roof cladding is dependent on the static response, suggesting that the IFC test must firstly replicate the static response of the cladding in order to replicate the fatigue behavior (Mahendran, 1990a). The results from the airbox studies performed by Lovisa (2011) and Henderson (2010) were used in the comparison with the IFC test results as the cladding samples used in the IFC tests were taken from the same coil that produced the samples tested by Lovisa (2011) and Henderson (2010). For the static response, the relative deflections from both the IFC and airbox tests should be similar. The relevant deflections for the airbox studies are at the mid-span, both the fixed and unfixed crest, and unfixed centre support, labelled as d_b , d_c and d_a respectively in Figure 3.6. As both the longitudinal (centre unfixed equivalent) and transverse edges (mid-span equivalent) of the cladding sample in the IFC test remain level as the fastener is displaced, then the displacement of the fastener alone can describe the static response of the cladding for the IFC test. The load-deflection curves for both the airbox and IFC tests are presented in Figure 3.6. Table 3.2 details the loads at which local plastic deformation (LPD) occurred for all five trials used to study the static response of the cladding within the IFC test.

Table 3.2: Local plastic deformation loads for static trials in IFC test

	Trial 1	Trial 2	Trial 3	Trial 4	Trial 5	Average
Load at LPD (N)	650	620	618	625	580	619

The IFC test effectively recreated the load-deflection behaviour of the cladding at the mid-span in an airbox study for both the fixed and unfixed crest (d_b and d_c). The load-deflection behavior of the cladding at the mid-span is comparable to that of a continuous beam and is subsequently simple to recreate in the IFC test. The behaviour of an unfixed crest at the centre support however is complex and dependent on very large membrane and bending actions. Furthermore, the IFC test forces the centre unfixed crest to effectively displace equal to the mid-span fixed and unfixed crest when in reality the deflection of the centre unfixed crest should be greater.

A second key variable used to describe the static response of corrugated cladding is the load at which LPD occurs; airbox studies for spans of 900 mm suggest LPD occurs at a fastener reaction of 720 N whilst LPD occurs at approximately 620 N for the IFC test. Mahendran (1990a) found the span of the cladding had little effect on the resulting local plastic deformation of the cladding. This suggests that the 100 N variation between results is not due to the shortened span but is more likely due to the stiffer boundary conditions concentrating the compressive force of the central fastener on the central crest rather than dissipating the force by allowing the cladding to rotate. Overall the static response of the cladding in the IFC test followed the four stages of response documented in airbox studies; linear deformation stage, softening stage, local plastic deformation stage and finally a geometric stiffening stage (Mahendran, 1990b).

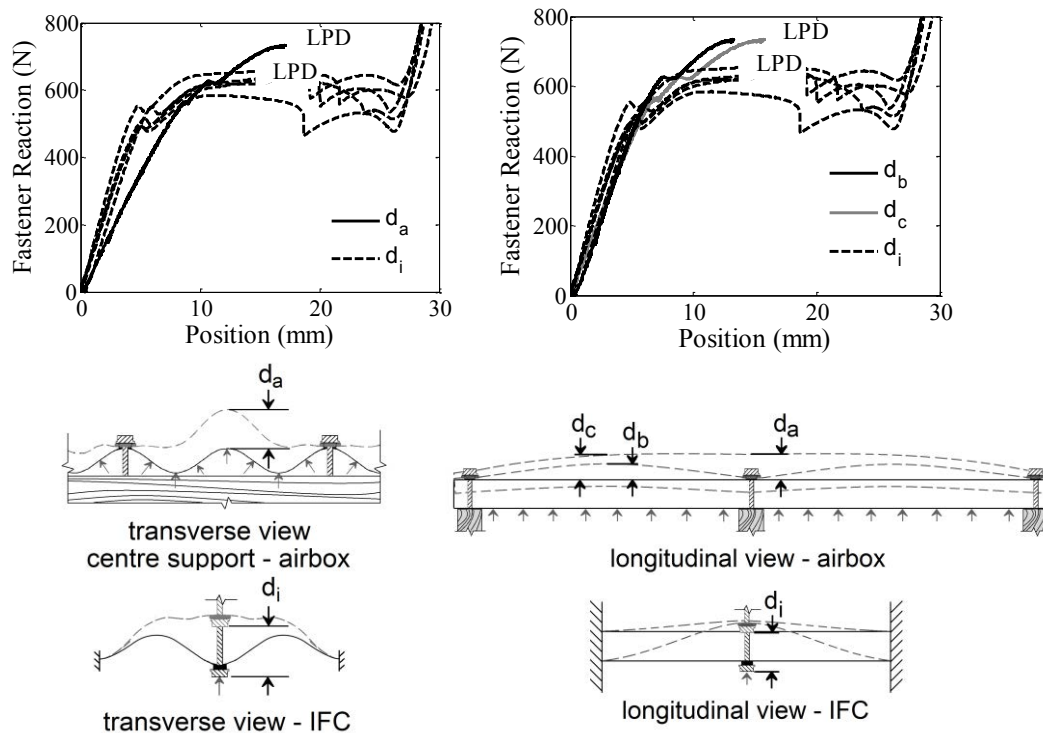


Figure 3.6: Comparison of cladding deflections observed in airbox and IFC studies.

When determining the effectiveness of the IFC test in recreating the fatigue response of cladding both the crack formations observed, and load range and number of cycles required to initiate and propagate those cracks must be considered. To monitor crack initiation and propagation, two high definition digital cameras were affixed to the fastener clamp. Crack initiation was then characterised as the first appearance of a crack more than 1 mm in length which is the same characterization used by Henderson (2010) during his airbox studies. To adequately compare the fatigue response of the cladding within the IFC test to that documented during airbox studies, the crack length used to define crack initiation must be consistent between the two experimental methods. Henderson (2010) used a crack length of 1 mm to define crack initiation during airbox studies; consequently a crack length of 1 mm was also used when validating the IFC test.

The desired crack formations are the ‘star’ type crack and the ‘H’ type crack which are typically formed when loading the cladding below LPD and through LPD respectively. For the IFC test, LPD occurs at a fastener reaction of approximately 620 N. Consequently, constant amplitude loading with load ranges of 0-400 N, 0-450 N and 0-500 N were applied to the cladding samples in the IFC test to form a ‘star’ type crack. Each load range was trialed once, producing three “star” type crack formations. The maximum load applied was limited to 500 N as anything greater consistently produced a third crack formation known as the ‘T’ type crack. This same crack formation was observed by both Mahendran (1989) and Henderson (2010) when the cladding was cycled close to the LPD load.

The ‘H’ type crack formation was also observed in IFC tests when the cladding was cycled through LPD, specifically with a load range of 0-1000 N. Ideally, the ‘H’ type crack formation would also be observed at peak loads of 700 N however the load control of the system was highly sensitive to the local plastic collapse of the cladding sheet, particularly given the fast

load rate required for cyclic testing. A peak load of 800 N was requested but 1000 N was reached before the cycle would reverse. Four trials subject to a peak load of 1000 N was performed, producing four “H” type cracks.

Figure 3.7 compares the ‘star’, ‘T’ and ‘H’ type crack formations produced by Henderson (2010) using an airbox with those created during IFC testing. The IFC test successfully produced all three crack formations however some distinct differences between relevant crack formations are evident. For example, the transverse leg of the ‘star’ type crack formation produced in the IFC tests is considerably longer than that formed in airbox studies. Airbox studies produce ‘star’ type cracks with the transverse and longitudinal legs almost equal in length whilst the transverse legs of a ‘star’ type crack in an IFC tests were typically two times greater in length than the longitudinal legs. This confirms that the boundary conditions of the IFC apparatus did change the biaxiality ratio of the cladding with the transverse stress unable to open the longitudinal leg of the crack at the same rate as the transverse leg.

The fatigue studies conducted in an airbox were based on a uniform surface pressure being applied cyclically to a cladding sheet whilst the IFC tests were based on fastener reaction. In order to quantitatively compare the results of both fatigue studies, the results must be made comparable. Studies on the static response of cladding using an airbox found that cladding would undergo LPD at an applied pressure of 4.5 kPa (Henderson, 2010). Previous studies also show that fastener reaction increases linearly with applied pressure until LPD were the fastener reaction reduces slightly. To make the two studies comparable, the peak applied pressure of the load cycles applied in the airbox studies was normalised by taking the ratio between the peak pressure and the pressure at LPD. The same was done for the IFC test where the fastener reaction was normalised by taking the ratio between the peak applied fastener reaction and fastener reaction at LPD. This method is only applicable if the ratio remains below or equal to 1 for the airbox studies otherwise fastener reaction and surface pressure are disproportionate. Figure 3.8 describes the number of cycles until failure for various crack formations observed in both the airbox and IFC studies. For the ‘star’ type crack the fatigue life of the cladding in an IFC test appears to be shorter than that of the airbox but at a comparable magnitude. Tables 3.3 and 3.4 details the specific number of cycles until crack initiation for each IFC test used to study the fatigue response of the cladding and includes the results from five trials performed by Henderson (2010) using an airbox.

Table 3.3: “Star” type crack initiation documented in IFC and five samples taken from the airbox tests

		Trial 1	Trial 2	Trial 3	Trial 4	Trial 5
“Star” type crack						
IFC test	Ratio of applied load to LPD load	0.84	0.75	0.72		
	No. of Cycles until crack initiation	2072	2958	2816		
Airbox	Ratio of applied load to LPD load	0.8	0.79	0.78	0.77	0.71
	No. of Cycles until crack initiation	3351	1215	1810	2718	6830
“H” type crack						
IFC test	Ratio of applied load to LPD load	1.87	1.82	1.79	1.74	
	No. of Cycles until crack initiation	91	58	90	64	
Airbox	Ratio of applied load to LPD load	0.97	0.93	0.91	0.86	
	No. of Cycles until crack initiation	630	1009	1676	808	

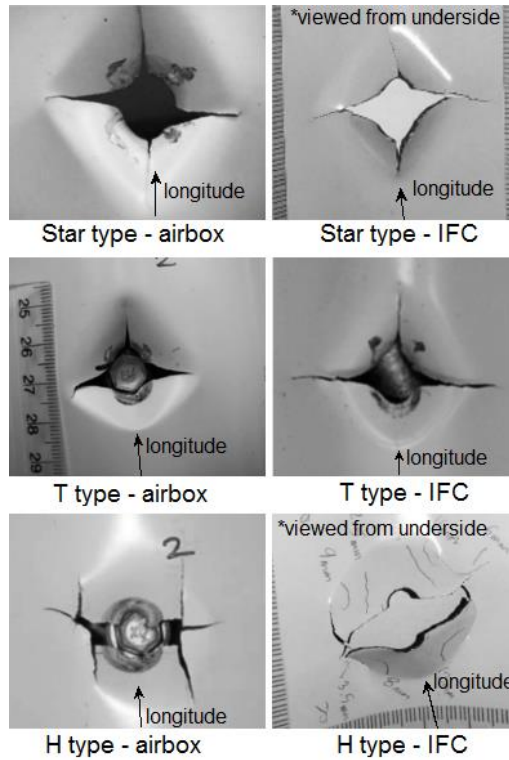


Figure 3.7: Crack formations observed during airbox and IFC studies.

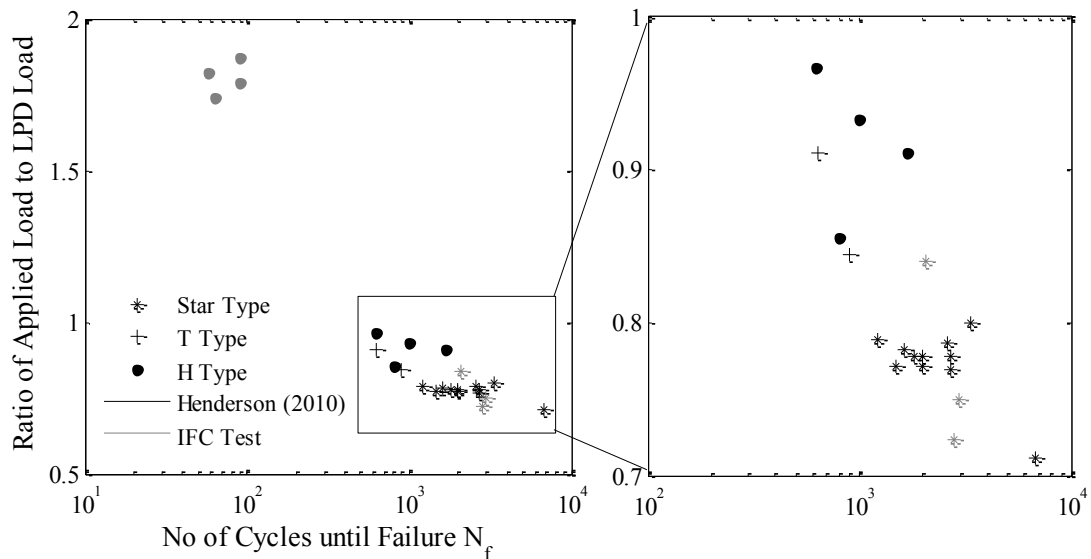


Figure 3.8: Number of cycles until failure documented during IFC and airbox studies.

3.1.5 Summary

Overall, the IFC test produced similar results to that observed in airbox studies concerning both the static and fatigue behaviour of the cladding. The cladding sample in the IFC test underwent local plastic deformation, similar to the airbox, but at a lower applied fastener reaction. The IFC test also produced similar crack formations to that observed in airbox studies although the fatigue life of the cladding in the IFC test was slightly shorter than its counterpart in the airbox. The IFC test apparatus also affords a clear view of the cladding surface and fastener hole, accommodates a varying span for future studies on the effect of biaxiality on

crack initiation and the boundaries of the IFC test can be simplified in a numerical model in a number of ways. The IFC test is therefore suitable for the study of crack initiation in corrugated cladding; enabling the development of an appropriate crack initiation criterion for an advanced numerical model.

3.2 MEASURING DEFLECTION USING PHOTOGRAMMETRY

Close range photogrammetry is an inexpensive tool that can create detailed digital reconstructions of objects that have deformed under applied loads, known as Digital Surface Models (DSMs). In addition to capturing the nature of the deformation; the deflection of the object subjected to load can also be inferred from the same DSM. Close range photogrammetry can also be used to extend validation studies of numerical models. The DSM of a deformed object can be compared directly with the deformed mesh produced using a corresponding numerical model to provide a full-field appreciation of the accuracy of the model.

Close-range photogrammetry is an effective tool for replicating objects as a 3D digitization, and has been adopted for a variety of applications in medicine, entertainment, archaeology, forensics and engineering. For civil engineering in particular, close-range photogrammetry (hereby referred to as photogrammetry) has become more popular for tracking the movement of structures in both the laboratory and field. Photogrammetry enables a large number of points to be measured in 3D and can be applied in situations that might be impractical for implementing traditional displacement transducers. Generally the method involves tracking discrete markers with a monoscopic system as demonstrated by Xiao et al (2011) or using multiple fixed cameras with accompanying proprietary software like the ARAMIS system used by Bambach (2009). Some systems, like OptiTrack (2013), use both markers and multiple fixed cameras to track the 3D movement of markers in real time. Each of these methods possesses differing strengths and limitations stemming from where the cameras can be located, accuracy, field of view and cost.

Current state of the art requires only a single camera and accompanying software to construct a complete DSM of any static surface or object or alternatively multiple stationary cameras could be used to construct a DSM of a dynamic object. As a result, photogrammetry is exceedingly popular in the archaeological sciences to survey and catalogue artefacts in great detail without compromising the integrity of the artefacts (Koutsoudis et al, 2013; McCarthy, 2014). Most DSMs even include texture mapping resulting in visually precise digital reconstructions of artefacts. The mobility of a single camera means photogrammetry is ideal in the field where complex imaging systems are too challenging to transport and implement. Multiple fixed cameras can be used in conjunction with photogrammetry software to capture and reconstruct dynamic objects such as the human face and body, this being a highly utilized tool for a number of fields including animation, cinematography, medicine and biology. Creating a DSM of an object has a number of potential applications in civil engineering as it can capture the deformation of an object in either the laboratory or field. These DSMs can then be used to infer the relevant displacement of an object as it deforms with an indeterminate number of points available for tracking, rather than a predefined set of markers.

The photogrammetry software needed to construct a DSM is readily available and affordable following the increased availability of 3D printers. DSMs created using photogrammetry can be sent directly to a 3D printer without the need for post processing in third party software.

Hobbyists and enthusiasts can now create DSMs of any object using a camera phone and free photogrammetry software, such as 123DCatch (Autodesk, 2014) or VisualSFM (Wu, 2011). Robust programs like Agisoft PhotoScan (Agisoft LLC, 2014) and PhotoModeler (Eos Systems, 2013) are available if accurate and detailed DSMs are required, particularly when used in combination with a high resolution digital camera. However, these programs are taxing on computer hardware which is why a number of photogrammetry programs, such as 123DCatch, rely on cloud computing rather than straining the hardware of a desktop computer. High resolution photographs and a large number of photographs in the relevant image set generally means more accurate DSMs but at a significantly greater computational cost (Lunmann, 2010). Programs such as Agisoft PhotoScan and VisualSFM have implemented GPU (Graphics Processing Unit) acceleration to reduce the computational runtime needed to process large, high-resolution image sets (Wu, 2011).

Photogrammetry matches feature points between an unordered set of photographs and uses the correlating photographs to calculate the 3D coordinate of each feature point, resulting in a dense point cloud of feature points each with x, y, z coordinates. Photogrammetry software uses algorithms such as Structure-From-Motion (SFM) and Dense Multi-View Surface Reconstruction (DMVR) to identify corresponding feature points within each photograph and calculate the resulting coordinates. The first stage in the photogrammetric process is identifying feature points within a photograph and assigning a descriptor based on their immediate surroundings. These descriptors are then used to identify that same feature point in any overlapping photographs. Following matching of the points, SFM then uses these points to calculate the intrinsic and extrinsic parameters of the camera (Agisoft LLC, 2014; Koutsoudis et al, 2014). The physical position of each camera location (extrinsic parameter) is then refined using a bundle-adjustment algorithm which adjusts both the locations of the feature point and camera based on optimisation of a statistical error model (McCarthy, 2014; Agisoft LLC, 2014). Several algorithms can then be used to convert the resulting point cloud to a 3D polygon mesh that represents the object surface; the selection of the appropriate algorithm depends on the user's desired outcome.

Few examples of DSMs being used to measure displacement and deformation in civil engineering have been documented. One such example is the structural monitoring of heritage buildings by Arias et al (2005). Arias et al (2005) used a single camera with the PhotoModeler Pro software to measure crack propagation in a structure. Both a textured DSM and wireframe DSM were used effectively in the analysis. Glaser et al (2012) also used a single camera with Photomodeler-6 to obtain a dense point cloud describing the deflection on an aluminium beam subject to a point load which was then converted to a DSM using custom written MATLAB (The MathWorks, Inc, 2012) code. The deflection at discrete points along the beam were inferred from the DSM and used to validate an analytical model. Bakhshinejad and Zamankhan (2012) effectively used six fixed cameras and 123DCatch to map the free surface of a dynamic bed of granular material and used the resulting DSM to extract the cross sectional profiles of the granular material.

A defining benefit of creating DSMs using photogrammetry is their potential use in extending validation studies of numerical models. A common means of validating numerical models is to qualitatively compare the deformed shape of the model with that observed experimentally followed by a quantitative comparison of variables at specific and discrete points. A DSM

created using photogrammetry can be compared directly with the deformed mesh predicted by a numerical model, providing a full-field comparison that comprehensively quantifies the performance of the numerical model.

The increased availability of powerful photogrammetry programs creates the potential for accurate measurement and documentation of complex structural responses with minimal expense. Such complex responses include the severe local deformation experienced by corrugated roof cladding at the fastener connection when subject to applied loads. The local response of the cladding is challenging to measure using traditional displacement transducers, and photogrammetry provides an effective and inexpensive means of measuring all local deformations. The IFC test apparatus, particularly the bulky load cell and fastener clamp means that traditional displacement transducers are difficult to implement. Of particular interest is the severe deformation surrounding the fastener which is localised to within a 30 mm radius around the fastener. Displacement transducers could be applied to the underside of the cladding sheet but with great difficulty given the small void made available by the apparatus. A significant number of transducers would also be needed to adequately capture both the displacement and the complex deformation surrounding the fastener. Such a large system of displacement transducers is not just limited by the physical space but also by the number of available channels in the data acquisition system and the resulting cost. However, only the deformation of the cladding subject to monotonic loads can be measured using this photogrammetric method. Capturing the deformation of the cladding subject to dynamic – such as cyclic – loads requires a number of stationary cameras photographing the surface of the cladding simultaneously. To obtain an accurate reconstruction of the cladding surface subject to cyclic loads would require a significant number of cameras; an expense that cannot be justified for this investigation.

3.2.1 Sample Preparation and Photoshooting

The accuracy of a DSM constructed using close range photogrammetry greatly depends on the user's photography skill, the camera, the lighting and the nature of the object itself. Consequently obtaining an accurate DSM is considered more of an art than a science with very little direction in literature on the best practice for photogrammetry. This photogrammetric method was largely based on trial and error to determine the best practice for this case to ensure an accurate DSM was obtained with each attempt.

Smooth and featureless surfaces are extremely difficult to process using photogrammetry given the lack of feature points on the object. Reflective objects are also challenging for photogrammetry as they reflect light at different angles making the same region appear different in two corresponding photographs. Unfortunately, corrugated cladding is smooth, featureless and reflective which means the sample had to be texturized prior to taking photographs. As other cladding profiles are also smooth, featureless and reflective, then the photogrammetric method developed here is likely to be suitable for other cladding profiles. A number of different textures were trialed which varied the mediums and colours used, and most critically the density of the texture. The optimum texturization was considered the one that produced the least noise in the DSM. From these trials it was found that a very dense and sporadic texture (less than 1 mm spacing) formed using blue and red acrylic paint was the most effective, efficient and non-destructive means of texturizing the surface of the cladding. Figure

3.9 shows an example of a cladding sample that has been texturized prior to mounting in the apparatus. However, the acrylic paint did not entirely reduce the shine on the cladding surface so an aerosolized corn-starch product (cosmetic dry shampoo) was used to lightly coat the surface.

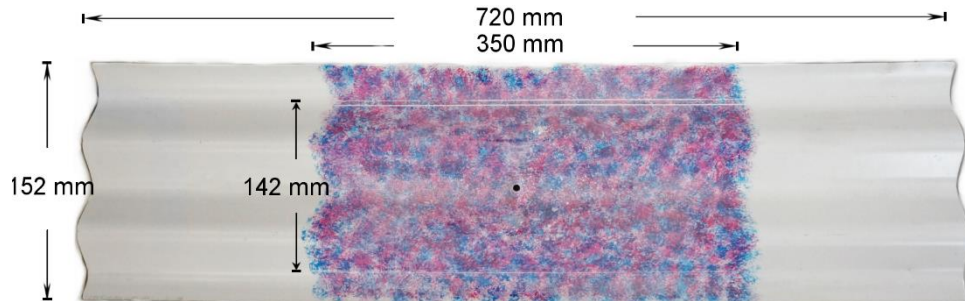


Figure 3.9: Texturized cladding sample

The clarity and resolution of the photographs comprising the image set affects the quality and accuracy of the DSM. Selecting an appropriate camera required careful consideration with four different cameras trialed prior to the purchase of a Sony NEX-5R digital camera. Both the image sensor and autofocus function were two deciding factors. The arrangement of the apparatus within a table mounted testing machine means that the photographs of the cladding surface were taken without a tripod and with the photographer maintaining an awkward posture. The autofocus on the Sony NEX-5R was quick and effective and avoided the need to use a manual focus. The awkward posture of the photographer also necessitated the use of a faster shutter speed to avoid motion blur in the image. A faster shutter speed results in a darker image so to avoid increasing the ISO and introducing unnecessary noise in the image two 500 Watt halogen lamps were installed above the apparatus to increase the available light. The lamps were powerful enough to accommodate a low ISO, a high shutter speed and a high aperture, producing noiseless images that had the entire cladding surface in focus.

A specific photoshooting method was also developed for the corrugated cladding surface. The planar aspect of the cladding sheet in addition to the waveform profile and the deformation surrounding the screw makes the generic shooting method for an object ineffective (as defined by Agisoft LLC (2014)). Following trials of various methods, the final shooting method combined both methods suggested for a façade and an object (Agisoft LLC, 2014). Figure 3.10 shows a schematic of the adopted shooting method although for clarity of the image not all camera positions have been included in the schematic. The photoshooting method had two distinct phases: Phase 1 focused on the whole cladding surface whilst Phase 2 focused on the local deformation surrounding the fastener at the centre of the sample. Each photograph also had approximately 80% overlap with the neighbouring photographs to ensure the DSM was fully constructed without gaps. This overlap was based on further trial and the suggestion that for areal photogrammetry each photograph must have 80% of forward overlap and 60% of side overlap.

Throughout the development of appropriate sample preparation and photoshooting methods the minimum number of photographs required to produce a DSM with minimal noise was established. An image set of approximately seventy photographs produced a DSM with acceptable surface quality. These seventy photographs focused on a localised section of the

cladding sheet measuring 350 mm × 142 mm, as indicated in Figure 3.9, which is approximately half of the whole sample area. By focusing on half of the sample the photoshooting and computational processing time required to construct a DSM was significantly reduced whilst still effectively capturing the local deformation and displacement of the sample.

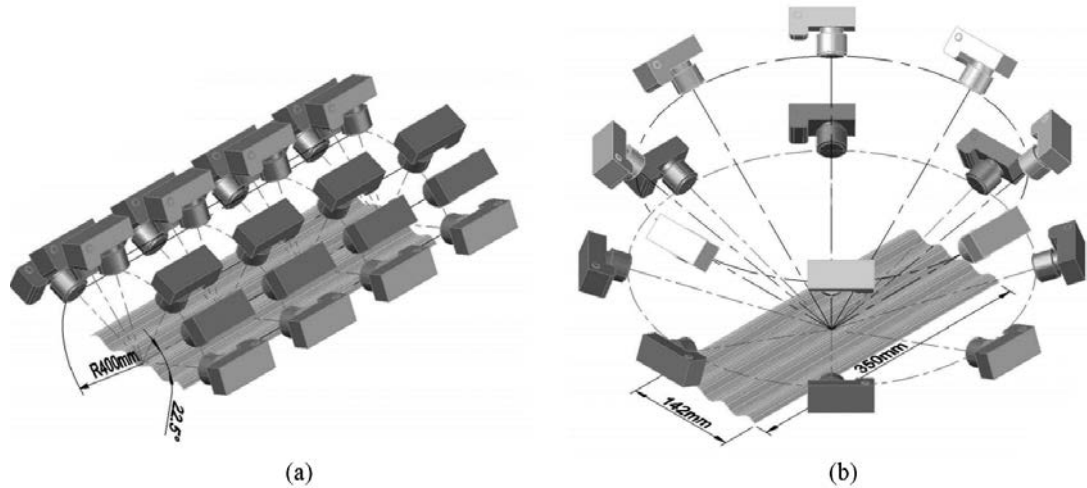


Figure 3.10: Photoshooting method (a) Phase 1 and (b) Phase 2

3.2.2 Using Agisoft PhotoScan to Create DSM

Once the photoshooting session was successfully completed, the relevant image set was input to PhotoScan Standard. Seventy photographs taken with a 16.1 MP camera represents a significant data set for processing and is considerably taxing computationally. To reduce the necessary run time of the digital reconstruction, a high performance desk top computer was used. The computer used an 8 core AMD FX processor at 4 Ghz, 32 GB of RAM and two AMD R9 290 GPUs running a 64 bit Windows operating system. The GPUs in particular accelerated the processing time.

The first stage of processing involves extracting feature points and matching them between the photographs which is described in the software as photograph alignment. This alignment stage automatically calibrates the camera, determining the intrinsic and extrinsic parameters. Agisoft also offers a free program called Agisoft Lens (2014) that allows the user to calibrate the camera and is particularly useful if a non-standard digital camera is being used. The Agisoft Lens program was used to calibrate the Sony NEX-5R digital camera and to confirm that the automatic calibration performed during photographic alignment was accurate. Within Agisoft PhotoScan, the user can specify a level of accuracy for the alignment ranging from high to low. For this analysis, a high accuracy was always specified. To compensate for the longer run time of the alignment stage induced by specifying a high accuracy, each photograph was manually masked prior to alignment. Masking a region of the photo, such as the background, reduces the number of feature points the SFM algorithm detects and thereby reduces the overall run time. The alignment stage took approximately 25 minutes to complete and generated a sparse point cloud of the cladding surface.

The second stage of processing is surface reconstruction using the dense point cloud produced by the alignment stage. Surface reconstruction involves refining the dense point cloud and

converting it into a DSM. The user can choose between two algorithms, Smooth and Sharp, for converting the point cloud to a DSM. Sharp reconstructions do not fill voids by introducing extra geometry while the Smooth reconstruction produces little to no holes in the resulting mesh. Both methods were attempted and the Smooth reconstruction produced a more agreeable representation of the cladding than the Sharp reconstruction. The Sharp reconstruction method tended to produce a noisy DSM of the cladding where the surface would appear pitted. The user could also specify a target quality of the reconstruction, ranging from Lowest to Ultrahigh. For all reconstructions a quality of High was specified rather than Ultrahigh as Ultrahigh tended to drastically increase the reconstruction time with minimal improvement in accuracy. The user can also specify the number of polygons used to discretise the DSM with a typical face count of 300,000 used in all reconstructions. The greater the number of polygons requested, the longer the reconstruction effort took where 300,000 polygons resulted in a reconstruction time of five hours. Finally, the user also has the ability to apply a texture map to produce a realistic DSM of the cladding. This feature was implemented for all DSMs to ensure the markers used for scaling in post-processing were then visible on the DSM.

3.2.3 Scaling and Post Processing

The DSMs produced by Agisoft PhotoScan Standard are not to scale and can be scaled manually in an open source program called MeshLab (Visual Computing Lab – ISTI – CNR, 2012). During sample preparation, when the cladding surface was texturized, a series of markers were placed on the photographed area. The distance between these markers were measured using Vernier micrometers. These markers are visible on the texture mapped DSM and MeshLab can be used to measure the unscaled distances between them. Knowing each of the unscaled distances and the respective micrometer measurements, an average multiplier can be determined to transform the unscaled DSM to scale. This scale transformation can be easily applied in MeshLab.

3.2.4 Accuracy of Photogrammetric Method

The accuracy of any photogrammetric method depends greatly on the nature of the surface of the object, the skill of the photographer, the photogrammetry software, camera quality and resolution, and the number of photographs in the image set. Each of these variables can change between applications and the determined accuracy documented by other researchers cannot be assumed applicable to all situations. To establish the potential accuracy of this photogrammetric method for the measurement of deformation and displacement of a cladding sheet, a DSM of a cladding sample was created using photogrammetry and compared with a DSM constructed using a 3D laser scanner.

A cladding sample was installed within the apparatus and constant amplitude loading was applied until the sample failed. Failure of the cladding sample involved initiating and propagating a fatigue crack beneath the head of the fastener until the fastener pulled through the cladding sample, resulting in gross permanent deformation. This cracked sample was then sent to a third party to be professionally scanned by a Surphaser 3D Laser Scanner which has an accuracy of within 250 microns for a sample of this size. The cladding was raised and secured by magnetic V-clamps so the scanner could capture the full extent of the cladding sample, including the edges. Upon return of the sample, the cladding was placed in the

apparatus to recreate the experimental conditions as close as possible with even the load cell and fastener clamp included in the arrangement. The fastener clamp cast a shadow in the vicinity of the fastener which obscured the deformation in that region so two LEDs were attached to the fastener clamp to negate the shadow. It was important to recreate the experimental conditions to ensure that the photoshooting process was executed in a similar manner to future trials. However, the lid of the apparatus was not placed atop the cladding sample. The considerable weight of the steel lid would flatten the permanent diagonal warp through the cladding sample, thereby changing the shape of the cladding that was scanned by the Surphaser scanner. The photogrammetric method, as described earlier, was then executed to create a DSM of the cracked cladding sample, with the markers needed for scaling the DSM placed on the cladding surface itself.

The two DSMs produced by the laser scanner and photogrammetric method can be compared directly using programs like CloudCompare (Girardeau-montaut, 2014), Polyworks Inspector (Innovmetric, 2014) and Geomagic Design X (3DSystems, 2014). In this investigation, the open source program CloudCompare (Girardeau-montaut, 2014) was favoured given its availability and robustness. CloudCompare (Girardeau-montaut, 2014) can register two DSMs and calculate the local distance between the two. Firstly, the two DSMs are aligned using the “Interactive Closest Point” algorithm documented by Besl and McKay (1992). This process of aligning the DSMs is often referred to as registration. Following registration, the local distance between the two DSMs can be calculated. When comparing two – ideally identical – DSMs, the local distance between the two DSMs reflects the surface deviation, or discrepancy, between them. To calculate the distance between the two DSMs the Cloud-to-Cloud function within CloudCompare was used as it can calculate the “true” distance between the two DSMs, rather than the nearest neighbour distance as distinguished in Figure 3.11, and describe that distance in terms of Cartesian components. In order to use the Cloud-to-Cloud function both DSMs were converted from polygon mesh to a point cloud using the “Sample points from mesh” function in CloudCompare, with both DSMs being discretised by 1,000,000 points. The “true” distance from the reference cloud is determined by fitting a mathematical model on the nearest point and six of its neighbours, and computing the shortest distance between this fitted surface and the compared point. Given the high curvature and smooth nature of the cladding surface, the quadratic mathematical model was used to fit the surface of the nearest point and its neighbours.

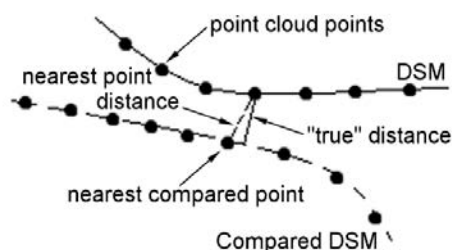


Figure 3.11: Definition of “true distance”

When comparing the two DSMs a large discrepancy across the diagonal became apparent. Figure 3.12(a) is contoured with respect to the signed surface deviation between the two DSMs with a histogram of the compared points alongside the colour bar. Each opposing corner being opposite signed demonstrates how the two DSMs differ across the diagonal. This suggests the

cladding supports used during laser scanning and photogrammetry may still vary, with each DSM having differing magnitude of warp in the diagonal.

The accuracy of the photogrammetric method is difficult to appreciate when comparing the full sample DSM due to the diagonal warp. The accuracy of the photogrammetric method is more assessable by comparing only a 70 mm × 70 mm section at the centre of the cracked cladding sample where the greatest deformation is featured. The surface deviation across the centre of the cladding sample is presented in Figure 3.12(b) and shows that 95% of the sampled points from the photogrammetry DSMs had a deviation less than 0.1 mm from that of the laser scanner DSM. The largest surface deviations occur around the crack perimeter. The void created by the crack was included in the photogrammetry DSM by manually removing the relevant points in MeshLab prior to importing the DSM into CloudCompare. The large deviations surrounding the crack perimeter could be attributed to superfluous points that should have been removed within MeshLab. The longitudinal streaks in the cladding surface, as highlighted by the contours, are features in the laser scanner DSM. The cladding surface was dusted prior to being scanned by the laser which left streaks along the surface. Given these uncontrolled variables, the accuracy of the photogrammetry method could confidently be stated as ± 0.1 mm.

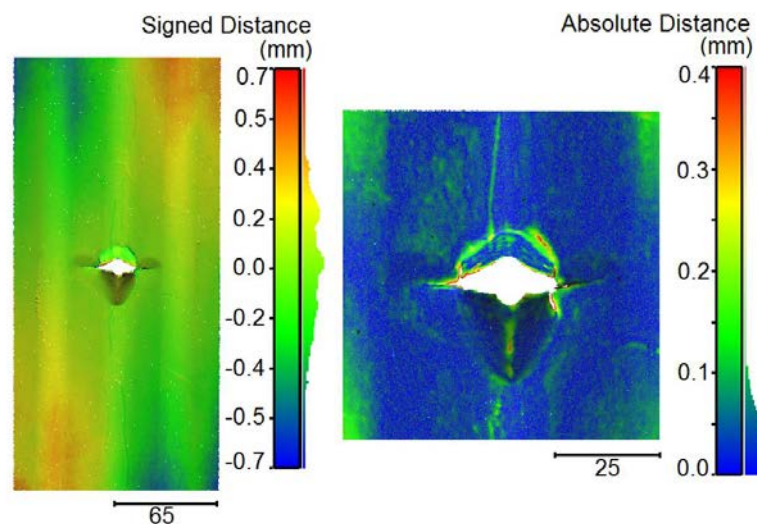


Figure 3.12: Surface deviation between DSMs from laser scanning and photogrammetric method for (a) 350 mm × 142 mm section and (b) 70 mm × 70 mm section

3.2.5 Inferring Displacement of the Cladding Sample

Some photogrammetry systems enable 4D reconstructions of deforming objects where history of the object deforming can also be recorded. These systems typically involve a system of cameras which are synchronized so they record images of the deforming object simultaneously. Each of these cameras offers a single perspective of the object which can then be aligned and interpolated using photogrammetry. Bakhshinejad and Zamankhan (2012) effectively used six fixed cameras to map the bed of a granular material which was predominantly planar. Should the object be planar, fewer cameras are required. Unfortunately the cladding requires a minimum of seventy camera angles and locations to create an accurate DSM. Therefore to implement the photogrammetry method whilst capturing how cladding deforms under load, the loading sequence was paused periodically. The displacement of the

fastener was paused at six intervals during loading and unloading to allow for collection of photographs; at 2.7 mm, 10 mm, 29 mm, 28 mm, 16 mm and 8 mm. The specific intervals where chosen to ensure the elastic deformation, local plastic collapse and permanent deformation of the cladding sample were captured. Prior to testing, the fastener was displaced until a fastener reaction of 5 N was reached which brought the fastener and the rubber seal into contact with the cladding crest without the rubber seal visibly deforming. Both the position and the fastener reaction were then zeroed and this was taken to be the cladding sample at rest (0 mm displaced). Figure 3.13 details the relationship between displacement and fastener reaction for three photogrammetry trials and indicates at which point in the load sequence the test was paused for photoshooting. Figure 3.13 also provides the eccentricity of the fastener from the centre of the cladding crest

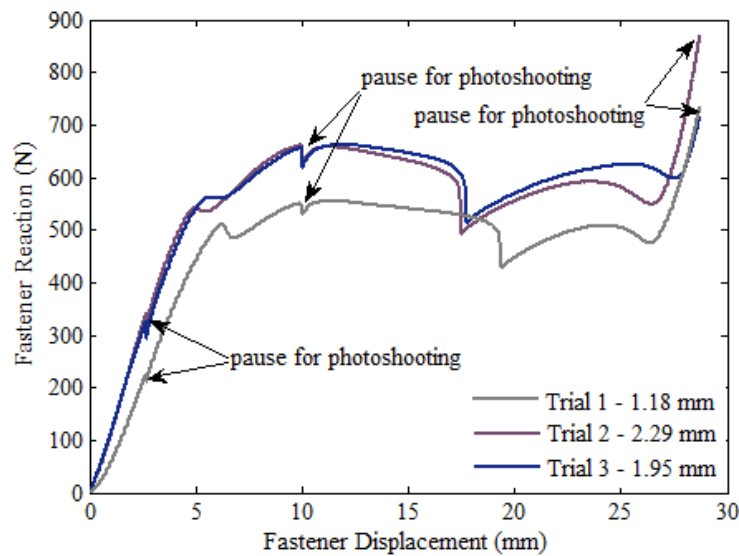


Figure 3.13: Fastener displacement-reaction curve for photogrammetry trials

The deflection of the cladding sample can be inferred using CloudCompare and MATLAB. The deflection of the cladding sheet was taken to equal the vertical (z) component of the distance between a DSM of the cladding under no applied load (at-rest DSM) and a second DSM of the cladding subjected to load (deformed DSM). In order to appropriately compare the two DSMs, the lid of the apparatus surrounding the localised area of the cladding sample was included in the DSM. Rather than registering the two DSMs to achieve a best fit, the two DSMs were registered based on a best fit of twelve markers etched on the lid of the apparatus. This lid is fixed and remains in a constant position during loading, thereby acting as a datum for the comparison. Following registration of the two DSMs in CloudCompare, the coordinates of every point comprising both DSMs was exported to MATLAB which then sorted the coordinates and calculated the difference between the z components of corresponding points. Figures 3.14 to 3.16 describe the various intervals of loading in terms of the deformed DSM contoured by the out-of-plane deflection of the sample. The centre point of the cladding sample did not deflect equally with the displacement of the fastener given the highly compressible rubber seal beneath the head of the fastener. The contour plots of the deflection clearly highlight the flattening of the central crest following local plastic deformation and particularly emphasize the highly localized dimpling at the fastener. The contour plots also effectively capture the gross permanent deformation that results due to

loading through local plastic collapse, with the cladding at the fastener permanently displaced by 8 mm and deformed in a diamond shaped dimple.

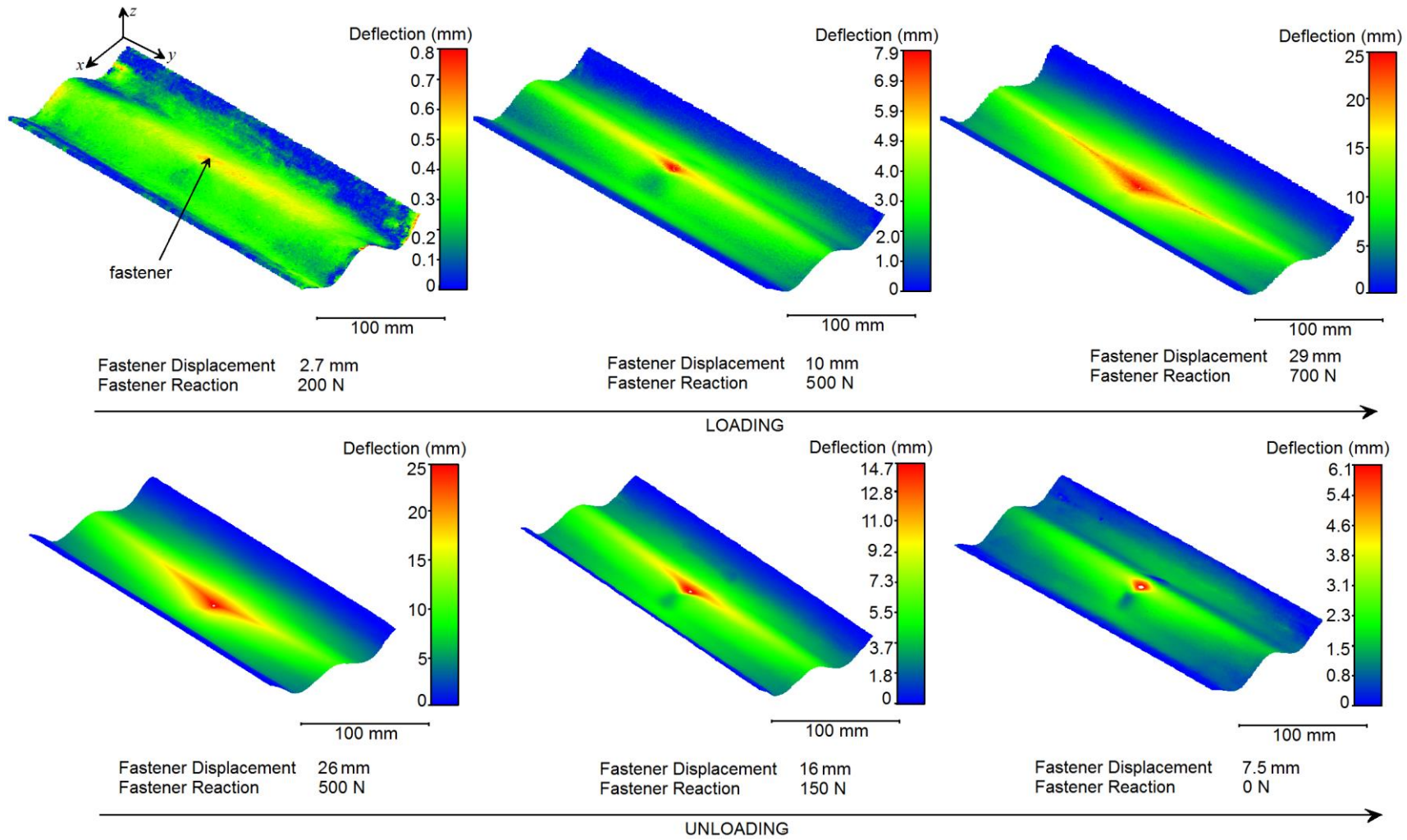


Figure 3.14: Out-of-plane deflection of cladding sample subject to differing magnitudes of loading for Trial 1

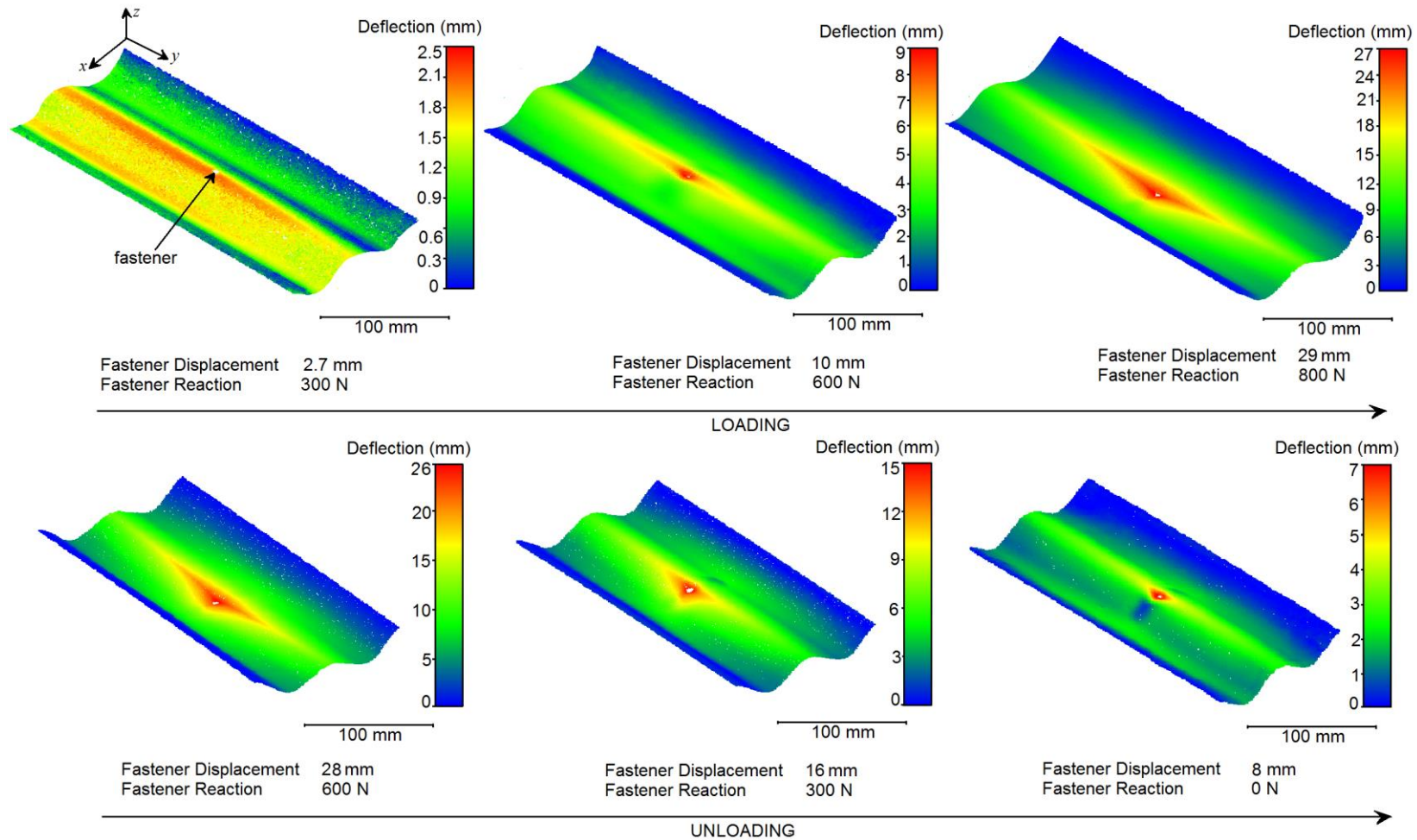


Figure 3.15: Out-of-plane deflection of cladding sample subject to differing magnitudes of loading for Trial 2

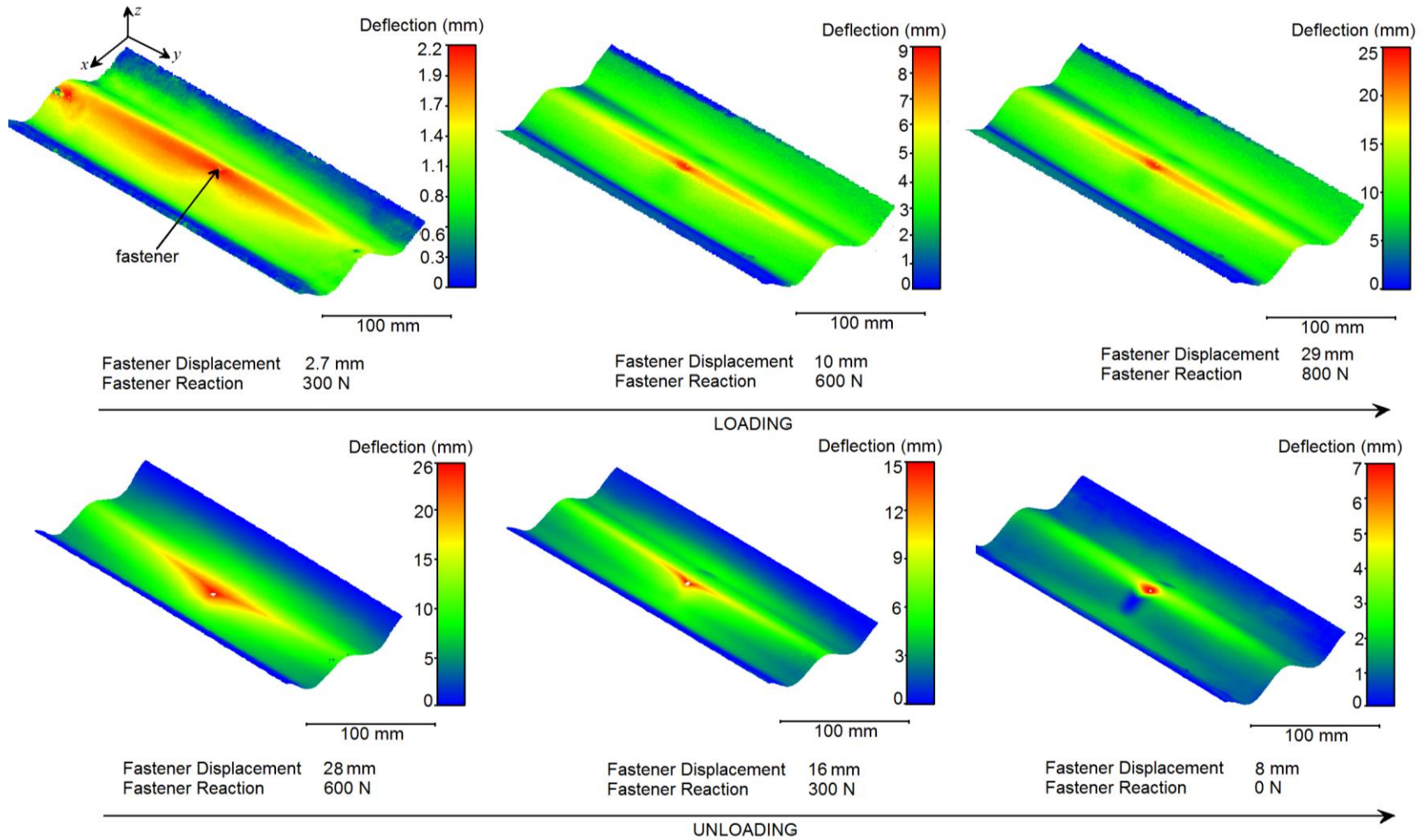


Figure 3.16: Out-of-plane deflection of cladding sample subject to differing magnitudes of loading for Trial 3

In both Figure 3.13 and Figure 3.14 the first photogrammetry trial appears to vary considerably from the two remaining photogrammetry trials in terms of both fastener reaction and resulting deflection. In particular at the first interval, when the fastener has been displaced by 2.7 mm, the cladding in the first trial has only deflected 0.7 mm at the underside of the fastener. It is unreasonable to assume that the washer had compressed a full 2 mm under a small applied load of 220 N, particularly when the remaining two trials suggest the washer can compress only 1 mm under a greater load of 350 N. It is more likely the cladding sample was not compressed securely between the apparatus lid and base, and under the initial stages of loading the cladding reseated itself within the boundary clamps. A smaller compressive force sandwiching the cladding between the apparatus lid and base could also justify the reduced stiffness of the cladding sheet. During development of a corresponding numerical model, relaxing the boundary conditions by reducing the compressive force resulted in a reduced stiffness of the structure. Figure 3.17 presents the cross sectional view of each photogrammetry trial for when the cladding was installed within the apparatus but with no load being applied. The profile of the cladding was extracted from the dense point clouds produced using photogrammetry. As progressively greater compressive force is applied to the cladding at the boundary, the centre of the cladding would deflect and lower in towards the fastener head. Clamping the cladding would result in deformation of the cladding sample as the longitudinal clamps were slightly inward of their designed positions, so rather than flattening the centre of the crests the longitudinal clamps partly compressed the rise of the crest. Strong compressive forces compressing the rise of the crest deflected the cladding sample and reduced the curvature of the rise of the crest. Focusing on the rise of the crest, as shown in the dashed segments of Figure 3.17, Trial 1 clearly still possess some curvature of the rise of the crest whilst the remaining two trials are relatively flat.

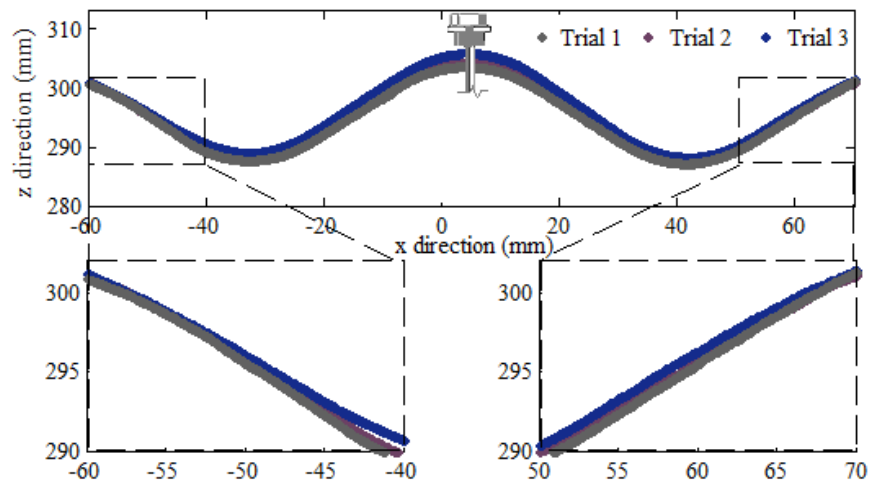


Figure 3.17: Cross sectional view of the cladding installed within the apparatus.

During photoshooting, the fastener was also captured in order to maintain the accuracy of the DSM at the fastener hole edge where the cladding undergoes significant deformation. The screw was texturized in a similar manner to that of the cladding and the lid of the apparatus. As the fastener was included in the resulting DSM, the eccentricity of the fastener was then measurable. A cross section was extracted from the DSM of the cladding installed within the apparatus with no load applied and the Cartesian coordinates of each data point from the cross section was passed through MATLAB. The turning points of the crests of the cladding were identified by fitting a circle to the relevant data points in MATLAB. The lines of best fit for

each crest returned a root mean square error of 0.998 or higher in all three DSMs. Figure 3.13 details the eccentricity of the fastener with respect to the midline of the central cladding crest. The eccentricity of the fastener, in addition to eccentricity in the cladding boundary, resulted in the cladding collapsing in two stages, where the rise of the crest to one side of the fastener would buckle prior to the opposing side. This two stage collapse is visible in Figure 3.13 as the two points in which the cladding suddenly lost stiffness. The contours of the cladding deflection also captured the two stage buckling process particularly during loading in Trial 1 (Figure 3.14), unloading in Trial 2 (Figure 3.15) and unloading in Trial 3 (Figure 3.16). The eccentricity of the fastener varied between 1.2 mm and 2.3 mm for the three photogrammetry trials, with the 1 mm variation between trials having little effect on the response of the cladding with respect to fastener reaction and fastener displacement.

3.2.6 Summary

Using a single digital camera and affordable photogrammetric software, accurate digital reconstructions of corrugated cladding deforming under applied load can be obtained. The photogrammetry method was able to achieve an accuracy of ± 0.1 mm for a 142 mm \times 350 mm section of the cladding. This photogrammetry method also enabled the deflection of the deformed cladding to be measured and helped identify different aspects of the cladding behavior. The greatest benefit of this method, however, is its application in full field comparisons for numerical model validation studies. The DSMs created here are used in full field comparisons with a corresponding numerical model in Section 5.7 – “Model Validation”.

4. FATIGUE RESPONSE OF CLADDING

4.1 CYCLIC MATERIAL PROPERTIES

4.1.1 Background

The material properties of metals, particularly plasticity, changes when subject to repeated rather than monotonic loading. Under monotonic loads, most metals either exhibit no hardening and are elastic-perfectly plastic, or exhibit strain hardening or softening. The latter hardening characteristics suggest that after plastic straining under a single monotonic load, the material will respond differently should it be reloaded. ABAQUS (Dassault Systemes, 2013) has a number of hardening definitions to account for this phenomenon with the default being isotropic hardening. Isotropic hardening is mostly suited to problems involving gross plastic straining, such as the cladding subject to monotonic loads in IFC tests. Isotropic hardening is characterised by an increase in the yield stress due to plastic strain. Figure 4.1 demonstrates the concept of isotropic hardening where an isotropic material is initially loaded through the yield stress σ_A to σ_B and unloaded. The load is then reapplied with yielding now occurring at σ_B which is greater than the initial yield stress σ_A . Should loading continue to σ_C prior to unloading, then the new yield strength of the material would be σ_C . Figure 4.1 (b) describes the expansion of the yield surface for the isotropic material due to isotropic hardening. As the material is isotropic, the yield surface is based on the Von Mises stress and appears circular. Isotropic hardening is characterised by an expansion in the yield surface with no translation. If a sufficient number of cycles are applied to the specimen subject to isotropic hardening, the yield strength of the material would continue to increase with each subsequent cycle until it

reaches a purely elastic response. For metals an eventual elastic state is unrealistic under repeated loading given the Bauschinger effect (Milne et al, 2003).

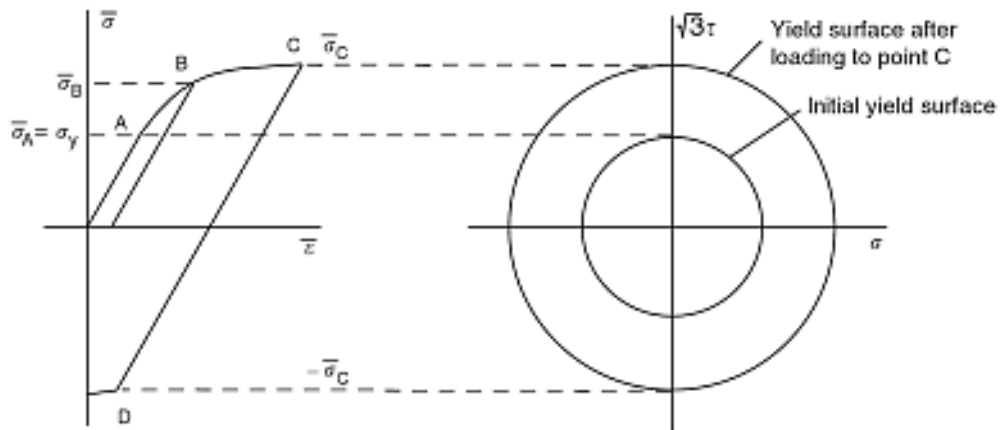


Figure 4.1: Example of isotropic hardening for an isotropic material (credited to Milne et al, 2003).

Kinematic hardening, rather than isotropic hardening, is suitable for cyclic models as it can account for the Bauschinger effect. Kinematic hardening is characterised by a *translation* in the yield surface with no change in size of the yield surface. However, some more complex cyclic loading sequences cannot be effectively simulated using kinematic hardening alone. ABAQUS offers a combined nonlinear kinematic and isotropic hardening model, based on the Chaboche model, to account for more complex loading sequences such as unsymmetric tension-compression cycling. During stress-controlled cycling with a non-zero mean stress, the strain with each cycle accumulates, a phenomenon known as ratcheting. For strain-controlled experiments with a non-zero mean strain a similar phenomenon occurred known as relaxation of the mean stress. Both ratcheting and relaxation of the mean stress occur due to cyclic hardening/softening but without the eventual stabilisation particularly when the mean strain/stress is sufficiently large (Milne et al, 2003). During the IFC fatigue tests, the resulting strain at the longitudinal edge of the fastener hole was entirely tensile, even during unloading; suggesting that either ratcheting or relaxation of the mean stress is in effect. The material may be subject to either condition given the IFC fatigue tests were neither stress nor strain controlled but simply load controlled. The nonlinear kinematic/isotropic hardening model provided in ABAQUS can accommodate ratcheting and relaxation of the mean stress (Dassault Systems, 2013).

The nonlinear combined isotropic and kinematic hardening definition available in ABAQUS is based on the Chaboche model (Lemaitre and Chaboche, 1990). The general expression for the yield surface, F , is:

$$F = f(\sigma - \alpha) - \sigma^0 \quad (4.1)$$

Where the backstress, α , describes the translation of the yield surface due to kinematic hardening and σ^0 describes the extent of the yield surface which varies due to isotropic hardening. The function $f(\sigma - \alpha)$ is the equivalent Mises stress or Hill's potential with respect to the backstress. Multiple kinematic hardening components can be superposed to more accurately model some materials, particularly the ratcheting phenomenon in metals (Lee et al, 2012). The hardening law for each component of kinematic hardening is dependent on two

material parameters which are typically calibrated from cyclic test data: C_k is the initial kinematic hardening moduli and γ_k describes the rate at which the hardening moduli decreases with increasing plastic strain. The isotropic hardening component of the Chaboche model depends on three material parameters: $\sigma|_0$ is the yield stress at zero plastic strain, Q_∞ is the maximum possible change in size of the yield surface and b describes the rate at which the yield surface changes with increasing plastic strain. In its simplest form, with only a single backstress, the nonlinear combined kinematic and isotropic hardening definition requires five material parameters and with each additional backstress two more material parameters are required.

The dynamic material properties of a material can be found using a cyclic bend test or by fully reversible tension-compression testing also referred to as symmetric tension-compression cycling. Cyclic bend tests are generally simple to perform, requiring only standardized material testing equipment. However, the stress distribution in the sheet during a bend test is not homogenous meaning the relevant strain values cannot be determined directly from the experiment. Typically, the bend test is simulated using FEA with the desired material parameters then inferred by correlating the simulation with the experimental force and displacement data (Eggertsen and Mattiasson, 2011). Inferring the dynamic material parameters of metals using a numerical model is incredibly challenging as a minimum of five unknown parameters are required to define the dynamic material properties. Alternatively, a tension-compression test can be used to directly determine the relevant dynamic material properties of a material, although tension-compression tests are typically unsuitable for thin specimens as they tend to buckle during the compressive cycle. Anti-buckling fixtures can be implemented to suppress the out-of-plane buckling of the specimens without directly interfering with the in-plane tensile and compressive response. These anti-buckling fixtures typically involve the application of a normal force to the face of the sample that is comparatively smaller in magnitude to the applied uniaxial force so as to avoid adversely changing the uniaxial stress state to a biaxial stress state.

An anti-buckling fixture for tension-compression testing of thin specimens has been the subject of significant study given the importance of dynamic material properties in the forming of sheet metals such as sheet stamping; the sheet following stamping springs back when the contacting load is removed in a clear reverse or unloading cycle. Researchers have observed the Bauschinger effect during the reverse cycle which requires knowledge of the dynamic material properties in order to recreate the forming process numerically, a common forming design tool implemented by the thin-walled structures industry (Dietrich et al, 2014).

One of the earliest designs for an anti-buckling fixture was described by Madden (1946) which simply involved two rigid plates that compressed the sample. The confining plates were machined smaller than the sample to allow a gap between the plates and the loading frame. A gap at each end allows for the necessary displacement of the loading frame which is required to produce the desired strain range. The gap also needed to be sufficiently small to avoid any possible buckling of the sample within this unsupported region. Consequently this type of anti-buckling fixture is most suitable for small strain tension-compression tests. A more advanced variation of the small strain anti-buckling fixture is shown in Figure 4.2. Two red silicone blocks were added to either end of the fixture in contact with the loading frame to ensure the gaps at either ends of the sample do not buckle whilst being sufficiently compressible to allow

for the required displacement. The fixture shown in Figure 4.2 also has a small window, narrower than the sample, to enable strain measurement using digital image correlation (Eggertsen and Mattiasson, 2011).

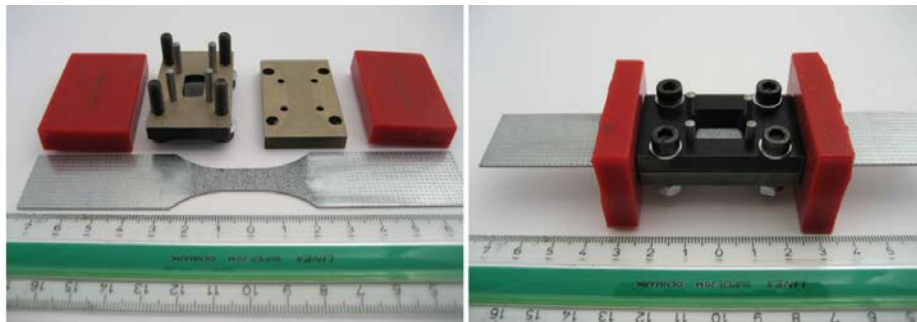


Figure 4.2: Small strain anti-buckling fixture implemented by Eggertsen and Mattiasson (2011)

More complex variations in anti-buckling fixtures have been created to accommodate larger magnitudes of strain. Kuwabara (2007) and Dietrich et al (2014) created variations of an anti-buckling fixture that support the surface of the sample using a series of thin plates as shown in Figure 4.3 (a). Every alternate side-supporting plate is attached to the top of the load frame whilst the remaining side-supporting plates are attached to the bottom of the load frame, therefore the side plates are displaced concurrently with the load frame without losing contact with the sample.

Cao et al (2009) and Magargee et al (2011) proposed an innovative solution to accommodate large strain ranges. The design uses multiple sliding blocks, connected by springs, which allows the anti-buckling fixture to displace with the loading frame whilst maintaining contact across the whole surface of the sample. Magargee et al (2011) found the sample installed within the fixture could withstand four times the theoretical buckling capacity of the sample. The design proposed by Magargee et al (2011) is presented in Figure 4.3 (b). By having two sliding wedges, the middle wedge remains stationary during loading to provide an unobstructed view of the speckle pattern painted on the surface of the sample. Using digital image correlation techniques, the strain across the gauge length of the sample can be calculated.

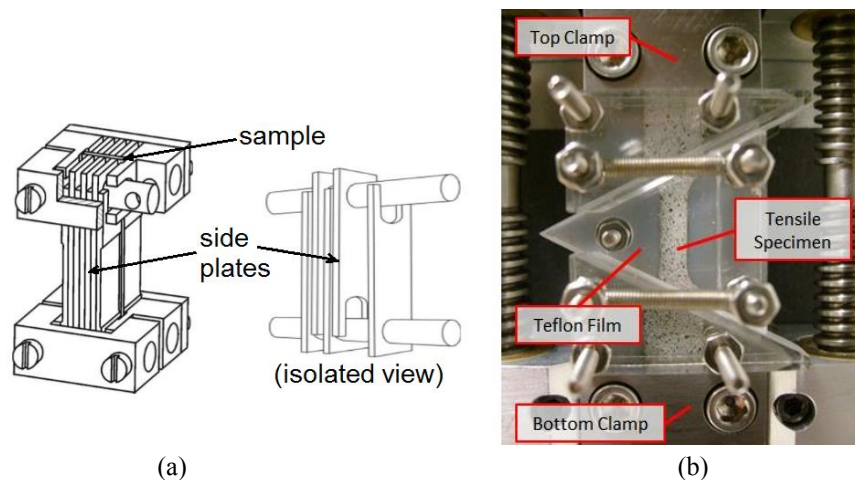


Figure 4.3: Anti-buckling fixture created by (a) Dietrich et al (2014) and (b) Magargee et al. (2011)

At zero applied load to the sample, the fixture created by Magargee et al (2011) exerts a small force on the load frame as the springs are extended. As a uniaxial tensile load is being applied, the tension in the spring displace the top and bottom wedge ensuring the anti-buckling fixture continually contacts the loading frame. During compressive loading of the sample, a fraction of the compressive load once again extends the spring. The force acting on the load frame during the tensile load cycle, the additional force required during the compressive load cycle and the component of friction between the sliding wedges can all be determined simultaneously by testing the anti-buckling fixture without a sample. These forces are then subtracted from the tension-compression test results during the data analysis to isolate the response of only the sample.

Finding the combined kinematic and isotropic hardening of the cladding under dynamic load requires reversible tension-compression tests with a strain range similar in magnitude to the strain range expected in the IFC fatigue tests. The strain amplitude documented during cladding fatigue tests (see Section 4.3 – “General observations”) ranges from 0.6% to 0.8% for the transverse and longitude respectively. The strain distribution surrounding a fastener is complex and spatially varying so the strain range measured using strain gauges was favored as it somewhat reflects the average strain range in the vicinity of the fastener and the data is available for multiple trials. For a strain range of $\pm 0.6\%$ to $\pm 0.8\%$ a displacement of the loading frame of approximately ± 0.4 mm to ± 0.5 mm for a gauge length of 65 mm is required. Such a small strain range suggests an anti-buckling fixture like that created by Eggertsen and Mattiasson (2011) and that created by Magargee et al. (2011) would both be acceptable in this investigation.

It is unlikely that a strain range of 0.6% to 0.8% is obtainable, however, as the longitudinal direction of the cladding appears to be very brittle. During monotonic tensile tests of samples cut from the longitudinal direction, fracture occurred suddenly at an average strain of 0.38% (Henderson, 2010). Consequently, the applied strain range is limited to less than 0.38% rather than the desired 0.6-0.8% as only longitudinal samples are available. This unfortunately limits the accuracy of future ‘H’ type crack models which have a suggested strain range of 2% (based on a numerical analysis).

4.1.2 Cladding Samples

The geometry of the cladding sample was based on Australian Standards AS 1391-2007 which describes the requirements for tensile testing of metallic substances, including thin sheets. Appendix A of AS 1391-2007 details the required dimensions for the dogbone-shaped tensile samples as demonstrated in Figure 4.4. The samples were cut from corrugated cladding having exhausted the coupons taken from the cladding material that was specially fabricated (Henderson, 2010). Cutting the samples from corrugated cladding limited the samples to the flat section of the cladding between crests and valleys which has a total width of 24 mm. A limiting width of 20 mm at the gripped end of the sample was selected to provide some tolerance to the laser cutting process. The corresponding width of the sample (b) was taken to be 12.5 mm to provide an adequate transition between gripped ends and gauge length. For a width of 12.5 mm, AS 1391-2007 recommends the following dimensions:

- a gauge length (L_o) of 50 mm
- parallel length (L_c) of greater than 75 mm

- free length (L_t) of greater than 87.5 mm
- a minimum transition radius of 12 mm

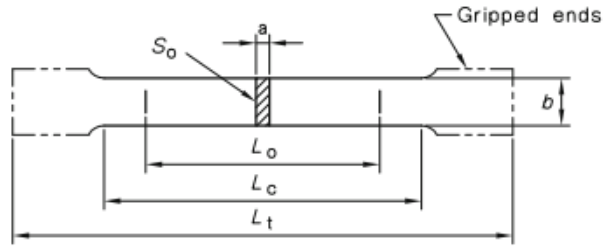


Figure 4.4: Dog bone sample as shown in AS 1391-2007

The suggested dimensions were used to create a numerical model of the tensile sample in ABAQUS. A tensile load was applied to the sample and the resulting strain distribution is shown in Figure 4.5 (a). The strain contour clearly highlights some localized strain at the transition to the gauge length. The transition radius was increased to 24 mm which in turn increased the overall length of the sample as the parallel length (L_c) was maintained. Figure 4.5 (b) describes the strain distribution for the modified sample. The increase in transition radius prevented the localization of strain at the transition and consequently reduced the peak strain from 9.0×10^{-3} to 8.8×10^{-3} which acts uniformly through the gauge length of the sample. Consequently all tension-compression tests used the modified geometry which has the following dimensions:

- gripped end width of 20 mm
- width (b) of 12.5 mm
- a gauge length (L_o) of 65 mm
- parallel length (L_c) of 75 mm
- free length (L_t) of greater than 151 mm
- a minimum transition radius of 24 mm

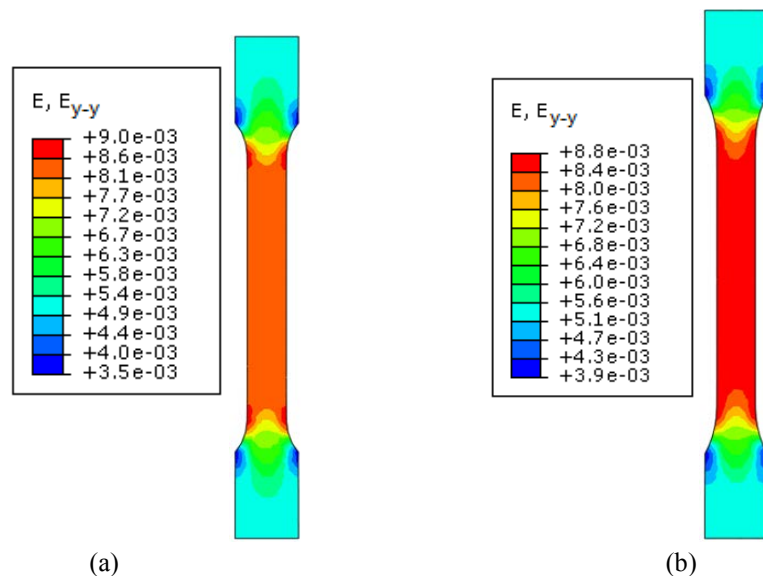


Figure 4.5: Strain contour for tensile sample with (a) AS 1391 recommended dimensions and (b) modified geometry

4.1.3 Test Apparatus

An anti-buckling fixture based on the design proposed by Magargee et al. (2011) was first trialed in this investigation. This design was favored as it interferes minimally with the tension-compression data and there is no risk of buckling in the small unconfined regions at either end of the fixture. The fixture was constructed from 6 mm thick Perspex with a small window included in the central piece to allow access to a strain gauge. Two Teflon sheets, 0.4 mm thick, were placed either side of the sample to minimize friction between the sample and the Perspex. The fixture, assembled and installed within United 50kN-STM, is shown in Figure 4.6. The fixture effectively increased the buckling capacity of the sample by a factor of 6 but failed to increase the critical buckling capacity to the desired strain range. Although the fixture did not provide sufficient resistance to buckling, it did operate well and would be highly effective for testing lower strength sheet metal such as aluminum. Increasing the moment of inertia of the fixture by adding a 20 mm deep web either side was considered, however the web would interfere with the springs and partially obscure the window in the central piece so the design was abandoned.

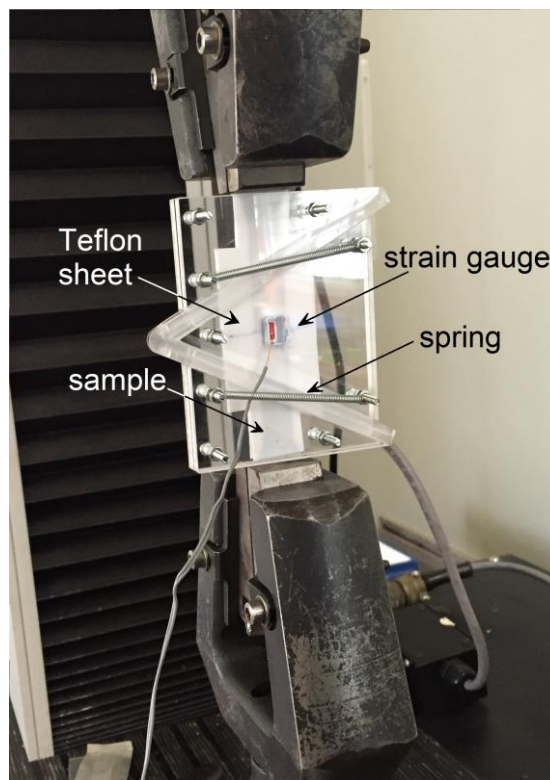


Figure 4.6: Anti-buckling fixture using sliding Perspex plates

A design similar to that proposed by Eggertsen and Mattiasson (2011) was then trialed and is shown in Figure 4.7. The fixture was constructed from 8 mm thick, 97 mm × 65 mm mild steel plates. The 97 mm long steel plates therefore leaves 1.5 mm of the sample above and below the plates unrestrained. Six 7 mm diameter screws in combination with six springs were used to press the plates together. The springs have a known stiffness of 1 N/mm which in conjunction with the known shortening of the spring allows for the normal pressure exerted on the sample to be approximated. Typically the normal pressure exerted on the sample should be less than 1% of the uniaxial stress, thereby ensuring any biaxial effect of the through-thickness

stress is negligible (Cao et al, 2009). With the springs fully compressed a normal pressure of 27 kPa was applied to the sample. As the springs were fully compressed and held in place by a nut, the stiffness of the out-of-plane direction as experienced by the out-of-plane action of the coupon would be that of the six 7 mm diameter bolts.

Teflon sheets were placed between the sample and the steel plate to minimize friction. The edges of each sample were also polished to remove any burrs produced by the laser when the samples were cut, further minimizing friction between fixture and sample. The friction forces and the weight of the fixture were quantified by comparing a tensile test of the sample without the fixture with the results of a tensile test of the sample with the fixture. In addition to reducing friction between sample and fixture, the Teflon sheets also provide some small damping given their compressibility. This damping ensures the sample is not subject to plain strain by allowing for the expansion and shortening of the sample during compressive and tensile loading respectively (Cao et al, 2009). Unfortunately this same damping would allow for some small out-of-plane buckling but the magnitude is sufficiently smaller than the resistance provided by the fixture itself.

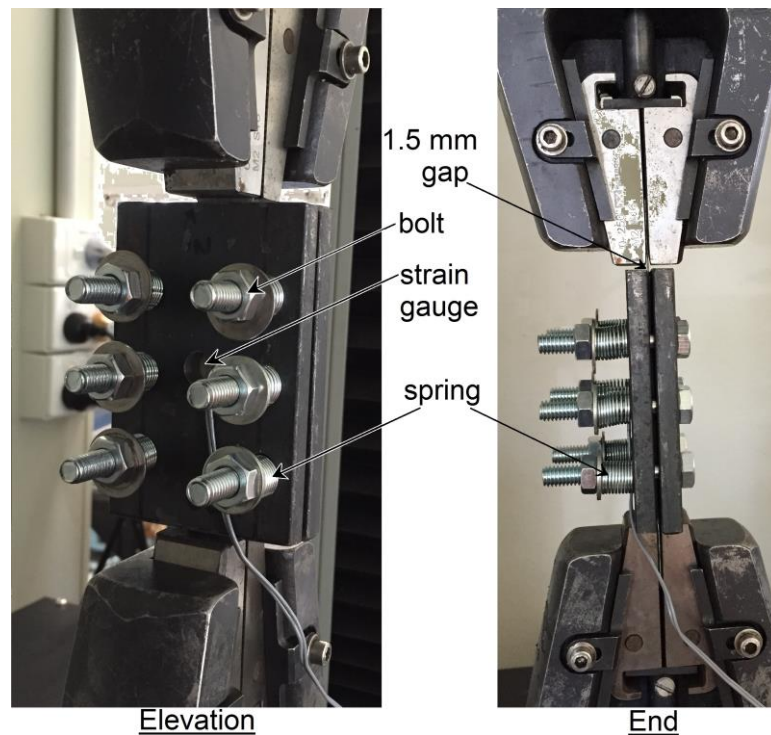


Figure 4.7: Anti-buckling fixture using steel plates

The new fixture successfully increased the buckling capacity by a factor of 35 which extends the compressive range of the sample to the desired strain range. Unfortunately the single compression test that successfully achieved the desired strain range was not repeatable as the compressed springs had a tendency to slip allowing the sample to transition to unstable equilibrium. Consequently the springs were removed and the sample compressed using only the 7 mm diameter bolts. As the normal pressure is now difficult to determine, the possible biaxial effects were quantified by viewing the change in uniaxial strain through use of the strain gauge as the bolts were tightened. Typically increasing the compressive pressure the steel plates exert on the cladding sample increases the buckling capacity of the sample. However, increasing the compressive force of the plates against the cladding sample beyond

67 MPa caused the friction between the sample and Teflon sheets to become too large; for the initial stages of loading the small unconfined section of the sample would deform while the confined section of the sample remain unchanged as the deformation was resisted by friction. Consequently the bolts were typically tightened to produce a maximum longitudinal stress in the sample of 20 MPa, which corresponds to a compressive force of 67 MPa being exerted by the steel plates.

4.1.4 Tension-Compression Cyclic Testing

Although the fixture successfully increased the buckling capacity of the cladding sample, under repeated loading only a single cycle was achievable. The sample was first loaded under a tensile force of 4000 N corresponding to a crosshead displacement of 0.8 mm, and subsequently reloaded under a compressive load of 2000 N corresponding to a crosshead displacement of -0.8 mm. However, when loaded into compression during the second load cycle, the cladding buckled in the exposed gap between clamp and fixture. This buckling is likely due to the significant softening of the steel subject to a single load cycle. In an attempt to extend the life of each cyclic test, an unsymmetric tension-compression load cycle was applied to the cladding which reduced the compressive component of the load cycle. The kinematic material properties of the cladding cannot be directly determined from the results of an unsymmetric tension-compression test, although the material properties could be inferred from the results using a corresponding numerical model. Figure 4.16 (a) is an example of an unsymmetric tension-compression test, where the cross head was raised to a maximum of 0.8 mm for tensile loading and lowered to a minimum of 0.2 mm for compressive loading, which based on a gauge length of 90 mm corresponds to a strain of 0.0089 and -0.0022 respectively. The unsymmetric load cycle caused the mean stress of each cycle to decrease, a phenomenon known as relaxation of the mean stress. Relaxation of the mean stress occurs regardless of whether the material cyclically softens or hardens. However, the rate at which the peak stress decreases at the upper strain limit, under tension, is more rapid than the reduction at the lower strain limit, under compression, which is an indicator of cyclic softening as the stress range decreases for a constant strain range. Figure 4.8 (b) compares the mean stress for the five recorded load cycles and shows a constant rate of decrease for the first four cycles. Typically the softening reaches saturation after a number of cycles and the mean stress would become constant across the remaining cycles. Unfortunately the material softened considerably and buckled at the end of the fifth cycle.

Inferring the kinematic material properties of the cladding using a numerical model proved challenging. For cold worked steel the nonlinear combined isotropic and kinematic hardening model is preferred. However, inferring the material parameters requires dealing with a minimum of five unknown variables. Ideally multiple backstress components are required to model the relaxation of mean stress in metals, which increases the number of unknown variables further. Furthermore, the cladding sample of each unsymmetric tension-compression test would buckle after a maximum of five cycles which does not provide a sufficient load history to observe the decay in kinematic/isotropic hardening.

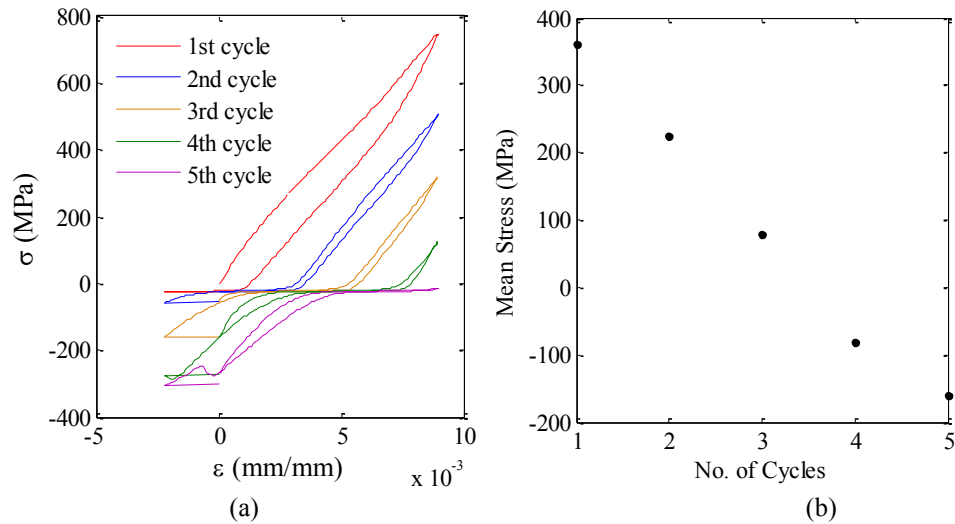


Figure 4.8: (a) stress-strain cycle for unsymmetric cycling and (b) mean stress of each load cycle.

Attention was once again focused on performing fully reversed, tension-compression tests having failed to infer the dynamic material properties from unsymmetric tension-compression tests. To avoid premature buckling of the sample, a significantly smaller strain range was trialed. Although the material parameters should be determined using an equivalent strain range to that expected in the IFC test, a lower strain range could potentially provide initial values for the material parameters or could be extrapolated to a large strain range based on multiple symmetric tension-compression tests. Figures 4.9 (a) and (b) describe the stress-strain curve for a strain range of 0.001 and 0.0005 respectively. Although the samples avoided buckling for a considerable number of cycles, there appears to be significant relaxation of the mean stress. For symmetric, strain-controlled, tension-compression tests there should be no observable change in the mean stress, only the stress amplitude should vary. Relaxation of the mean stress suggests that the strain cycles within the cladding sample are unsymmetric. As the applied strain was determined based on the movement of the cross head on the United STM then the cross head position does not correlate to the strain within the sample. This discrepancy was first observed in monotonic tensile tests of the sample and was attributed to the combined effects of slip at the grips, elasticity of the grips and localized necking of the sample. These factors were thought to be controlled as additional measures were taken to tighten the grip on the sample by applying greater force and increasing the friction between grip and cladding coupon, and the applied strain rates were smaller than that required to cause localized necking.

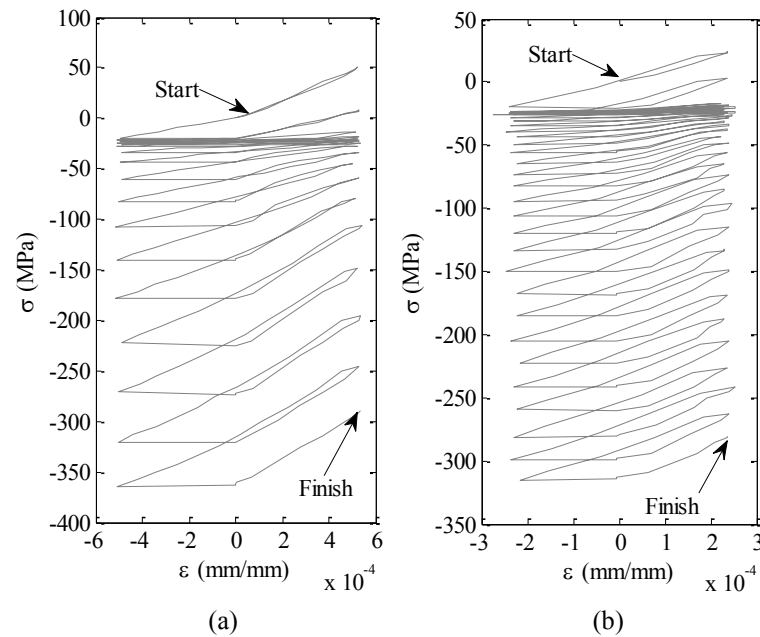


Figure 4.9: Symmetric tension-compression tests for a strain range of (a) 0.001 and (b) 0.0005

Strain controlled tension-compression tests were challenging using the United STM as the strain within the sample did not correlate with the cross head position. Stress controlled tension-compression tests were then attempted to study the dynamic material properties of the cladding. Typically stress controlled tension-compression tests are not favourable given plastic straining is required to study the dynamic properties of materials (Liu, 2005). To avoid premature buckling, a small stress range that was well below the buckling capacity of the sample without the anti-buckling fixture was applied. The strain within the sample was measured using a single strain gauge at the midsection of the sample. The strain gauge was positioned well away from where localized necking was observed in earlier tensile tests. Figures 4.10 and 4.11 detail the resulting change in mean strain and strain amplitude observed when a symmetric stress cycle with a range of 80 MPa was applied to the sample with the strain results in Figure 4.10 taken directly from a strain gauge while the results in Figure 4.11 are based on the cross head position. Unfortunately the servo control of the United STM machine resulted in an unsymmetric stress cycle being applied with a peak stress of 60 MPa, rather than the requested 40 MPa, and a minimum stress of -40 MPa. The same issue with the servo control also caused the peak stress to vary between each cycle as highlighted by the resulting strain range shown in Figure 4.10. Reducing the speed of the cross head motion would have minimized this variation in peak stress. However, the cross head speed was set to 5 mm/min and any further reductions in speed would have resulted in an excessive durations of each test. The strain gauge data presented in Figure 4.10 suggests an increase in the mean strain with each cycle which is indicative of ratcheting. In contrast, the strain data calculated from the cross head position, as shown in Figure 4.11, implies a decrease in both strain amplitude and mean strain. The reduction in both amplitude and strain is most likely due accumulated slip during the compressive cycle as the jaws of the grip are styled to provide a stronger grip in tension.

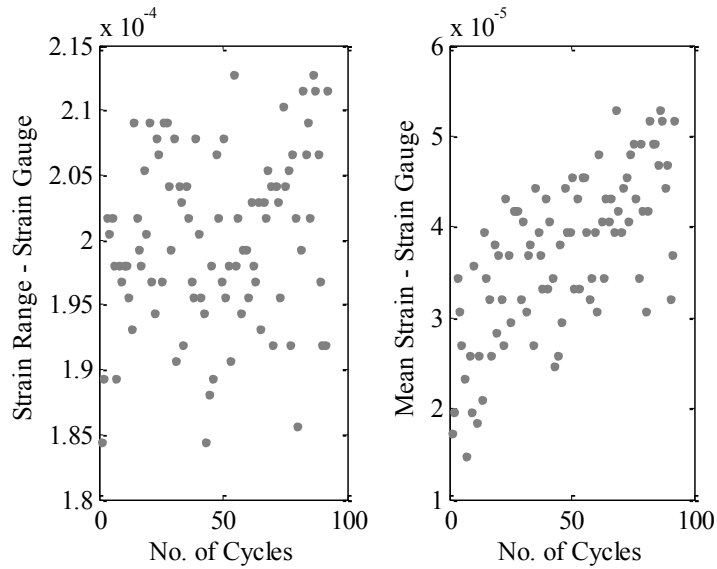


Figure 4.10: Strain range and mean strain based on attached strain gauge, resulting from stress controlled cycling.

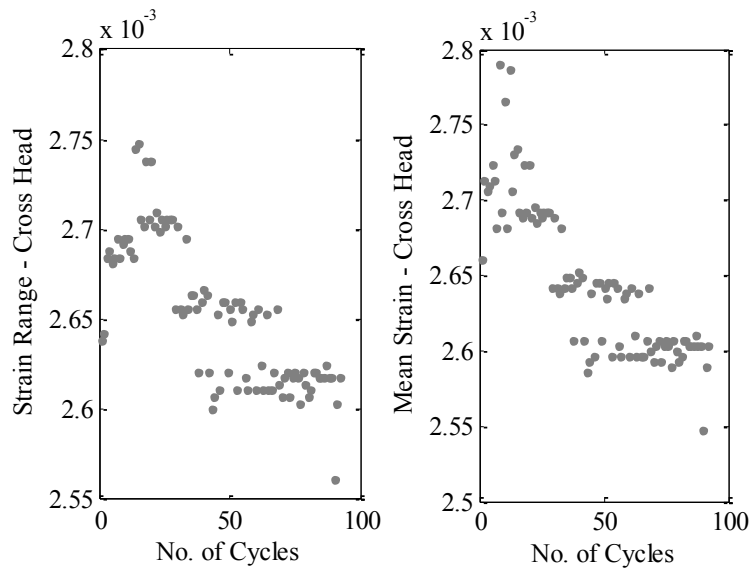


Figure 4.11: Strain range and mean strain based on cross head position, resulting from stress controlled cycling

4.1.5 Summary and Recommendations

Performing tension-compression tests on corrugated cladding did not yield sufficient information regarding the dynamic material properties of the cladding. The antibuckling fixtures developed for the cladding coupon tests did successfully increase the buckling capacity of the cladding although the significant softening of the cladding resulted in premature buckling even at low strain ranges. Strain-controlled cycling also proved to be difficult as the controls of the United STM were based on the cross head position which does not correlate with the strain within the cladding due to localized necking of the cladding and slip at the grips. Stress controlled cycling also proved difficult as the servo control of the United STM resulted in unsymmetric and widely varying stress amplitudes. Consequently a cyclic bend test is recommended for finding the dynamic material properties of the cladding, similar to the bend test outlined by Zao and Lee (2004).

Zao and Lee (2004) performed a three-point bending test of sheet metal and used a correlating numerical model to inversely estimate the material properties of the sheet. Two bearings, comprising two pairs of rollers support the ends of the sheet while a central punch also comprising two rollers applies the forward and reverse bending force, as pictured in Figure 4.12. The rollers of the punch are slightly grooved to accommodate a strain gauge on the top and bottom surface of the sheet sample. These strain gauges were included to compensate for some slight membrane deformation. The rotation of the specimen and the required punch force was measured during each test in addition to the surface strains of the sheet. From these variables the relevant bending moment can be determined and compared to that calculated using finite element analysis. A modified Levenberg-Marquardt method was then used in the optimization procedure which iteratively compared the experimental and numerical bending moments and adjusted the material parameters based on minimizing an error function. During a bending test of the cladding coupon, the surface strains along the surface of the coupon at fracture should also be monitored to investigate the effect of flexural strain on fracture of the steel.

Performing such a bend test would require fabrication of a custom apparatus capable of accommodating the small cladding samples which are limited in size by the corrugations of the cladding sheet. Another testing machine must also be sourced as the United STM is unsuitable for bend tests given smaller load ranges and more accurate servo control are required.

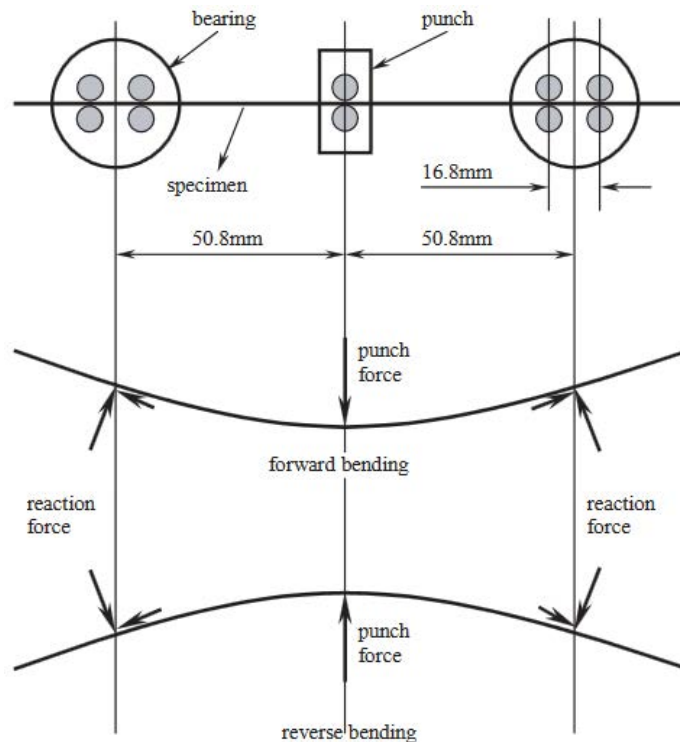


Figure 4.12: Three point bend test used to inversely estimate material properties of sheet metal (credited to: Zao and Lee, (2004))

4.2 CHARACTERISING FATIGUE MACROCRACK INITIATION

4.2.1 Background

Cladding fatigue design is entirely reliant on standardized prototype testing of specific prototype assemblies. It is the responsibility of manufacturers to test each cladding type, fastener arrangement, and support system together, with any variation in a single component requiring additional testing. Any arrangement must be tested multiple times or risk applying a large factor of safety to compensate for the known variation in structural characteristics (Standards Australia, 2002). Should fatigue design of cladding shift to a semi-empirical approach, like that used to design a number of structural components such as pressure vessels, the type of prototype test could be simplified and the number of prototype tests required would be reduced. One means of moving the problem to a semi-empirical approach would be to adopt a fracture mechanics based design similar to the defect tolerant approach. The defect tolerant approach is based around the stress intensity factor which depends only on local boundary geometry, magnitude of resultant force and material type. In the same way that the defect tolerant approach reduces the number of dependent variables, fracture mechanics could lead to a reduction in the dependent variables affecting cladding fatigue design; for example, the problem could be limited to the load spectra, cladding profile and material properties. However, a fracture mechanics based experimental investigation of roof cladding is unrealistic given the complexity of studying the stress state within cladding. Advances in finite element analysis and the eXtended finite element method could provide an alternate means of studying cladding fatigue numerically; effectively enabling a fracture mechanics based analysis. A numerical model that can simulate crack initiation and propagation would be an invaluable tool for characterizing the dependence of cladding fatigue on each dependent variable.

In order to create a numerical model capable of simulating fatigue of roof cladding, the model must implement a crack initiation criterion. A crack initiation criterion is an extension of the material definition; a logic statement that identifies when cohesive nodes can separate to simulate a crack based on either the stress or strain tensor in the region. To investigate crack initiation in detail in order to develop a relevant criterion, constant amplitude loading was applied to cladding samples in an IFC test. This investigation focused only on the ‘star’ type crack formation which occurs when corrugated cladding is loaded at lower load ranges and is therefore subject to more measurable magnitudes of strain. Consequently the resulting crack initiation criterion cannot be confidently applied to the ‘H’ type crack formation until further studies are completed. The ‘H’ type crack initiates away from the fastener hole after local plastic deformation where the cladding undergoes gross plastic deformation producing strain that is immeasurable. A numerical model is required to infer the strain values within this region as it undergoes excessively large plastic straining which is difficult to measure experimentally.

The scope of this investigation was also limited to crack initiation rather than crack growth. Ideally a numerical model that can simulate cladding fatigue would include both crack initiation and crack propagation, although the resources required to study crack propagation were not available for this investigation. This study gives not indication of the fatigue life of the cladding – in terms of the popular S-N curve – regardless of the fact that constant amplitude loading was applied. These S-N curves for roof cladding have been successfully developed in earlier investigations by Henderson (2010), Mahendran (1990b) and Xu (1995) and any crack

initiation criterion developed in this investigation should be independent of applied load (S) and number of applied cycles (N).

4.2.2 Experimental Set-up

Two digital microscopes were fitted to the fastener using a custom printed bracket as pictured in Figure 4.13(a) to monitor crack initiation in the cladding sheet. The digital microscopes were capable of 20× to 500× magnification and focused on the longitudinal and transverse hole edge. Figure 4.13 (b) is an example of the view from the digital microscope with a crack highlighted in red. Foil strain gauges were then attached to the underside of the cladding sheet, immediately adjacent to the fastener hole. Two stacked rectangular rosettes with a gauge length of 1 mm were placed in the transverse and longitudinal direction as shown in Figure 4.14. The longitudinal and transverse rosettes were typically 1.9 mm and 1.7 mm from the hole edge respectively. Strain gauges could not be applied at the same location on the opposing side of the cladding as the EPDM seal would contact the strain gauge and interfere with the measurement of the surface strains.

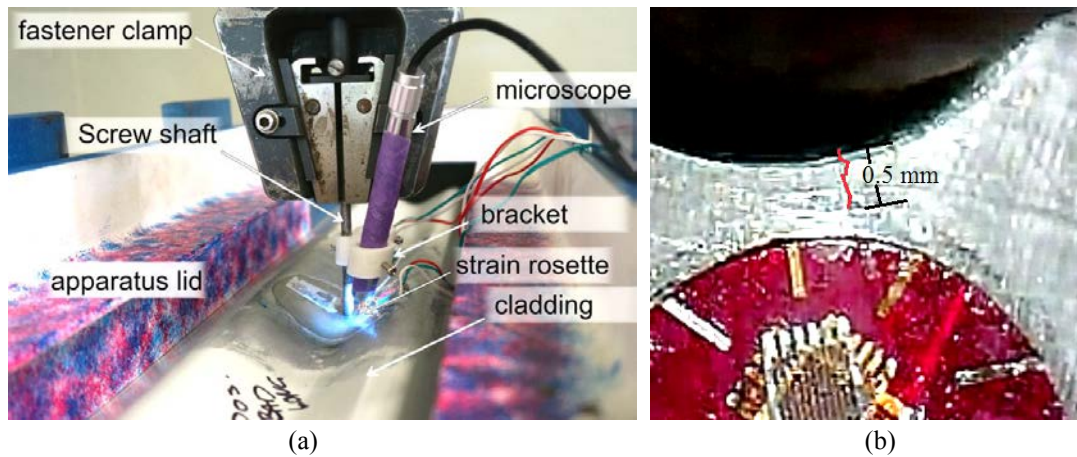


Figure 4.13: (a) IFC test for fatigue of cladding and (b) view of cladding from digital microscope

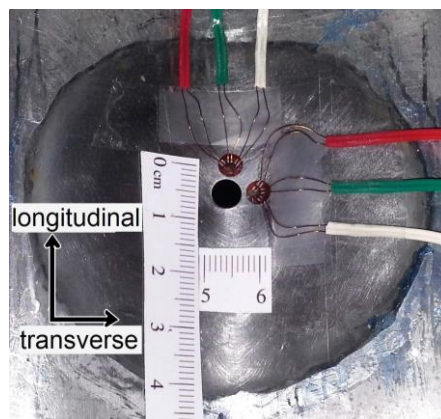


Figure 4.14: ariel view of strain gauges

4.2.3 Defining Crack Initiation

The fatigue life of a structure has two distinct periods, crack initiation period and crack growth period. Crack initiation is microscopic and begins with the development of cyclic slip bands on the free surface of a structure. Eventually a crack nucleates as the slip bands deepen along

the line of maximum shear stress. Once the slip bands bisect grain boundaries, microcrack growth occurs. Following microcrack growth, the second period of fatigue life commences, that is, crack growth. The transition point between crack initiation and crack growth is difficult to define but in qualitative terms it is considered to be the point at which crack growth no longer depends on the material surface conditions but rather the bulk material properties (Schijve, 2009). Typically the material surface conditions govern crack nucleation, except when a stress concentrator, such as the fastener hole in the cladding, is included. Stress concentration of that magnitude overcomes the smaller stress concentrations created by surface roughness ensuring that fatigue cracks initiate at a free edge of the notch where the maximum shear stress is located (Suresh, 1991).

Defining crack initiation greatly depends on the scale of observation. A practicing engineer will often define crack nucleation based on the resolution of the crack detection technique whilst a materials scientist focuses on the microscopic mechanism of crack nucleation. Consequently a practicing engineer will assess crack initiation using macroscopic stress concentrations whilst the material scientist would use the surface conditions such as microscopic flaws at grain boundaries (Suresh, 1991). As this crack initiation criteria is intended to be implemented into a numerical model, then a macroscopic scale will be used given the general element size at the region of interest would be in the order of magnitude of 10^{-1} mm. Modelling abstractions such as the submodeling technique would allow even finer discretization of the model but at significant computational cost. By considering crack initiation on a macroscopic scale the definition of crack initiation is no longer a process of nucleation, but appears more as the transition point between traditional definitions of crack initiation and crack growth. By redefining crack initiation as the transition point to crack growth, the crack initiation criterion becomes more dependent on the bulk material properties.

A critical crack length is often used to define crack initiation. This critical crack length is often arbitrary, varying between investigations and with the differing crack detection methods used. Henderson (2010) used a crack length of 1 mm to define crack initiation as a 1 mm crack length was detectable by the digital cameras used to monitor the region. Typically the critical crack length is selected based on the capability for a crack to be detected but careful consideration must be given to the size of the crack as small cracks behave differently to long cracks (Field et al, 1983). Smaller cracks, particularly located near a notch, are affected by the stress concentration at the notch whilst longer cracks are controlled by the bulk strain. Dowling (1979) suggests a limiting crack length of one tenth the notch radius to avoid short crack behaviour. As the fastener hole in roof cladding is 5.5 mm in diameter, a limiting critical crack length of 0.28 mm is recommended; meaning any critical crack length used in this investigation must be greater than 0.28 mm to avoid short crack behaviour. Ellyin (2012) also suggests that the transition point from crack initiation to crack propagation is when the crack growth becomes stable. As the selection of a critical crack length is somewhat arbitrary the initial stages of crack propagation, as captured by the digital microscopes, were analysed in a bid to qualitatively characterise crack initiation as recommended by Ellyin (2012).

The smallest detectable crack length varied between 0.2 mm and 0.4 mm depending on the lighting during a fatigue IFC test. The digital microscopes were equipped with variable LED light sources which were adjusted at the beginning of each test to optimize the view of the cracks. However, ambient lighting and the polished steel finish of the cladding did challenge crack detection regardless of the localised light source. Figure 4.15 describes crack growth with number of cycles for both the longitudinal and transverse directions. Cracks in the

longitudinal direction would open on the underside of the cladding sheet at the fastener hole edge and propagate outwards in the longitudinal direction. For the first 2 mm of crack growth, the longitudinal crack propagated in stages; initially the crack grew quickly followed by apparent crack retardation and finally crack growth became rapid and stable. For the transverse direction only the retardation stage and rapid and stable growth stage were observed. To highlight the various stages of growth, a stylized crack growth curve is shown in Figure 4.16.

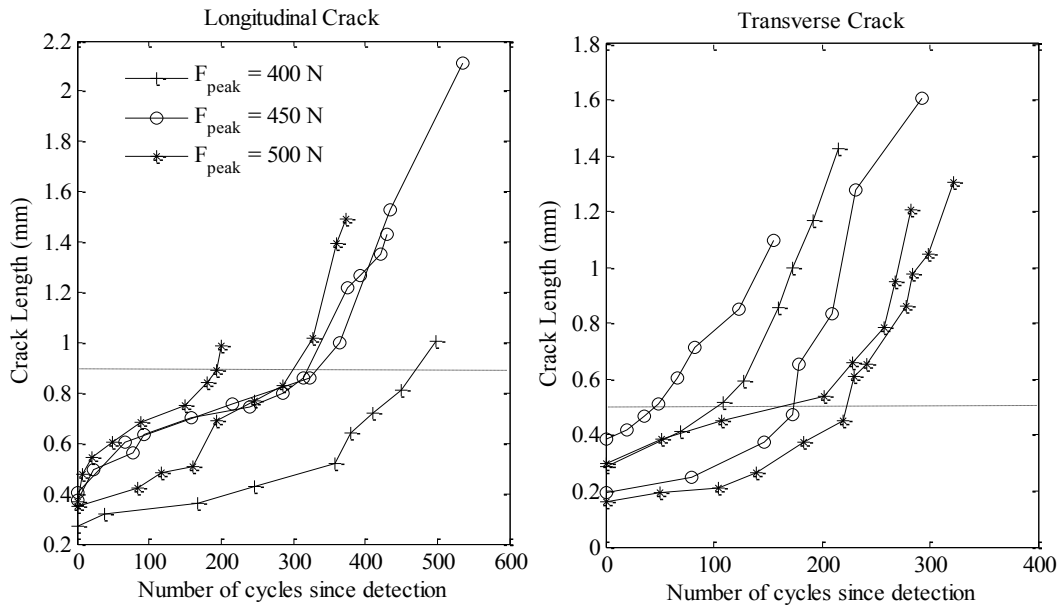


Figure 4.15: Crack growth curves for differing load amplitudes in the (a) transverse and (b) longitudinal direction

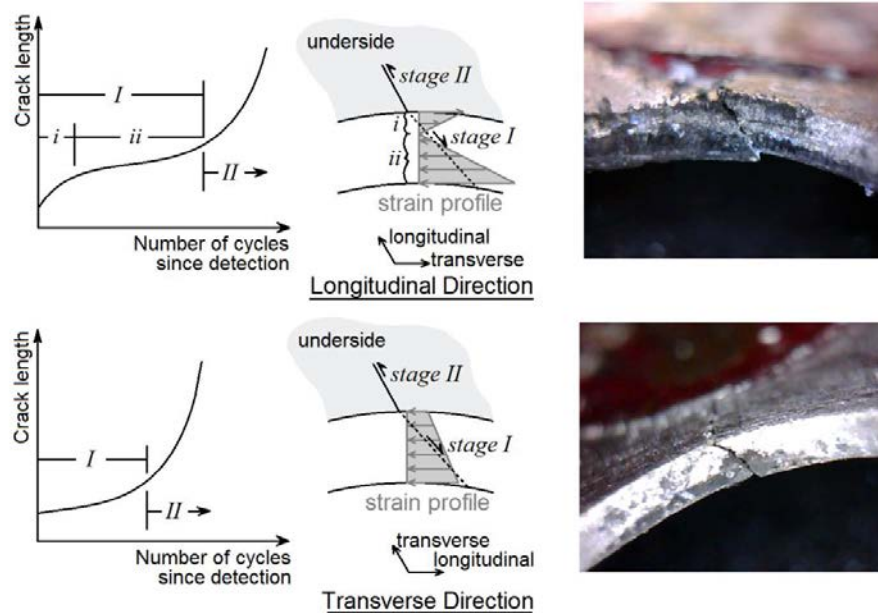


Figure 4.16: Stylized crack growth curves, strain profiles and fractographic analysis

A fractographical analysis was performed to identify the mechanism of crack propagation to identify the cause for each stage of growth. Each fatigue IFC test was manually terminated prior to the fastener pulling through the cladding sample as the focus of the test was on crack initiation only. Terminating the test early preserved the cracks as pull-through incurs

significant plastic deformation of the fracture plane. Using the same digital microscopes, the cracks in both the longitudinal and transverse directions were examined with samples pictured in Figure 4.16. Both the longitudinal and transverse cracks bisected the thickness of the cladding at a 45° angle. Considering that the inside edge of a hole is purely uniaxial due to hoop stress, then the 45° angle suggests crack initiation occurred along the plane of maximum shear which is consistent with ductile fracture. Some trials had the through thickness crack reverse direction part way through the thickness to travel along the opposing shear plane; an example is shown in Table A1– “Fractographical Analysis” of the Appendix A, specifically Trial 2 under a peak load of 500 N. Cracks first opened on a free surface; at the hole edge on the underside of the cladding sheet prior to propagating through the thickness of the cladding and then opening along the longitudinal/transverse direction.

The strain profile at the longitudinal and transverse edges of the hole was examined using both the strain data from similar static IFC tests in combination with a validated static numerical model. Figure 4.16 details the strain profiles at the hole edge for a monotonic fastener reaction ranging between 400 N and 500 N (the range in cyclic loads applied). The strain profile at the longitudinal hole edge transitions from tension at the underside of the cladding to compression at the topside of the cladding. For the transverse direction, the strain profile was entirely in compression. However, these strain profiles are only relevant for the first few cycles as the steel of the cladding softens significantly under repeated loading. The cyclic softening of the cladding causes ratcheting when unsymmetric load cycles are applied, such as cycling from a minimum fastener reaction of zero to a maximum fastener reaction of 400 N. At the transverse hole edge in particular, the initially compressive strains on the underside of the cladding sheet changed to tensile strain in less than 200 cycles. Figure 4.17 describes the opening strain at the transverse hole edge for the first 200 cycles of the load trace and highlights the change in state of the strain. The non-zero strain at the commencement of loading was due to the compressive force applied to the cladding when it was installed in the IFC test apparatus. Regardless of the softening effect, the strain profiles under monotonic loads are an indicator of the likely variation in strain profile between the two directions at crack initiation. Once the dynamic material properties of the steel are established, a numerical model capable of simulating the dynamic response of the cladding can be developed and utilized to investigate the strain profile following a number of load cycles and consequent cyclic softening.

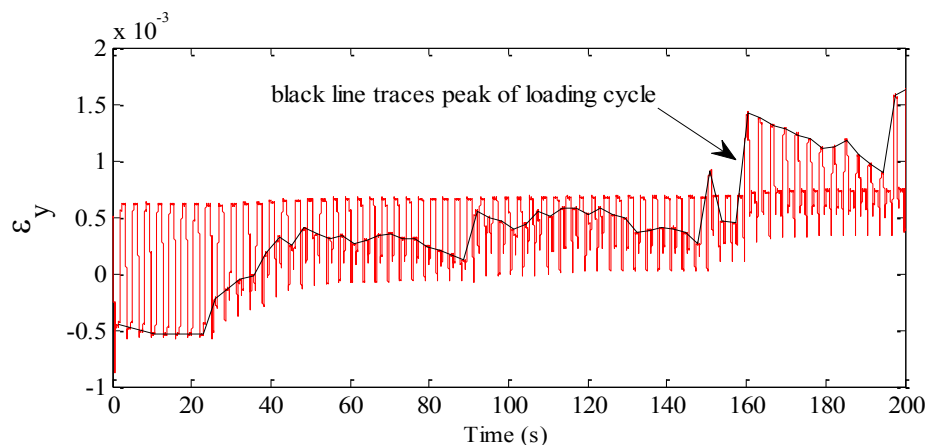


Figure 4.17: Changing state of strain at transverse hole edge under constant amplitude loading

Crack growth in the longitudinal direction can be discretised in two major stages. The first stage, labelled *I* in Figure 4.16, involves the crack propagating through the thickness of the

cladding sheet whilst the second stage, *II*, is the crack opening and propagating in the longitudinal direction. Within Stage *I* there are two subclasses of crack growth, *i* and *ii*. Stage *i* has rapid growth given the tensile flexural strain opens the crack whilst Stage *ii* has a significantly slower growth rate as the compressive flexural strains are attempting to close the crack. The validated numerical model also suggests the neutral axis at the longitudinal hole edge is closer to the underside of the cladding which may justify Stage *i* being smaller than Stage *ii*.

Crack growth in the transverse direction is similar to that of the longitudinal where cracks must initiate and propagate through the thickness, Stage *I*, then proceeds to propagate into the plane of the cladding in Stage *II*. Stage *I* shows only a slow growth rate, consistent with compressive flexural strains attempting to close the crack as it propagates through the thickness. As both the transverse and longitudinal directions rely on the same mechanism of crack initiation and propagation, that is, propagating through the thickness and overcoming compressive flexural strains prior to freely propagating into the plane of the cladding, both directions possess crack growth curves with comparable characteristics.

Based on the crack growth curves for each direction a critical crack length of 0.5 mm and 0.9 mm for the transverse and longitudinal cracks respectively was selected. For both the transverse and longitudinal cracks, regardless of applied load, Stage *II* crack growth occurred at these critical lengths. The commencement of Stage *II* was favoured as the definition of crack initiation not just for the stable nature of the crack growth but also because the crack had propagated through the entire cladding thickness and was beginning to propagate into the cladding plane. A crack initiation criterion that is only applicable to through thickness cracks would allow for shell elements to discretise a numerical model. Shell elements provide an efficient means of modelling thin structures such as the cladding and are planar elements. If a critical crack length coinciding with Stage *I* was used, then solid continuum elements would be required to appropriately model cracking through the thickness of the cladding. However, to obtain accurate representations of flexure in the model, at least four rows of continuum elements are required through the thickness. As the thickness is only 0.42 mm then a minimum element dimension of 0.1 mm would be required to maintain appropriate aspect ratios, resulting in a very dense mesh and consequently a computationally inefficient model.

4.2.4 Creating a Strain Based Crack Initiation Criterion

Theory

Most crack initiation criteria for fatigue are similarly based on the applied load, particularly the strain or stress amplitude, in a similar manner to that of fatigue life models. A crack initiation criterion based on the bulk material properties rather than load would allow for considerably greater flexibility when numerically modelling the fatigue response of roof cladding. Differing loading scenarios such as load spectra observed at differing locations across the building envelope during a cyclone could be applied to such a numerical model without the need to modify the constitutive description. Such a crack initiation criterion is most similar to the fracture models used for monotonic loading. These fracture models are based on a macro scale to ensure the variables affecting fracture are current components of the stress or strain and their histories. These variables are readily available as the output of a numerical model and as a result most commercial finite element analysis programs have accommodated a number of differing fracture criteria. The criteria available in the FEA program ABAQUS are based on either strain or stress with a maximum principal strain/stress criterion, maximum

nominal strain/stress criterion, quadratic traction-interaction criterion and quadratic separation-interaction criterion (Dassault Systemes, 2013). The simplest criterion is the maximum principal strain criterion which states that the cohesion between two enriched nodes will degrade, allowing the nodes to move apart, should the maximum principal strain at the centre of the element exceed a limiting value.

Electing to base a crack initiation criterion on either stress or strain can affect the precision of the criterion. Most low cycle fatigue models, using the total fatigue life approach, are based on strain parameters rather than stress as crack propagation in particular depends on the constraining deformation of the bulk material and therefore the bulk strain (Brown and Miller, 1973). When fatigue tests are performed by controlling the load, rather than the stress or strain, the strain throughout the life of the material then varies. Yao and Munse (1961) performed constant load test on steel and found that strain is a more sensitive measurement of the specimen life than the nominal stress for lives less than 1000 cycles. Low cycle fatigue is also characterised by plastic deformation making interpolating stress from measured strain data difficult. In this investigation, stress cannot be derived from the loads as the curved profile of the cladding, and the resulting deformation of the cladding, complicates the stress distribution. This complexity is what motivated previous researchers to use FEA for simulating the static response of cladding. As strain is the simplest and most accurate variable to measure it was consequently the focus of the experimental investigation.

Monotonic fracture models were used as inspiration for an appropriate fatigue crack initiation criterion. The cladding, even at the smaller loads required to produce a 'star' type crack, undergoes significant deformation, which suggests that a ductile fracture model is more appropriate. Ductile fracture is heavily dependent on the stress state of the material during multiaxial loading and as a result most ductile fracture models include a stress triaxiality parameter. A common ductile fracture model for thin sheets in particular, is the Fracture Forming Limit Diagram (FFLD) typically used to describe both the necking and fracture limits for sheet metal being drawn by a die. A FFLD depends on the principal strains present at the surface of a material and the stress state ranging from uniaxial tension to equibiaxial tension. Other ductile fracture models such as Johnston-Cook fracture model or the Xu-Wierzbicki (Wierzbicki et al, 2005) model requires knowledge of both the strain and stress at the point of fracture. These models are typically usable for whole structures that do not include large stress concentrators like the fastener hole. Typically stress intensity factors are used to characterise crack initiation at a notch or hole in a manner akin to the defect tolerant approach. However, stress intensity factors are dependent on the load and geometry of a crack where an ideal crack initiation criterion would be entirely dependent on the material only.

Mahaarachchi and Mahendran (2009) investigated the splitting characteristics of trapezoidal cladding under monotonic loads and created a FFLD to characterise crack initiation. Mahaarachchi and Mahendran (2009) installed a fastener in trapezoidal cladding and proceeded to apply a monotonic load to the cladding until the cladding split and the fastener pulled through the cladding sheet. Splitting of the cladding occurred either side of the fastener hole in the transverse direction. A typical FFLD did not yield a definitive criterion for crack initiation of the trapezoidal cladding as the samples that did split were not distinguished from those that did not. Mahaarachchi and Mahendran (2009) postulated that the FFLD was incapable of accommodating combined membrane and flexural action. A modified version of the FFLD was then created which depended on the flexural component of the principal strain

and the maximum tensile strain. The final resulting strain criterion states that the flexural component of the principal strain must exceed 60% of the maximum tensile strain (based on the modified FFLD) while the maximum tensile strain must also be equal to the fracture strain from coupon tests of the cladding material.

The stress and strain within the cladding, particularly at the hole edge, can only be inferred from a numerical model capable of simulating the response of the cladding subject to cyclic loads. As such a model is still in development, the crack initiation criterion developed in this investigation is based on the strain data collected from constant amplitude loading in an IFC test. The resulting crack initiation criterion is more a description of the state of strain at the crack tip rather than the particular strain that drives crack initiation. Consequently the crack initiation criterion developed in this investigation is more suitable as a limiting criterion in a numerical analysis, where an analysis is terminated should the criterion be reached, than a criterion required by numerical models to simulate crack initiation and propagation. Regardless, a crack initiation criterion based on the experimental strain data provides a foundation for what is likely an iterative process required to obtain a criterion entirely dependent on the material.

Results and Discussion

Developing a strain based crack initiation criterion involved constant amplitude loading of cladding samples in order to form the ‘star’ type crack formation. Throughout the loading, the fastener hole edge in both the transverse and longitudinal directions were monitored using digital microscopes and strain gauges. The point of crack initiation was determined by inspection of the video where a crack was considered to have initiated when it reached a critical length of 0.5 mm and 0.9 mm in the transverse and longitudinal directions respectively. Four cladding samples were tested for three different load amplitudes based on the recommendation by Osgood (1970) who suggested that a minimum of four trials are required in any fatigue study. Although the sample size of the fatigue tests was increased to provide greater reliability of the resulting test results, no formal reliability study of the fatigue test results was performed. As a ‘star’ type crack forms when the cladding is loaded below LPD, and LPD occurs at an applied load of approximately 600 N, the three target peak loads were 400 N, 450 N and 500 N with a minimum load of 0 N for all trialled amplitudes. The range of peak loads trialled in this investigation was limited to between 400 N and 500 N. At peak loads less than 400 N the effects of fretting fatigue at the hole edge became more prominent and began to obscure the mechanism of crack initiation driven by loading through the fastener; and at peak loads above 500 N the ‘T’ type crack would form which was beyond the scope of this investigation. The servo control within the United STM also made any load interval less than 50 N difficult to distinguish during cyclic loading.

The cladding studied in this investigation was restricted to corrugated cladding produced by BlueScope Steel. Ideally, any crack initiation criteria used in a numerical model should be entirely dependent on the bulk material rather than the applied load, sample geometry or boundary conditions. However, testing cladding with differing geometries – even from the same manufacturer – could result in differing bulk material properties. To extend the investigation beyond the corrugated cladding manufactured by BlueScope Steel would require rigorous tensile testing of the cladding to establish how the bulk material properties may vary in order to extrapolate how the crack initiation criteria may too vary. The tensile properties of the cladding used in this investigation had previously been studied by Henderson (2010) and

were well documented. The scope of this investigation was restricted to only a single cladding geometry, thickness and manufacturer in order to first provide a proof of concept; successful implementation of this crack initiation criterion in a corresponding numerical model was required prior to evolving the criterion to be applicable with all cladding types.

For each trial, the strain from each rosette was transformed to determine the strain in the transverse and longitudinal directions, and the resulting principal strains. However, during a number of the trials a single gauge of the rosette placed in the longitudinal direction would fail prior to a crack initiating. The foil gauges have an upper limit of $\pm 5\%$ although failure of the gauges typically occurred at 2%. The failure rate of the strain gauges was 64%. Although a single gauge failed in the rosette, the two remaining gauges were still operational. The strain data for the failed gauge was then inferred from the strain data of the two remaining gauges. First, the measured strain at the peak of each load cycles was collected from the failed gauge prior to failure and fitted with a power function. The unknown data between gauge failure and crack initiation was then assumed to follow the power function. The assumed strain data and the strain data from the two operational gauges were then transformed to calculate the principal angle. Mahendran (1989) and Xu (1995) both documented that the principal angle at the hole edge was approximately 90° , with the principal axes coinciding with the transverse and longitudinal axes. A numerical model of the IFC test subject to monotonic loads of a similar magnitude also showed that the principal angle at the hole edge is 90° . The principal angles calculated from the inferred data at the peak of each cycle is also approximately 90° , suggesting that the method used to infer the missing strain data is valid. In all cases of premature gauge failure, the power function provided an effective approximate of the resulting strain. Figure 4.18 describes two examples of the inferred strain data and the resulting principal angle.

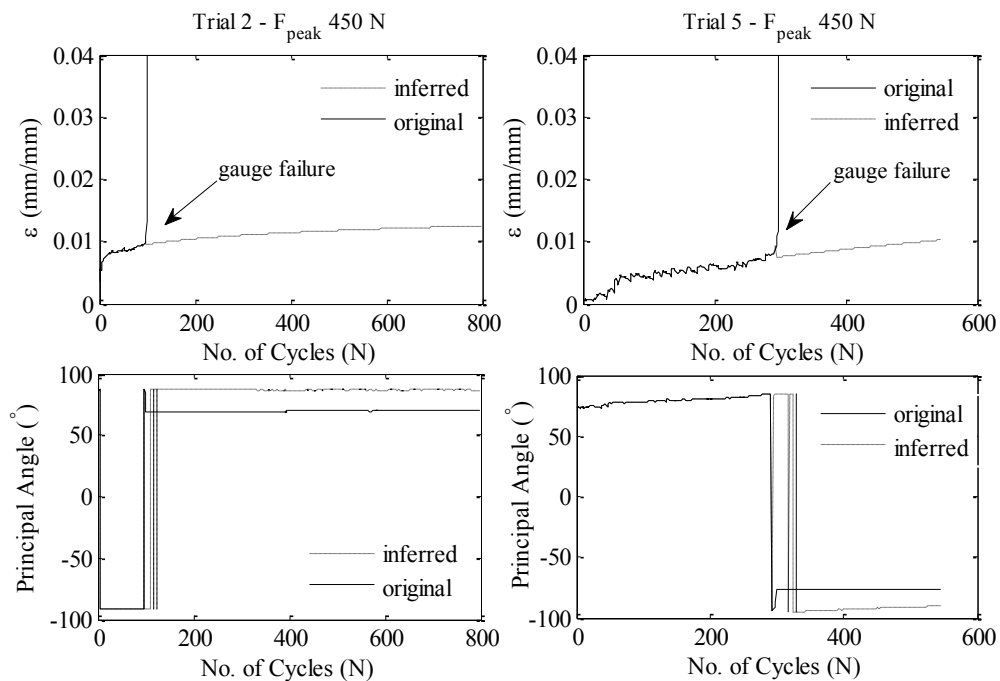


Figure 4.18: Original and inferred strain data for two differing trials

At the peak of every cycle, for all three loading amplitudes, the principal axes aligned with the longitudinal and transverse axes. The maximum principal strain in the longitudinal direction was directed along the transverse direction and therefore normal to the longitudinal crack

whilst the maximum principal strain in the transverse direction was directed along the longitudinal direction and normal to the transverse crack. Clearly the maximum principal strain drives crack propagation into the plane of the cladding suggesting that crack initiation is predominantly a Mode 1 mechanism. Figure 4.19 describes the three modes of cracks opening used in conventional fracture mechanics.

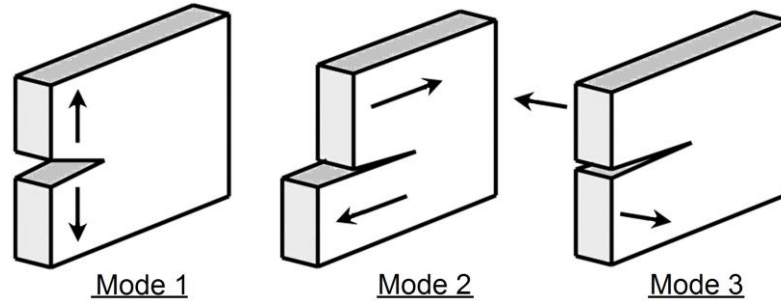


Figure 4.19: Crack opening modes

Given that crack opening is clearly driven by the maximum principal strain, the crack initiation criterion was then based in terms of principal strain. Analysis of the strain data at crack initiation shows a clear pattern emerging when the relationship between principal strains was considered in a similar manner to a FFLD. Figure 4.20 (a) describes the relationship between the principal strains as distinguishable by the applied peak loads. As shown in Figure 4.20 (a) two distinct crack initiation criteria are required for the longitudinal and transverse directions. Crack initiation in each direction is unique given that the cladding is anisotropic.

Typically a FFLD is affected by the strain hardening of a material, and when subjected to repeat loading the cladding is prone to softening. At three different peak loads, and consequently three different stress amplitudes, the degree of cyclic softening would vary although the strain data for all three peak loads align well, suggesting that the variation in cyclic softening has little effect on the crack initiation criterion. The four data points for crack initiation in the transverse direction when loaded to a peak fastener reaction of 500 N do not align well with the remaining data points. At a peak load of 500 N, a 'T' type crack would form with the crack at the transverse hole edge initiating approximately 5 mm away from the transverse strain gauge rather than immediately in front of the gauge.

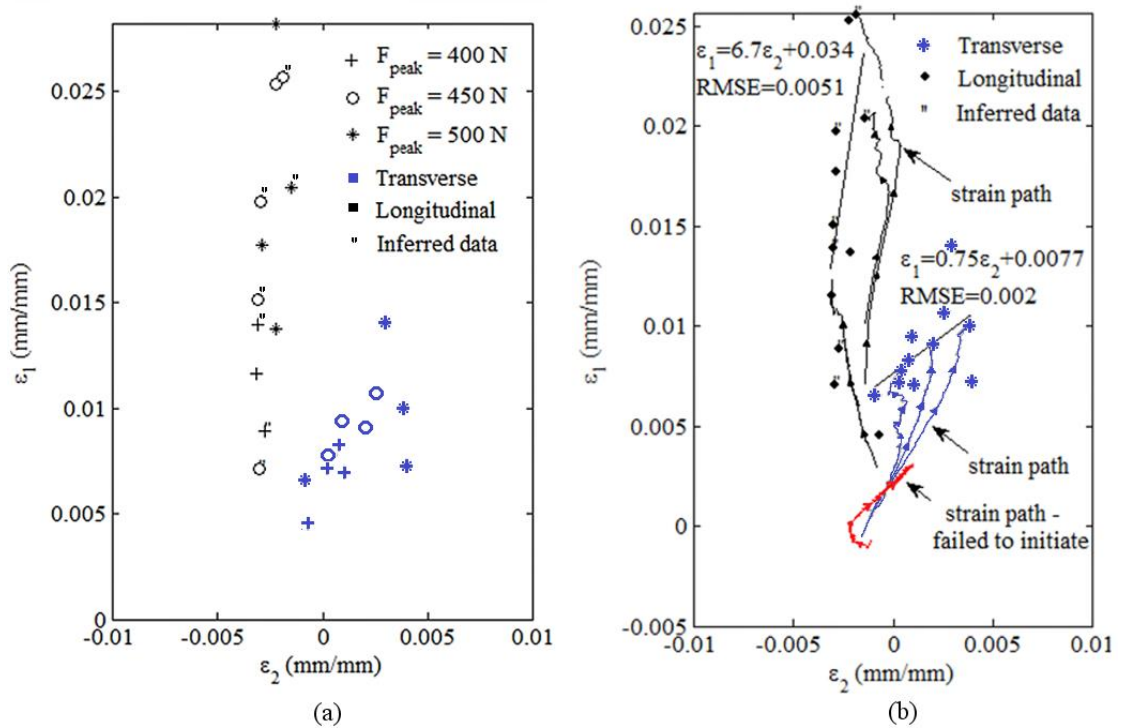


Figure 4.20: (a) Principal strains at crack initiation as distinguished by peak load and (b) Crack initiation criteria for corrugated cladding

A linear function was fitted to the longitudinal strain data and transverse strain data respectively as shown in Figure 4.20 (b). A linear function fitted to the longitudinal strain data resulted in a root mean square error (RMSE) of 0.005 whilst a linear function fitted to the transverse direction resulted in a RMSE of 0.002. The linear functions described by Equations 1 and 2 represent the crack initiation criteria for each direction.

$$\text{Longitudinal crack initiation criterion:} \quad \varepsilon_1 = 6.7\varepsilon_2 + 0.034 \quad (1)$$

$$\text{Transverse crack initiation criterion:} \quad \varepsilon_1 = 0.75\varepsilon_2 + 0.0077 \quad (2)$$

Also included in Figure 4.20 (b) are the respective strain paths at the peak of each cycle for both the longitudinal and transverse direction, the three strain paths for each direction are a sample of the strain paths observed for each trialled load amplitude. The strain paths for both the transverse and longitudinal directions do not intersect the fitted linear functions until crack initiation, further validating the chosen crack initiation criteria. During a single anomalous trial with a peak applied load of 400 N, a crack in the transverse direction failed to initiate. Cracks were present in the longitudinal directions on either side of the hole, and in the transverse direction at the opposing side to the transverse strain gauge. The strain path as recorded by that transverse strain gauge is included in Figure 4.20 (b) and shows the strain path running parallel to the linear function fitted to the transverse strain data. The crack initiation criterion for the transverse direction is therefore justified as a strain path that fails to intersect the criterion corresponds to a crack failing to initiate. The circumstances that lead to such an anomalous strain path are unknown and attempts to recreate this result failed.

A second anomalous trial also produced an unusual strain path. During a trial subject to constant amplitude loading at a peak force of 400 N, the transverse leg of the crack did not initiate until the sample had been subject to over 6000 cycles, compared to the 1600 cycles

required in other trials at the same amplitude. On closer examination of the strain data, the transverse edge of the hole appeared to remain in compression for the majority of the load history rather than transitioning to tensile strain after as few as 200 cycles. The region surrounding the transverse edge of the hole remained in tension until the longitudinal crack had propagate to a sufficient length to redistribute the stress at the transverse edge of the fastener hole, transforming the compressive strains to tensile trains. Once the region had transitioned to tension, a crack initiated. The resulting strain path is therefore different to other documented trials but still adheres to the developed crack initiation criterion, suggesting that to some extent the criterion is independent of load history. Figure 4.21 shows the anomalous strain path for the trial in question including how the strain state was initially in compression. The strain path is somewhat similar in appearance to that of the strain path that failed to initiate a crack. The key difference between the two trials appears to be the presence of a transverse crack at the opposing transverse hole edge. For the trial that failed to initiate there was a distinct crack at the opposing edge whilst for the anomalous trial only the longitudinal cracks initiated and propagated until the strain state reverted to tension at the transverse hole edge.

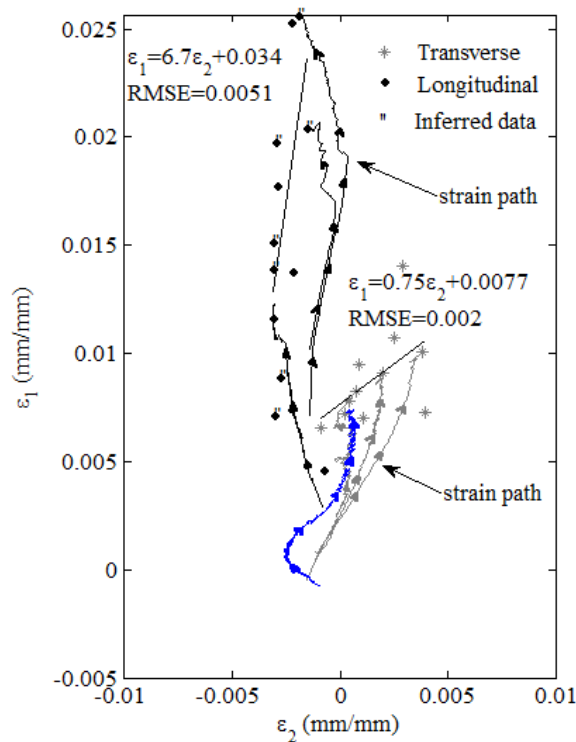


Figure 4.21: Anomalous strain path

4.2.5 Limitations

Ideally, a crack initiation criterion for cladding fatigue should be entirely dependent on the bulk material rather than the applied load, sample geometry or boundary conditions. This investigation focused on the fatigue performance of corrugated cladding subject to low load ranges in an IFC test and provides the foundation for a material specific crack initiation criterion. All corrugated cladding samples that were trialled in this investigation were taken from a single coil provided by a single manufacturer. It was this stringent control of variables that yielded somewhat consistent results for a fatigue study. Subsequently future investigations should focus on identifying the effects of each variable using a similar procedure to that implemented in this investigation in order to reduce the dependence of the crack initiation

criterion to solely that of the bulk material. In particular, future investigations will need to address the following limitations to the crack initiation criterion:

- Although an FFLD accounts for differing biaxiality of the strain field, the crack initiation criterion gives no indication of the dependence of crack initiation on flexural strain. This investigation suggests that the propagation of the crack through the thickness of the cladding may be dependent on flexural strain. Mahaarachchi and Mahendran (2009) also suggested that the splitting of trapezoidal cladding under monotonic loads was dependent on flexural strain. Unfortunately the strain directly beneath the EPDM seal on the topside of the cladding cannot be measured experimentally and any direct investigation into the nature of the flexural strain must be done numerically. As the changed boundary conditions of the IFC test, in comparison to an airbox test, directly affected the flexural strain within the cladding, further investigations into the effects of flexural strain are required prior to applying the crack initiation criterion to other corrugated cladding assemblies. The fastener used during the trials also controls the stress state in regions of crack initiation and should be varied to further establish the effects of flexural strain on crack initiation.
- All samples tested were taken from a single coil, consequently the crack initiation criterion does not account for the variation in material properties that occurs from coil to coil. The longitudinal and transverse directions have differing material properties which resulted in two differing crack initiation criterion. The longitudinal and transverse directions also have differing grain structures due to the rolling process and crack initiation is highly dependent on the grain structure of a metal. A working numerical model that simulates crack initiation based on a crack initiation criterion could easily be employed to study how varying each parameter of the crack initiation criterion impacts the fatigue life of the cladding.
- The crack initiation criterion is relevant only to the corrugated cladding profile produced by one manufacturer. Ideally the crack initiation criterion should be entirely independent of sample geometry, depending only on the bulk material properties of the G550 steel. Further investigations would introduce samples of corrugated cladding from a range of manufacturers in addition to samples of trapezoidal cladding. The various residual stresses produced by the respective rolling processes would likely cause some variation in the initiation criterion for each profile.
- The crack initiation criterion is relevant to the ‘star’ type crack formation. A second common crack formation is the ‘H’ type crack which forms when the cladding is loaded repeatedly through the local plastic collapse stage. However, the strain at the crease point where the crack initiates is too large to measure experimentally. A numerical model capable of simulating crack initiation of a ‘star’ type crack could be extrapolated to investigate crack initiation of ‘H’ type cracks. Ideally the crack initiation criterion developed for a ‘star’ type crack should be able to characterise crack initiation for an ‘H’ type crack.
- Finally and most importantly, future investigations should focus on the strain at the hole edge where the stress state is likely to be uniaxial. Measuring the strain at the hole edge is challenging experimentally. Finding the strain at the hole edge will require a combined numerical and experimental approach and should yield a criterion

independent of the minor principal strain and more akin to the monotonic crack initiation provided in the library of commercial finite element analysis programs.

4.2.6 Summary

The following observations were made when investigating the mechanism underlying fatigue crack initiation of ‘star’ type crack formations in corrugated cladding:

- Cracks nucleate on the plane of maximum shear through the cladding thickness. Once the thickness of the cladding has been entirely bisected, the crack then opens into the plane of the cladding, normal to the maximum principal strain.
- For ‘star’ type crack formations, where the cladding is cycled below local plastic collapse, a critical crack length of 0.9 mm in the longitudinal leg and 0.5 mm in the transverse leg of the crack was taken to be the transition point between crack initiation and propagation. For all trialled load amplitudes - below that of local plastic collapse - these critical crack lengths correspond to a crack that has completely bisected through the cladding thickness and is on the cusp of propagating into the plane of the cladding.
- The longitudinal and transverse directions clearly presented with a linear relationship between the principal strains at crack initiation. This strain based crack initiation criteria is independent of applied load and potentially independent of span. The following crack initiation criterion was established:

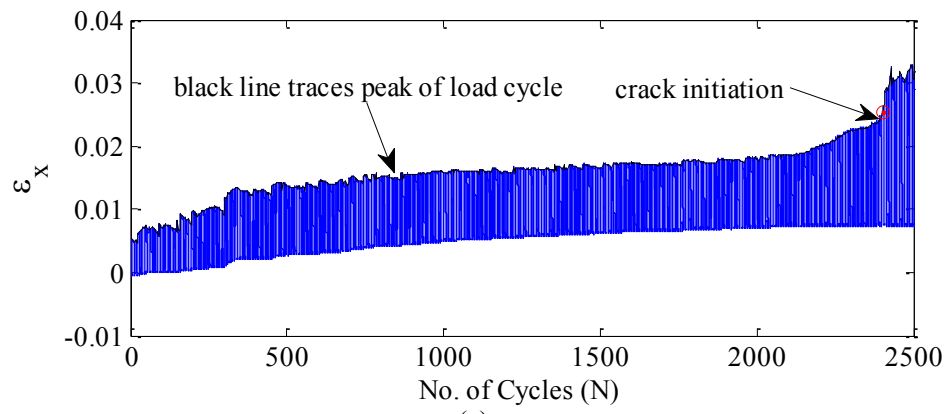
$$\text{Longitudinal crack initiation criterion:} \quad \varepsilon_1 = 6.7\varepsilon_2 + 0.034$$

$$\text{Transverse crack initiation criterion:} \quad \varepsilon_1 = 0.75\varepsilon_2 + 0.0077$$

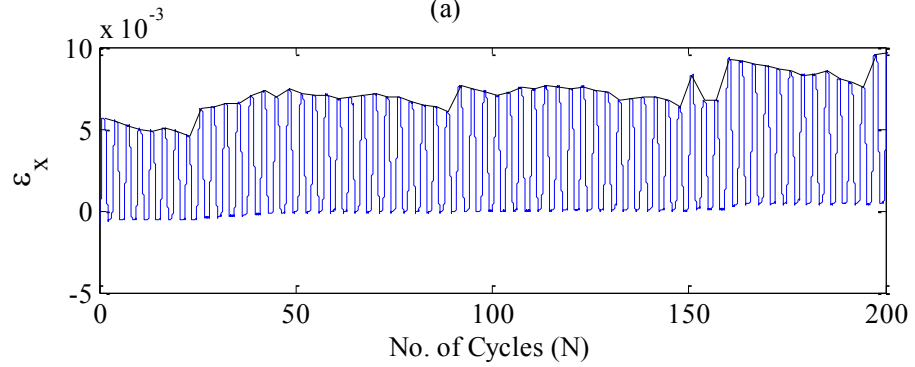
- Included in the experiments was a single trial in which no crack initiated. The strain path relating to this trial failed to meet the crack initiation criterion for that direction, further validating the crack initiation criterion.

4.3 GENERAL OBSERVATIONS

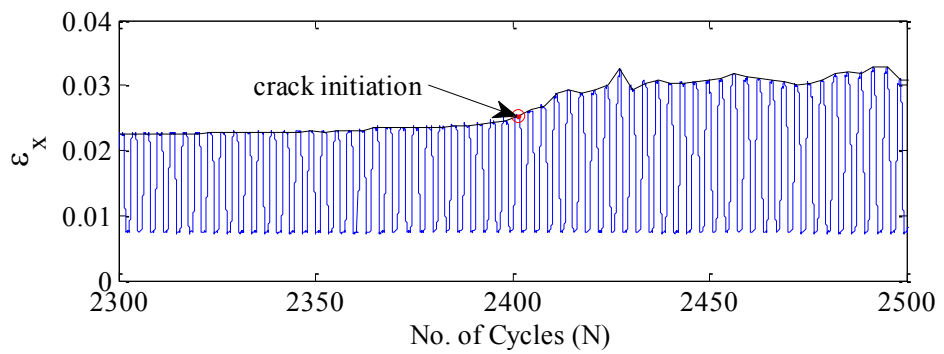
In the pursuit of creating a crack initiation criterion the local response of the cladding subject to constant amplitude loading was also studied. Figure 4.22 (a) is an example of the transverse strain history at the longitudinal hole edge. Figure 4.22 (b) and (c) present the first and last 200 cycles respectively. The point of crack initiation is indicated in Figure 4.22 (c) and corresponds to when a crack with a length of 0.9 mm was observed by the digital microscope. Figure 4.23 is an example of the longitudinal strain history at the transverse hole edge and similarly describes the first and last 200 cycles in Figure 4.23 (b) and (c) respectively. The point of crack initiation indicated in Figure 4.23 (c) was identified by monitoring the feed of the corresponding digital microscope until a crack with a length of 0.5 mm was detected. These strain histories were used to create the crack initiation criterion detailed in Section 4.2.2 – “Creating a strain based crack initiation criterion” but they could also be used to indirectly investigate the effects of cyclic softening, ratchetting and whether the loading is proportional or nonproportional. The strain at the beginning of the first cycle for both the transverse and longitudinal hole edges are non-zero as installing the cladding within the apparatus and clamping the cladding edges introduced strain within the cladding.



(a)



(b)



(c)

Figure 4.22: Transverse strain history at longitudinal hole edge for (a) entire history, (b) first 200 cycles and (c) last 200 cycles

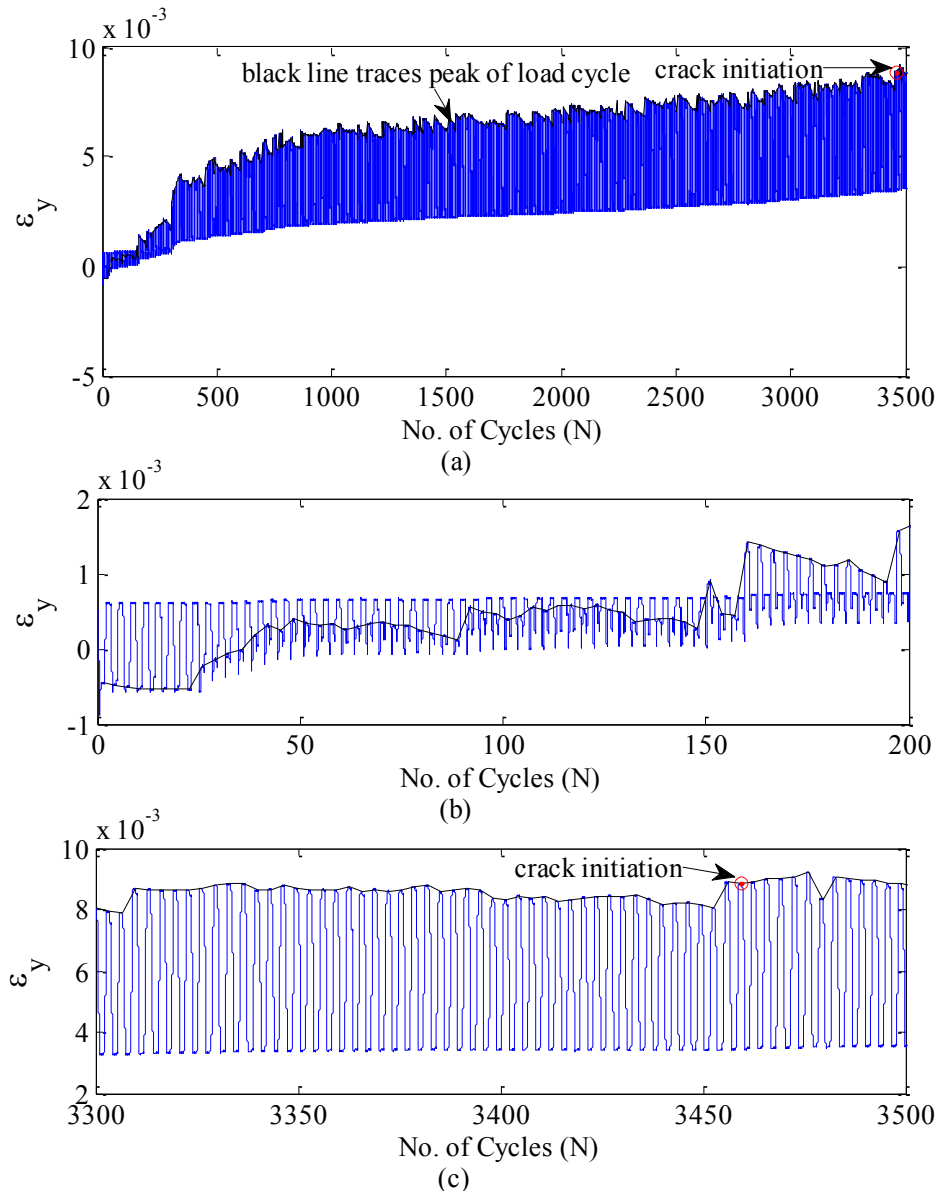


Figure 4.23: Longitudinal strain history at transverse hole edge for (a) entire history, (b) first 200 cycles and (c) last 200 cycles

As discussed earlier in Section 4.1 – “Cyclic material properties”, the cladding does in fact soften under repeated loading. This softening of the cladding can attribute to the exaggerated ratcheting of the cladding material under unsymmetric loading, such as the tension only constant amplitude cycles that were applied in the IFC tests. Ratcheting is the accumulation of strain with each cycle typically due to unsymmetric stress controlled cycling. As the cladding is force controlled, the loading is neither stress nor strain controlled suggesting that both mean stress relaxation and ratcheting are likely to occur. However, the stress is immeasurable so there is no way to study the relaxation of the mean stress in each cycle. Materials that cyclically soften will accumulate ratchet strain indefinitely whilst for materials that cyclically harden the ratchet strain per cycle reduces to zero and the strain cycle stabilizes (Halford, 2006). The ratcheting of the cladding material is what caused the compressive surface strains shown in Figure 4.17 and Figure 4.23 (b) to transition to tensile strain.

Figure 4.24 details an example of how the mean principal strain changes with each cycle at both the transverse and longitudinal edge. The mean strain with each cycle for all trials appeared to follow a power function with only the anomalous trials mentioned earlier in Section 4.2.2 – “Creating a strain based crack initiation criterion” producing a different result. Ellyin (2012) documented a similar trend in mean stress with number of cycles for A-516 Gr. 70 carbon steel, which is prone to cyclic softening, subject to stress controlled cycling.

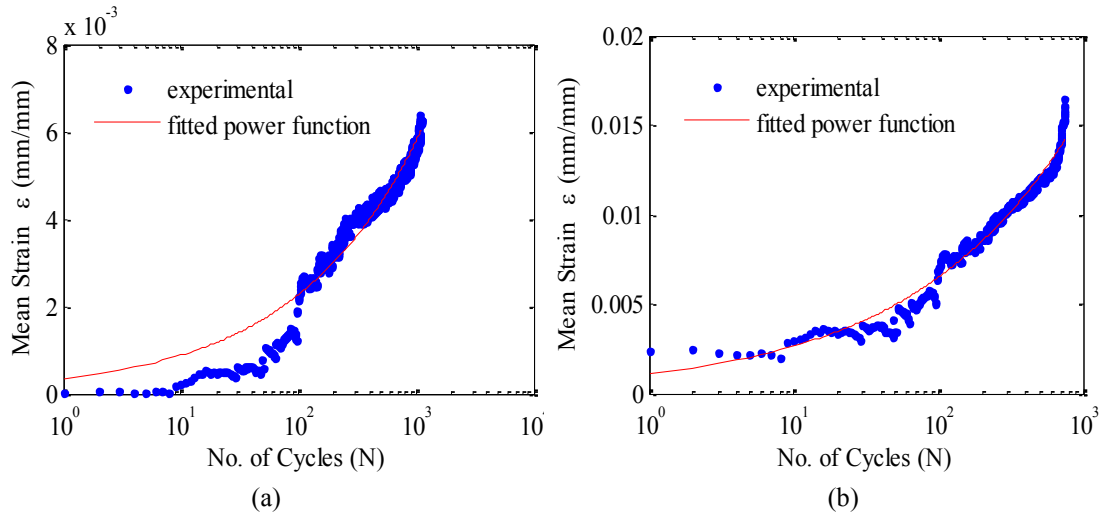


Figure 4.24: Changing mean principal strain with number of cycles at (a) the transverse and (b) longitudinal hole edge

Figure 4.25 presents examples of how the principal strain amplitude varies with increasing number of cycles. For increasing number of cycles the strain amplitude also increased which is indicative of cyclic softening; for the same force amplitude, greater straining is achieved. At the transverse hole edge there is initially a significant rate of increase of the strain amplitude which then reduces, suggesting the material has somewhat stabilized after approximately 400 cycles. At the longitudinal hole edge a similar phenomenon was observed but with a final rapid increase in strain amplitude occurring prior to crack initiation. This rapid increase is likely due to the material yielding, rather than softening.

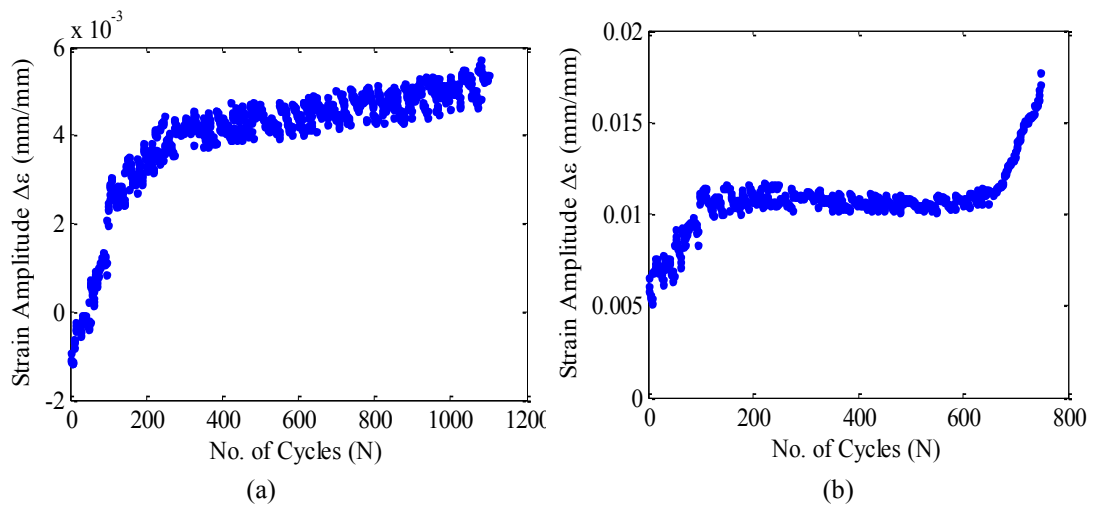


Figure 4.25: Changing principal strain with number of cycles at (a) the transverse and (b) longitudinal hole edge

The nature of the applied cyclic loading can also affect how a material hardens or softens, particularly when a structure is subject to nonproportional loading. Nonproportional loading is any type of loading in which the principal strain axes rotate in time. The effects of nonproportional loading are particularly significant when the principal strain axes rotate by 90°. Figure 4.26 (a) and (b) presents the major principal strain with respect to the in-plane shear stress throughout loading at the longitudinal and transverse hole edge respectively. Figure 4.26 effectively describes the strain history on a Mohr's Circle, where a linear line represents proportional loading. At the longitudinal hole edge the loading appears to be proportional whilst loading at the transverse hole edge appears to be non-proportional. This same trend was observed for all loading amplitudes excluding a peak load of 500 N where the longitudinal hole edge began to demonstrate some non-proportional loading as shown in Figure 4.27.

However, the stress state at a hole edge is typically uniaxial with the measured strain suggesting otherwise, since the strain rosettes were placed a small distance from the hole edge. The uniaxial stress state at the hole edge ensures that the loading is always proportional. Typically non-proportional loading will produce multiple cracks of varying orientation as the maximum shear plane is continually rotating, while proportional loading produces a single definable crack. A fractographic analysis of the fastener hole edge did not reveal any additional cracks at differing orientations which suggests the loading is proportional at both the transverse and longitudinal edge of the fastener hole.

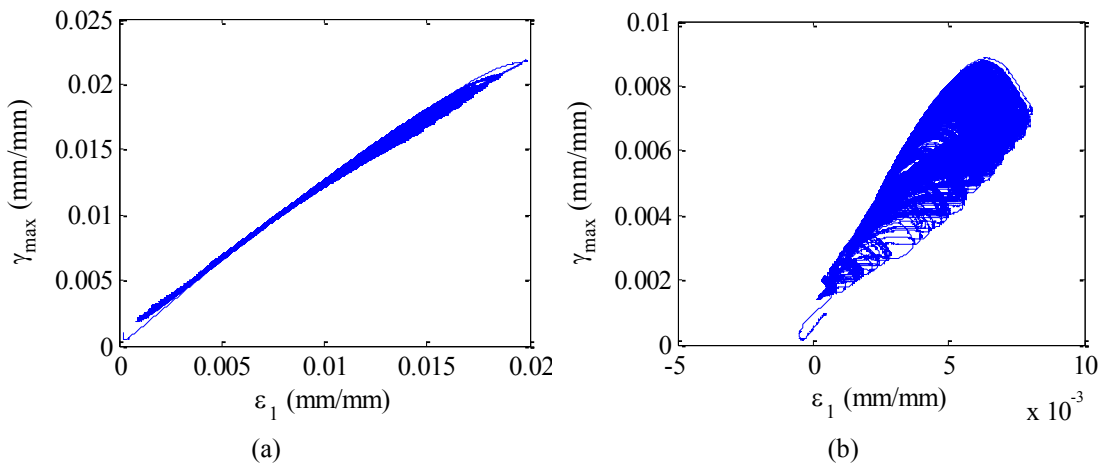


Figure 4.26: Principal strain with in-plane shear at (a) longitudinal and (b) transverse hole edge

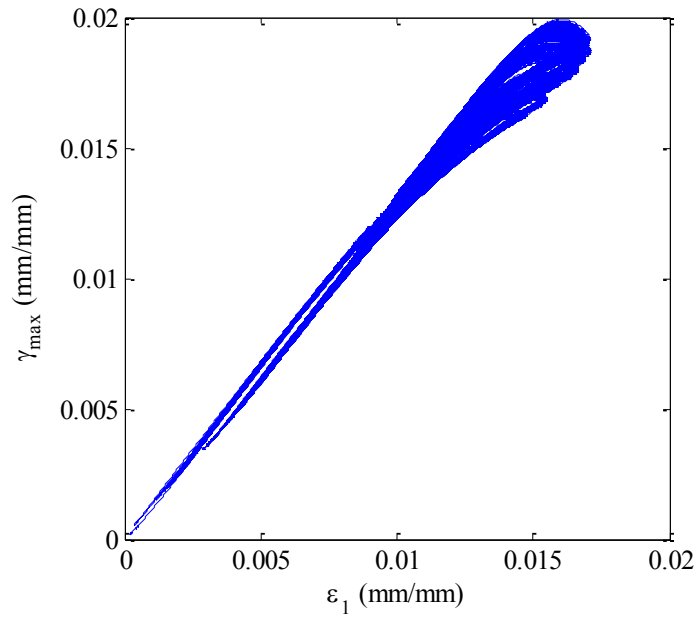


Figure 4.27: Principal strain with in-plane shear at longitudinal hole edge under a peak load of 500 N

5. FINITE ELEMENT SIMULATIONS

An objective of this thesis was to create a numerical model that could simulate the fatigue response of roof cladding. The crack initiation criteria developed for such a fatigue model were obtained using the IFC test. To ensure that the crack initiation criteria are actionable, the first edition of the cladding fatigue model must recreate the fatigue response of the cladding within the IFC test itself. This fatigue model can then be extrapolated to model the full scale fatigue response of the cladding. The simplest means of developing a fatigue model may be to first develop a model that can successfully simulate the static response of the cladding. By focusing on the static response of the cladding, the constitutive description, loading and boundary conditions can be confirmed without the fatigue effects obscuring the results. Therefore the first stage of developing a fatigue model of the cladding is the development of a model that can simulate the static response of the cladding within an IFC test.

5.1 CONSTITUTIVE DESCRIPTION

During the roll forming process the cladding material becomes anisotropic with the longitudinal (rolling) direction becoming less stiff than the transverse direction. The specific yield strength and Young's moduli of the cladding in each direction were determined through analysis of tensile test data. The coupons used in the tensile tests were cut from a cladding sheet that was specially rolled flat and was specific to the coil from which the cladding samples used in this investigation originated. Henderson (2010) cut the coupons from the flat sheets in both the transverse and longitudinal (rolling) directions and performed uniaxial tensile tests. Only a little strain hardening was observed in the resulting tensile test data for both directions, so all definitions of the cladding were taken to be elastic-perfectly plastic. Table 5.1 details the average material properties of the cladding for each direction including the number of coupons that were tested. Table 5.1 also describes the strength of the cladding in terms of true stress and strain as the numerical model requires that the yield stress and strain be input in these terms rather than the engineering stress and strain. Equations 5.1 and 5.2 were used to convert the engineering stress (σ_{eng}) and strain (ϵ_{eng}) to the true stress (σ_{true}) and strain (ϵ_{true}) which is applicable for small strains only.

$$\epsilon_{true} = \ln(1 + \epsilon_{eng}) \quad (5.1)$$

$$\sigma_{true} = \frac{\sigma_{eng}}{(1 + \epsilon_{eng})} \quad (5.2)$$

Table 5.1: Cladding material properties (credited to: Henderson, 2010)

	Number of Samples Tested	Average Young's Modulus (GPa)	Average Yield Strain (%)	Average Yield Stress (MPa)	True Yield Strain (%)	True Yield Stress (MPa)
Longitudinal	14	210	0.38	796	0.38	800
Transverse	9	221	0.40	877	0.40	880

For the elastic definition of the cladding, the Young's moduli for each direction were specified with the through thickness Young's modulus assumed to be the same as the transverse

direction. A Poisson's ratio of 0.3 was also assumed for all directions which were considered suitable given that the cladding is made from high strength steel. The shear modulus (G) for each direction was also required and was calculated based on the Young's modulus of the steel (E) and the assumed Poisson's ratio (ν), using Equation 5.3.

$$G_i = \frac{E_i}{2(1 + \nu_i)} \quad (5.3)$$

To describe the cladding behaviour within the plastic range, the constitutive description requires a yield criterion, a flow rule and a hardening rule. Firstly, the yield criterion is necessary to describe the limit of the elastic response, thereby identifying the range of the plastic response (Mendelson, 1968). The Hill's yield criterion was utilised in the constitutive model to define the anisotropic plasticity of the material rather than the von Mises yield criterion which is commonly used to describe isotropic plasticity. The Hill's yield criterion is an extension of the von Mises yield criterion and accounts for the differing strengths in the principal directions. As a result, the Hill's criterion is often referred to as the anisotropic von Mises yield criterion (Crisfield, 1997).

Following yielding, the flow rule is required to describe the plastic behaviour of the material, particularly to capture the nonlinearity of the stress-strain relationship and the dependence of the material behaviour on the loading history. As the associated flow rule is directly related to the yield criterion and is most commonly implemented to describe metal plasticity, it was employed within the constitutive description (Mendelson, 1968).

Finally, the constitutive description for a typical numerical model incorporates some form of hardening such as isotropic hardening or kinematic hardening. The cladding material in the IFC model was taken to be elastic-perfectly plastic and consequently is not subject to isotropic hardening under positive monotonic loads. Most metals subject to positive monotonic loads exhibit isotropic hardening where the yield stress increases due to plastic strain. However, for materials subject to repeated loading kinematic hardening, rather than isotropic hardening, is more suitable as it can account for the Bauschinger effect. Some more complex cyclic loading sequences cannot be effectively simulated using kinematic hardening alone. ABAQUS also offers a combined nonlinear kinematic and isotropic hardening model to account for more complex loading sequences such as a non-zero mean stress where the tension and compression components of the applied stress cycle are not equal. The cladding was subject to constant tensile cyclic loading which resulted in the longitudinal hole edge being subject to entirely tensile strains, even during unloading; suggesting that either ratcheting or relaxation of the mean stress is in effect. The nonlinear kinematic/isotropic hardening model provided in ABAQUS can accommodate ratcheting and relaxation of the mean stress (Dassault Systems, 2013).

Two limitations to the nonlinear kinematic/isotropic hardening model are firstly, that the isotropic hardening component is the same for all strains and secondly, that hardening due to nonproportional loading is not included. The component of isotropic hardening typically varies at differing strain ranges so to accommodate for this limitation the isotropic hardening qualities of the cladding must be found at a comparable strain range to that observed in IFC fatigue tests. The limitation of the model predicting the same hardening qualities for both proportional

and nonproportional loading cannot be controlled. The cladding is subjected to nonproportional loading in the vicinity of the crack tip, as shown in Section 4.3 – “General Observations”. Future development of the model will need to incorporate the hardening effects of nonproportional loading.

5.2 EXPLICIT ANALYSIS METHODS

The commercial finite element analysis package ABAQUS has two primary computational programs. The first is ABAQUS/Standard which is a general purpose finite element program and the second is ABAQUS/Explicit which is an explicit dynamic finite element program. ABAQUS/Standard can perform both static and dynamic analyses using an implicit solver. In ABAQUS/Standard, static and dynamic analyses use differing governing equations; the governing equations for a static analysis depend on the applied load whilst the governing equations for a dynamic analysis depend on time and, as a result, include inertial effects. As the name suggests, ABAQUS/Explicit solves only dynamic problems using an explicit method.

Both the implicit and explicit methods can be used to solve a dynamic analysis. As a dynamic analysis is time dependent both the implicit and explicit methods progressively move through the problem history solving for a set of variables at t_{n+1} based on the same variables at t_n . The implicit method solves a set of variables at t_{n+1} using algebraic equations that depend on both the variables at t_n and the still unknown variables t_{n+1} . To solve for the unknowns an additional numerical method, such as the Newton-Raphson method, is required. The size of the time increment (difference between t_{n+1} and t_n) is determined when solving the algebraic equations and can vary from one iteration to the next. A defining benefit of the implicit method is the accuracy of the solution as the governing equations are satisfied. Should the governing equations not be solvable due to some form of instability, the solution will diverge and the analysis will abort.

The explicit method is also a time marching method. The unknown variables at t_{n+1} depend only on the variables at t_n as an assumed time increment is used. The time increment chosen in an explicit method depends on the properties of the model and is typically one to two orders of magnitude smaller than the time increments determined in its implicit counterpart. However, no additional numerical methods are required to solve for the variables making each recursion of the explicit method inexpensive compared to that of the implicit method which can offset the time required to solve a greater number of recursions. The small time increments used in an explicit analysis make it particularly effective for impact load problems where the loading period is small and the problem is discontinuous (Dassault Systems, 2013; Wriggers, 2008). Explicit methods are powerful and not subject to convergence issues. As a result, any solution, although achieved, must be considered in relation to the problem directly to ensure that the results of the simulation are realistic.

Oftentimes a dynamic analysis is required to solve quasi-static problems particularly for problems involving localized buckling. In any problem where there is a reduction in displacement for an increase in applied load, like the case when a structure buckles, the force equilibrium equations used by a static analysis cannot account for the excess strain energy that is dissipated as a structure buckles. In reality this excess strain energy is dissipated in the form of kinetic energy, the effects of which are assumed to be negligible in a static analysis. A dynamic analysis includes inertial effects and can consequently represent the transfer of the

excess strain energy into kinetic energy. There are modified static analyses that use the Riks method to artificially simulate the dissipation of strain energy by modifying the applied load directly (Dassault Systems, 2013). This type of modified static analysis was used by researchers such as Xu (1993) and Mahaarachchi and Mahendran (2004) to successfully model the local plastic collapse of cladding subject to static loads. However, to use the Riks method the finite element analysis must be terminated when the solution becomes unstable and restarted with the Riks method now active to solve for the post buckling response of the structure. This method can be undesirable if repeated cycling through the local plastic collapse of the cladding is required, such as that which would be required should the model extend to fatigue studies.

There are many forms of nonlinearity in a finite element analysis that must be included to obtain a realistic result. These nonlinearities can be classified as geometric, material and contact or support nonlinearities. All types of nonlinearities, although originating from different circumstances, all ultimately lead to an effective nonlinear stiffness matrix. The stiffness matrix within FEA relates force to displacement and is featured in the fundamental FEA equilibrium equation:

$$[F] = [K][d] \quad (5.4)$$

Where $[F]$ is the known vector of nodal loads, $[K]$ is the known stiffness matrix and $[d]$ is the unknown vector of nodal displacements. In a linear finite element analysis the stiffness matrix is calculated once at the beginning of the analysis and remains constant throughout the analysis. For a nonlinear analysis the stiffness matrix is updated with each iteration.

Geometric nonlinearities typically occur when there are large displacements, strains and rotations. Within ABAQUS, geometric nonlinearities can be accommodated by specifying that a large-displacement formulation should be used. It is generally recommended that a nonlinear analysis be used when the deformations exceed $1/20^{\text{th}}$ of the largest dimension of the structure, for this analysis that limit is 35 mm which is greater than the maximum displacement of the fastener (Dassault Systemes, 2013). However, geometric nonlinearities can also occur in small deformation problems where membrane stiffness significantly affects the overall stiffness of a structure, such as that experienced by corrugated cladding as it deforms.

Nonlinear materials are any material that is not perfectly elastic throughout its loading history. The corrugated cladding in this model was indirectly specified as nonlinear when an elastic-perfectly plastic material definition was used. The model was further complicated by including the EPDM seal which was specified as a hyperelastic material. Although the washer does not undergo permanent deformation, the stress-strain relationship is slightly nonlinear at the expected load levels.

Contact nonlinearities and support nonlinearities are often characterised together. Should the supports or the contact conditions change during the analysis then a nonlinear analysis is required. Contact between deformable bodies in particular is nonlinear as the contact area increases with the applied load (Dassault Systemes, 2008). For the IFC model the EPDM seal deforms significantly over the curved crest of the cladding. The supports or boundary conditions of the model include clamps that use a friction condition which in the most basic form contains two stages of loading, therefore nonlinear loading. The first stage of loading has

the cladding sticking to the surface of the clamps and the second stage sees the cladding slipping between the clamps.

Each of the nonlinearities contained within the model increases the computational time required for each recursion of an analysis, particularly the implicit analysis that must solve these equations using numerical methods as the inverse of the stiffness matrix is required. The explicit analysis is less affected by the nonlinearities of the model as the inverse of the stiffness matrix is not required, with the expressions being evaluated directly. The severity of the nonlinearities, not just the number of nonlinearities, can also affect the analysis. Local instabilities in the structure which cause sudden discontinuities in the response, like those experienced during some types of buckling, can severely impact the effectiveness of the implicit solver. These types of local instabilities are commonly encountered in drawing or forming processes. Such discontinuities force the implicit method to reduce the time increment size in order to achieve convergence, with some solutions being unable to converge regardless of increment size. The same discontinuities do not affect an explicit analysis as the time increment is sufficiently small, making the explicit analysis ideal for impact load problems which are by their nature highly nonlinear and discontinuous (Dassault Systemes, 2013).

Extensive efforts were first made to create a working model of the IFC test using a nonlinear dynamic implicit analysis, particularly since the eXtended Finite Element Method can only be used in ABAQUS/Standard. However, an implicit analysis proved to be less appealing for this problem than the explicit analysis. The number of nonlinearities within the model made each recursion extremely costly. The concentrated load of the fastener compressing against the curved crest of the cladding also introduced local instabilities similar in nature to wrinkling of sheet metal in a forming analysis. These local instabilities required a small time increment to solve within an implicit analysis, with the time increment required only a single order of magnitude larger than that required in an explicit analysis. Although the implicit analysis continued to converge, the cost of the computation was too great. Compromising the accuracy of the model by simplifying the boundary conditions and removing all contact interactions, even relaxing the convergence criteria, did not adequately reduce the cost of an implicit analysis. Having exhausted every feasible option, all efforts were then directed at creating a working numerical model using a nonlinear dynamic explicit analysis.

When using a dynamic explicit analysis to solve a quasi-static problem a number of considerations must be made. Firstly, the small time increment size required to maintain a stable solution in an explicit analysis is incredibly small. Most quasi-static problems have a load history spanning minutes at the very least. Literally millions of time increments would be required to solve a quasi-static problem in its natural time period. Two possible methods can be used to reduce the number of increments required, the first is to increase the load rate thereby artificially reducing the time period of the problem, and the second is to artificially increase the material density which increases the size of the required time increment. Both methods of reducing the computation cost of the analysis increase the effects of inertia which ideally should be negligible for a quasi-static problem.

The more suitable method of reducing the computation cost for this analysis would be increasing the load rate of the problem as the steel of the cladding is not a rate sensitive material for the load rates being considered. The threshold of the load rate in which the inertial effects

become dominant can be approximated using the wave speed of the component. A rule of thumb is to ensure the load rate of the problem does not exceed 1% of the material wave speed (Dassault Systemes, 2013). The wave speed of a material is the speed in which sound waves pass through the material, for typical steels the wave speed is 5940 m/s and for EPDM is 1600 m/s (Lide, 2004). The lower wave speed of the EPDM seal limits the appropriate load rate for the IFC model to 16 m/s.

A second means of approximating a suitable load rate for a quasi-static problem is based on the natural frequency of the structure. The natural frequency of the structure, particularly the first structural mode, is the dominant response of a quasi-static problem and consequently the time period of the problem should not be less than the equivalent period of the first structural mode. The first structural mode of the IFC model was determined using the natural frequency extraction procedure in ABAQUS/Standard. The natural frequency extraction procedure was applied to a cladding model that contained only the cladding and the boundary clamps. The first structural mode of the IFC model with the clamped boundary conditions is 370 Hz which corresponds to a time period of 0.0027 seconds. The fastener in the IFC test displaces a total of 29 mm which over a period of 0.0027 seconds corresponds to a load rate of 11 m/s. A load rate of 11 m/s is less than the recommended 16 m/s and is taken as the upper limit of the acceptable load rate.

Following the initial approximation of an acceptable load rate required to maintain a quasi-static response, a more in-depth analysis is required to ensure that both the local and global response of the model is unaffected by adverse inertial effects. The adverse inertial effects include a steeper load-displacement curve as inertia resists the initial deformations or highly localized deformation surrounding the EPDM seal as it first makes contact with the cladding surface, commonly referred to as jetting. To confirm that the inertial effects are limited all deformed shapes must be inspected to ensure that no excessive deformation is occurring. The effects of varying load rate on the resulting strain and displacement within the model must be quantified and the energy balance throughout each simulation must also be inspected. Typically for a quasi-static analysis, the kinetic energy of the structure must be less than 5% of the total internal energy of the structure (Dassault Systemes, 2013).

A series of simulations were run that varied the load rate of the model to investigate the resulting change in the strain field. Strain, rather than displacement, was the primary focus as the effects of the load rate are typically more prominent in the strain results. To capture the effects of the load rate throughout the whole model, strain results were extracted along the transverse and longitudinal directions from the fastener hole edge to the boundaries. Figure 5.1 features a quarter view of the model and details the relevant locations at which the strain data was monitored. The load rate of the model was varied by changing the total time period of the analysis with the fastener then displaced linearly over that time period; the load rates that were trialed are detailed in Table 5.2 along with the resulting run time of each simulation. Revision X1 of the model (as defined in Appendix B) was used for the load rate trials relating to Table 5.2 and Figures 5.2. The run time for each simulation largely depends on the hardware of the computer that ran the simulation and has consequently been specified based on the shortest run time required for a simulation to complete i.e. simulation with a load rate of 5.8 m/s.

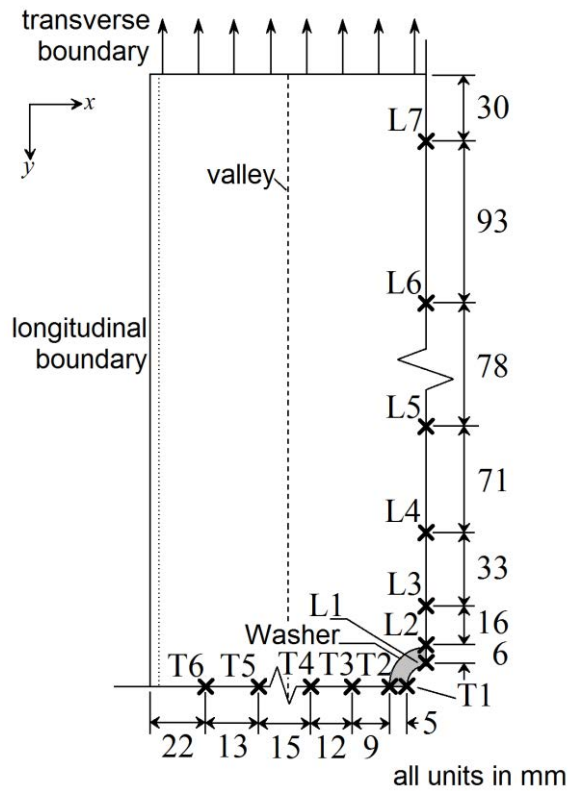


Figure 5.1: Strain data layout on cladding model for load rate trials

Table 5.2: Load rate simulations and required simulation run times

Load Rate (m/s)	Ratio of simulation run time with respect to load rate 5.8 m/s simulation	Comments	Ratio of kinetic energy to internal energy
58	×0.18	14% completed. Analysis terminated due to excessive wave speeds in EPDM.	26%
5.8	×1	100% complete	10%
0.58	×10.6	100% complete	0.03%
0.058	×25.4	100% complete	0%
0.0058	×393.9	38% complete. Analysis manually terminated due to excessive run time.	0%

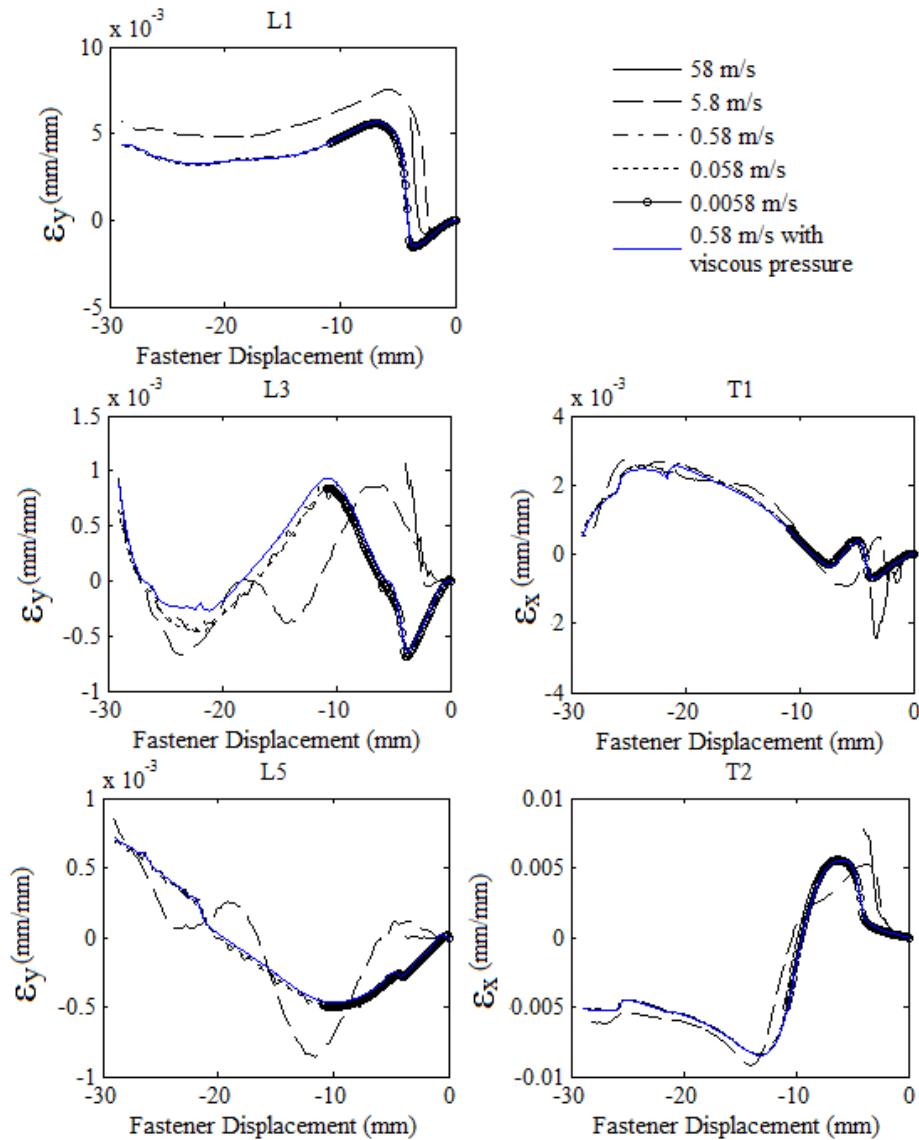


Figure 5.2: Effect of load rate on strain along the surface of the cladding

Figure 5.2 shows very little change in the resulting strain within the cladding for load rates 0.58 m/s, 0.058 m/s and 0.0058 m/s suggesting that a load rate of 0.58 m/s is optimum. Only selected locations are included in Figure 5.2 for brevity; specifically locations L1, L3, L5, T1 and T2 which showed greater sensitivity to the applied load rate. The only observable difference in the result is the slight oscillations in the strain data when the cladding was subjected to a load rate of 0.58 m/s. These oscillations can be easily damped using a mild viscous pressure across the cladding surface. A viscous pressure is a surface pressure that is applied proportionally to the deformation speed of an element making it an effective means of damping dynamic effects such as oscillations. Figure 5.2 also describes the resulting strain data when the model is subjected to a viscoelastic pressure of 2×10^{-7} MPa.s/mm which align well with the strain results from the slower load rates. The total kinetic energy rates produced by a load rate of 0.58 m/s is also optimum as it is as low as 0.03%, significantly less than the acceptable 5% for a quasi-static analysis.

Considerations must also be made to avoid an initial increase in the gradient of the load-deflection curve as inertia can artificially stiffen a structure. Figure 5.3 describes the load-

deflection curve for a simulation in which the screw was displaced linearly over a time period of 0.05 seconds and another that utilized the load amplitude smoothing function within ABAQUS/Explicit applied over the same time period. The smoothing function within ABAQUS/Explicit ensures that initially the EPDM seal does not contact the cladding at a load rate of 0.58 m/s, but rather the load rate gradually increases from 0 m/s. Figure 5.3(a) details the smooth and linear load amplitudes applied to the model. The results presented in Figure 5.3 were obtained using Revision X3 of the model, as detailed in Appendix B. Clearly a smooth displacement of the fastener is ideal as the cladding does experience some initial stiffening when the fastener is linearly displaced. However, the smooth step function in ABAQUS/Explicit increases the load rate of the fastener to a maximum of 1.1 m/s rather than the more ideal 0.58 m/s. The maximum load rate can be reduced if a time period of 0.09 seconds is used rather than 0.05 seconds, but this doubles the simulation run time. Even with a maximum load rate of 1.1 m/s, and a viscous pressure reduced by 53% to accommodate the increased load rate, the results were still consistent with those obtained using a load rate of 0.58 m/s making the smoothing function with a time period of 0.05 seconds acceptable.

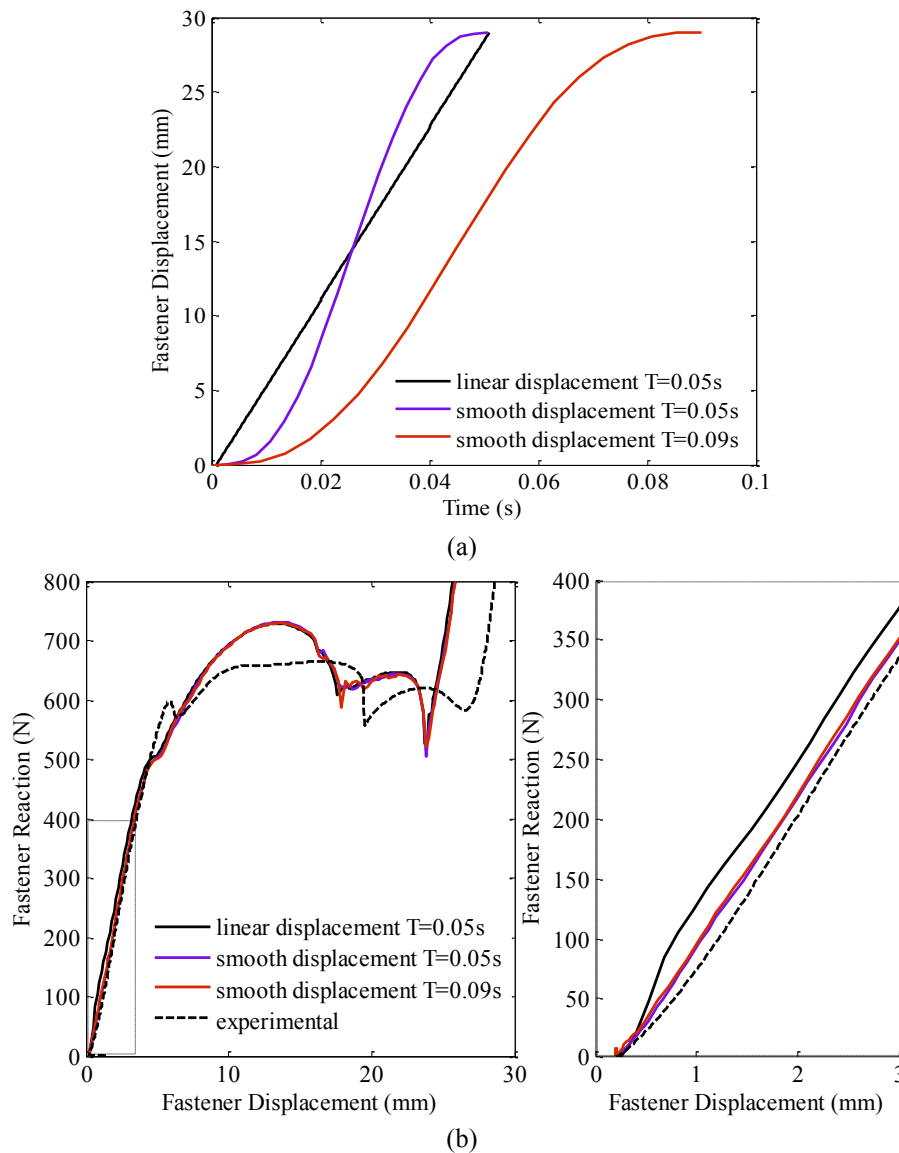


Figure 5.3: (a) load amplitude curves and (b) load-displacement curve for differing load amplitudes

5.3 MESH GEOMETRY

The model developed for this investigation focused on recreating the IFC test with the expectation that should the model accurately predict the static response of the cladding and the “star” type crack initiation then the model could help infer the strain data at crack initiation of an “H” type crack. However, such a localized model is highly complex with the load applied over a concentrated area rather than the whole specimen as a wind load typically does. The curved profile of the cladding complicates the model further, necessitating the use of the powerful explicit method. Such a localized model is also sensitive to small changes in geometry and boundary conditions.

The model geometry was largely based on the reconstructed surfaces of the cladding captured using photogrammetry. Previous versions of the model (including those documented by Lovisa 2012; 2013a,b) were created using the cladding profile provided by the manufacturer as a CAD drawing. This profile can be discretized into a series of straight and circular segments as described in Figure 5.4. However, there are observable differences between the profile provided by the manufacturer and that of the cladding samples being tested. These variations could have been incurred during manufacturing, transport or cutting. During the photogrammetry trials the cladding samples were rested on a level surface before being installed into the apparatus in order to capture the surface of the cladding at rest. A cross section of the reconstructed surface was then extracted to view the profile. Figure 5.5 compares the profile provided by the manufacturer (CAD profile) with the profiles extracted using photogrammetry.

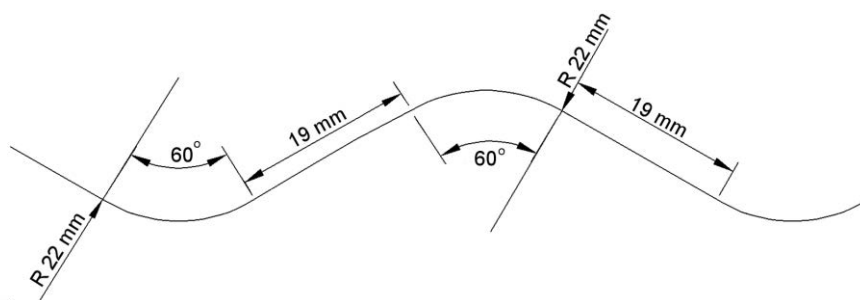


Figure 5.4: Cladding profile provided by manufacturers

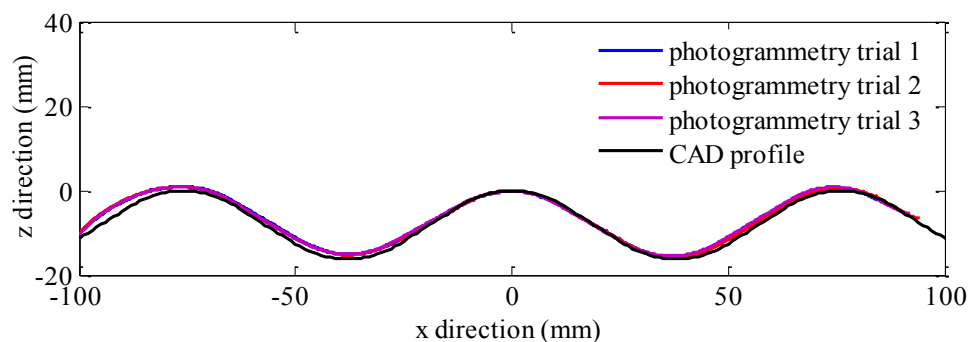


Figure 5.5: Comparison of cladding profiles taken from manufacturer and photogrammetry

The profiles of the cladding samples obtained using photogrammetry were averaged and discretized into a series of circular curves, parabolic curves and straight lines using the curve fitting tool in MATLAB. These curves were used within a specialized MATALB function that

would create a mesh of the corrugated cladding where the number of elements in the transverse (x) and longitudinal (y) direction could be varied in the input to automatically produce a geometrically precise mesh. To examine the sensitivity of the model to changes in the cladding profile, two simulations were run. The first used the CAD profile provided by the manufacturer whilst the second used the profiles based on photogrammetry. Figure 5.6 describes the fastener displacement-reaction curve and shows how the nature of the local plastic collapse changed due to the small change in profile. To complete the model the profile was effectively extruded in the longitudinal (y) direction to form the cladding surface. The results presented in Figure 5.6 were obtained using Revision X4 of the model, as detailed in Appendix B.

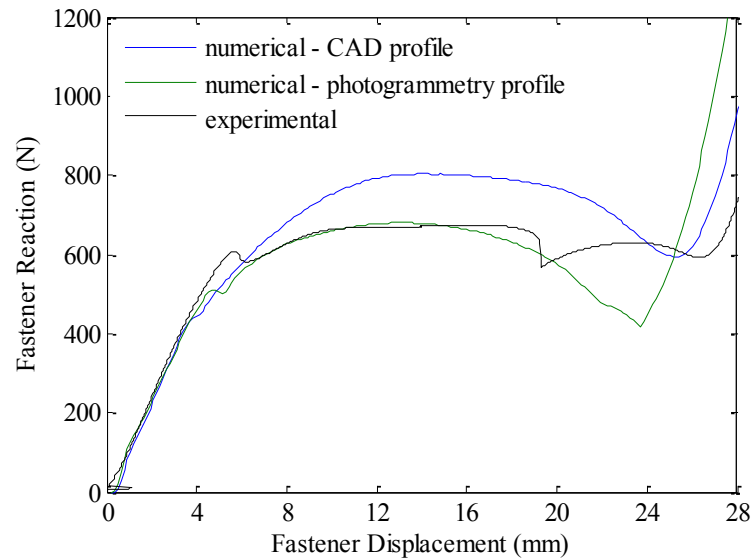


Figure 5.6: Effect of cladding profile on the static response of cladding

The model was discretized using the S4R element in ABAQUS/Explicit. The S4R element is a four-node quadrilateral reduced integration shell element that is considered a general purpose element. These general purpose elements can automatically elect to use either thick or thin shell theory depending on the thickness of the element. Thick and thin shell element theories are distinguished by the treatment of the transverse shear stresses; should the transverse shear stresses be negligible then thin shell theory is required whilst thick shell theory is needed when transverse shear flexibility is present. Given the large distance between supports in the model compared with the thickness of the cladding surface, the cladding would behave more as a thin shell than a thick shell. Unfortunately, ABAQUS/Explicit has a limited element library and lacks a thin shell element leaving only general purpose first order elements, such as the four-node quadrilateral element, available. Reduced integration was favoured to both reduce the run time of the simulation and avoid membrane locking which can occur due to in-plane bending, creating artificial stiffness of the structure. For both the benchmark examples provided by ABAQUS that feature a thin curved structure subject to a concentrated load, namely the pinched cylinder and pinched hemisphere problems, the S4R element performed well with the results varying mostly based on the nature of the mesh and the size of the elements contained within (Dassault Systemes. 2013). The S4R element is capable of accurately calculating stresses caused by bending and membrane action which are both heavily involved in the IFC test.

The mesh generating function created using MATLAB discretized the cladding surface in three discrete regions as shown in Figure 5.7. Region 1 covers the bulk of the cladding surface where the stress is less plastic and ideally a larger element can be used. Region 2 is localized to the region that experiences complex deformations and plastic strains and consequently maintains an element aspect ratio of 1 to ensure accuracy of the solution, and Region 3 immediately surrounds the fastener and contains the smallest elements of the model to accommodate the stress concentration at the fastener hole. Region 2 extends the width of the cladding sample and 70 mm either side of the fastener hole with Region 3 at the centre of the cladding surface occupying a 50 mm \times 50 mm area. The mesh for Regions 1 and 2 was generated directly using the MATLAB function whilst the mesh for Region 3 was created using ABAQUS/CAE which is more robust and can accommodate the small circular hole made for the fastener. The mesh generated by ABAQUS/CAE is input into the mesh generating function in MATLAB to form one continuous mesh. Any eccentricity of the fastener hole is processed in the mesh generating function rather than applying that eccentricity when creating the mesh for Region 3 in ABAQUS/CAE. This ensured that varying the magnitude of the fastener eccentricity required changing only a single input rather than repeatedly laboring in ABAQUS/CAE.

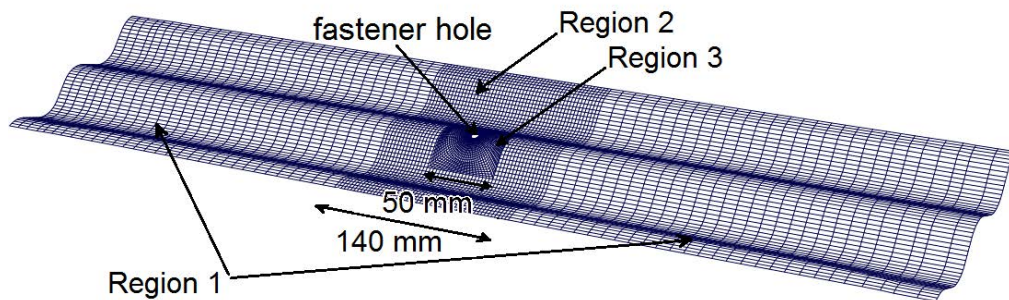


Figure 5.7: Discretized cladding model

5.4 MESH SENSITIVITY FOR NUMERICAL MODEL

A numerical model is prone to numerous errors ranging from rounding errors, mesh error, constitutive description error, and boundary condition errors. Most of the errors that occur through the numerical calculations are corrected by the solution controls imbedded in the analysis. ABAQUS is a general purpose FEA program and uses stringent controls and convergence criteria to ensure that the solution is accurate for an array of simulation types. It becomes the users' responsibility to minimize errors being incurred through the mesh, boundary conditions or constitutive description. To minimize the error incurred by the mesh a mesh sensitivity study is required. A mesh sensitivity study involves continued mesh refinement until the solution converges. Typically, the finer the mesh the more accurate the solution but at a significant computational cost.

The mesh sensitivity study for the cladding numerical model involved systematically reducing the element size for each of the three regions of the model. The ultimate goal of this numerical model is to be used to analyze crack initiation at the fastener hole. Consequently the strain in both the top and bottom surfaces of the cladding surrounding the hole is of great importance. The variables of interest are the strain at the edge of the fastener hole, specifically the surface strains on both the topside and underside of the cladding. Figure 5.8 shows the locations at

which the strain data was extracted from the numerical model to identify the sensitivity of the result to changes in mesh density.

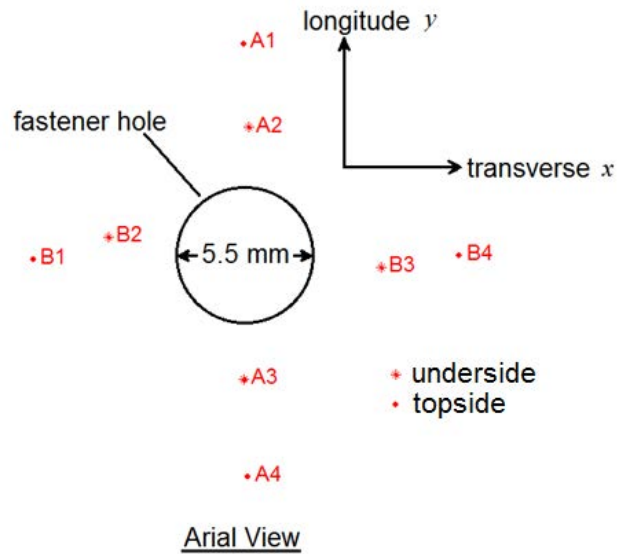


Figure 5.8: Strain variable locations surrounding fastener hole

Region 1 was varied first to establish the sensitivity of the model to changes in the aspect ratio (R_a) of these elements. The aspect ratio of the elements in Region 1 was varied from 1 to 4 by extending the element dimension in the longitudinal (y) direction. The strains at the locations described in Figure 5.8 were then monitored for any change. Typically an aspect ratio of 4 is not exceeded in numerical modelling and was consequently taken to be the upper limit. Strains at the locations shown in Figure 5.8 did not show any noticeable sensitivity to changes in the aspect ratio of the elements in Region 1. Figure 5.9 presents an example of the strain comparison specifically for location A3 in both the transverse (x) and longitudinal (y) directions.

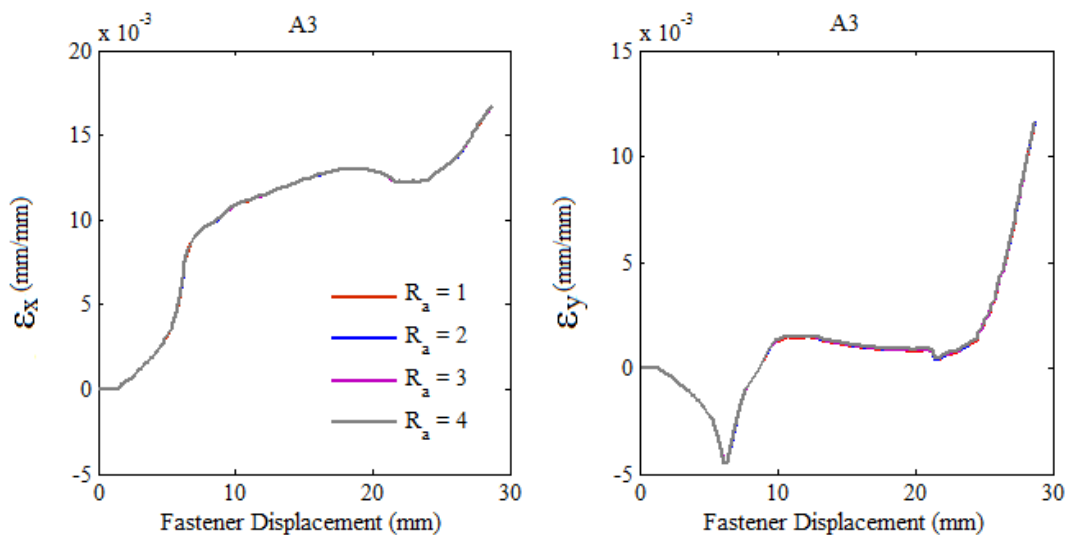


Figure 5.9: Strain comparison for differing aspect ratios of the elements in Region 1

Region 2 maintains an aspect ratio of 1 for all elements to ensure accuracy of the solution; as these elements would then more closely conform to the general element shape used to develop

the shape functions within the finite element method. The size of the element was therefore varied by changing the number of elements required to discretize the cladding in the transverse direction. However, reducing the element size in the transverse direction greatly increased the number of elements within Region 2 as an aspect ratio of 1 was maintained. Increasing the number of elements, however, increased the simulation run time considerably, so a brief trial was conducted in which the area of Region 2 was halved to determine if any changes in the strain data resulted. Rather than Region 2 extending 140 mm in the longitudinal direction as shown in Figure 5.7, this value was reduced to 70 mm. Halving the area of Region 2 did not affect the final strain results which was expected given how little sensitivity the model demonstrated to changes in mesh density in the longitudinal direction. Consequently all succeeding models adopted the reduced Region 2 to minimize simulation run time.

Changing the element size in the transverse direction was expected to cause significant changes to not only the strain field around the fastener hole but also to the resulting deformation and fastener reaction. The sensitivity of the model to the mesh density in the transverse direction is due to both the complex curved profile of the cladding and the highly localized restraint of the longitudinal boundary. As the element size was reduced in the transverse direction, Region 3 remained the same to ensure all changes in strain were a result of changing the mesh density in Region 2. The transverse dimension of the elements in Region 2 was varied from 2.4 mm to 0.714 mm. Figure 5.10 describes the resulting change in strain at locations B1 and B4 which appeared to be the most sensitive of all locations. B1 and B4 are located at the edge of the crest curvature where the cladding typically experiences dimpling. Once the transverse dimension of the elements reached 0.714 mm Region 3 was refined as the mesh transition from Region 2 to Region 3 was becoming too irregular. An irregular mesh can introduce additional errors that might obscure the convergence of the strain results during the sensitivity study. Figure 5.11 shows the change in strain for a transverse dimension ranging from 0.78 mm to 0.606 mm and compares the strain results for a transverse dimension of 0.714 mm for an unrefined and refined Region 3. The strain results converged at a transverse element dimension of 0.714 mm, with the results for a transverse dimension of 0.606 mm producing essentially identical results.

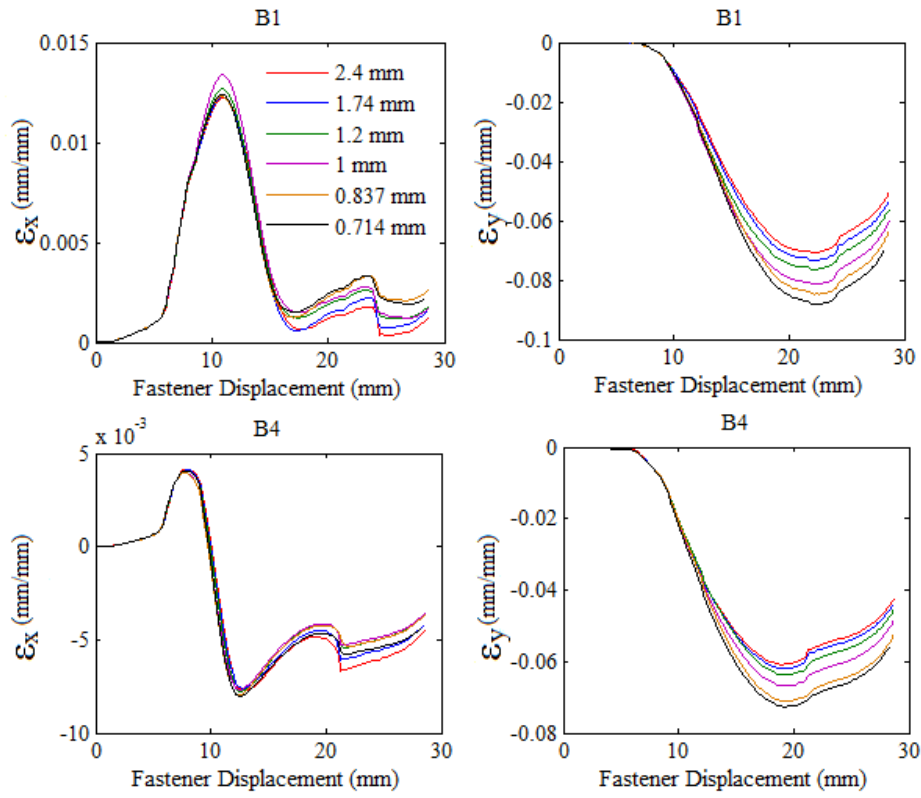


Figure 5.10: Strain comparison for different transverse dimensions of elements in Region 2

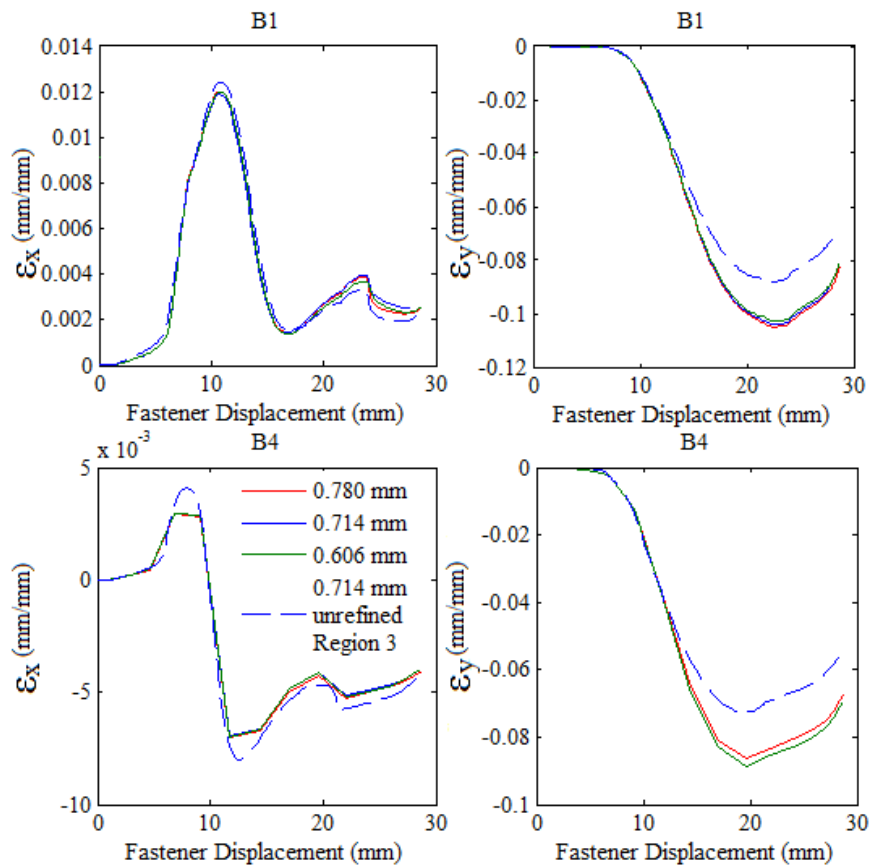


Figure 5.11: Strain comparison for different transverse dimensions of elements in Region 2 with a refined mesh in Region 3

Finally the sensitivity of the strain results to the density of the mesh within Region 3 was examined and is demonstrated in Figure 5.12. Each refinement of the mesh within Region 3 was done using ABAQUS/CAE and the localized mesh was then imported to MATLAB to be integrated into the global mesh. The mesh in Region 3 is characterised by the element dimension discretizing the fastener hole edge. Originally the size of the element in Region 2 remained constant while the mesh within Region 3 was varied. However, maintaining an element dimension of 0.714 mm in Region 2, and therefore at the border of Regions 3 and 2, resulted in a progressively more irregular mesh within Region 3. For example, once the element at the hole edge reduced to 0.3 mm in size, the mesh was forced to transition from 0.714 mm down to 0.3 mm in a development length of only 20 mm. The errors incurred by using such an irregular mesh obscured the convergence of the strain results, challenging the selection of an appropriate element size for Region 3. The mesh sensitivity study for Region 3 was revised with the aim to use only a regular mesh by reducing the element size in Region 2 in accordance with the reduction in element size in Region 3. The change in the mesh density in Region 2 is not likely to affect the strain results shown in Figure 5.12 as all element dimensions trialed were below 0.714 mm – the limit of convergence for Region 2.

The element sizes trialed for Region 3 were 0.7 mm, 0.6 mm and 0.5 mm. The mesh convergence study for Region 3 was then abandoned as an element size of 0.5 mm within Region 3, and consequently Region 2, resulted in excessive run times and no trend towards convergence had manifested. Figure 5.12 describes the change in strain at locations B1 and B4 which appeared to be the most sensitive to changes in element size within Region 3.

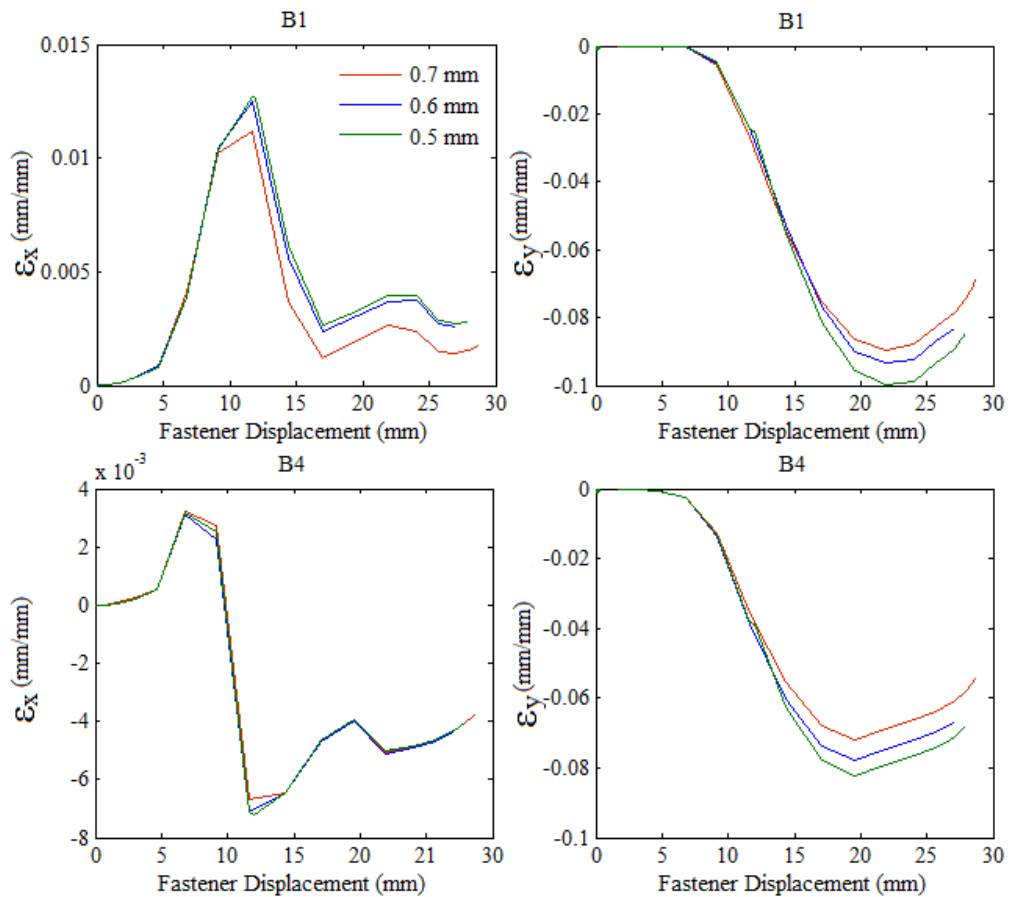


Figure 5.12: Strain sensitivity to changes in mesh density in Regions 3 and 2.

Given that simulating the full cladding sample with appropriate mesh refinement was not viable, a new approach was required such as submodeling a localized section of the cladding. Submodeling is a modelling abstraction where a highly localized section of a model is analyzed through interpolation of the results from a coarse global model. Submodeling requires the selection of a localized area of the cladding whose response does not affect the overall global response of the cladding. The 50 mm × 50 mm section at the centre of the cladding, Region 3, was trialed first as the local submodel. Submodeling works by applying boundary conditions at the border of the submodel which are extracted from the global model. These boundary conditions, when using node based submodeling, are the translation and rotation of the border nodes.

An appropriate mesh density for the global model was required which was sufficiently coarse to reduce the computational cost of the simulation whilst maintaining the accuracy of translational and rotational displacements at the border to Region 3. Consequently the displacement and rotation at the midpoint of each four sides of the border to Region 3 were compared for various mesh densities. The mesh densities trialed were based on a changing element size in the transverse dimension which has previously been shown to greatly affect the strain result at the fastener hole. The mesh density within Region 3 was varied with the change in transverse element dimension to maintain a regular mesh, although two trials included an irregular mesh to further examine the sensitivity of the translational and rotational result at the border of Region 3 to the quality of the mesh. Figure 5.13 presents the resulting fastener reaction of each model trialed and highlights the lack of sensitivity to changes in the transverse element dimension. Figure 5.14 describes the out-of-plane (z) deflection and out-of-plane rotation for two points along the boundary to Region 3 which showed the greatest sensitivity to changes in mesh density. The locations of the two points in question are indicated in Figure 5.14. Clearly the global response of the model is not sensitive to changes in the transverse element dimension although a transverse element dimension of 2.4 mm did result in a slight increase in the out-of-plane deflection of the left most edge of the boundary to Region 3. The appropriate mesh density for the global model was taken to be 1.5 mm which provided consistent results with a significantly reduced computational cost.

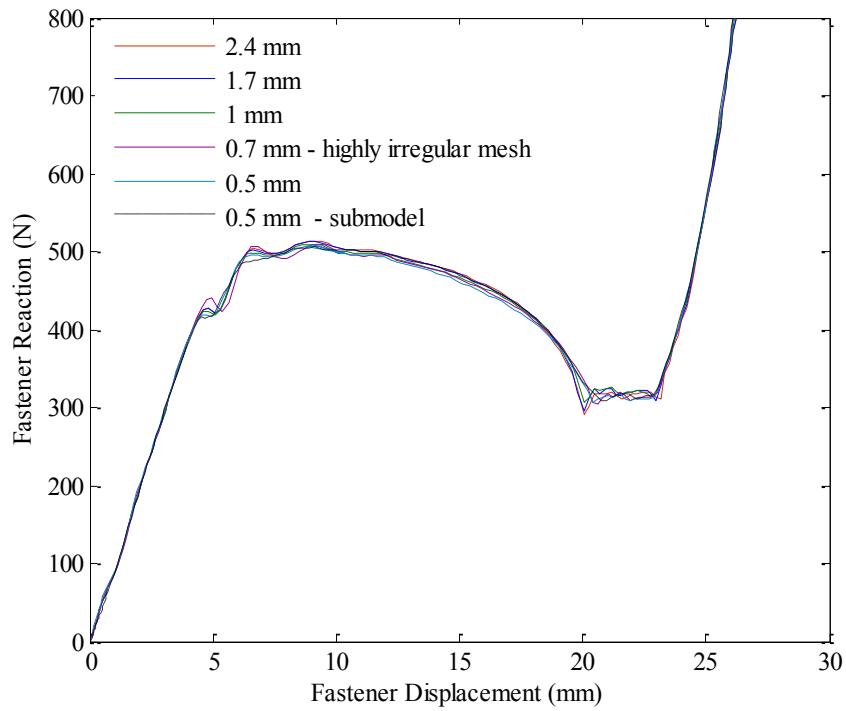


Figure 5.13: Fastener reaction for differing transverse element dimensions

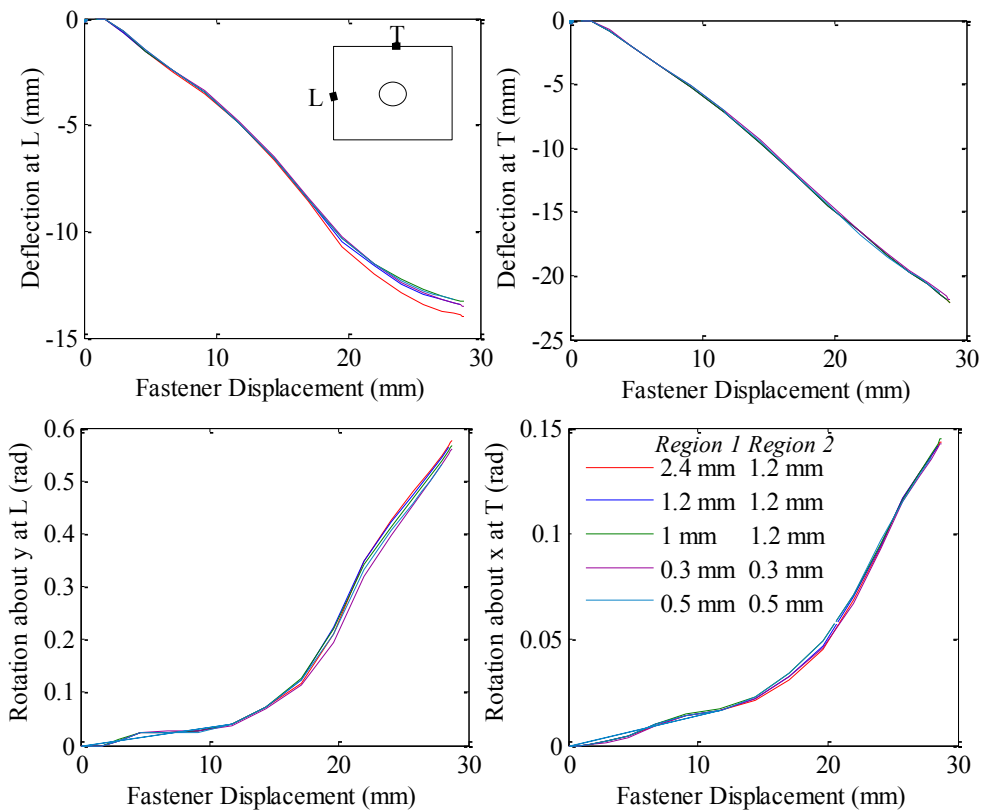


Figure 5.14: Out-of-plane translation and rotation at the border to Region 3 for differing transverse element dimensions

One of the greatest challenges to using a submodel in this investigation is ensuring the EPDM seal contacts the cladding at the same moment in both the global and local models. The

differing mesh densities of the local and global model in combination with the curved profile of the cladding can cause the location of the topmost node at the crest of the cladding – which contacts with the EPDM seal first – to differ between models, as shown in Figure 5.15 (a). Even a small difference in elevation (Δz) of up to 0.02 mm produced a variation in the resulting fastener reaction of up to 4% causing the strain at the fastener hole to vary significantly. To counteract the differing locations of the topmost node of the cladding crest the strain free adjustment function for contacting bodies was implemented. This function repositions the nodes within two contacting surfaces without incurring strain to ensure that no overclosure is present. Figure 5.15 (b) describes the repositioning of nodes in the contacting surface of the EPDM seal using the strain free adjustment function.

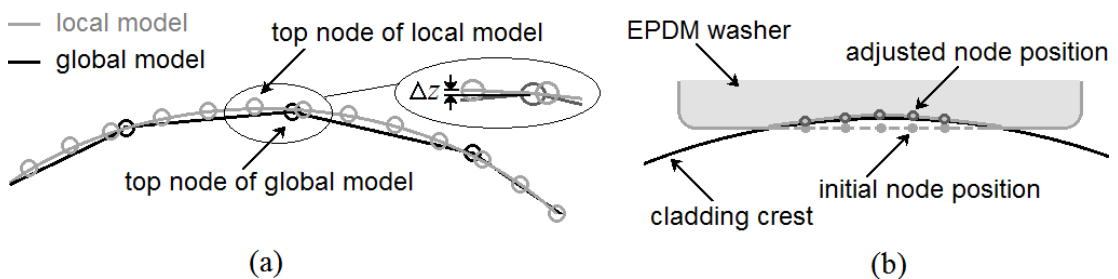


Figure 5.15: (a) Variation in node height at the crest of the cladding between local and global model and (b) an example of strain free adjustment of two contacting surfaces.

The submodel when first implemented was discretized using an element dimension of 0.5 mm. The strain results from the submodel were then compared directly with the strain results from the full model that had an element dimension of 0.5 mm in both Region 3 and 2 to ensure that the submodel results were consistent. Figure 5.16 describes the strain results for the full model (as previously shown in Figure 5.12) and the submodel at locations B1 and B4 for various element sizes, and shows good agreement between the two models for an element size of 0.5 mm. Figure 5.13 also contains the fastener reaction for a submodel with an element size of 0.5 mm, once again demonstrating the good agreement between the full model and the submodel. Submodeling appears to be an effective method for analyzing the response of the cladding. The selected 50 mm \times 50 mm region also appears to be appropriate for the submodel. When viewing the deformation of both the global and local models there appears to be discrepancies between the two which are recovered within 3 mm of the submodel boundary as highlighted in Figure 5.17.

Figure 5.16 compares the strain calculated by the submodel for an element size of 0.5 mm to 0.2 mm. The results appear to converge at an element size of 0.3 mm for the longitudinal strain at location B1. For location B4, the strain at first appeared to converge for an element size of 0.4 mm but the strain calculated using an element size of 0.2 mm contradicts those results. The true convergence of the strain results is likely being obscured by the geometric quality of the elements at which the strain data is extracted. Locations A1 to B4 were based on the average position of the strain gauges implemented during the static IFC experiments and they tend to lie slightly off centre to the fastener hole. The various meshes used in the submodel were created using the mesh generating tools in ABAQUS/CAE and imported for further processing in MATLAB. A specially scripted function in MATLAB then finds the nodes closest to each of the strain gauge locations and shifts the nodes to those positions respectively. To minimize the resulting warping of the four adjoining elements, the change in location is then distributed

to each node within the elements. However, depending on the size of the relocation, the four surrounding elements can still remain somewhat warped. By happenstance, the original position of the nodes closest to the locations of the strain gauges in the mesh that used an element size of 0.3 mm was closer to that of the mesh that had an element size of 0.2 mm so once the nodes locations were adjusted, the mesh using an element size of 0.2 mm contained more irregular elements. Figure 5.18 shows the four elements sharing the nodes at B1 and B4 for an element size of 0.2 mm and 0.3 mm and highlights the more irregular geometry of the elements with a size of 0.2 mm. Considering the effects of element irregularity, an element size of 0.3 mm was taken to be the element size at which the mesh converged.

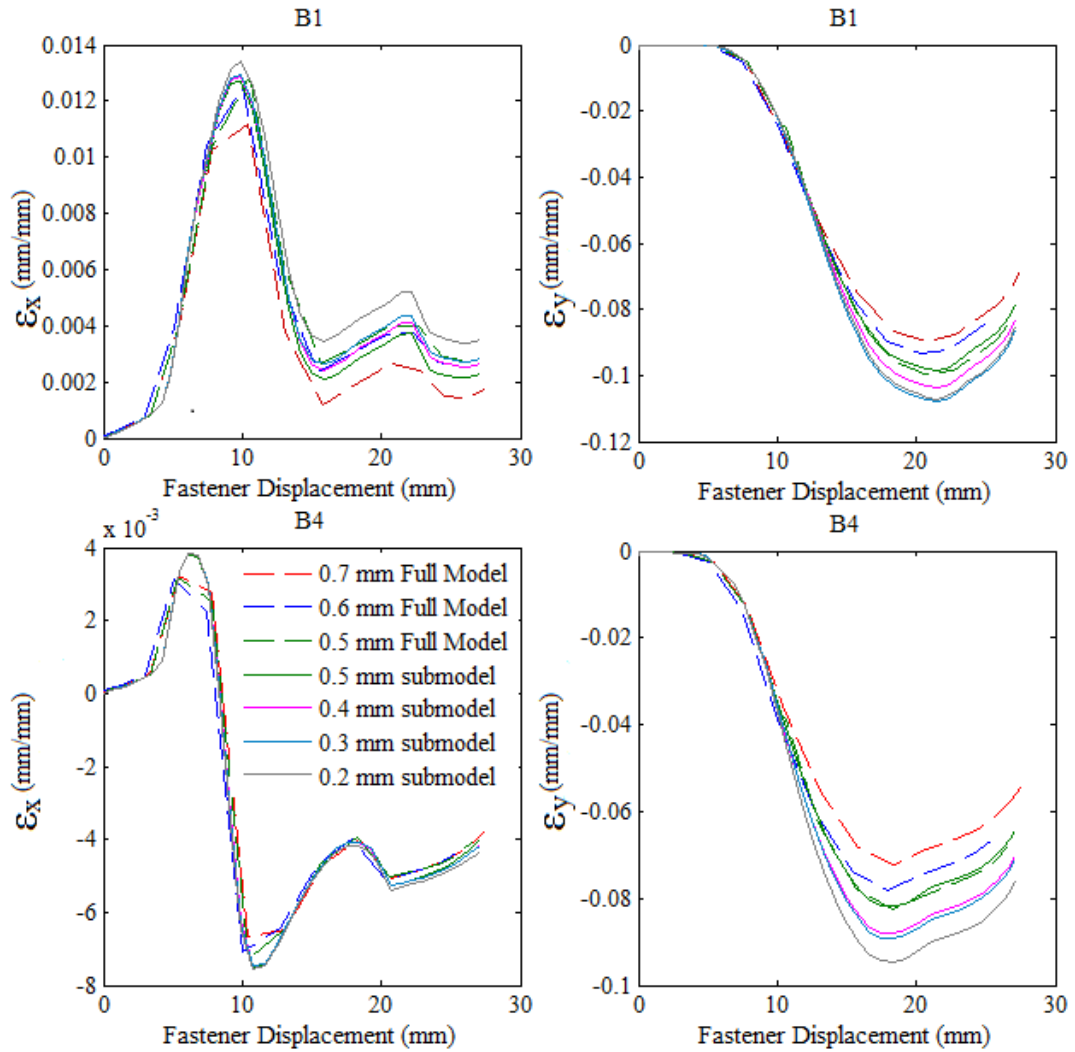


Figure 5.16: Comparison of strain for various mesh densities of the submodel and full model.

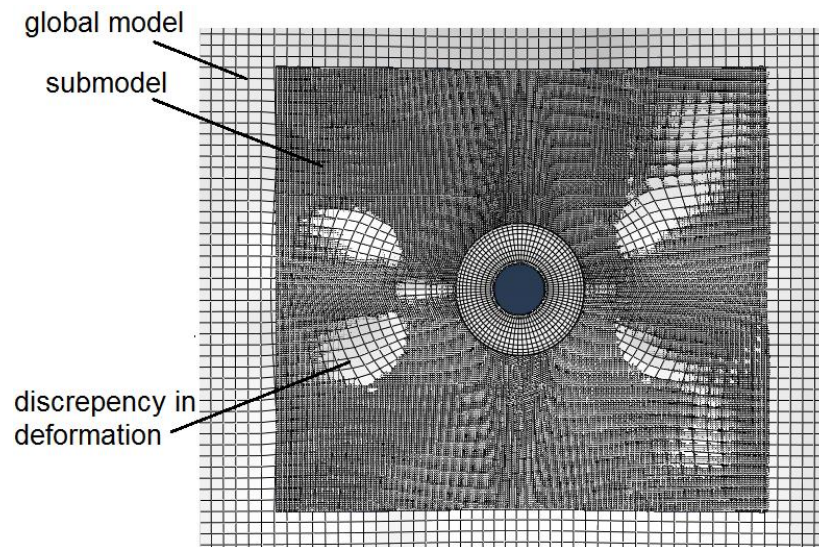


Figure 5.17: Overlay plot of submodel and global model deformed shape

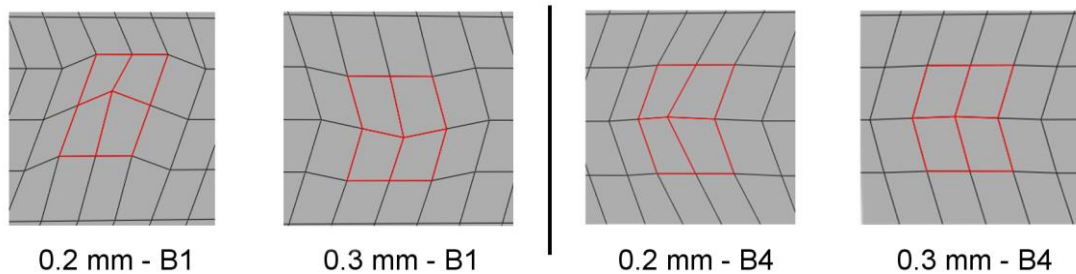


Figure 5.18: Comparing element geometries at the point of extraction for the submodels with an element size of 0.2 mm and 0.3 mm.

At low applied loads the strain field surrounding the fastener appears to be less sensitive to changes in mesh density which suggests that a more coarse mesh could be implemented to model the cyclic response of the cladding. The ‘star’ type crack is formed when the cladding is cycled below local plastic deformation which corresponds to a fastener displacement of approximately 10 mm. Considering a fatigue test of roof cladding can take upwards of 5 hours, a more coarse mesh would to some extent compensate for the extended loading history. Figure 5.19 describes the resulting change in strain at locations B1 and B4 for a variety of mesh densities. Both Regions 2 and 3 were varied to establish the overall sensitivity of the strain field for the first 10 mm the fastener was displaced. The apparent discrepancy between the strain data for the model with element dimensions 0.61 mm and 0.4 mm in Regions 2 and 3 respectively, and the model with element dimension of 0.5 mm in both Regions 2 and 3 is due to the frequency at which the results were saved to the output database. The strain results for these models were extracted at fewer intervals than the remaining models to reduce the size of the output database. Based on Figure 5.19 a model with transverse element dimension of 1.2 mm in Region 2 with a refined element dimension of 0.8 mm in Region 3 would provide sufficient precision of the strain data whilst avoiding a computationally costly simulation for simulating the dynamic response of the cladding. A coarse mesh of these element dimensions is even more efficient than using the submodeling method.

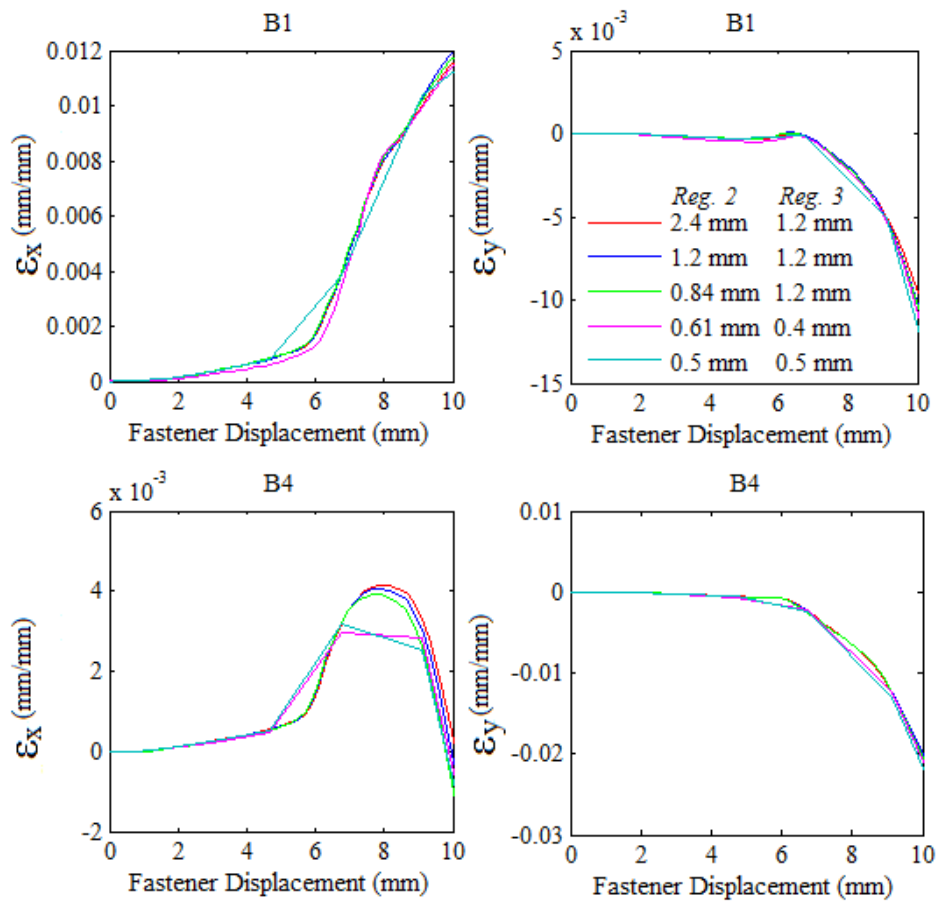


Figure 5.19: Strain comparison for different transverse dimension of elements in Region 2

The general contact algorithm in ABAQUS/Explicit was used to simulate all contacting interactions in the model; these interactions include: the cladding and EPDM seal, EPDM seal and screw, boundary rails and cladding, screw shaft and cladding. The general contact definition is preferred for models with multiple interactions, with each interaction then contained within a single contact domain which greatly simplifies the problem. Edge contact, such as the fastener hole edge interacting with the screw shaft, is also available in the general contact algorithm. Overall the general contact domain is robust and easy to implement, with most ABAQUS/Explicit analyses now implementing this algorithm rather than the contact pairs algorithm (Dassault Systemes, 2013).

Each interaction within the general contact domain can then be manipulated independently by providing different friction coefficients for each interaction. The friction coefficient for steel on steel contact such as the fastener hole edge pressing against the screw shaft was taken to be 0.78 (Blau, 2009). For the boundary rails clamping the cladding edge the friction coefficient was taken to be an assumed 0.6, slightly less than that for steel on steel contact as the Colorbond coating on the cladding is smoother than typical steels.

The friction coefficient for EPDM pressing against the exposed steel of roof cladding is not widely documented so a basic sliding test was performed to determine the friction coefficient. The sliding test involved a block with a variable mass resting on an inclined plane, connected to a spring as shown in Figure 5.20. The box had four EPDM seals adhered to the base while the inclined plane had a level section of treated cladding adhered to the centre. The box was

slowly moved away from the spring and released to determine the maximum point of extension in the spring at which the box did not slide back towards the spring. Knowing the stiffness of the spring (k), the extension of the spring (e), mass of the box (m) and the incline of the plane (θ) allows the friction force resisting the spring to be calculated using static equilibrium. To reduce the errors inherent in a sliding test, multiple trials were completed in which both the mass of the block and incline of the plane were varied. Figure 5.21 details the resulting friction coefficient calculated for each trial which corresponds to an average coefficient of 0.4.

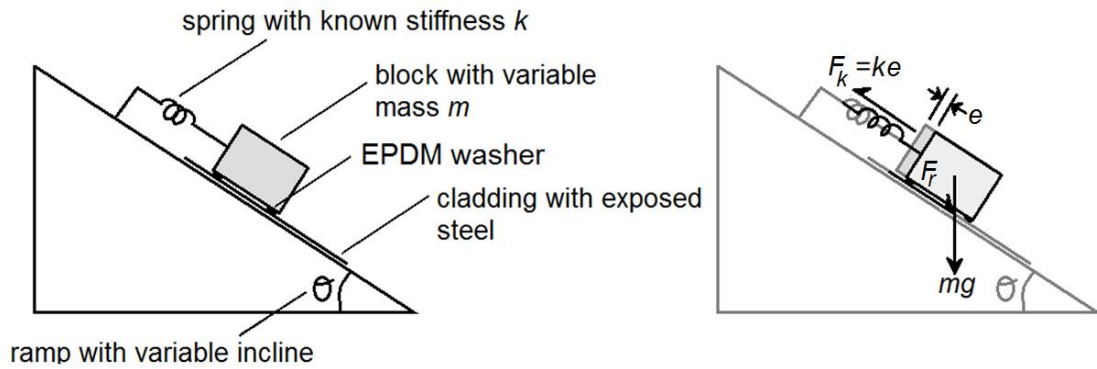


Figure 5.20: Basic sliding test used to calculate coefficient of friction

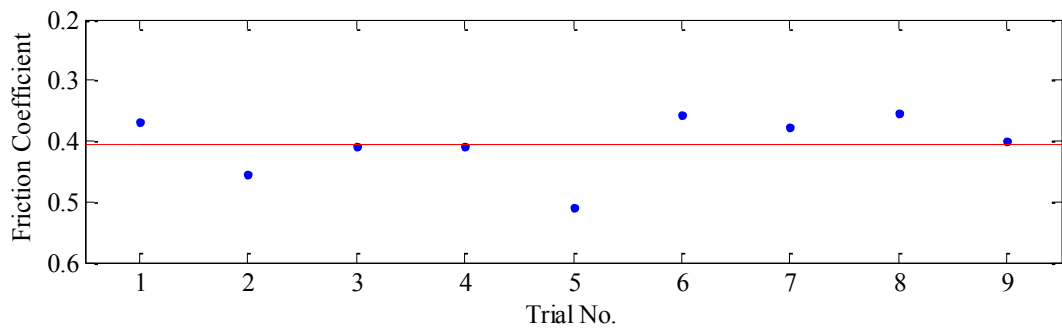


Figure 5.21: Coefficient of friction for contact between EPDM seal and exposed steel of cladding

The discretization of the EPDM seal was simpler than that of the cladding. Different mesh types and densities were explored during the washer compression study (following in Section 5.6 – “Washer Compression Study”) with the final mesh of the EPDM seal using eight-node reduced-integration brick elements (C3D8R) with an average dimension of 0.3 mm as shown in Figure 5.22. The geometry of the EPDM seal was modified slightly with all edges rounded using a 0.2 mm radius fillet. Rounding the edges of the washer reduced the numerical singularities that tend to occur when sharp corners are compressed. In traditional contact algorithms used in a FEA the two contacting bodies must have similar mesh density with the more deformable body being slightly more refined than its stiffer counterpart. This condition is more relaxed for the general contact algorithm although some versions of the cladding model involved large differences in the mesh densities, for example during the mesh convergence study 1.5 mm elements were in contact with 0.3 mm elements. To ensure that no errors were being introduced by the large variation in mesh densities, the elements in the washer were increased in size to 0.7 mm but there was negligible change in strain within the cladding at locations A1-A4 and B1-B4.

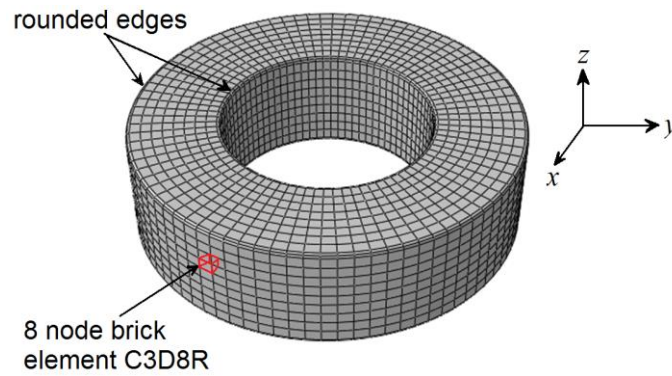


Figure 5.22: Discretised EPDM seal

5.5 BOUNDARY CONDITION SIMULATIONS

Originally the boundary conditions of the IFC model were enforced by simply restraining the nodes along the edges of the cladding sample where the inside edge of the cladding lid would typically clamp the cladding. However, the model was over constrained and the cladding appeared to be significantly stiffer than was observed experimentally. Significant efforts were made to identify why the model was excessively stiff with numerous numerical studies finally concluding that the model is incredibly sensitive to small changes in the boundary conditions. The numerical studies included modeling both the longitudinal and transverse boundaries as a series of elastic springs, inelastic springs, sliding slot connections with friction, sliding plane connections with friction, sliding slot connections in parallel with elastic springs, rigid surfaces clamping the boundary, rigid surfaces in combination with elastic springs and finally deformable surfaces clamping the boundary. Figure 5.23 describes some examples of the boundary conditions that were trialed, with most examples demonstrating the boundary conditions for the transverse edge. For each of these arrangements the individual parameters such as spring stiffness, normal force and friction coefficient were varied to establish the sensitivity of the model. How these elements, such as the spring elements, were connected to the cladding edge was also trialed which included direct connections to the boundary nodes or kinematic constraint connections to the cladding edge. Additional information regarding the trialed boundary conditions is contained in Table B1 and Table B2 in Appendix B.

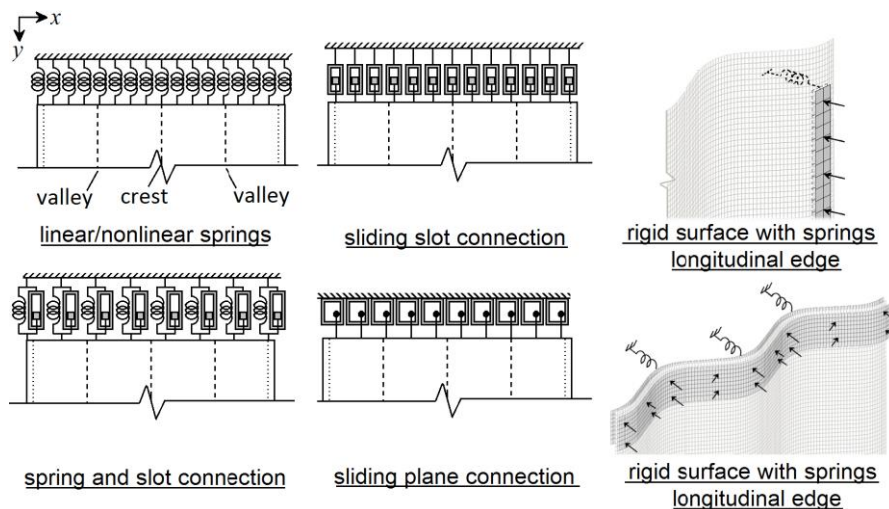


Figure 5.23: Examples of boundary conditions used during numerical trials

Once the sensitivity of the model was firmly established the focus of the numerical studies then shifted to recreating the boundary conditions imposed by the apparatus as accurately as possible. To do so additional information regarding the specific geometry of the apparatus, the contacting force of the apparatus and the clamping mechanics at the cladding boundary was required.

Firstly the geometry of the apparatus lid in relation to the fastener and the cladding sample was required. The digital reconstructions of the cladding surface created using photogrammetry included the lid of the apparatus and the fastener. The lid of the apparatus was texturized and marked to provide a datum and scale for comparing two DSMs, which resulted in the inside edge of the apparatus lid being captured in detail. The fastener was also texturized in a similar manner to ensure that the cladding surface immediately surrounding the fastener was accurately reconstructed which resulted in the fastener itself being included in the DSM.

During the photogrammetry trials the cladding surface clamped within the apparatus without loading through the fastener was captured. A cross sectional view of the resulting DSM provides an accurate measure of the position of the cladding in relation to both the fastener and the longitudinal boundary. The DSMs show significant eccentricity of the fastener which corresponds with the asymmetric deformation observed during static IFC trials. Figure 5.24 provides an example of a cross section taken from a DSM and the measured eccentricity of the screw and longitudinal boundaries. The turning points of the crests and valleys of the cladding were identified by using a curve fitting tool in MATLAB. The cross section of the DSM was extracted as a point cloud and passed through MATLAB. Specially scripted functions then identified each valley and crest and found the line of best fit based on a circle function from which the turning point could be calculated. The lines of best fit each valley and crest returned a root mean square error of 0.998 or higher in all three DSMs. Table 5.3 details the relevant distances measured from each DSM. The average eccentricity of the fastener and the average distances to the inside edge of the longitudinal clamp were used in the numerical model. All other dimensions were measuring using micrometer and tape measure.

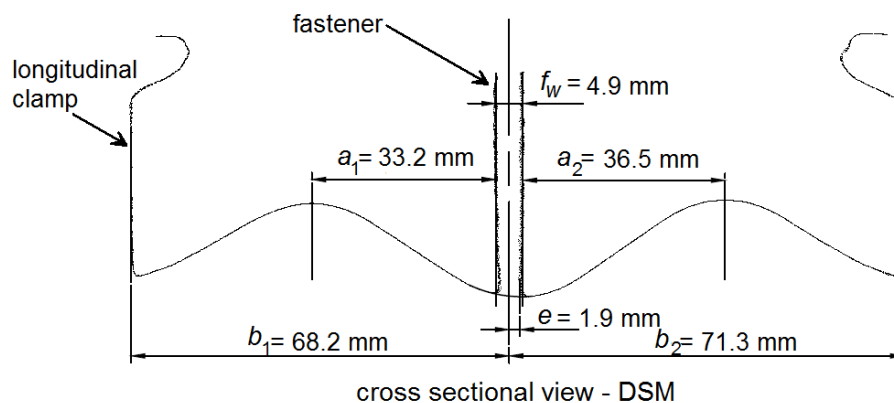


Figure 5.24: Cross sectional view of DSM created during Photogrammetry Trial 3.

Table 5.3: Geometry of cladding boundary in the transverse direction

Trial Number	Fastener width f_w (mm)	Distance to valley crest a_1 (mm)	Distance to valley crest a_2 (mm)	Distance to longitudinal boundary b_1 (mm)	Distance to longitudinal boundary b_2 (mm)	Fastener eccentricity e (mm)
1	4.9	33.8	35.4	69.8	69.4	1.2
2	4.7	32.8	36.7	69.0	70.5	2.3
3	4.9	33.2	36.5	68.2	71.3	1.9
<i>Average</i>	<i>4.8</i>	<i>33.3</i>	<i>36.2</i>	<i>69</i>	<i>70.4</i>	<i>1.8</i>

Next the compressive force applied to the cladding at the boundary was required. Twelve high tensile steel bolts were used to compress the lid of the apparatus to the base with the cladding sandwiched between the two. Attempts were made to measure the compressive force within each bolt using a load cell. A single bolt was used to compress the lid of the apparatus to its base whilst a load cell, positioned immediately adjacent to the bolt, recorded the compressive force applied. The same procedure was used for various locations of the bolt to accommodate the changes in compressive force that can occur when the user's posture changes. The bolts within the apparatus typically experienced a compressive force ranging from 810 – 1100 N depending on the location of the bolt which corresponds to a total compressive force of approximately 11 kN including the weight of the apparatus lid.

ABAQUS was then used to approximate the distribution of the compressive force at the interface between the cladding and apparatus. The apparatus lid was drawn as a 3D object using CAD software and imported to ABAQUS as a part. The compressive force in each bolt was then applied as a point load at the relevant locations of the bolts as shown in Figure 5.25. The HDPE clamps were included as a rectangular prism. The apparatus lid was constructed from mild steel with an approximate Young's modulus of 200 GPa. The HDPE blocks were modeled as a composite material to account for the additional stiffness provided by the steel substrate within the HDPE block. The Young's modulus of the HDPE was taken to be 800 MPa acting over 80% of the element while the steel substrate had a Young's modulus of 200 GPa acting over the remaining 20% of the element. The base of the longitudinal clamps and HDPE blocks were restrained from translation and rotation and the contact between the lid and HDPE blocks was modeled using the contact pairs algorithm with an assumed friction coefficient of 0.4. ABAQUS/Standard was used to analyse the apparatus to determine the reaction force at the base of each clamp and block. The analysis calculated the total compressive force through the rear HDPE block to be 800 N with 800 N through the front HDPE block and 4.4 kN in each longitudinal clamp. These forces were then applied to the numerical model to account for the deformation within the cladding caused by installing the cladding within the apparatus.

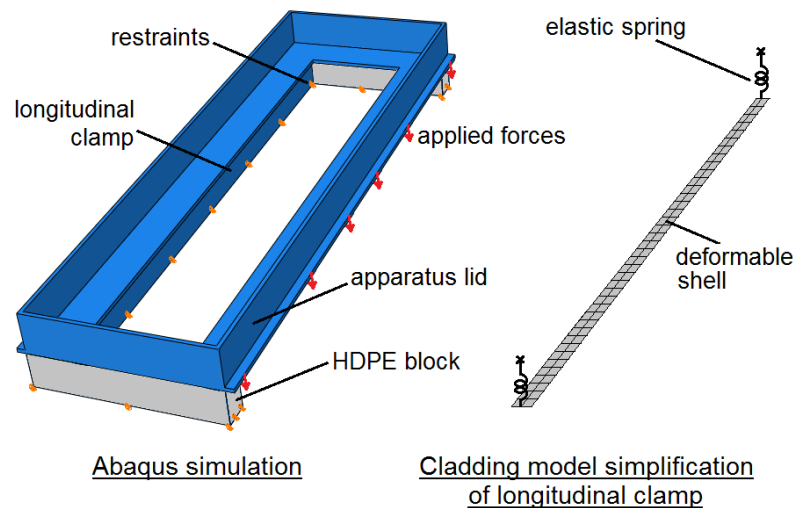


Figure 5.25: ABAQUS simulation of apparatus lid and equivalent simplification used in cladding model

The same model was then analysed a second time to determine the equivalent stiffness of the structure. Rather than applying concentrated forces at the locations of the bolts, these nodes were restrained. Compressive pressures were then applied to the base of the longitudinal clamps and the resulting displacement at the base of each clamp was measured. The compressive loads were then removed from the longitudinal clamps and applied to the base of the HDPE blocks while the deformation of the blocks was monitored. A HDPE block constructed entirely from HDPE was trialed first followed by a composite section that included the steel substrate. Knowing the applied load and resulting deformation, the transverse and longitudinal boundaries were simplified as a system of 1 mm thick deformable shells and elastic springs. For example, the longitudinal clamp was simplified to a 6 mm × 630 mm rail with two elastic springs connected to each end which is pictured in Figure 5.25. Using ABAQUS/Standard, the stiffness of the springs and the Young's modulus of the deformable shell material in each direction was varied until the rail would deform and displace in a similar manner to the longitudinal clamp. The springs at either end displaced to account for the global deflection of the longitudinal clamp whilst the deformable shell accounted for the localized deformation of the longitudinal clamp. The same simplification and procedure was then used for the HDPE clamp. Unfortunately when the deformable shell and spring systems were included in the IFC model the resulting run time was excessively large. The deformable shell was then replaced by a rigid surface and the stiffness of the springs was relaxed to ensure the overall displacement of the rigid surface was of similar magnitude to both the local and global deflection of the longitudinal clamp.

The fastener was also simplified in the numerical model as a system of springs and rigid surfaces. To determine the appropriate stiffness of the springs for the fastener, the screw was analyzed using ABAQUS/Standard. The screw used during the IFC tests is a long slender screw 5.2 mm in diameter. The screw is restrained by a clamp, effectively acting as a cantilever with a length of 49 mm where the cladding surface applies load at the free end. The resulting movement and rotation of the screw was captured during the photogrammetry trials with an example of the captured translation shown in Figure 5.26. The DSMs for each applied load, created using photogrammetry, were aligned using the markers on the lid of the apparatus which undergoes minimal movement. Using the lid as the datum for comparison, the

translation of the screw is easily visible. In ABAQUS/Standard the screw was modeled using 3D quadratic tetrahedral elements with the top end restrained from translation and rotation, and loads applied 3 mm up from the screw head to account for the thickness of the EPDM seal. The resulting displacement was then used to calculate the required spring stiffness, in N/mm, needed to simplify the screw as a rigid surface suspended on a spring. Figure 5.27 compares the experimental setup with the detailed ABAQUS simulation of the screw and the resulting simplification made for the cladding model.

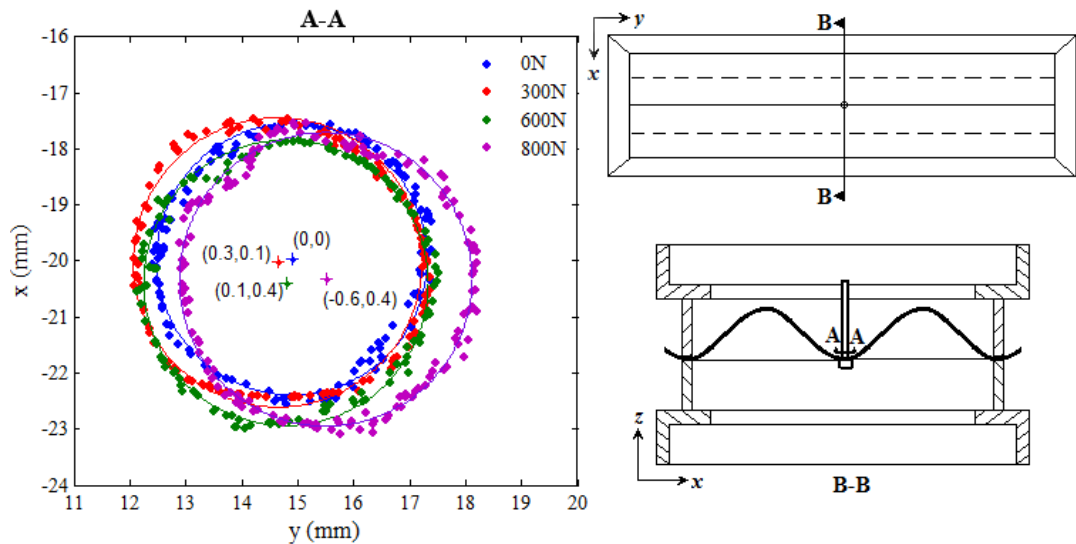


Figure 5.26: Translation of screw head documented during Photogrammetry Trial 3

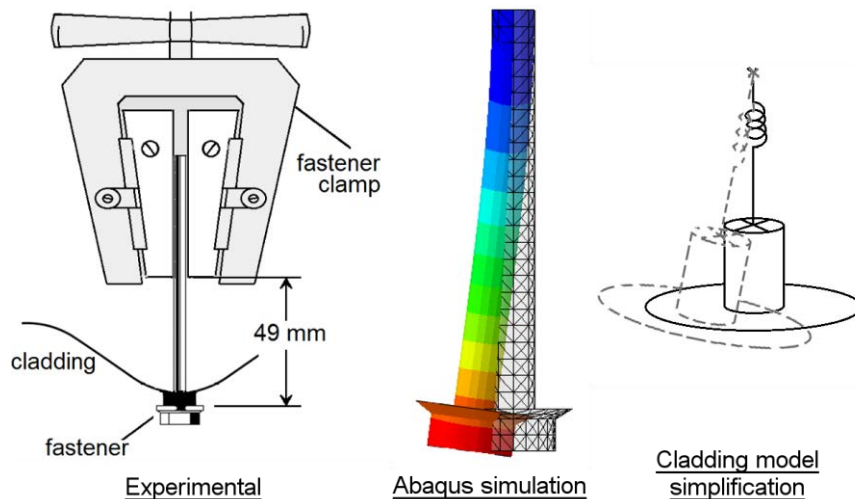


Figure 5.27: Experimental set up of fastener, detailed simulation of fastener in ABAQUS and the spring and rigid surface system used in the cladding model

Following a detailed investigation of the geometry and loading at the cladding boundary further experimental data was collected with a focus on the global response of the cladding. Previous experiments measured the strain, fastener reaction and deformation of the cladding in a localized area surrounding the fastener which characterised both the local and global response of the cladding. Specialised trials were conducted to gather data at the cladding boundaries in order to validate the boundary conditions without obscuring the data with

localized effects. For example, attempts were made to measure the slip at the boundaries of the cladding while subjected to a static load. A digital microscope was placed normal to the cladding surface at the transverse boundary facing an HDPE block and at the longitudinal boundary facing the longitudinal clamp with a 1 mm scale adhered to the surface of the cladding in view of the cameras. The movement at the boundary was then recorded as the static load was applied through the fastener by tracking markers on the cladding surface. Still images were extracted from the video at equal intervals and scaled using the 1 mm scale in view of the camera. Based on the movement of the markers, the cladding at the longitudinal boundary appeared to slip up to 0.15 mm whilst the cladding at the transverse boundary only moved 0.05 mm. The measured movement was smaller than expected and given the small magnitude and the approximate nature of this method, very little confidence can be placed in these values.

The poor approximation of the slip at the boundaries necessitated a second approach to quantifying the effects of the boundary conditions. A simple but accurate means of characterizing the global response of the cladding is measuring the strain in the cladding near the boundary itself. Uniaxial strain gauges were placed at the locations specified in Figure 5.28 to measure the longitudinal strain in the longitudinal direction and the transverse strain in the transverse direction. For Trial 2, strain gauges were placed on both the underside and topside of the cladding sheet.

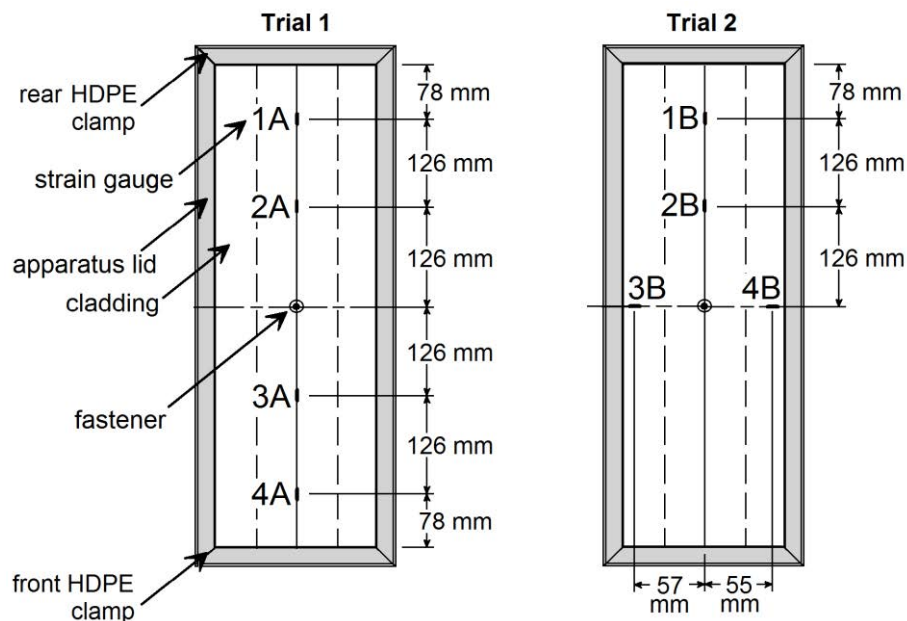


Figure 5.28: Strain gauge locations for investigating the boundary conditions

Figures 5.29 and 5.30 present the results from the final working numerical model of the IFC test. The boundary conditions of the model comprised a combination of springs and rigid surfaces, as described earlier in this section. Figure 5.29 compares the fastener reactions predicted by the model with the experimental results. There is good agreement between numerical and experimental results, particularly for the first 10 mm that the fastener was displaced. The numerical and experimental results diverge once the cladding undergoes local plastic collapse although the model did successfully simulate the right side of the cladding crest collapsing prior to the left side which was observed experimentally. This sequential collapse of the cladding is due to the eccentricity of the fastener, eccentricity of the longitudinal

clamps and movement of the fastener clamp. Each of these variables is difficult to control and Figure 5.29 clearly emphasizes the resulting variation in the response of the cladding between experimental trials. Consequently, the discrepancy between numerical and experimental data following local plastic collapse of the cladding is likely due to a mechanism within the boundary rather than the cladding constitutive description. However, further refinement of the boundary conditions within the model would result in unrealistic simulation run times with the current working model carefully optimizing accuracy and efficiency.

Figure 5.30 compares the numerical and experimental strain data at the boundary of the cladding for the locations shown in Figure 5.28. The strain in the longitudinal and transverse directions predicted by the model shows good agreement with the experimental data particularly prior to local plastic collapse of the cladding which corresponds to a fastener displacement of 10 mm. Following local plastic collapse of the cladding the strain at locations 2B and 3A begin to slightly deviate from the experimental results.

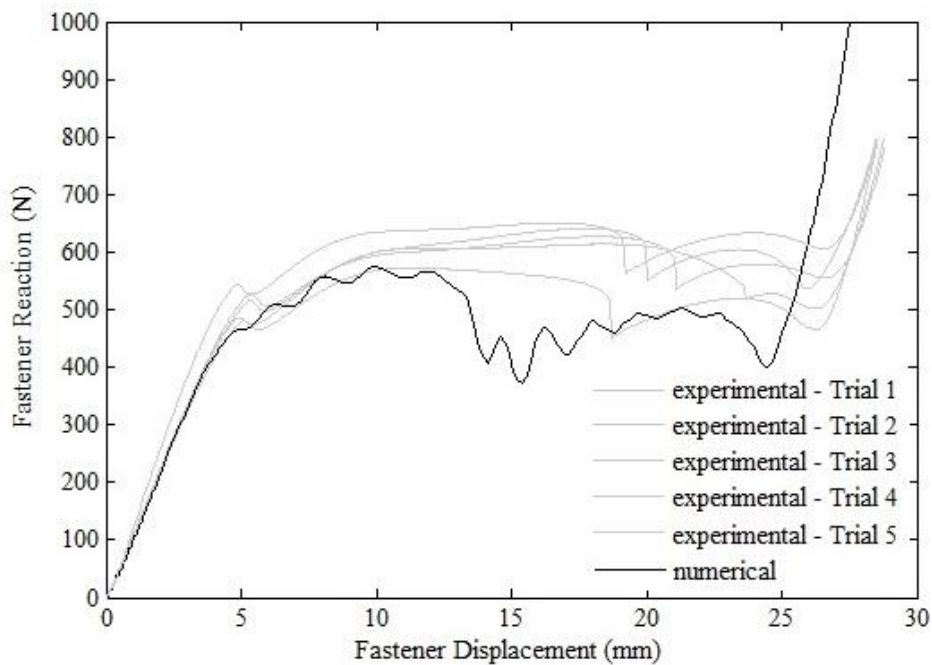


Figure 5.29: Numerical and experimental fastener reaction – fastener displacement curve

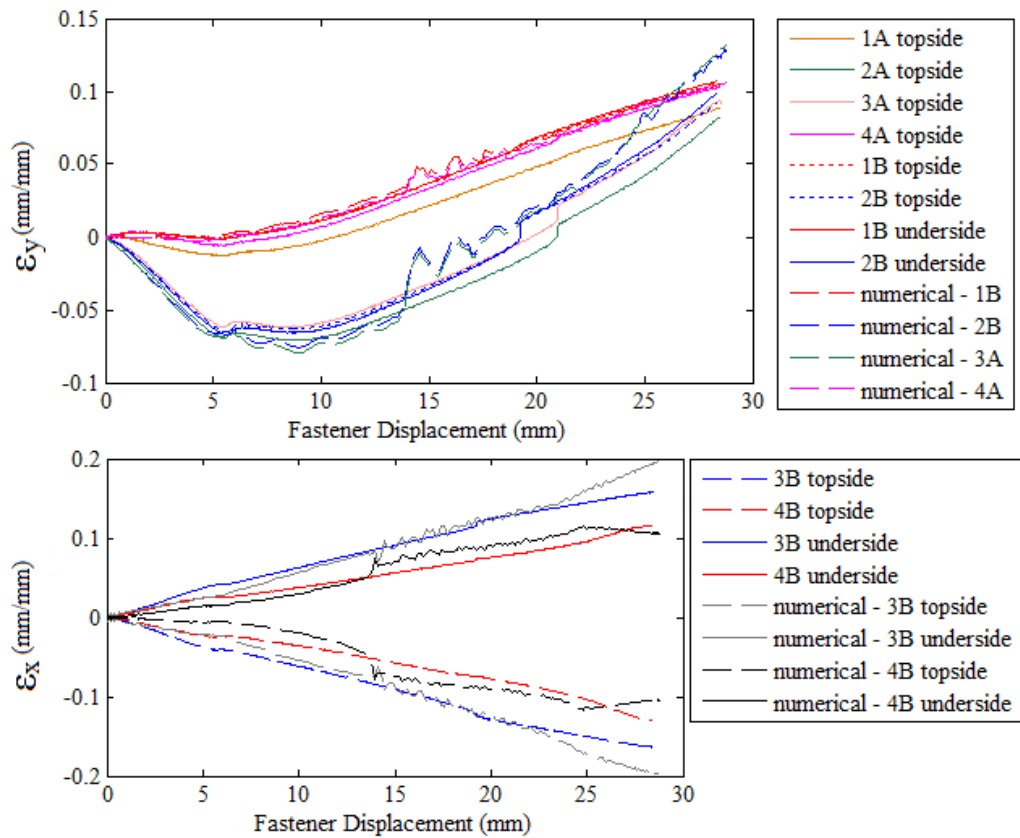


Figure 5.30: Numerical and experimental strain data at the cladding boundary

Significant efforts were made to accurately simulate the static response of corrugated cladding which resulted in continued refinement of the cladding boundary conditions. However, during the initial revisions of the model in which the boundary conditions were simplified as a series of springs and sliding slot connections, it was observed that some of the simplified models predicted the initial response of the cladding fairly accurately. A simplified model that can simulate the response of the cladding prior to local plastic collapse would be favorable when simulating the dynamic response of the cladding, particularly when the focus of the simulation is on the formation of ‘star’ type cracks. Removing the contact definitions involved in the boundary conditions of the current model greatly reduces the simulation run time. The most effective simplification appears to be fixing the nodes along the longitudinal boundary whilst constraining the transverse boundary with sliding slot connections in parallel with elastic springs as shown in Figure 5.31. The elastic spring has a stiffness of 300 N/mm whilst the sliding slot has a normal force of 100 N and a friction coefficient of 0.3. These values were obtained by simply varying each variable until the resulting strain at the boundaries aligned with the corresponding experimental data. The spring included in the fastener was also removed to further reduce simulation run time.

Figures 5.32 and 5.33 compare the experimental data with the numerical data produced by the simplified numerical model. Figure 5.32 details the fastener reaction with respect to the fastener displacement for both the final working model and the simplified model. The most significant limitation of the simplified model was its inability to simulate the sequential collapse of the cladding crests which results in more significant geometric stiffening. However, for the first 10 mm that the fastener is displaced, the simplified model accurately simulates the

response of the cladding. Figure 5.33 describes the strain at the cladding boundary as predicted by the simplified numerical model and shows good agreement between the numerical and experimental strain data particularly for the first 10 mm that the fastener was displaced.

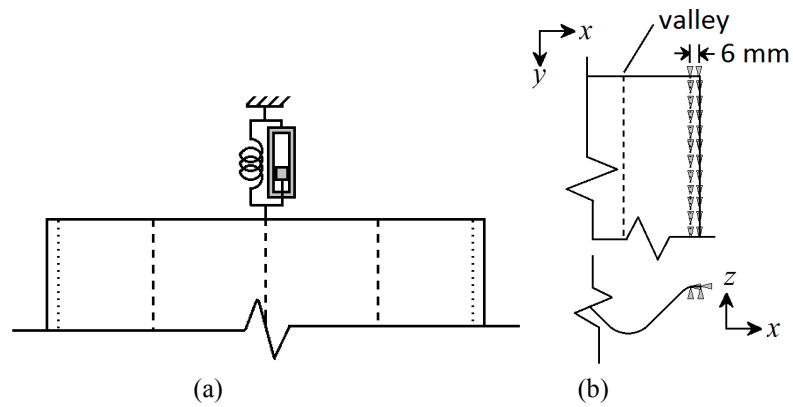


Figure 5.31: (a) Transverse boundary and (b) Longitudinal boundary of simplified model

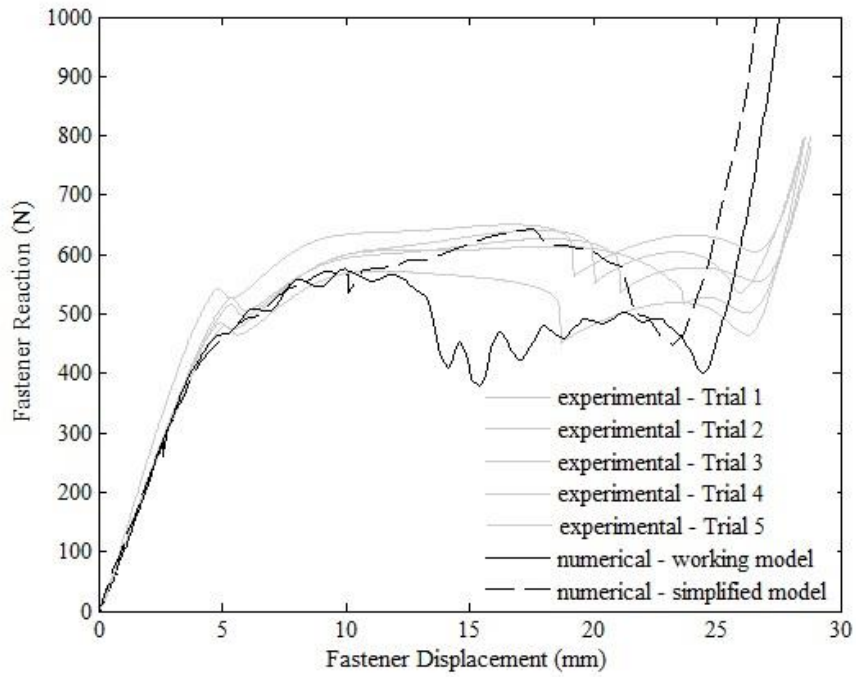


Figure 5.32: Numerical and experimental fastener reaction – fastener displacement curve using both the working model and simplified model

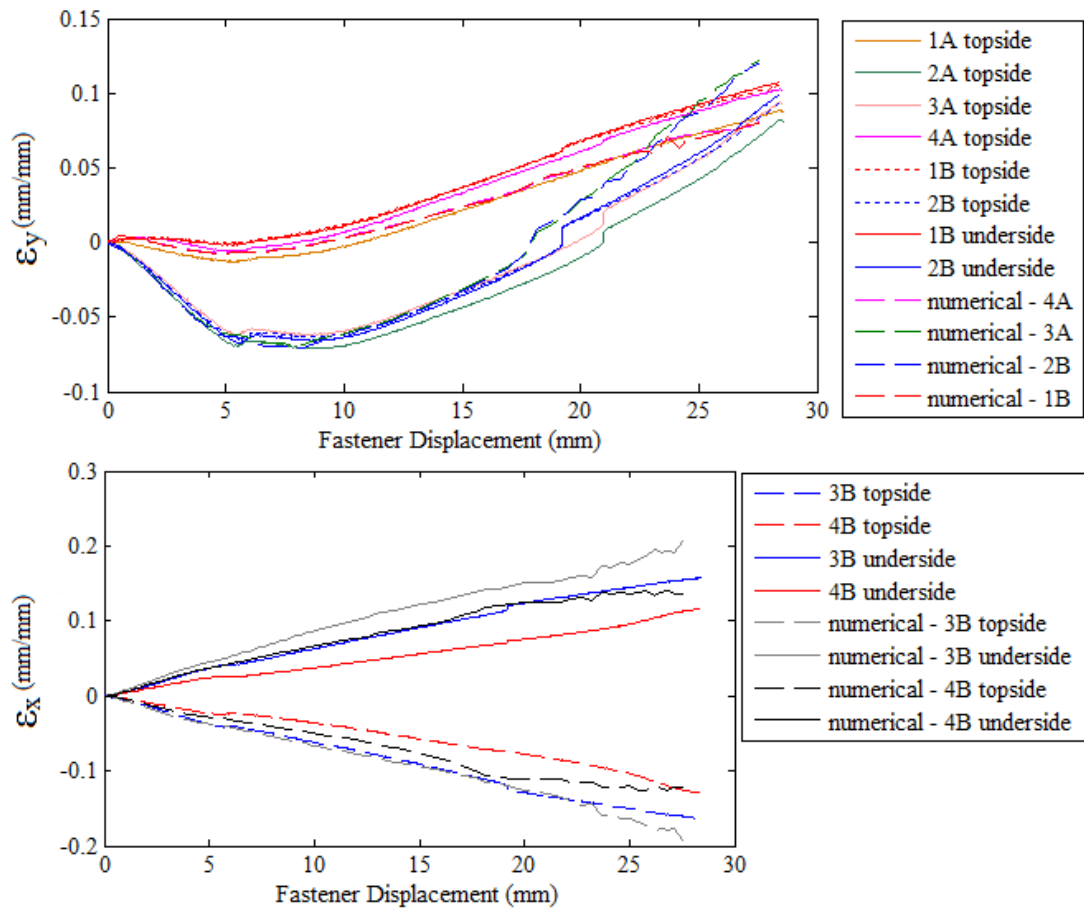


Figure 5.33: Numerical and experimental strain data at the cladding boundary using the simplified model

5.6 WASHER COMPRESSION STUDY

The EPDM seal was made from a hyperelastic material. However, the specifics of the washer material properties were unknown but necessary for creating a model that can accurately predict the stress field surrounding the fastener hole. To determine the material properties of the EPDM seal a series of washer compression studies were undertaken that measured the shortening and expansion of the washer under a compressive load. Given the Poisson's ratio for the EPDM material was unknown; the expansion of the washer under a compressive force was required. For each EPDM seal that was tested, the dimensions were measured to calculate the relevant strain in the washer. The dimensions of each washer were then averaged to establish the dimensions of the washer required in the numerical model. Figure 5.34 (a) describes the average dimensions of an EPDM seal taken from a sample of 20 washers and Figure 5.34 (b) describes the shortening and expansion of an EPDM seal under a compressive load.

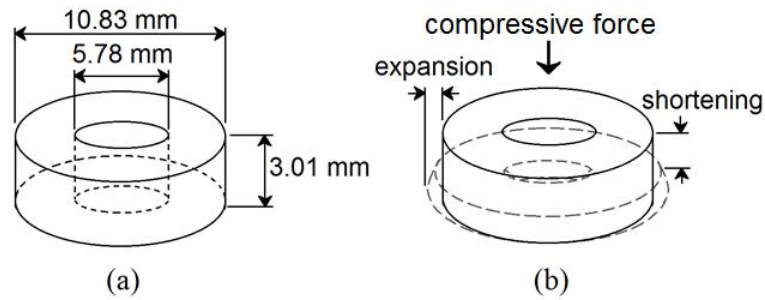


Figure 5.34: (a) average dimensions of EPDM seal and (b) shortening and expansion of EPDM seal under compressive load

The EPDM seal compression studies involved compressing the washer between two smooth steel platens and measuring the shortening and expansion of the washer under a given compressive force. The United 50kN-STM machine used in the IFC tests was also used to test the EPDM seals. Two specially fabricated platens made of 12 mm thick steel plate were precisely leveled and polished smooth in order to reduce the friction between the EPDM steel and the platens. The platens were also cleaned and lubricated between each trial to further reduce friction. The United 50kN-STM machine is capable of measuring both the shortening of the washer and the applied compressive force. To measure the expansion of the EPDM seal a high definition video camera, level with the EPDM seal, recorded the expansion of the washer as it was loaded. Still images were extracted incrementally from the recorded video and input into a specially created MATLAB function that measured the expansion of the washer. Figure 5.35 shows the EPDM seal being compressed between the platens using the United 50kN-STM machine. Figure 5.36 describes the resulting response of the washer subject to a compressive load for 10 different trials and highlights the extreme nonlinearity of the hyperelastic response.

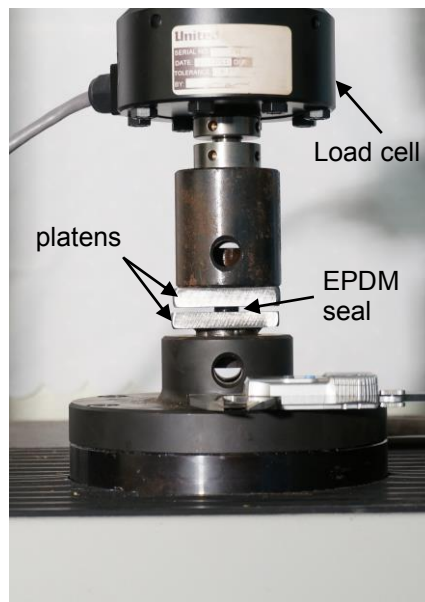


Figure 5.35: EPDM seal compression study test

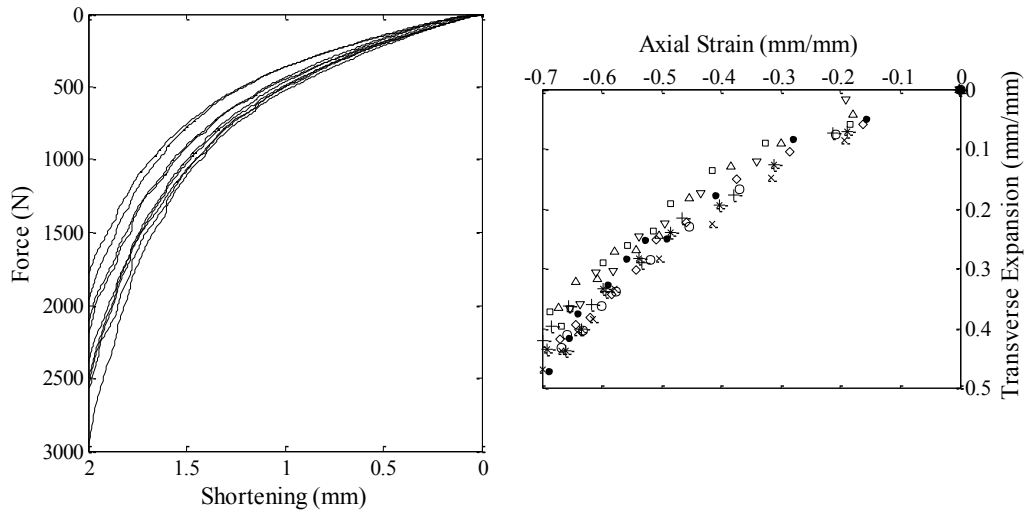


Figure 5.36: Shortening and expansion of EPDM seals under compressive load

The steel surface was polished smooth and lubricated in an attempt to minimize the friction between the washer and platens although the characteristic bulging at the side of the washer as it compresses suggests these efforts were in vain. Unfortunately the unavoidable friction still evident between the EPDM seal and platens, and the hollow at the centre of the washer prevents the washer material properties, such as the Poisson's ratio, being calculated directly from the test results. Instead, a numerical model of the washer compressing between the platens in combination with the experimental data was used to infer the material properties of the washer. The washer compressing between two smooth steel platens was simulated using ABAQUS/Explicit. The platens were modelled as two rigid surfaces while the washer was discretised using deformable elements with a hyperelastic material definition. The symmetry of the washer compression allowed a quarter model to be used rather than a full model.

The model of the washer involves a highly confined and highly deformable object which can lead to singularities in the solution. Corners of a deformable material compressing against a rigid surface in particular are prone to singularities. Typically most problems involving confined rubber like materials can be effectively solved using both ABAQUS/Standard and ABAQUS/Explicit. However, significant mesh refinement and solution controls are required to solve these problems in ABAQUS/Standard. For the washer compression studies the Explicit method was more desirable given its efficiency in simulating highly confined hyperelastic materials. Figure 5.37 describes the washer compression model both in its initial and deformed states.

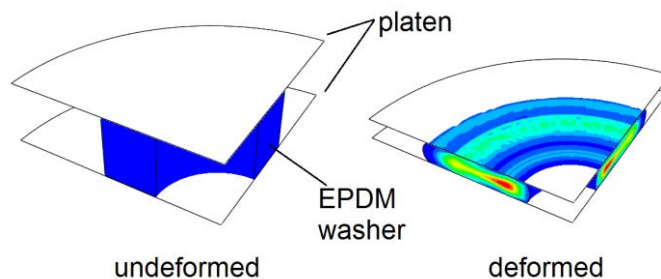


Figure 5.37: Numerical model of washer compression

ABAQUS/Explicit provides numerous hyperplastic material definitions which each have differing limitations and strengths depending on the model. Typically the material properties of a hyperplastic material can be specified in terms of a stress-strain curve obtained from uniaxial, biaxial or planar tests. These tests are idealized and should typically not include friction effects or unusual sample geometry. When stress-strain data can only be recovered from one of these tests, the Marlow hyperplastic material definition is preferred as it most accurately recreates those results. However, the Marlow hyperelastic definition assumes that the material is completely incompressible (a Poisson ratio of 0.5) which causes an unstable solution in an Explicit analysis. Mahaarachchi (2003) used the Ogden material definition to model the EPDM seal based on the popularity of the definition for modelling rubber O-rings and seals. Given the number of unknowns relating to the compressive behavior of the washer, a sensitivity study of the different material definitions was performed. The remaining material definitions available in the ABAQUS library were each trialed with the experimental data obtained from the compression studies input as an idealized stress-strain curve along with an assumed Poisson ratio of 0.475 and a static friction coefficient of 0.4. Figure 5.38 describes the resulting response of the washer using the different material definitions. The model used a very refined mesh for the EPDM seal, at a substantial cost to simulation run time, to ensure that the compressive response of the washer was firmly dependent on the chosen material definition.

Clearly only the Yeoh model produced an unusual result with the analysis terminating prematurely due to excessive distortion of elements discretizing the washer. The van der Waal model also produced an unusual result with the outer edge of the washer folding in rather than extending outwards. Figure 5.39 compares the deformed shape of the washer produced by the van der Waal model in comparison to the shape produced using all other models. Although not immediately visible in Figure 5.38, both the Polynomial and Mooney-Rivlin model produced identical results. Although the majority of the models (Mooney-Rivlin, Polynomial, Yeoh and Neo Hooke) produced similar results to one another, the Ogden model was favoured given that the model produced results most consistent with the experimental studies for both the shortening and expansion of the washer. Only the first-order Ogden model is presented in Figure 5.38 as higher-order Ogden models produced similar results but were unstable at moderate to large strains. Ideally the model definition selected is not critical as the material properties will be varied until the numerical model produces results consistent with the experimental studies.

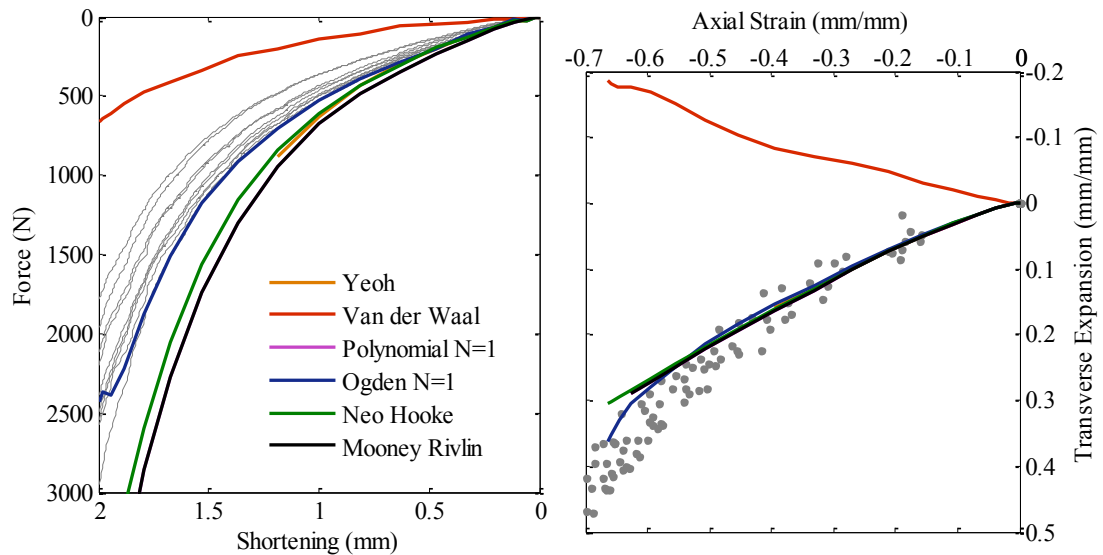


Figure 5.38: Model sensitivity to changes in material definition

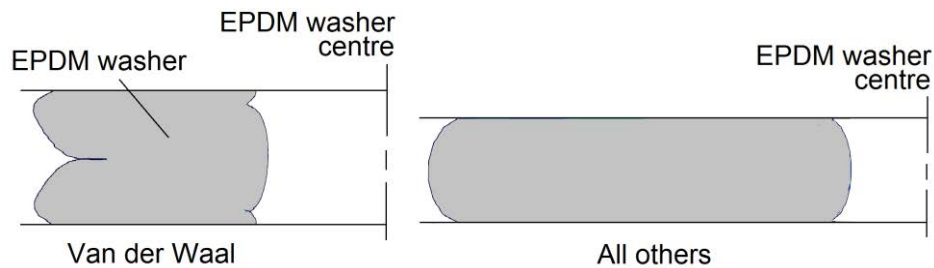


Figure 5.39: Cross section of the deformed washer using the different material definitions

Prior to completing a parametric study of the material properties, the mesh used to discretise the EPDM seal was studied to determine the appropriate density and configuration. Three different geometries of the EPDM seal were trialed, all of which used the general body dimensions described in Figure 5.34 (a). The three geometries, simply referred to as Model A, B and C, are shown in Figure 5.40 and are distinguishable by the degree of filleting at each edge. Edges that are forced to compress are prone to singularities which reduce the stable time increment of the analysis resulting in a longer simulation run time. These singularities can often be avoided by physically rounding the edges or through submodeling. Each of the three model geometries was discretised using a variety of elements including reduced-integration eight-node brick elements (C3D8R), first-order tetrahedral elements (C3D4) and the ten-node modified tetrahedral element (C3D10M).

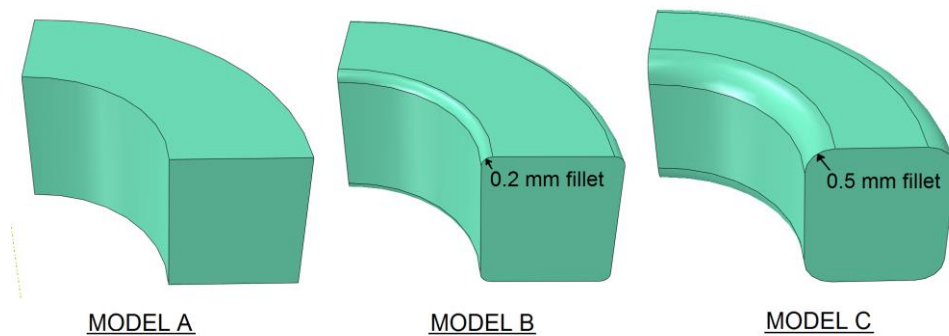


Figure 5.40: Model geometries used for mesh convergence study

As expected the differing geometries and mesh densities caused a significant variation in the compressive response of the EPDM seal. Figure 5.41 describes the various force-shortening relationships calculated by the differing models. The results appeared to converge when the EPDM seal was discretised using a tetrahedral element with a 0.1 mm dimension for both Models A and B. An almost identical solution was also produced when the washer was discretised with the modified tetrahedral element (C3D10M) or when a penalty factor was applied to the model discretised by the C3D8R element. All models that used the C3D8R element allowed the surface of the EPDM seal to penetrate the contacting surface of the platen, resulting in what appeared to be a less stiff material. Penetration of the platen suggests that the default penalty stiffness factor used in the contact definition is too small. Scaling the penalty stiffness factor by a magnitude of 10 significantly reduced the penetration and improved the accuracy of the response. Table 5.4 compares the simulation run times and stable time increment for each of the trialed mesh densities and model geometries. Using a more coarse mesh density with a modified penalty stiffness factor appears to be the most efficient means of producing an accurate response. Rounding the edges of the model slightly increased the stable time increment of the analysis as expected. However, using a fillet of 0.5 mm was excessive and affected the compressive response of the washer. A fillet of 0.2 mm improved the simulation run time without compromising the accuracy of the solution.

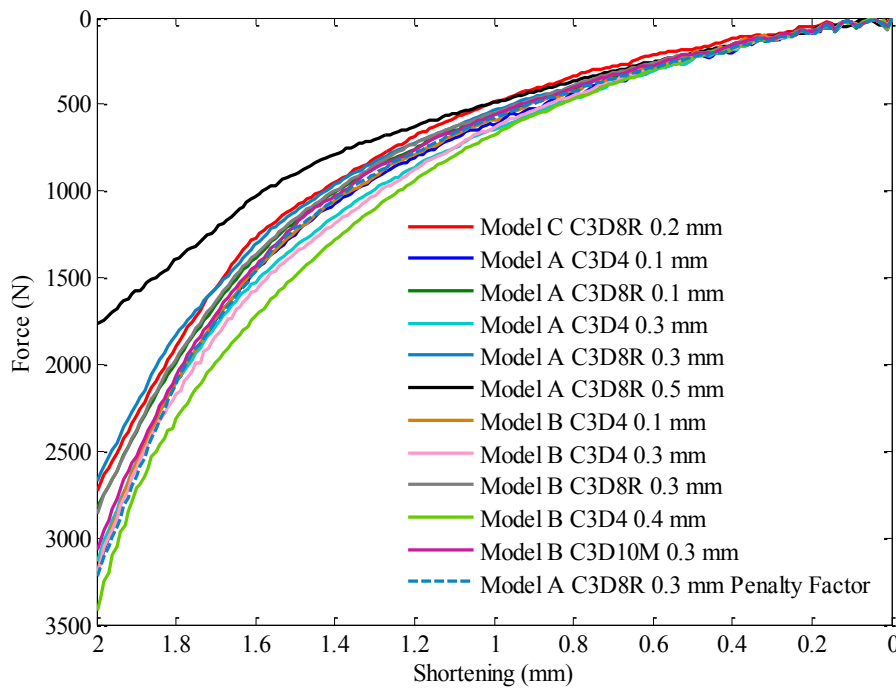


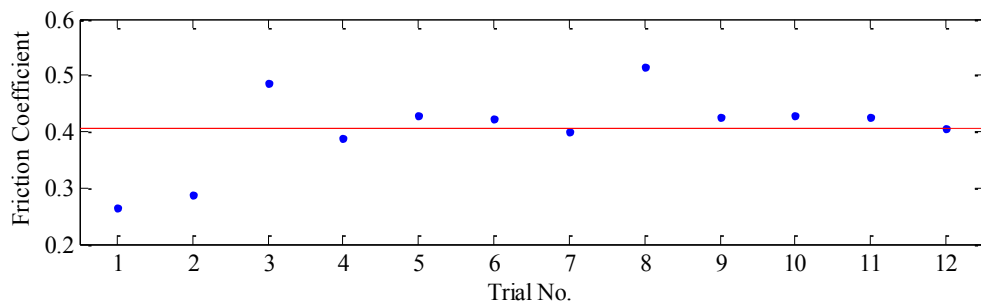
Figure 5.41: Force-shortening response of EPDM seal for different mesh densities and geometries

Table 5.4: Washer mesh convergence study – simulation run time comparison

Model Geometry,	Element type,	Element size	Number of Elements	Stable time increment	Simulation run time
Model C	C3D8R	0.2 mm	4917	5.28e-8	14s
Model A	C3D4	0.1 mm	99306	9.201e-9	14 min 58s
Model A	C3D8R	0.1 mm	63750	6.576e-9	4 min 44s
Model A	C3D4	0.3 mm	14223	2.39e-8	49s
Model A	C3D8R	0.3 mm	3960	6.54e-8	8s
Model A	C3D8R	0.5 mm	260	3.29e-7	0s
Model B	C3D4	0.1 mm	100221	1.06e-8	14 min 31s
Model B	C3D4	0.3 mm	8097	2.805e-8	39s
Model B	C3D8R	0.3 mm	3892	6.21e-8	10s
Model B	C3D4	0.4 mm	2716	2.4e-8	17s
Model B	C3D10M	0.3 mm	8097	4.72e-9	4 min 14s
Model A	C3D8R	0.3 mm	3960	2.246e-8	18s

with Penalty Factor

The friction between the EPDM seal and the smooth lubricated steel was approximated using a basic sliding test which was previously described in Section 5.4 – “Mesh Sensitivity for Numerical Model”. A box with a known mass had four EPDM seals adhered to its base and rested against a smooth lubricated steel surface that was fabricated in a similar manner to that of the platens. Numerous trials were performed in which the mass of the box and the incline of the plane were varied. Figure 5.42 details the friction coefficients calculated for 12 different trials and show an average of 0.4. However, with lubricated surfaces in contact the resulting friction coefficient becomes dependent on the applied load as the lubricant can be squeezed from between the contacting surfaces or at low enough loads the surface tension of the lubricant can contribute to friction. The mass of the box used in the sliding plane tests was limited to 500 grams whilst the compression of the washer in the UTS machine exceeds 1 kN. Further research uncovered a few examples of an EPDM material paired with lubricated steel; Békési and Váradi (2009) lubricated a 4 mm thick plate of EPDM and pressed the surface with a hemispherical steel pin. They found a coefficient of friction ranging between 0.06-0.16 for an applied normal force of 1-100 N. The lower coefficient of friction than that determined by the inclined plane tests could be due to the steel pin having a smoother surface than the platens with a roughness of less than 0.1 μm , different lubricant being used, differing types of EPDM material and the more controlled method of testing implemented by Békési and Váradi (2009). To compensate for the approximate nature of the inclined plane test and the unknown effects of the lubrication, the friction coefficient between the washer and platens was also varied in the numerical model to establish the sensitivity of the model to those parameters.

**Figure 5.42:** Friction coefficient for EPDM seal and smooth lubricated steel

Using the Ogden material definition with an assumed Poisson's ratio of 0.475 and the experimental compression data as an idealized stress-strain curve, the friction coefficient between the EPDM seal and lubricated platens was varied to establish the sensitivity of the model. A friction coefficient of 0.6 and 0.4 returned the same result whilst a friction coefficient of 0.2 resulted in a slight variation in the compressive behaviour of the washer. A notable difference in the expansion of the washer during compression occurred with a friction coefficient of 0.1. A friction coefficient of 0.16 was also trialed as this was the upper limit of documented by Békési and Váradi (2009). A friction coefficient of 0.16 can conservatively be considered as the lower limit of the friction potentially in effect in the washer compression studies given that the steel pin used by Békési and Váradi (2009) was significantly smoother than the polished platens. Increased surface roughness greatly increases the friction between two contacting surfaces. The differing viscosities of the lubricating oils would also affect the friction between the contacting surfaces although the small difference in viscosity in this scenario (75 mm²/s for Békési and Váradi (2009) verse 100 mm²/s) would affect the friction between the surfaces significantly less than that of the surface roughness (Lee et al. 2002). As shown in Figure 5.43 a friction coefficient ranging from 0.6 to 0.16 did result in some small changes to the compressive response of the EPDM seal.

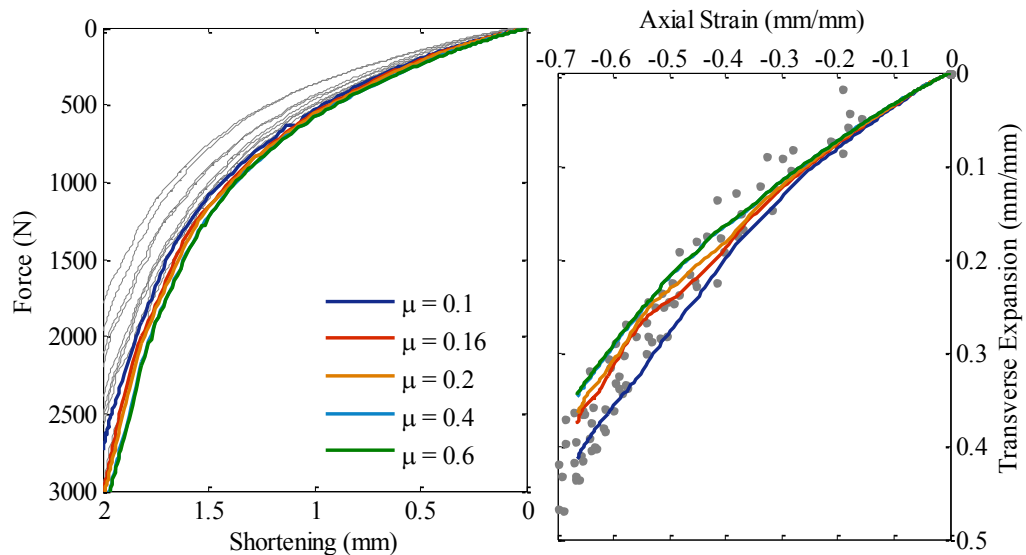


Figure 5.43: Sensitivity of washer compression to friction between washer and platens

Finally a parametric analysis of the washer material properties was performed to establish the true properties unaffected by friction. A first-order Ogden model is defined using three material parameters μ_p , α_p and D_p . For small strains, where a hyperplastic response can appear elastic, the shear modulus (μ) and the bulk modulus (κ) of a hyperelastic material can be approximated by:

$$\mu = \mu_p \quad (5.5)$$

$$\kappa = \frac{2}{D_p} \quad (5.6)$$

ABAQUS automatically calculates the material parameters of any hyperelastic definition when the material is defined using test data. When the experimental washer compression results were used as an idealized uniaxial stress-strain curve with an assumed Poisson’s ratio of 0.475 ABAQUS calculated the corresponding material parameters to be:

$$\mu_p = 3.722 \text{ MPa} \qquad \alpha_p = 0.136 \qquad D_p = 0.0273 \text{ MPa}^{-1}$$

Using these values as an initial estimate, with a friction coefficient of 0.4, each constant was systematically varied to determine the effect on the compressive behaviour of the washer. The material constants required to reproduce the compressive response of the washer as documented experimentally were found through trial and error. The results of the final working model are presented in Figure 5.44 alongside an average of the experimental results to highlight the correlation between the two. The force-shortening relationship predicted by the numerical model with the updated material properties agrees well with the average shortening response of the experimental results. However, the expansion of the washer predicted by the numerical model deviates from the average experimental results for axial compressive strains greater than 0.5. This deviation would reduce if a smaller friction coefficient were used or if the change in friction with respect to compressive load were included. These variables were not considered however as compressive strains greater than 0.5 occur at loads larger than 1000 N which exceeds the relevant limits in both the static and fatigue tests of corrugated cladding.

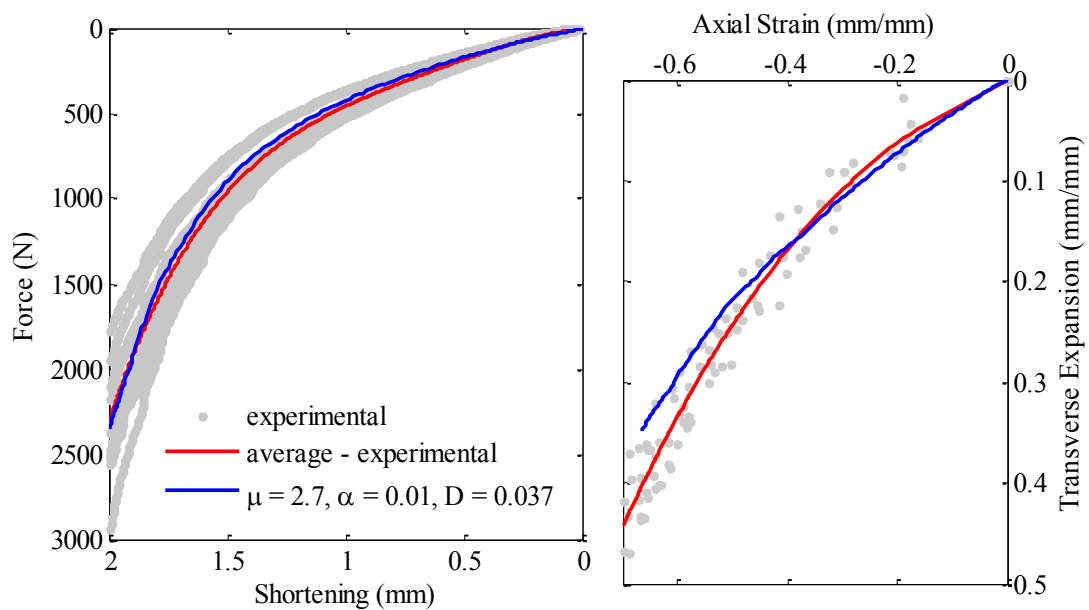


Figure 5.44: Comparison of final working model with experimental data

5.7 MODEL VALIDATION

The model described in Section 5 – “Finite Element Analysis”, and last referred to as the working model, was validated through direct comparison with corresponding experimental data. The variables of interest were the fastener reaction, strain in the underside and topside of the cladding surrounding the fastener hole and deformed shape of the cladding. The deformed shape of the cladding was recorded at three levels of loading during the photogrammetry trials, as presented in Section 3.2 – “Measuring deflection using photogrammetry”. The strain data used for model validation was obtained through five trials of the IFC test. For both the

photogrammetry trials and strain trials the fastener reaction with respect to fastener displacement was recorded.

Validating a numerical model typically involves comparing experimental and numerical variables at discrete and finite locations across the structure. Two commonly used variables are stress/strain and displacement. Given the ultimate goal of this thesis was to develop a numerical model that could predict fatigue crack initiation at the fastener hole, the strain surrounding the fastener hole is crucial. Comparing the strain surrounding the fastener hole at discrete points is therefore an acceptable means of validating the model given the intent focus on the strain in that region. The locations of the strain gauge rosettes in relation to the fastener hole for each trial are shown in Figure 5.45. The primary locations of interest were adjacent to the fastener hole in the transverse and longitudinal direction on both the topside and underside of the cladding. The rosettes placed on the topside of the cladding are located further away from the fastener hole than that of their counterparts on the underside of the cladding as the EPDM seal limited the placement of the rosettes. Figure 5.45 also shows the location at which the strain was extracted from the numerical model. These locations were selected based on the average position of the rosettes from each trial. Ideally the strain at any position can be extracted from the numerical model. However, predetermined locations ensured the integration point or node of an element could be positioned accordingly when discretizing the model.

Figures 5.46 and 5.47 compare the numerical and experimental strain data for the three monitored locations surrounding the fastener hole. Unfortunately the strain gauges were prone to failure and would fail at approximately 2% strain rather than the manufacturer specified limit of 5%. Consequently comparisons between the numerical and experimental strain data are limited to a fastener displacement of 10 mm for the transverse direction and approximately 20 mm for the longitudinal direction. Only three rosettes successfully measured the strain on the cladding surface throughout the entire load history; the longitudinal rosette on both the underside and topside in Trial 4 and the longitudinal rosette on the topside of the cladding in Trial 3.

Figure 5.46 and Figure 5.47 show good agreement between numerical and experimental strain data, particularly at the longitudinal locations. The numerical and experimental data diverges after local plastic collapse as the model predicted a deeper snap through than that observed experimentally (as mentioned previously in Section 5.5 – “Boundary Condition Simulations”). This deeper snap through was attributed to variations in the boundary conditions of the model to that of the IFC test, particularly with respect to the eccentricity of the fastener, eccentricity of the longitudinal clamps and movement of the fastener clamp, all of which varied between each trial. The eccentricity of the fastener and longitudinal clamps was in the transverse direction and consequently affected the sequential buckling of the cladding crest, where by the right crest face collapsed prior to the left crest face. As the discrepancy between the numerical model and the IFC test is mostly attributed to these variables, the model is less accurate predicting the strain at the transverse locations.

During the development of the numerical model, a second more simplified version of the model was created specifically to simulate the cyclic response of the cladding when loaded below local plastic collapse. This model, referred to as the simplified model, involved a more coarse mesh and simplified boundary conditions. Once again the accuracy of the strain field

surrounding the fastener as predicted by the simplified numerical model is crucial. The numerical and experimental strain data for the locations shown in Figure 5.45 were compared directly in Figure 5.48 and 5.49. The simplified model is only applicable to the first 10 mm that the fastener was displaced as the simplified boundary conditions affect the local plastic collapse of the cladding. Figure 5.48 and 5.49 also show the strain data for the working numerical model in addition to the simplified model.

Figure 5.48 and 5.49 show good agreement between numerical and experimental results for all locations, with particularly good agreement at all locations on the underside of the cladding excluding the Left Transverse location. Cracks nucleate on the underside of the cladding shear along the maximum shear plane through the cladding thickness; consequently the model must accurately simulate the surface strains on the underside of the cladding. The poor agreement between numerical and experimental strain data at the Left Transverse location could be attributed to the eccentricity in the fastener and longitudinal clamp. The strain at the longitudinal locations is of greater importance to that of the transverse locations as cracks in the longitudinal direction initiate prior to the cracks in the transverse direction. However, the accuracy of the numerical model for predicting strain in the transverse direction will need to be revisited should the fatigue model progress to crack propagation, rather than focusing on crack initiation.

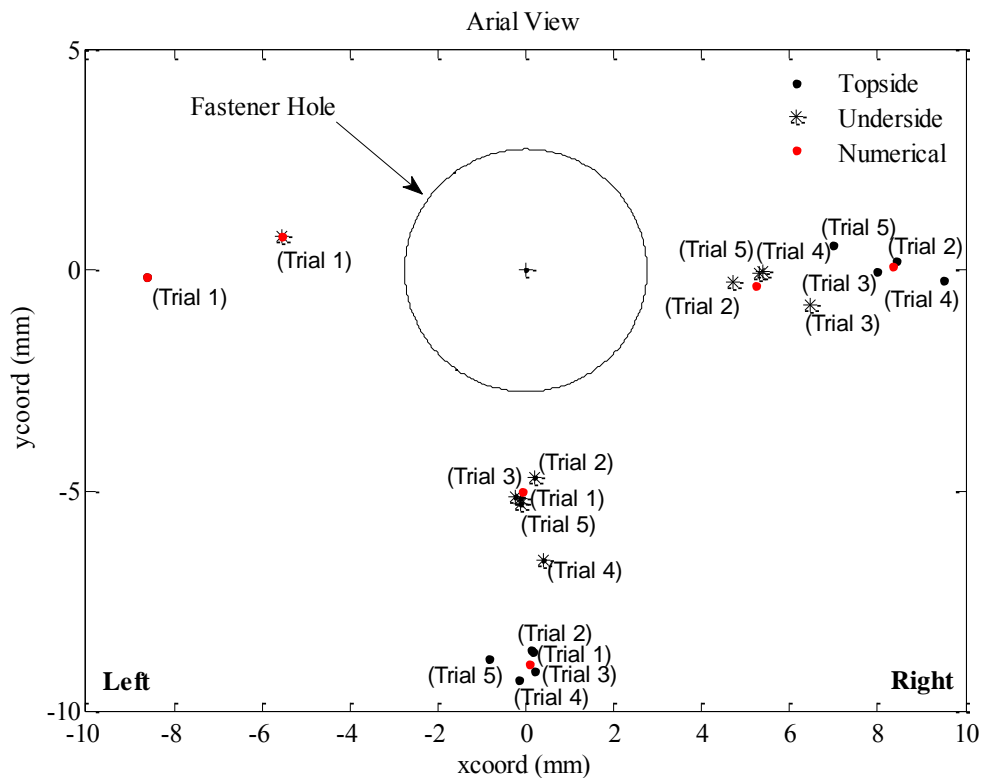


Figure 5.45: Location of strain gauge rosettes

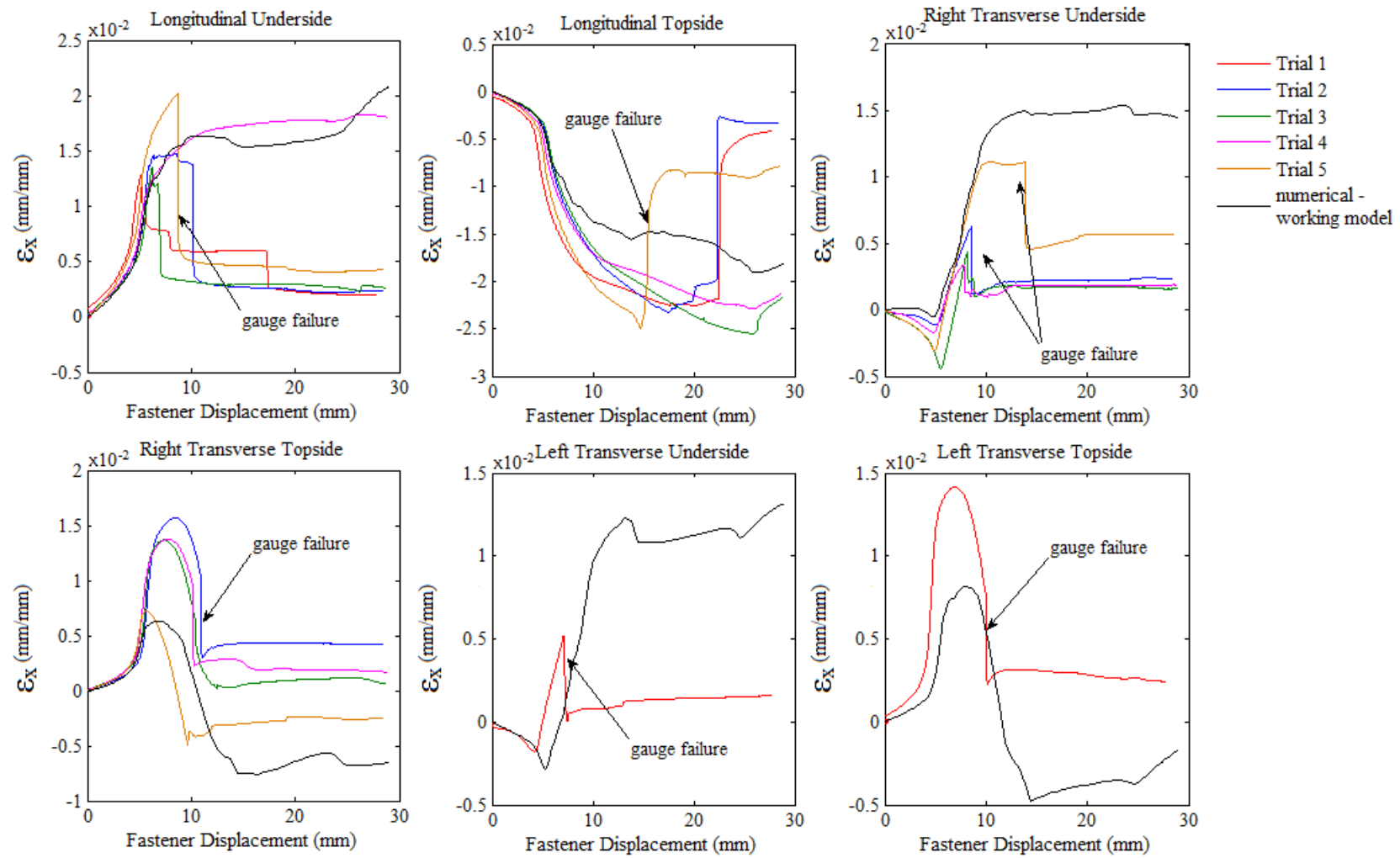


Figure 5.46: Comparison of numerical and experimental transverse strain data

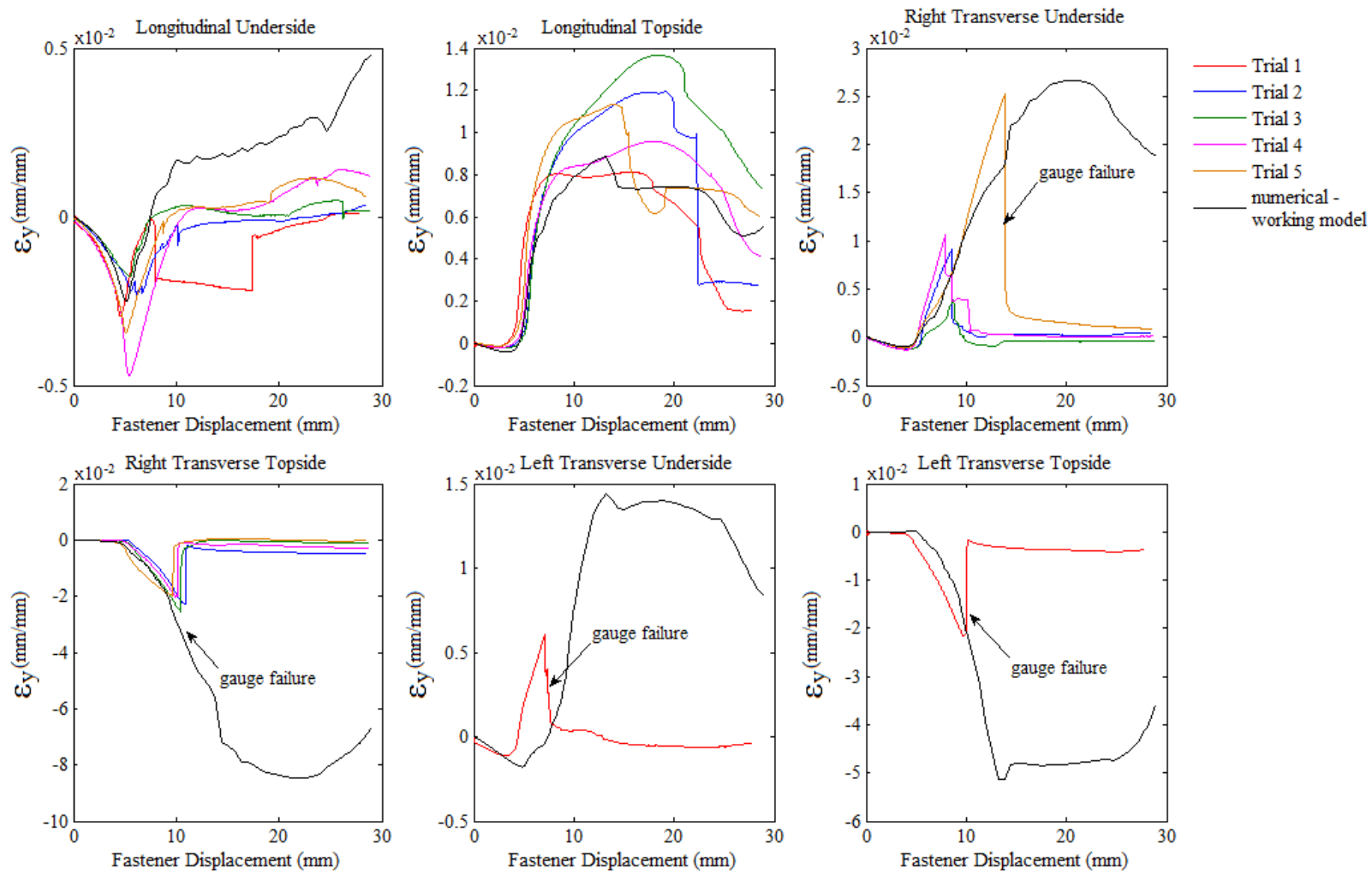


Figure 5.47: Comparison of numerical and experimental longitudinal strain data

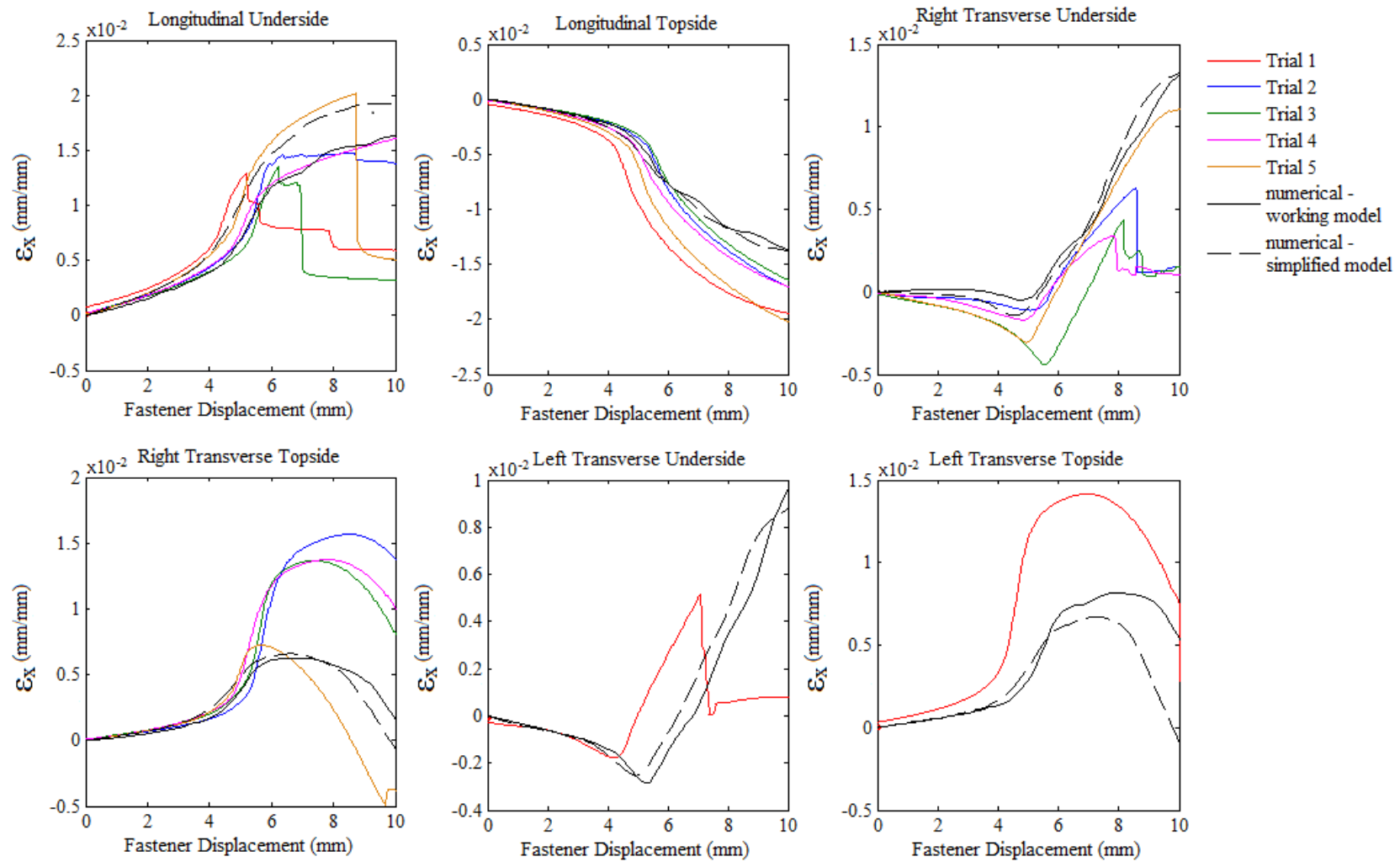


Figure 5.48: Comparison of numerical and experimental transverse strain data for simplified model and working model

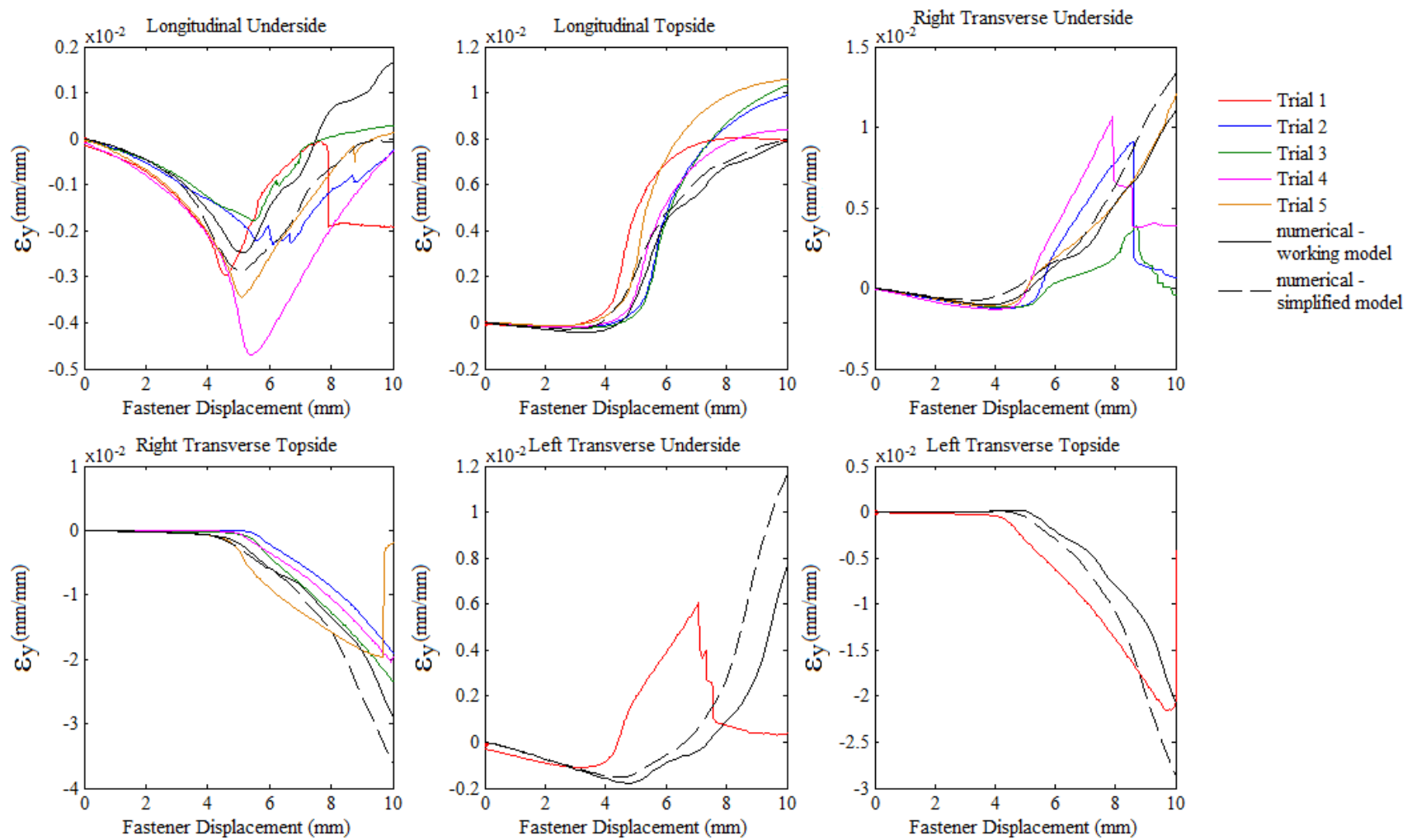


Figure 5.49: Comparison of numerical and experimental longitudinal strain data

Comparing numerical and experimental data at discrete points, although acceptable for this analysis, limits the appreciation of the accuracy of the model. Full field comparisons for model validation are becoming more popular as they provide a measure of the accuracy of the model for both the global and local response. Full-field comparisons, of strain in particular, are becoming more common in validation studies. Spranghers et al (2012; 2013) used digital image correlation – similar to the proprietary system ARAMIS (GOM mbh, 2015) – to measure the deformation and strain of an aluminium plate subject to free air explosions. They created a digital surface model (DSM) of the plate deforming at various stages of loading and captured the distribution of strain across the entire plate. Full-field comparisons of the experimental and numerical strains were made with the residuals described across the whole plate. The DSM of the deformed plate was not compared directly with the deformed mesh of the numerical model; instead Spranghers et al (2013) exploited the predominantly symmetric response of the plate and focused on the deflection along the cross section of the plate in both the transverse and longitudinal directions. Groning et al (2012) also explored the benefits of full-field comparisons for improving validation studies of finite element models. Digital speckle pattern interferometry was used to measure the distribution of strain across the surface of a bone – the mandible – which was then compared with a numerical model. Approximately 500 points were sampled across the relevant area and superimposed on the numerical model by manually matching landmarks. A nearest neighbour algorithm was used to identify the node in the finite element model that was closest to each sample point. The experimental and numerical strains were then compared directly, with the mean difference and standard deviation calculated to succinctly describe the accuracy of the model.

A DSM created using photogrammetry (as described in Section 3.2 – “Measuring deflection using photogrammetry”) can be compared directly with the deformed mesh predicted by a numerical model, providing a full-field comparison that comprehensively quantifies the performance of the numerical model. Generally in numerical model validation studies, the deformed shape observed experimentally is *qualitatively* compared with that predicted numerically followed by a *quantitative* comparison of select point across the model. The deformed mesh predicted by a numerical model is effectively a DSM that can be compared with the experimental DSM using CloudCompare in a similar manner to the comparison that was made to verify the accuracy of the photogrammetric method. CloudCompare can be used to calculate the surface deviation between the experimental and numerical DSMs thereby quantifying the accuracy of the numerical model across the whole model. The nature of the comparison means both the in-plane and out-of-plane deformation of the cladding are considered in the analysis.

In order to directly compare two corresponding DSMs, they must first be aligned and registered to obtain the closest fit. Aligning the models involves simply manually maneuvering the two DSMs until they visually align. The two DSMs are then registered to refine the alignment using the “Interactive Closest Point” algorithm documented by Besl and McKay (1992) which finds the fit corresponding to the lowest mean square error. Once the two DSMs are registered the absolute distance between the two surfaces, referred to as surface deviation, is then calculated using the Cloud-to-Cloud function described in Section 3.2 – “Measuring deflection using photogrammetry”. Figures 5.50 to 5.52 describe the surface deviation between the numerical DSM and the corresponding experimental DSM obtained using photogrammetry for all three photogrammetry trials. The numerical DSM is comprised of both the global model and the

submodel. Figures 5.50 to 5.52 also include a histogram of the surface deviation for every point that comprises that DSM alongside each colour bar.

The contours describing the surface deviation between the two DSMs can also help identify the potential causes of discrepancies in the numerical model. This defining benefit of the full field comparison was utilized during development of the numerical model particularly for identifying the eccentricity within IFC test apparatus. Figure 5.53 describes the surface deviation between experimental and numerical DSMs for an earlier version of the numerical model where the eccentricity of the fastener and longitudinal clamps had not been included. The contours show greater surface deviation to one side of the cladding surface in the transverse direction.

Although the surface deviation between the experimental and numerical DSMs provides some measure of the accuracy of the numerical model, relative error is more digestible. CloudCompare can assign two scalar values to every point, for example, both the surface deviation (as shown in Figures 5.50-5.52) and the deflection at every point is recorded. Using only the vertical (z) component of the surface deviation and the deflection at each point, the relative error across the full area can be calculated. The process of assigning two scalar values to each point in the DSM involves registering and comparing three surfaces simultaneously; the numerical DSM, the deformed experimental DSM and the at-rest experimental DSM. The deformed experimental DSM is the digital reconstruction of the cladding under load and the at-rest experimental DSM is the digital reconstruction of the cladding under no load but installed within the apparatus. The deformed experimental DSM is first compared with the at-rest DSM to establish the deflection followed by a comparison with the numerical DSM to calculate the surface deviation. Approximately 3000 points were then sampled from the deformed experimental DSM and imported to MATLAB to calculate the relative error where the relative error describes the surface deviation as a percentage of the total deflection. Figures 5.54 to 5.56 present the relative error across the DSM in aerial view, with a histogram of the relative error alongside each colour bar. The greatest errors for each of the three intervals of loading occur at the border of the DSM where the deflections are small. The photogrammetric error is greatest at the border given fewer overlapping photos are available for its reconstruction. This photogrammetric error is then compounded by the small deflection in those regions resulting in large relative errors. Under a maximum applied load of approximately 700 N to 800 N, the numerical model has a mean error ranging from 10.8% to 11.5% when predicting the deflection of the cladding.

Comparing the deformed shape observed experimentally with that predicted by a numerical model is an effective means of validating that numerical model. Rather than comparing the displacement and strain at a few limited number of points, the experimental and numerical DSMs were compared to simultaneously measure the accuracy of both the global and local response predicted by the numerical model. Based on the comparisons between numerical and experimental data, specifically for the fastener reaction, strain and deformation, the numerical model developed in this investigation appears to effectively simulate the response of cladding under monotonic load.

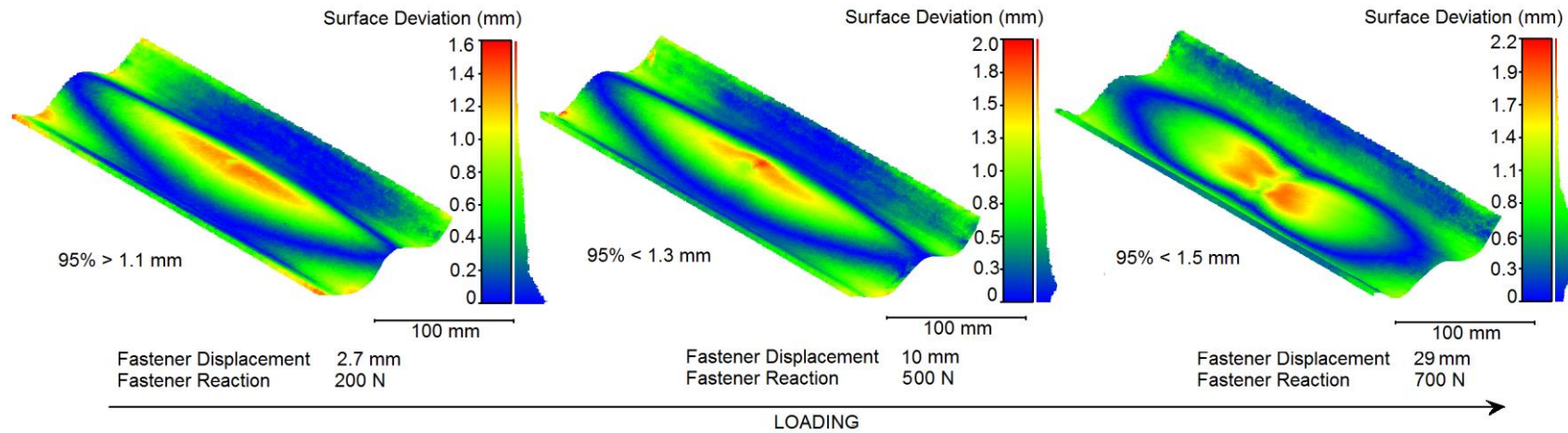


Figure 5.50: Surface deviation (or absolute distance) between numerical and experimental DSMs for Photogrammetry Trial 1

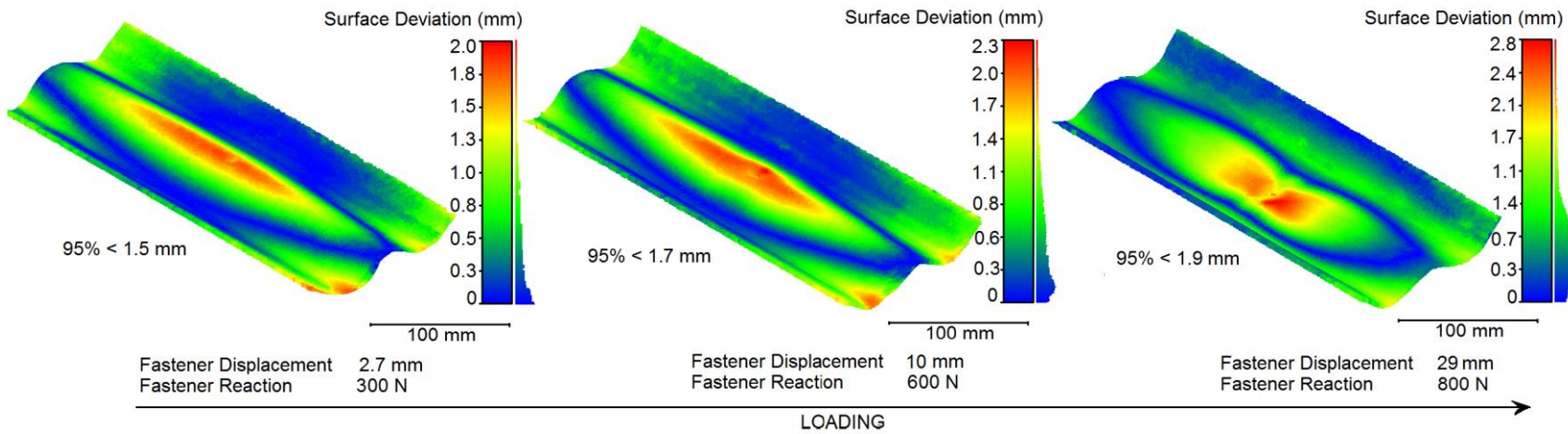


Figure 5.51: Surface deviation (or absolute distance) between numerical and experimental DSMs for Photogrammetry Trial 2

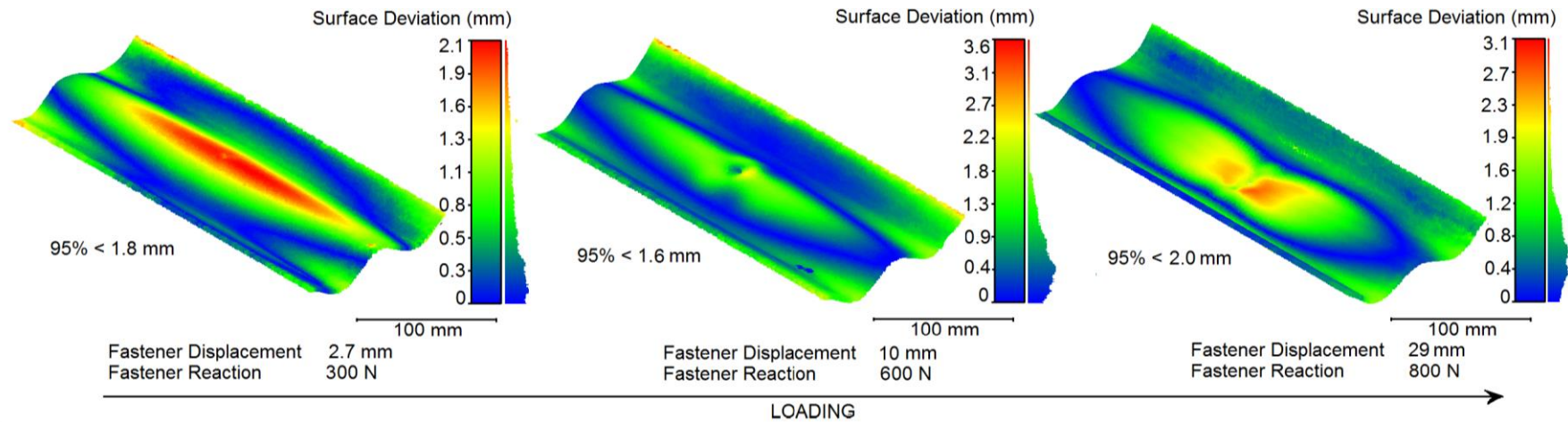


Figure 5.52: Surface deviation (or absolute distance) between numerical and experimental DSMs for Photogrammetry Trial 3

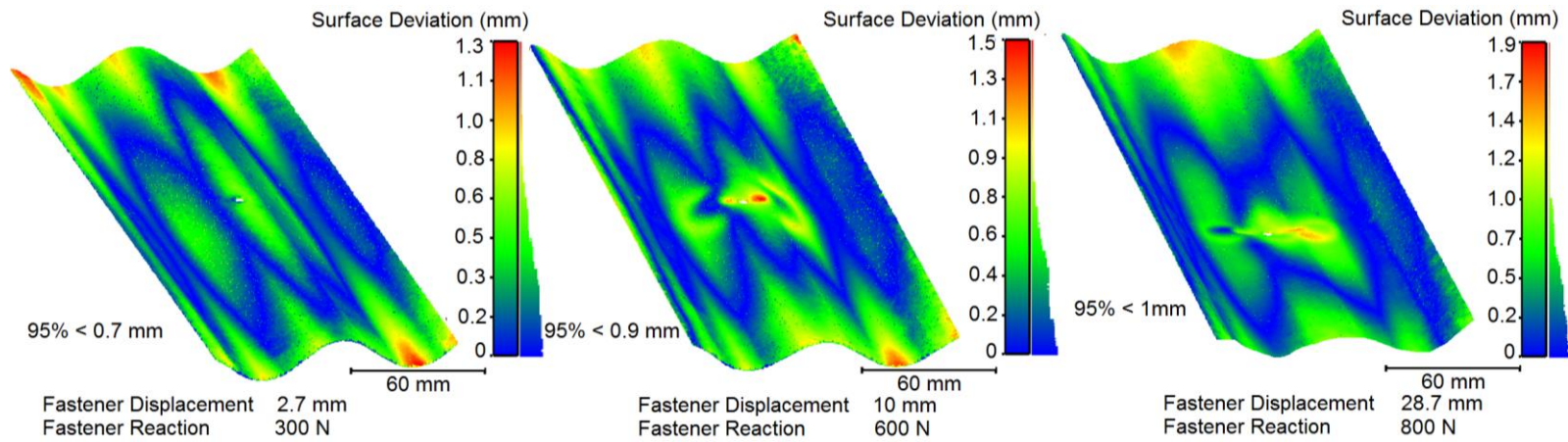
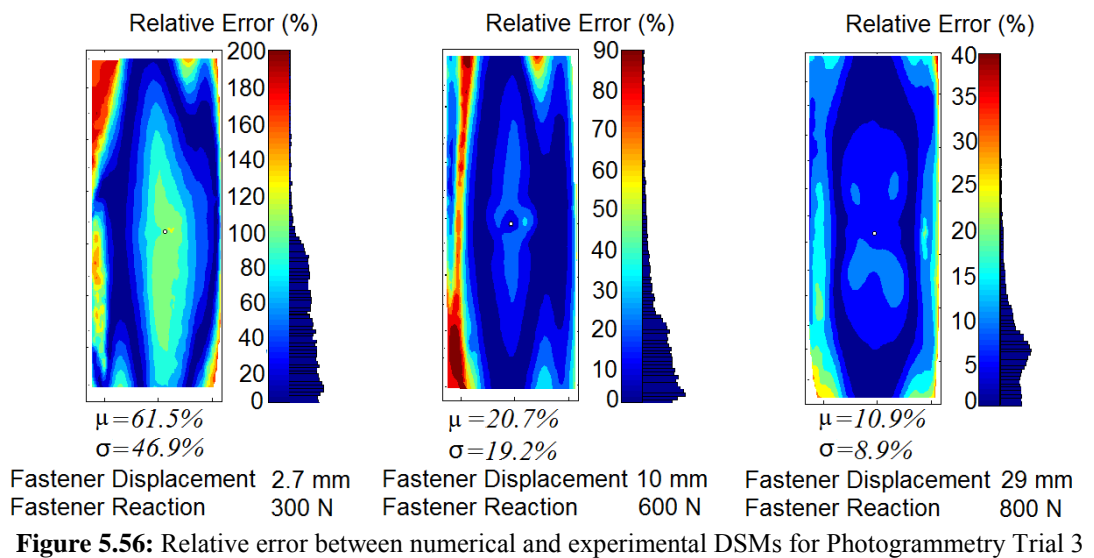
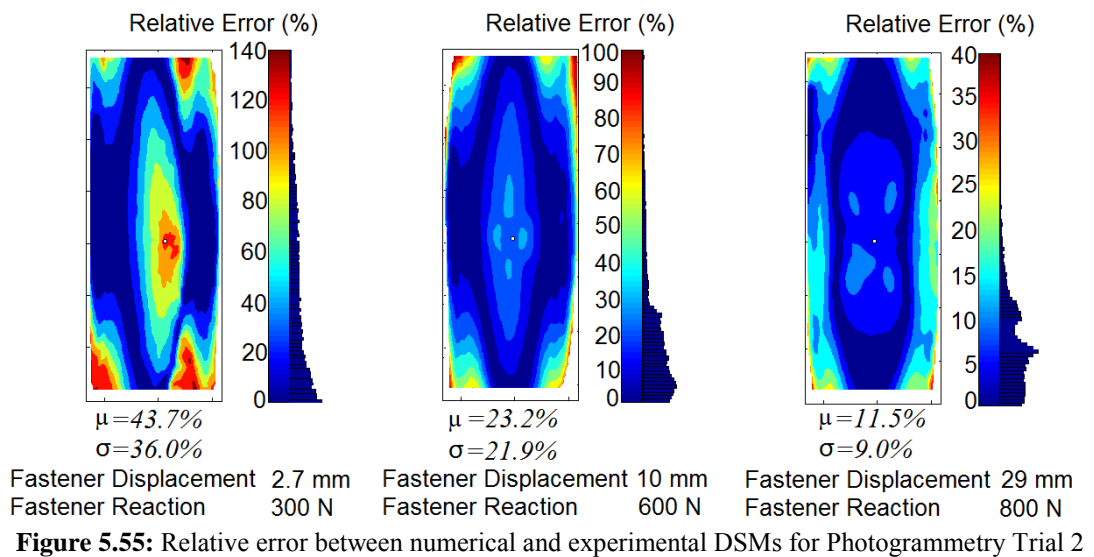
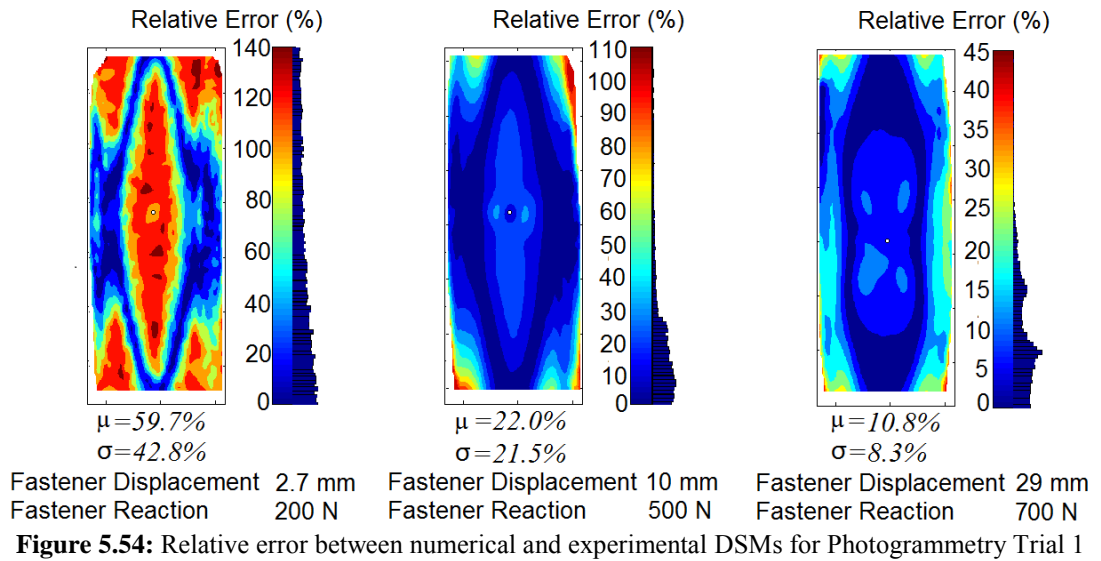


Figure 5.53: Surface deviation (or absolute distance) between numerical and experimental DSMs for earlier version of numerical model



5.8 FATIGUE MODEL

The secondary aim of this study was to ideally develop a numerical model that could simulate fatigue crack initiation in corrugated cladding. During development of a numerical model that could simulate the response of the cladding under monotonic load, a simplified version of the model was created specifically for simulating the response of the cladding subject to cyclic loading. This simplified model featured a more coarse mesh and a series of springs and sliding slot connections as the boundary conditions. The simplified model was necessary to reduce the run time of the simulation as a typical cyclic test that produces a ‘star’ type crack can require more than 2000 cycles to initiate a fatigue crack. However, even with the necessary simplifications of the model geometry and mesh, the simulation run time was still too great to effectively simulate the fatigue response of the corrugated cladding in an IFC test. The rate at which the load is applied can be accelerated numerically to reduce the resulting simulation run time, unfortunately any increase in the rate of applied load introduces stiffening of the structure due to inertia and potentially increases the localized deformation experienced by the cladding where it contacts the EPDM seal.

ABAQUS does contain a number of procedures to simulate low cycle fatigue in order to reduce the simulation run time of such a model. In particular, ABAQUS has a “Low Cycle Fatigue” regime which is based on the direct cyclic approach. The direct cyclic approach determines the stabilized response of a structure by extrapolating the nonlinear material behavior of a structure using a combination of Fourier series and time integration. The low cycle fatigue regime incorporates damage using a damage initiation criterion which is based on accumulated inelastic hysteresis energy per cycle. Damage evolution is then based on Paris’ Law and the stabilized response of the structure (Dassault Systemes, 2013). It is unlikely however that the cladding in the vicinity of the fastener would ever stabilize given the significant cyclic softening of the material and the changing contact conditions with the EPDM seal due to deformation of the cladding. Furthermore this procedure assumes the geometric response of the structure is linear. Even at low loads the response of the curved crest of the cladding being deformed by a hyperelastic material is nonlinear. Consequently the low cycle fatigue regime available in ABAQUS is not applicable to this investigation.

Further development of a numerical model capable of simulating the fatigue response of roof cladding was also halted given the kinematic material properties of the cladding material remain unknown. Attempts were made to obtain the kinematic material properties of the cladding steel as documented in Section 4.1 – “Cyclic Material Properties” with preliminary trials suggesting the cladding is prone to significant cyclic softening. This conclusion was further verified in Section 4.3 – “General Observations” where the strain histories described a continually increasing mean strain, which is, ratcheting of the cladding. The significant cyclic softening of the cladding material, and the observed effect on the strain history of the cladding, suggests that the kinematic material properties are a crucial component of a numerical fatigue model. Should the hardware available for running a fatigue simulation become available and the bend test recommended in Section 4.1 – “Cyclic Material Properties” be implemented to find the kinematic material properties of the cladding sheet, the simplified model presented in this investigation could be evolved to a fatigue model.

6. CONCLUSION AND RECOMMENDATIONS

6.1 CONCLUSION

During severe wind storms such as cyclones, cracks can initiate within the cladding in the vicinity of its fixings. These cracks can propagate to sizeable holes that lead to failure of the connection which results in windblown rain penetrating the building. Current design methods for cladding fatigue failure are entirely based on repetitive and costly prototype testing. This reliance on prototype testing could be reduced through use of a numerical model that is capable of simulating cladding fatigue. A numerical model that employs fracture mechanics to simulate crack initiation and propagation could replace some aspects of the prototype test or enable development of a semi-empirical design approach.

This investigation in particular aimed to identify and characterise fatigue crack initiation in corrugated cladding, ideally leading to the development of a numerical model capable of simulating the phenomenon. Characterising fatigue crack initiation in corrugated cladding required extensive experimental studies including development and validation of an appropriate testing method. The testing method developed in this investigation is known as an Isolated Fastener Connection (IFC) test since it includes only a single cladding-fastener connection. Isolating a single connection reduced the variability in the fatigue response of the cladding and reduced the area of interest to a single localized point. The IFC test successfully reproduced the response of the cladding observed in airbox studies when subject to both monotonic and constant amplitude loading. In particular, the IFC test successfully reproduced all three crack formations common to corrugated cladding with the cracks initiating at a similar number of cycles to that observed in airbox studies.

The IFC test was used to study the response of the cladding to both monotonic and cyclic loads. Under monotonic loads the cladding demonstrated three distinct stages of response, a linear deformation stage, local plastic deformation stage and a final geometric stiffening stage. At each stage of response, the deformation of the cladding sample was recorded using an inexpensive photogrammetric method. This photogrammetric method reproduced the deformed shape of the cladding as a 3D digital reconstruction with an accuracy of ± 0.1 mm. The displacement of the cladding was then inferred from the digital reconstructions by comparing the deformed surface under load with that of the cladding subject to no load.

Crack initiation within the cladding subject to constant amplitude cyclic loading was also studied in great detail. Digital microscopes and strain gauges were used to monitor the highly localised region where cracks initiate to form a 'star' type crack. The cladding was subjected to three different load amplitudes all of which had a minimum load of 0 N through the fastener and peak loads of 400 N, 450 N and 500 N. Cracks were seen to initiate on the underside of the cladding sheet and slowly propagated through the cladding thickness along the plane of maximum shear. Once the thickness has been entirely bisected, the cracks would then propagate into the plane of the cladding. Once the longitudinal crack had reached a critical length of 0.9 mm it had entirely bisected the thickness and begun to propagate into the plane of the cladding. The transverse crack had a critical length of 0.5 mm once it had bisected the thickness of the cladding. Based on these critical lengths the strain field surrounding the crack

tip was monitored at crack initiation to discern a pattern. For the longitudinal and transverse cracks respectively, cracks initiated when the principal strains achieved the following criterion:

$$\text{Longitudinal crack initiation criterion:} \quad \varepsilon_1 = 6.7\varepsilon_2 + 0.034$$

$$\text{Transverse crack initiation criterion:} \quad \varepsilon_1 = 0.75\varepsilon_2 + 0.0077$$

Attempts were also made to quantify the kinematic material properties of the cladding steel using a tension-compression cyclic test. A custom anti-buckling fixture was created to increase the buckling capacity of the small steel coupons being tested. The anti-buckling fixture featured two 6 mm thick steel plates that would compress the cladding coupon between them using six bolts. The steel plates had a void in the centre to accommodate a strain gauge and a gap at the top and bottom to ensure the vice grips of the material testing machine did not contact the steel plates. This anti-buckling fixture increased the buckling capacity of the coupon by a factor of 35. However, the steel very quickly softened under reversed loading and would buckle after few cycles regardless of the anti-buckling fixture. Preliminary results indicate that the steel is prone to significant cyclic softening and as a result demonstrates severe mean stress relaxation under constant strain amplitudes and severe ratcheting under constant stress amplitudes. The severity of the cyclic softening means an accurate description of the kinematic material properties are required to create a numerical model capable of simulating the fatigue response of the cladding. As the dynamic material properties of the cladding were not found in this investigation, future investigations should use a complex form of a bend test to establish the dynamic material properties of the cladding.

In parallel to the experimental studies, a numerical model was also developed using the finite element analysis program ABAQUS. The numerical model developed in this investigation recreated the IFC test for the cladding subject to monotonic loads. The model discretised the cladding surface using four-node, reduced integration, quadrilateral shell elements and included the EPDM seal as a series of eight node, reduced integration, brick elements. The material properties of the cladding sheet were taken to be anisotropic elastic-perfectly plastic where the Young's moduli and yield strengths were obtained through coupon testing of the steel. The EPDM seal used a hyperelastic material definition where the parameters used to describe the hyperelastic material were obtained through an exhaustive compression study. EPDM seals were compressed and the shortening and expansion of the washer measured. A numerical model of the washer being compressed was then created and the material parameters iteratively modified until the simulation aligned with the experimental results.

Development of the numerical model also involved a detailed analysis of the apparatus in order to reproduce the boundary conditions within the model accurately. A load cell was used to monitor the compressive force being applied to each bolt that secured the lid of the apparatus to the base within the IFC test. The apparatus lid itself was then modelled using finite element analysis to determine the equivalent stiffness of both the transverse and longitudinal clamps restraining the edges of the cladding sample. Within the numerical model the apparatus lid was then simplified as combination of elastic springs and rigid surfaces clamping the edge of the cladding. The stiffness of the springs at the boundary was determined during the analysis of the apparatus lid. A similar analysis of the fastener was also undertaken to similarly simplify the fastener as a combined rigid surface and elastic spring.

The fastener reaction, strain surrounding the fastener and deformation of the cladding sheet under monotonic load as predicted by the numerical model closely aligned with that documented experimentally. The numerical model successfully captured the sequential collapse of the central crest which was first observed experimentally. The digital reconstructions of the cladding surface produced using the photogrammetric method were used in a full field comparison with the deformed mesh of the numerical model. This comparison showed that under a peak fastener reaction of 800 N, the numerical model predicted the deformation of the cladding to within 89% of that measured using photogrammetry.

The numerical model of the IFC test was simplified to accommodate the longer loading history associated with constant amplitude loading. The original boundary conditions that involved rigid surfaces and springs clamping the edge of the cladding sample were removed and replaced by elastic springs at the transverse edge with the nodes along the longitudinal edge being fully restrained. The spring in the fastener assembly was also removed, leaving the rigid surface of the screw head and shaft. These simplifications of the boundary conditions successfully reduced the computational cost of the simulation although the required run time remained unpractical. Advancement of the fatigue model was further hindered as the kinematic material properties of the cladding remain unknown. Consequently a numerical model capable of simulating crack initiation was not developed in this investigation.

However, the numerical models produced in this investigation, both the detailed and simplified versions, in combination with the strain based crack initiation criterion do provide a strong foundation for the development of a future fatigue model. Creating a working fatigue model is likely to be an iterative process combining both experimental and numerical analysis.

6.2 RECOMMENDATIONS

In order to create a numerical fatigue model and address the limitations of this investigation, the following suggestions are included to direct the next stage of investigation:

- First and foremost, use the bending test documented by Zao and Lee (2004) to determine the kinematic material properties of the cladding steel. Employ these material properties in the simplified numerical model using the combined kinematic and isotropic hardening law.
- Use the updated numerical model to simulate the response of the cladding under constant amplitude loading. To further reduce the run times of the simulation consider using greater parallel computing power. Investigate the strain profile through the thickness of the cladding sheet at the transverse and longitudinal hole edge to verify the stages of crack initiation described in Section 4.2.3 – “Defining crack initiation”. Validate the numerical model by comparing the strain field at the crack tip with the crack initiation criterion developed in this investigation.
- Modify the span of the cladding sample in the IFC test by adjusting the HDPE block. Investigate the effect of flexural strain on crack initiation, particularly at the transverse hole edge.
- Using the validated model, investigate the correlation between strain at the crack tip with the strain at the hole edge for both the transverse and longitudinal direction.

Adjust the crack initiation criterion to accommodate the strain at the hole edge rather than the crack tip.

- Implement the adjusted crack initiation criterion in the updated numerical model to simulate crack initiation numerically.
- Trial simulating an 'H' type crack using the updated numerical model and crack initiation criterion.

Additional investigations may include studying the effects of differing material properties by taking samples from a variety of coils, testing differing cladding profiles, testing differing fasteners and implementing the crack initiation criterion in a simulation of an airbox test.

6.3 SUMMARY

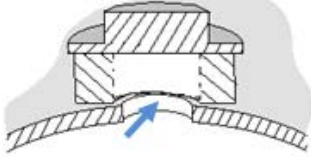

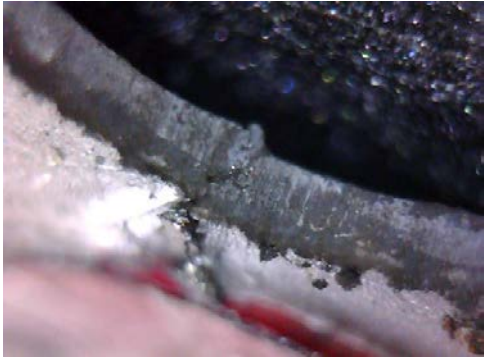
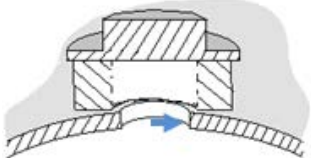

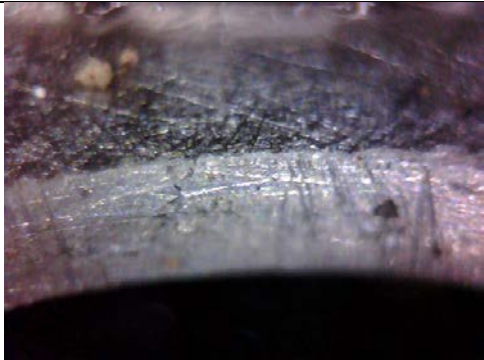
This investigation successfully characterised the localized mechanism of fatigue crack initiation in corrugated cladding by identifying how cracks initiate within corrugated cladding under cyclic loads, defining what crack initiation is and quantifying the strain field required to produce a crack. A numerical model capable of simulating the response of the cladding subject to monotonic loads was also developed with steps taken to prepare a corresponding fatigue model. Both the numerical model produced in this investigation and the crack initiation criterion provides a foundation for the development of a fatigue model capable of simulating crack initiation. Such a numerical model would be the first of its kind, providing a much needed analytical tool that would greatly assist the cladding fatigue design process. Currently, industry is totally reliant on prototype testing for the fatigue design of profiled steel roof cladding; an expensive and time consuming process. An analytical tool, such as a numerical fatigue model, could significantly speed the testing process and reduce our total reliance on prototype testing leading to lower costs and improved safety.

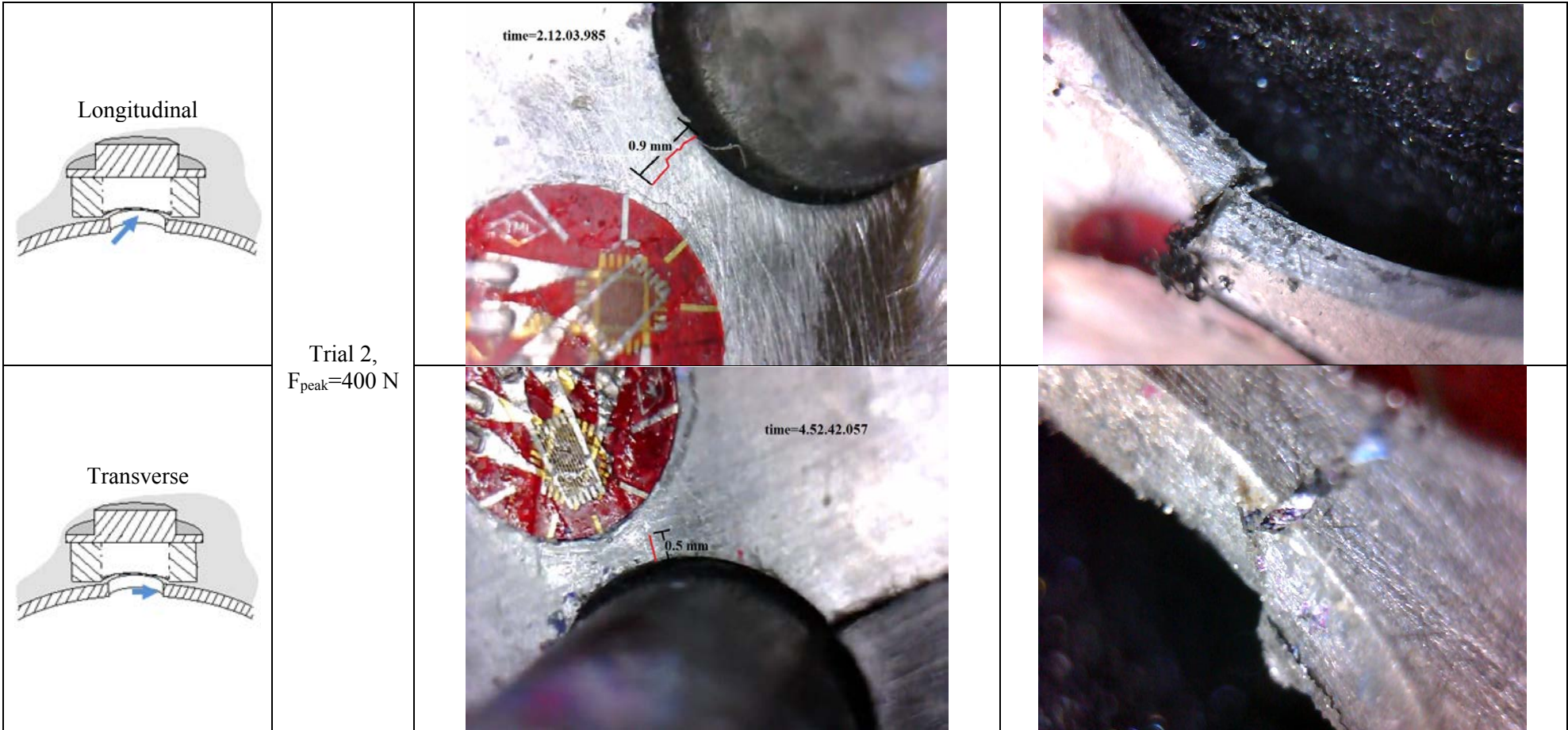
APPENDIX A

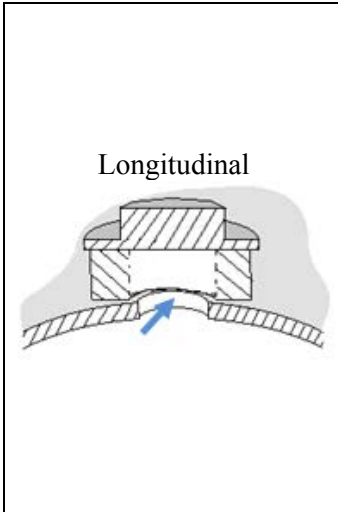
CRACK ORIENTATION FOR CONSTANT AMPLITUDE LOADING

Table A1 provides a fractographical analysis of the cracks observed during constant amplitude loading of the corrugated cladding.

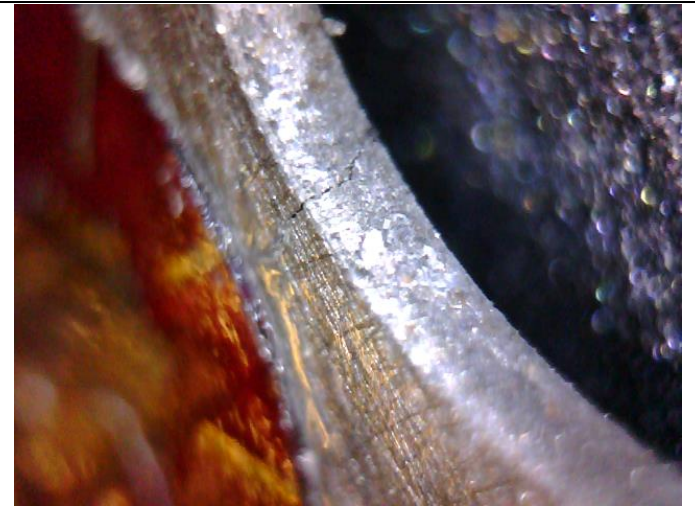
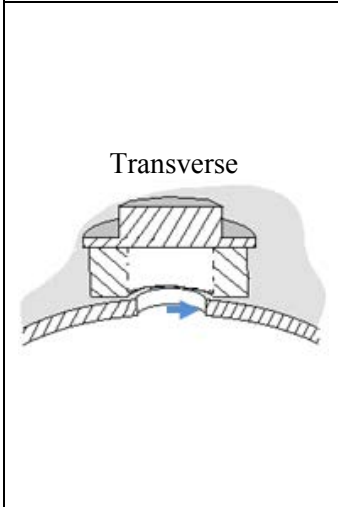
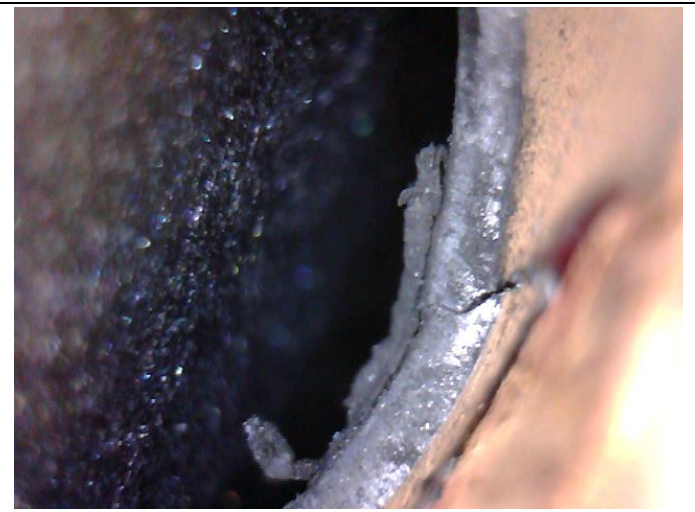
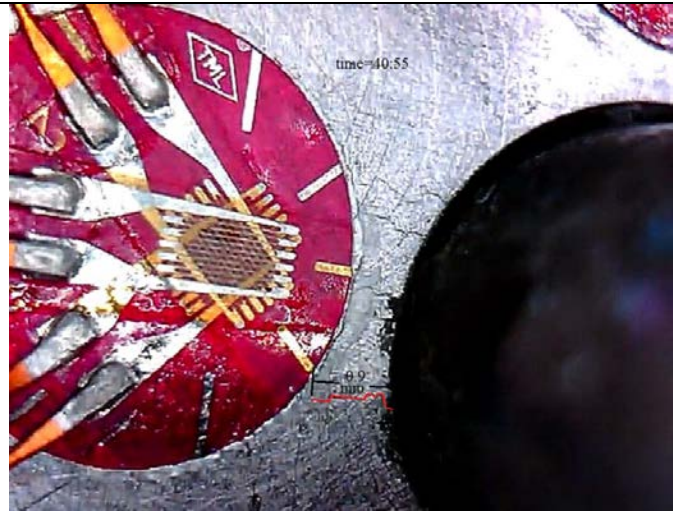
Table A1: Fractographical analysis of ‘star’ type crack initiation

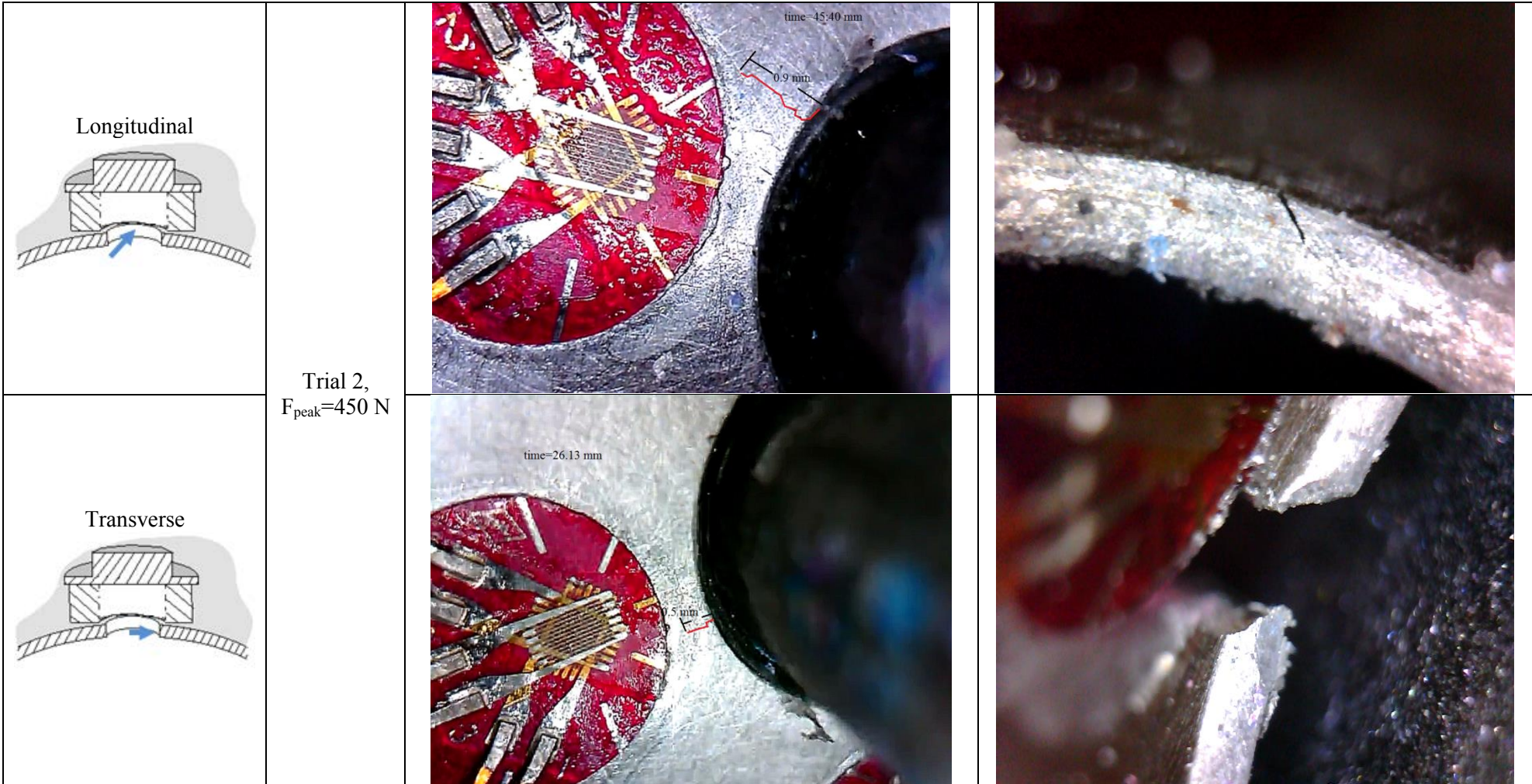
Cycle Trial	View from digital microscope	View of crack orientation
<p>Longitudinal</p> 		
<p>Transverse</p> 		

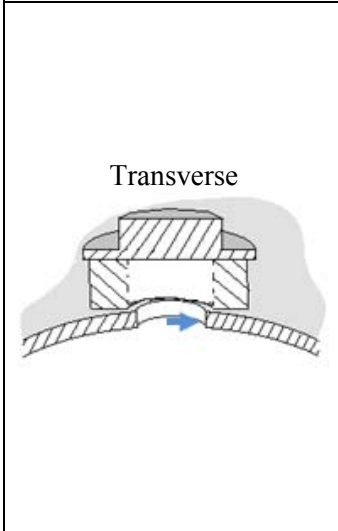
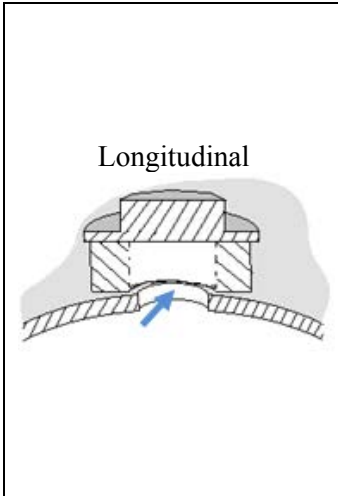




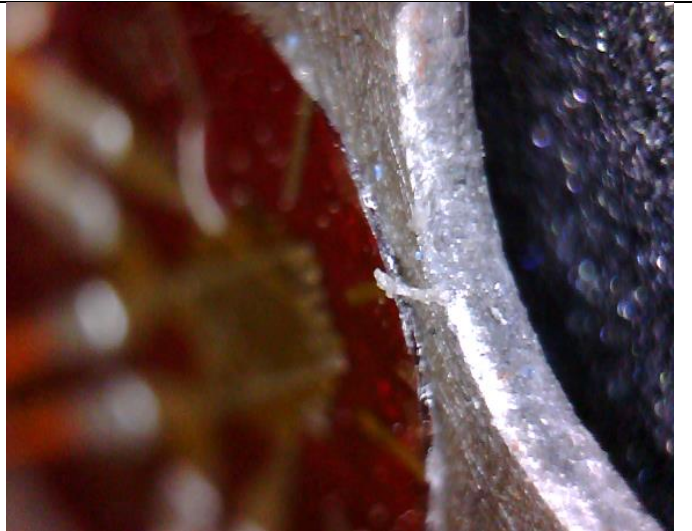
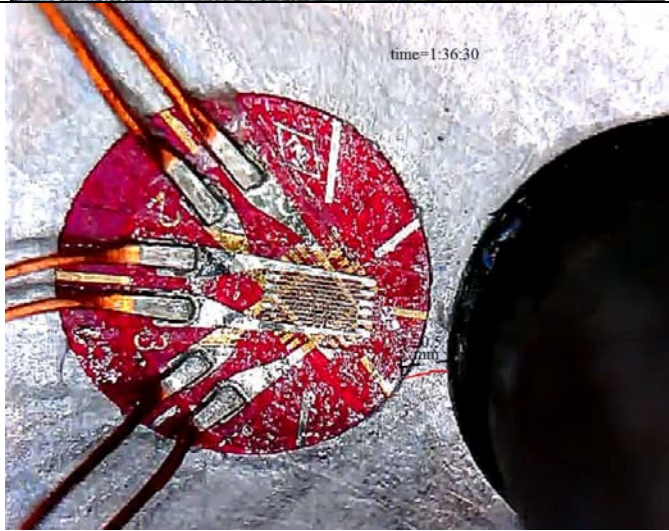
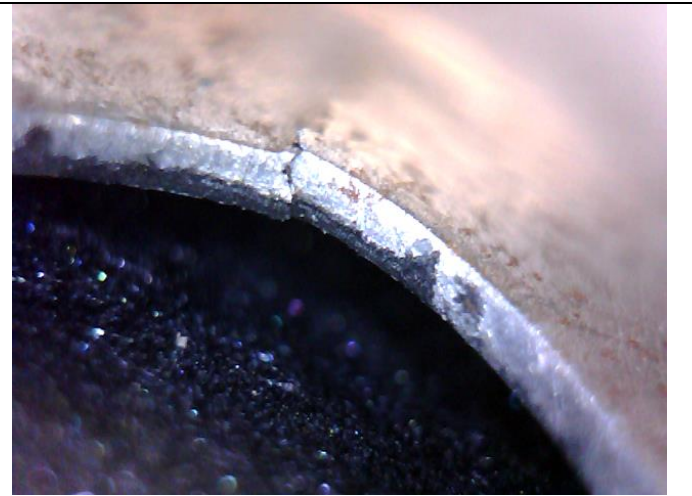
Trial 1,
 $F_{\text{peak}}=450 \text{ N}$

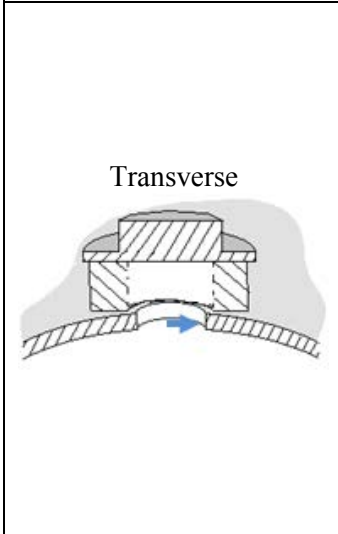
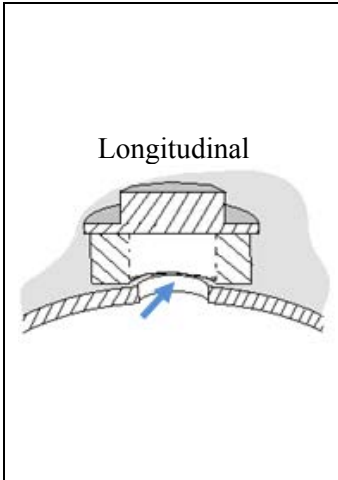




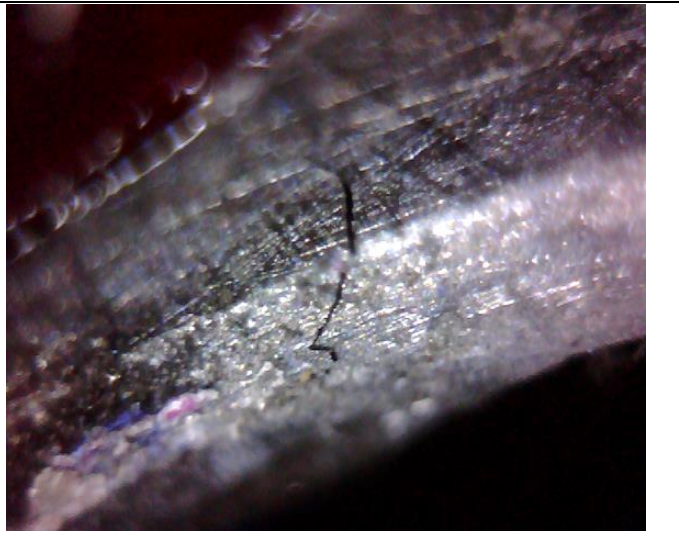
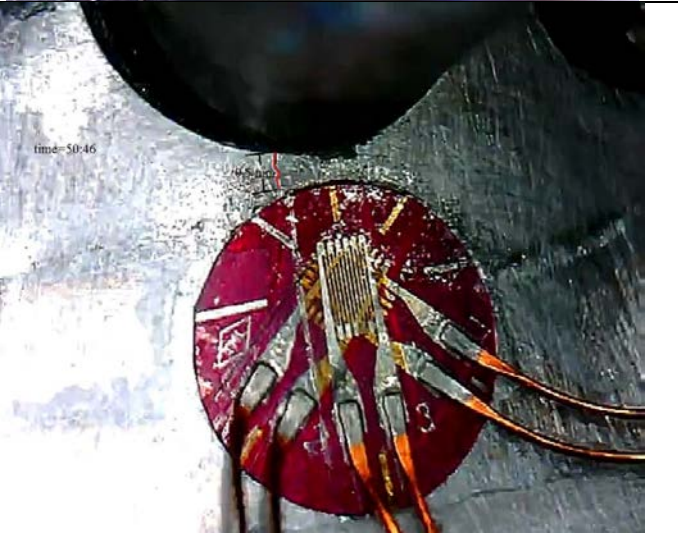
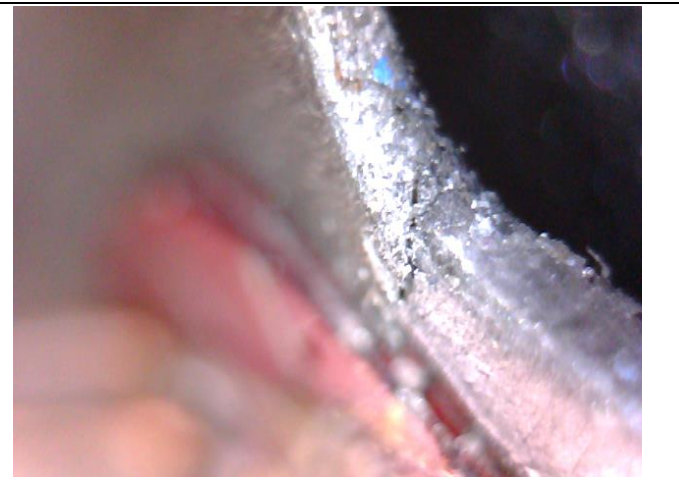
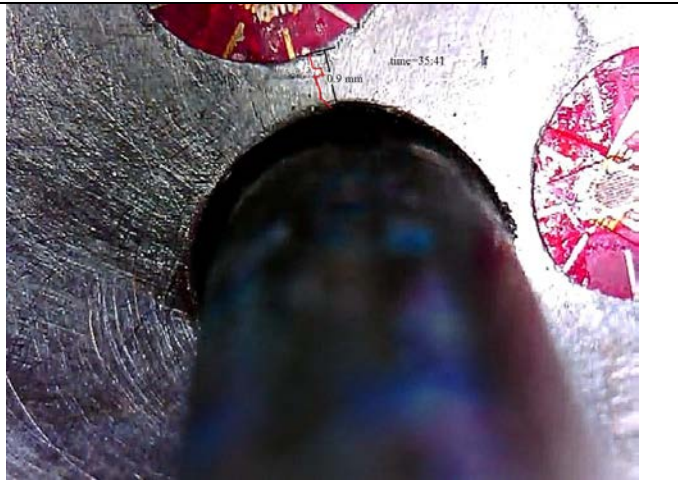


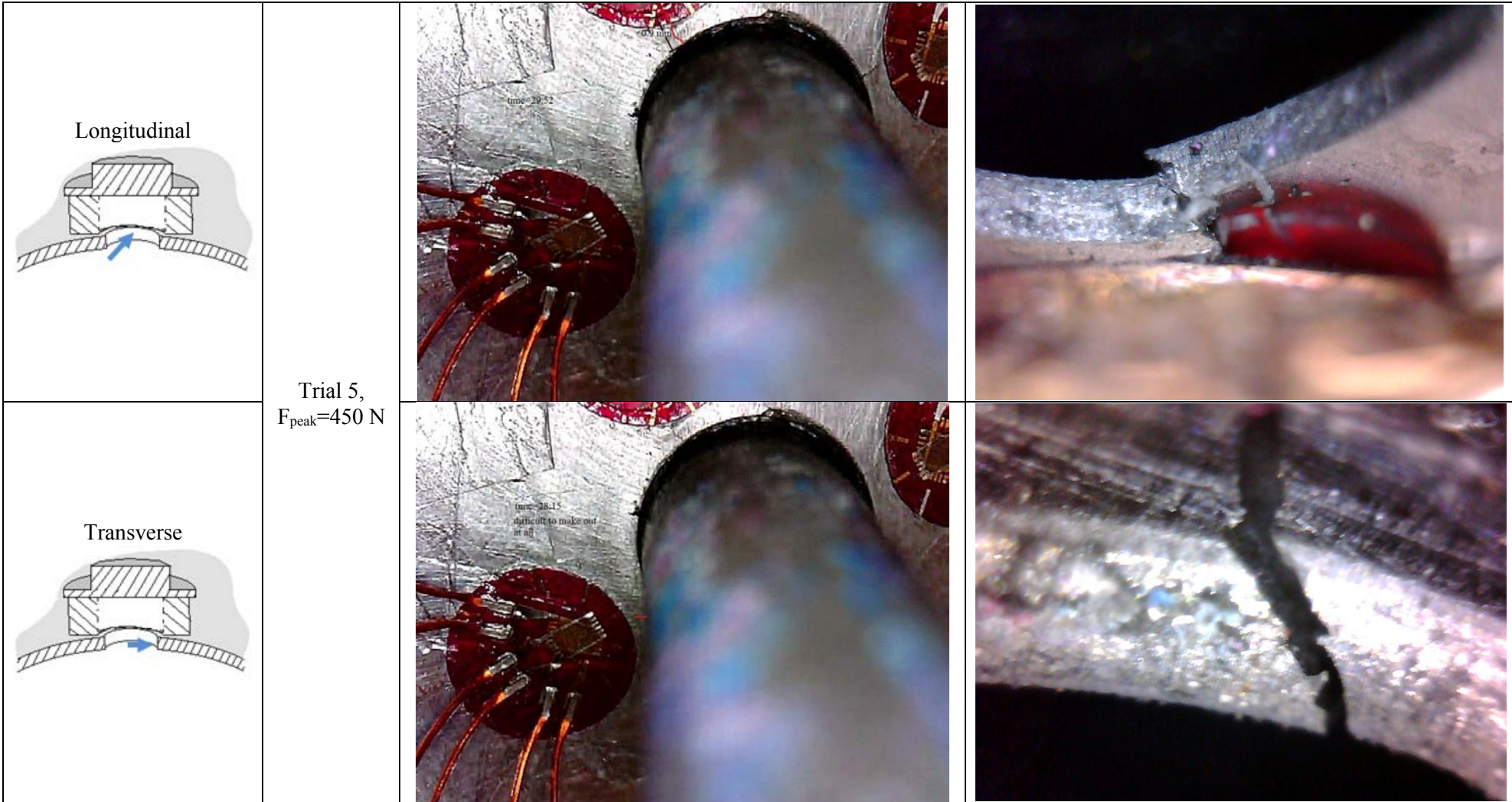
Trial 3,
 $F_{\text{peak}}=450 \text{ N}$

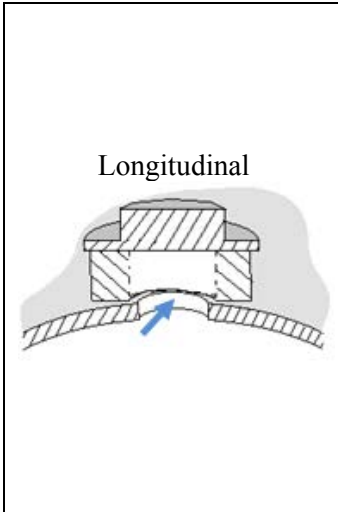




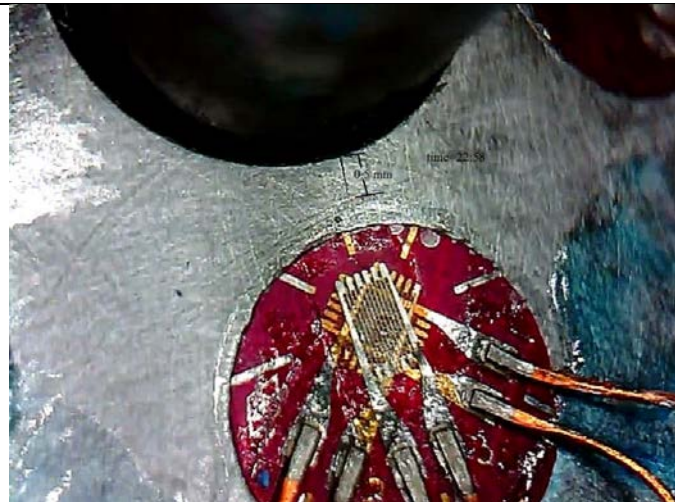
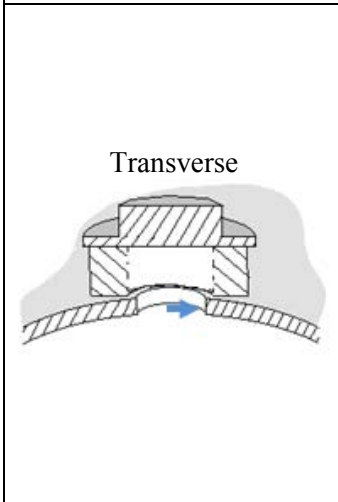
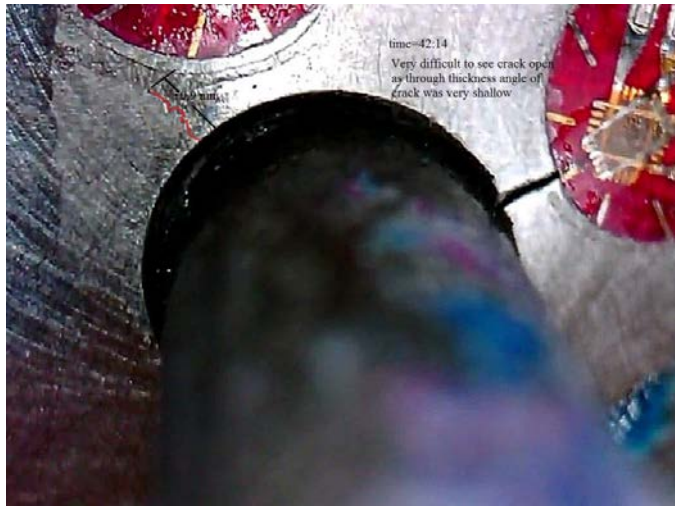
Trial 4,
 $F_{peak}=450\text{ N}$

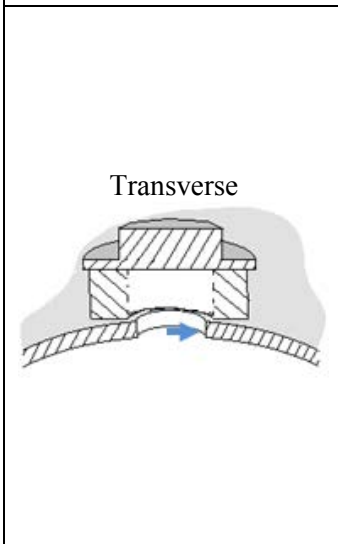
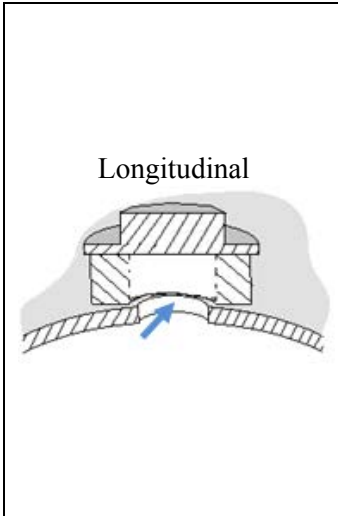




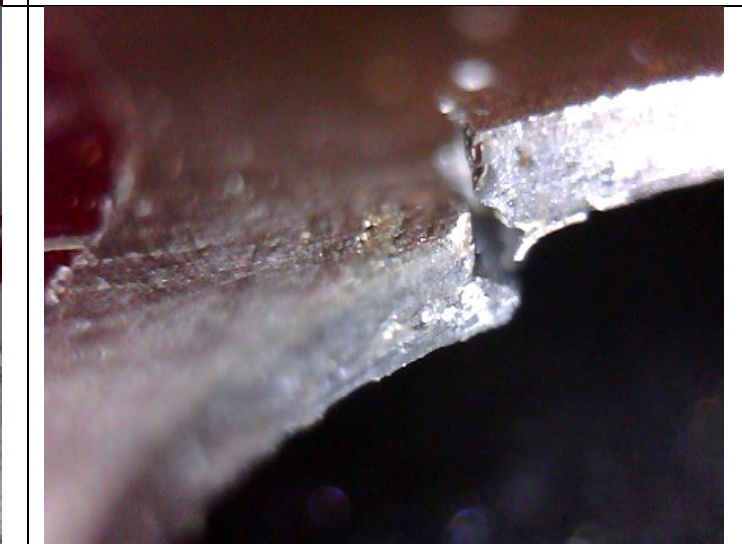


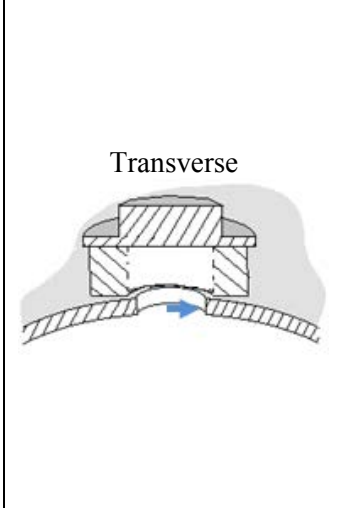
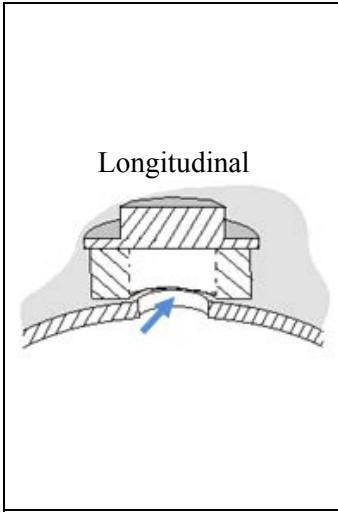
Trial 1,
 $F_{\text{peak}}=500 \text{ N}$



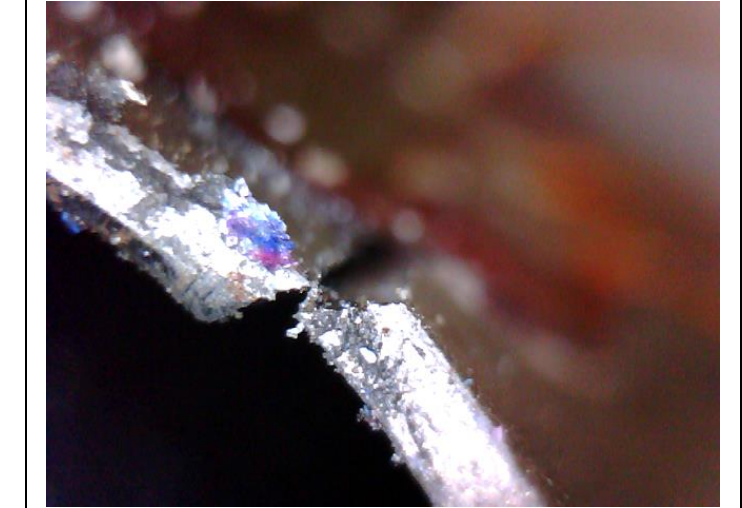
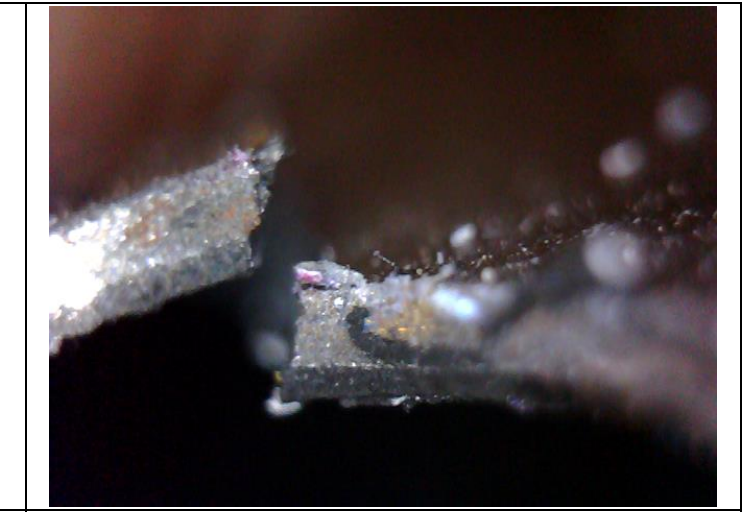
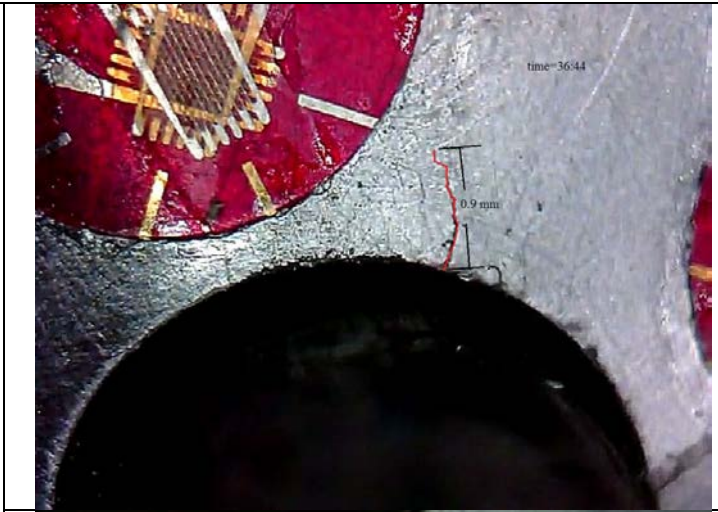


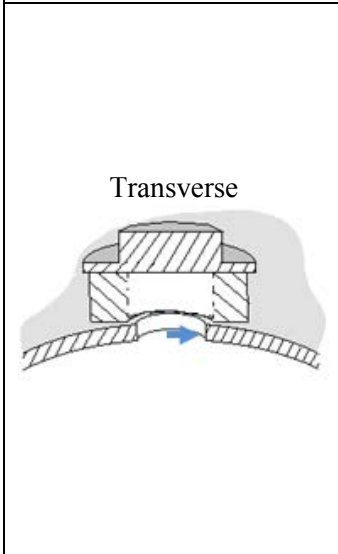
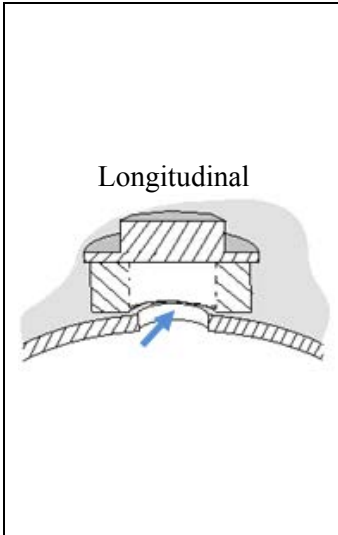
Trial 2
 $F_{peak}=500N$



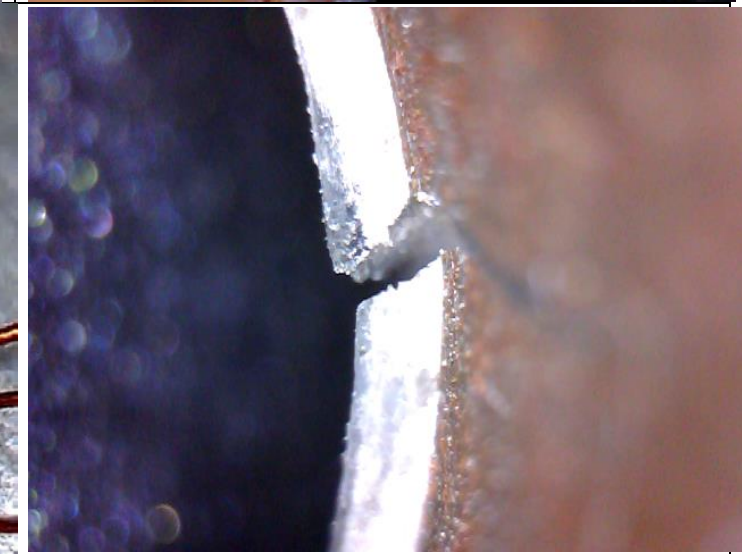
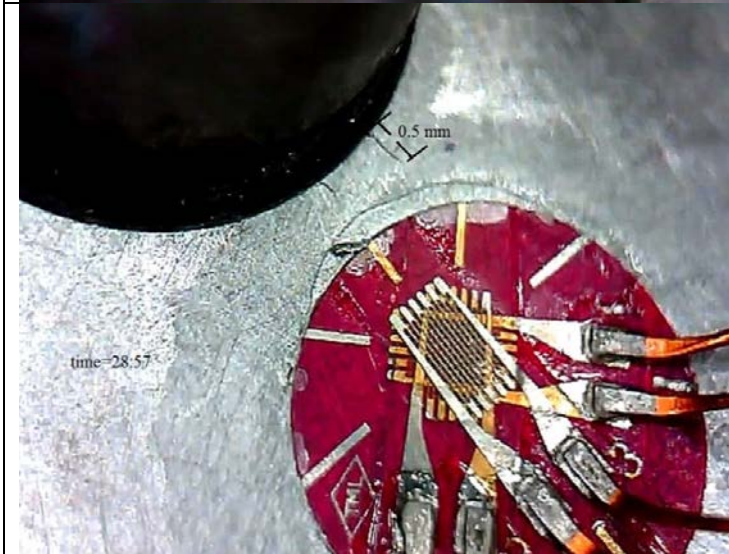


Trial 3,
 $F_{\text{peak}}=500 \text{ N}$





Trial 4,
 $F_{\text{peak}}=500 \text{ N}$



APPENDIX B

MODEL REVISION INDEX

Table B1 details the various versions of the model that were used to obtain the data presented in Section 5 – Finite Element Simulations in the pursuit of a final working version of the model. The table refers to different configurations for transverse and longitudinal boundary which are illustrated in Table B2.

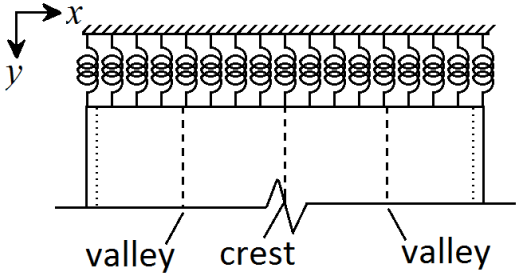
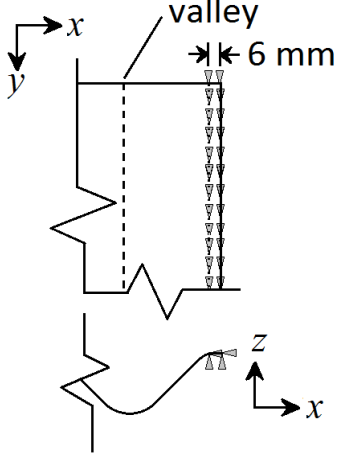
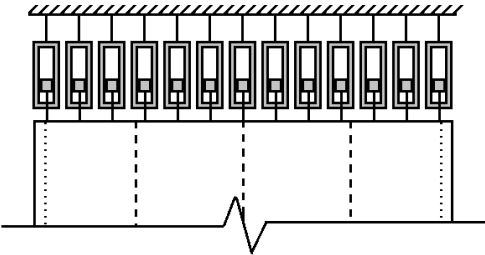
Table B1: Model revisions referred to in Section 5 – Finite Element Simulation

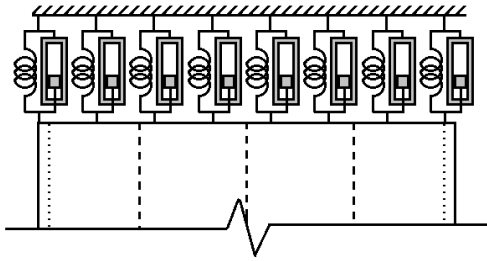
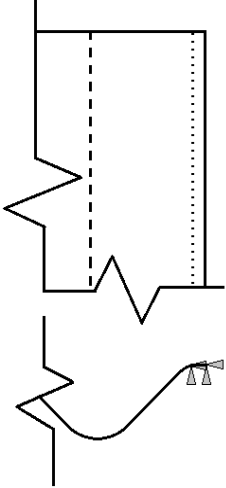
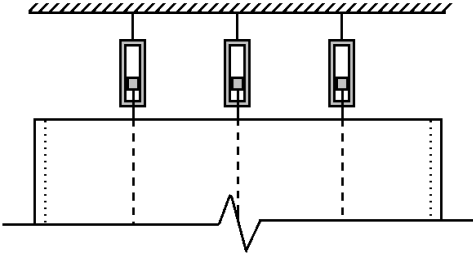
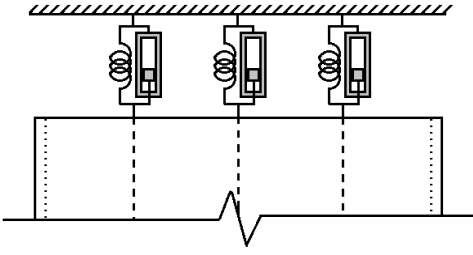
Revision Code	Load Rate	Cladding Profile	Mesh Density	Transverse Boundary	Longitudinal Boundary	EPDM seal	Platen
X1 (predates X4)	Variable	Based on AutoCAD file provided by manufacturer	42247 nodes 41784 S4R shell elements. Largest element dimension 2.4 mm. Shortest element dimension 1 mm.	Top: Applied point loads to each boundary node in the y direction which were extracted from Revision X2 and modified to decrease to 0 N by the end of the simulation. The boundary nodes were restrained from translating in the z direction rotating about the x axis. Bottom: Configuration A. Cartesian spring elements with a stiffness of $k_y = k_z = 50 \text{ N/mm}$.	Left: 70 mm from fastener hole edge using Configuration II. Right: 65 mm from fastener hole edge using Configuration II.	C3D8R element with dimension size 0.3 mm. Friction coefficient of 0.4 between cladding and EPDM. Top surface of the washer displaced to apply load. Nodes within the hollow were restrained from translating in x and y direction.	No platen included. Nodes on perimeter of fastener hole edge were restrained from translating in x and y direction.
X2 (predates X1)	0.58 m/s	Based on AutoCAD file provided by manufacturer	42247 nodes 41784 S4R shell elements.	Top: Configuration B. Normal load of 220 N and $\mu = 0.6$. Damping also	Left: 70 mm from fastener hole edge using Configuration II.	“	“

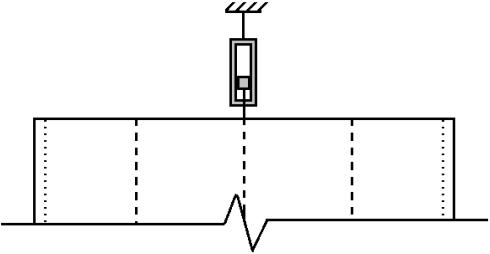
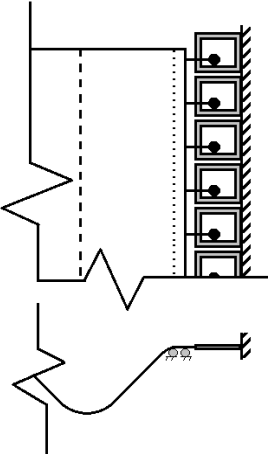
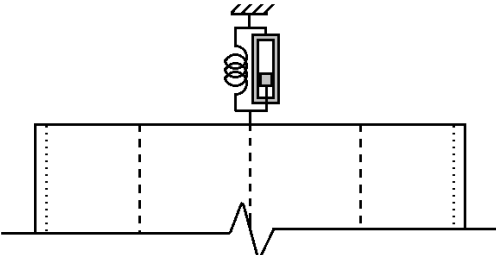
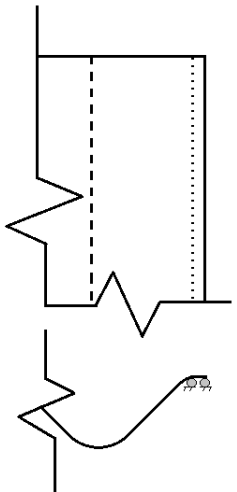
		Fastener hole is 0.5 mm off centre.	Largest element dimension 2.4 mm. Shortest element dimension 1 mm.	included with a damping factor of 2 N/(m/s). Bottom: Configuration C. Cartesian friction connection in parallel with spring. $k_y = k_z = 100$ N/mm, normal load 50 N and $\mu = 0.6$. Boundary nodes restrained against rotation about x and translation in z .	Right: 65 mm from fastener hole edge using Configuration II.		
X3	Variable	Smoothed profile based on photogrammetric results. Fastener hole is 1.5 mm off centre.	46444 S4R shell elements. Largest element dimension 2.4 mm. Smallest element dimension 0.4 mm	Top: Configuration J. Restrained by two 20 mm wide rigid plates with a spring stiffness of $k_z = 10000$ N/mm and a preload pressure $P_{TOP} = 0.486$ MPa Top: Configuration J. Restrained by two 20 mm wide rigid plates with a spring stiffness of $k_z = 10000$ N/mm and a preload pressure $P_{BOT} = 0.243$ MPa.	Left: Configuration V. Two 6 mm wide rigid plates with the inside edge sitting 68 mm to the left of the fastener hole edge. Right: Configuration V. Two 6 mm wide rigid plates with the inside edge sitting 66 mm to the right of the fastener hole edge.	C3D8R element with dimension size 0.3 mm. Friction coefficient of 0.4 between cladding and EPDM.	Platen included, features a 5 mm diameter shaft and head of the screw with a Cartesian connector acting as a spring to resist lateral forces with spring stiffness of $k_x = k_y = 1000$ N/mm.
X4 (predates X3)	0.58 m/s	Variable	46444 S4R shell elements. Largest element dimension 2.4 mm.	Top: Configuration J. Restrained by two 20 mm wide rigid plates with a spring stiffness of $k_z = 10000$ N/mm and a	Left: Configuration V. Two 6 mm wide rigid plates with the inside edge sitting 68 mm to the	C3D8R element with dimension size 0.3 mm.	Platen included, features a 5 mm diameter shaft.

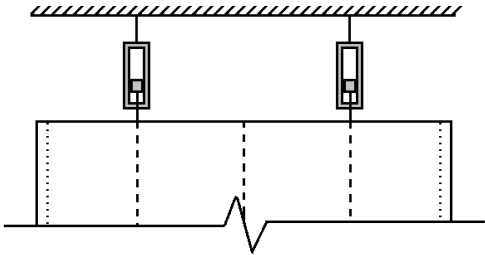
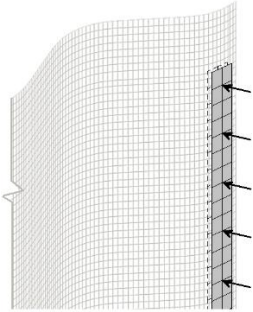
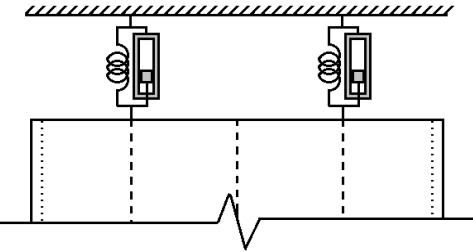
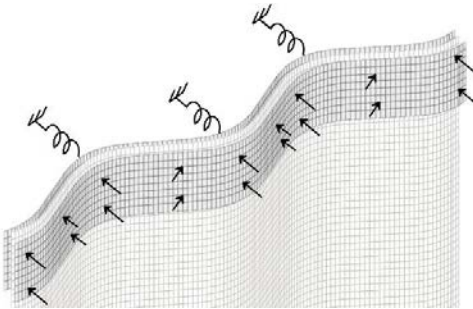
		Fastener hole is 1.5 mm off centre.	Smallest element dimension 0.4 mm	<p>preload pressure $P_{TOP} = 0.486$ MPa</p> <p>Top: Configuration J. Restrained by two 20 mm wide rigid plates with a spring stiffness of $k_z = 10000$ N/mm and a preload pressure $P_{BOT} = 0.243$ MPa.</p>	<p>left of the fastener hole edge.</p> <p>Right: Configuration V. Two 6 mm wide rigid plates with the inside edge sitting 66 mm to the right of the fastener hole edge.</p>	Friction coefficient of 0.4 between cladding and EPDM.	
--	--	-------------------------------------	-----------------------------------	---	---	--	--

Table B2: Illustrations of differing configurations for transverse and longitudinal boundaries

Transverse Boundary		Longitudinal Boundary	
<p>Configuration A.</p> <p>Linear spring placed at every transverse boundary node.</p>		<p>Configuration I.</p> <p>The two edges of the rail (6 mm apart) restrained from translation in x, y and z.</p> <p>Free to rotate.</p>	
<p>Configuration B.</p> <p>Axial friction connection placed at every transverse boundary node.</p>			

<p>Configuration C.</p> <p>Axial friction connection in parallel with a linear spring at every transverse boundary node.</p>		<p>Configuration II.</p> <p>The two edges of the rail (6 mm apart) restrained from translation in x and z only.</p> <p>Free to rotate.</p>	
<p>Configuration D.</p> <p>Axial friction connection at the valleys and crest of the cladding (3 in total).</p>		<p>Configuration IIa.</p> <p>The two edges of the rail (6 mm apart) restrained from translation in x and z only.</p> <p>Restrained from rotation about y.</p>	
<p>Configuration E.</p> <p>Cartesian friction connection in parallel with a linear spring at the valleys and crest of the cladding (3 in total).</p>		<p>Configuration III.</p> <p>x-y friction sliding plane restraining the outer edge. Internal rail boundaries restrained from translating in the z direction.</p>	

<p>Configuration F.</p> <p>Axial friction connection at the crest of the cladding (1 in total).</p>			
<p>Configuration G.</p> <p>Cartesian friction connection in parallel with a linear spring at the crest of the cladding (1 in total).</p>		<p>Configuration IV.</p> <p>Longitudinal boundary only restrained from translation in the z (along both boundaries of each rail).</p>	

<p>Configuration H.</p> <p>Axial friction connection at the valleys of the cladding (2 in total).</p>		<p>Configuration V.</p> <p>Two long rigid plates being sandwiched to the cladding, sitting 6 mm below the transverse clamps. Front plate is preloaded by pressure P then restrained from translating and rotating in x, y and z. Back plate is restrained from translating and rotating in x, y and z.</p>	
<p>Configuration I.</p> <p>Cartesian friction connection in parallel with a linear spring at the valleys of the cladding (2 in total).</p>			
<p>Configuration J.</p> <p>Two rigid plates being sandwiched to cladding. Back plate restrained by a spring in the z direction. Front plate is preloaded by pressure P.</p>			

APPENDIX C

WIND LOADING TRIBUTARIES

This paper was first published at the Australian Wind Engineering Society Workshop in Brisbane (Australia) on July 11th, 2013.

REFERENCES

- 3DSystems (2014) Geomagic Design X. <http://www.rapidform.com/products/xor/overview/>. Accessed 28 October 2014
- Agisoft (2014) Agisoft Lens. <http://agisoft.ru/products/lens>. Accessed 24 February 2014
- Agisoft LLC (2014) Agisoft Photoscan User Manual.
- Australian Building Codes Board. (2007). *BCA 2007: Building Code of Australia*. Canberra (ACT), Australian Building Codes Board
- Autodesk (2014) Autodesk 123D Catch. <http://www.123dapp.com/catch>. Accessed 24 February 2014
- Anand L. & Parks D. M. (2004) *2.002 Mechanics and Materials II – Spring 2004: Supplementary Notes*. Massachusetts Institute of Technology, Department of Mechanical Engineering, Massachusetts. USA
- Arrieux R., Bedrin C. & Boivin M. (1982) Determination of an intrinsic forming limit stress diagram for isotropic metal sheets. *Proceedings of the 12th biennial meeting of the international deep drawing research group, working group meetings*, WG I. Santa Margherita Ligure, Italy.
- Arias P, Herraes J, Lorenzo H, Ordonez C (2005) Control of structural problems in cultural heritage monuments using close-range photogrammetry and computer methods. *Computer Structures*, 83:1754-1766.
- Bakhshinejad A, Zamankhan P (2012) Swirling flows in horizontally vibrated beds of dense granular materials. *Particuology* 10:683-691.
- Bambach M (2009) Photogrammetry measurements of buckling modes and interactions in channels with edge-stiffened flanges. *Thin Wall Structures*, 47:485-504.
- BCA (2009) *Building Code of Australia*. A. B. C. Board, ed., ABCD.
- Beck, V. (1975) *Appraisal of roof cladding under dynamic wind loading – Cyclone Tracy Darwin 1974: Appendix 4*. Report on Cyclone Tracy – Effect on buildings – Dec 1974, G. Walker, ed., Australian Department of Housing and Construction.
- Beck, V. R., & Stevens, L. K. (1979). Wind loading failures of corrugated roof cladding. *Civil Engineering Transactions, I. E. Australia*, CE21(1):45-56.
- Békési N. & Váradi K. (2009) Experimental and numerical evaluation of lubricated friction of EPDM rubber. *Periodica polytechnica Mechanical Engineering*. 53(2):69-73.
- Belytschko, T. & Black, T. (1999) Elastic growth in finite elements with minimal remeshing. *International Journal for Numerical Methods in Engineering*, 45:602-620

- Besl P, McKay N (1992) A Method for Registration of 3-D Shapes. *IEEE T Pattern Anal* 14(2):239-256.
- BHP. (1992). *The making of iron and steel, 7th Edition*. Melbourne, BHP Steel Group
- Blau, P. J. (2009). *Friction Science and Technology: From Concepts to Applications, Second Edition*. CRC Press, Boca Raton, USA.
- Boughton G. N., Henderson D. J., Ginger J. D., Holmes J. D., Walker G. R., Leitch C. J., Somerville L.R., Frye U., Jayasinghe N. C. and Kim P. Y. (2011) Tropical Cyclone Yasi Structural Damage to Buildings. *Cyclone Testing Station Technical Report No. 57*, James Cook University.
- Bonora N. and Newaz G. (1998) Low cycle fatigue life estimation for ductile metals using a nonlinear continuum damage mechanics model. *International Journal of Solids and Structures*, Vol. 35(16), 1881-1894.
- Brown M. W. & Miller K. J. (1973) A theory for fatigue failure under multiaxial stress-strain conditions. *Proceedings of the Institute of Mechanical Engineers*, Vol. 187, 1973, 745-756
- Cao J., Lee W., Cheng H. S., Seniw M., Wang H. and Chung K. (2009) Experimental and numerical investigation of combined isotropic-kinematic hardening behavior of sheet metals. *International Journal of Plasticity* 25 p942-972.
- Coffin, L. F. (1954) A study of the effects of cyclic thermal stresses on a ductile metal. *Transactions of the American Society of Mechanical Engineers*, 76, 931-950.
- Crisfield, M. A. (1991). *Non-linear Finite Element Analysis of Solids and Structures, Volume 1*. West Sussex, John Wiley and Sons Inc.
- Crisfield, M. A. (1997). *Non-linear Finite Element Analysis of Solids and Structures, Volume 2*. West Sussex: John Wiley & Sons Ltd.
- Darwin Reconstruction Commission (DRC) (1976) *Darwin Area Building Manual*, Darwin (Australia).
- Dassault Systemes. (2013). *ABAQUS 6.13 Analysis User's Manual*. Providence (USA): Dassault Systemes Corp.
- Dassault Systemes. (2008). *White paper: Understanding Nonlinear Analysis*, Massachusetts (USA): Dassault Systemes SolidWorks Corp.
- Dietrich L, Socha G. & Kowalwski Z. L. (2014) Anti-buckling fixture for large deformation tension-compression cyclic loading of thin metal sheets. *Strain*, 50, 174-183
- Dowling, N. E. (1972). Fatigue failure predictions for complicated stress-strain histories. *Journal of Materials*, 7(1), 71-87.
- Dowling N. E. (1979) Notched member fatigue life predictions combining crack initiation and propagation. *Fatigue of engineering materials and structures*. (2) p129-138

- Eaton, K. J. and Mayne, J. R. (1975) The measurement of wind pressures on two-storey houses at Aylesbury. *Journal of Industrial Aerodynamics*, 1, 67-109
- Eggertsen P. and Mattiasson K. (2011) On the identification of kinematic hardening material parameters for accurate springback predictions. *International Journal of Material Forming*, 4:103-120.
- Ellyin F. (2012) *Fatigue Damage, Crack Growth and Life Prediction*. Springer Science and Business Media.
- Eos Systems (2013) PhotoModeler Products.
<http://www.photomodeler.com/products/default.html>. Accessed 10 July 2014
- Experimental Building Station (EBS). (1978). *TR440 - Guidelines for the testing and evaluation of products for cyclone prone areas*. Sydney.
- Field, J. L., Behnaz F. and Pangborn R. N. (1983) Characterization of Microplasticity Developed During Fatigue. *Fatigue Mechanisms: Advances in Quantitative Measurement of Physical Damage, ASTM STP 811, J. Lankford, et al., Editors, ASTM, Philadelphia*, 71-94
- Giner, E., Sukumar, N., Tarancon, J. E., & Fuenmayor, F. J. (2009). An ABAQUS implementation of the extended finite element method. *Engineering Fracture Mechanics*, 76:347-368.
- Ginger, J. D., & Holmes, J. (2003). Effect of building length on wind loads on low-rise buildings with a steep roof pitch. *Journal of Wind Engineering and Industrial Aerodynamics*, 91:1377-1400.
- Ginger, J. D., & Letchford, C. (1999). Net pressures on low-rise full-scale buildings. *Journal of Wind Engineering and Industrial Aerodynamics*, 83:239-250.
- Ginger, J. D., Mehta, K. C., & Yeatts, B. B. (1997). Internal pressures in a low-rise full-scale building. *Journal of Wind Engineering and Industrial Aerodynamics*, 72:163-174.
- Ginger, J. D., Reardon, G. F., & Whitbread, B. J. (2000). Wind load effects and equivalent pressures on low-rise house roofs. *Engineering Structures*, 22:638-646.
- Girardeau-montaut D (2014) CloudCompare v2.5.3 Documentation. Wiki:
<http://www.cloudcompare.org/doc/wiki/>. Accessed 24 February 2014
- Glaser R, Caccese V, Shahinpoor M (2012) Shape Monitoring of a Beam Structure from Measured Strain or Curvature. *Experimental Mechanics* 52:591-606
- GOM mbh (2015) *ARAMIS – Optical 3D Deformation Analysis*, Retrieved: 26 07, 2015, from: <http://www.gom.com/metrology-systems/system-overview/aramis.html>
- Goswami, Y. (2004) *The CRC Handbook of Mechanical Engineering, Second Edition*. CRC Press.

- Grön ng F, Bright J, Fagan M, O’Higgins P (2012) Improving the validation of finite element models with quantitative full-field strain comparisons. *Journal of Biomechanics* 45:1498-1506
- Halford, G. R. (2006) *Fatigue and Durability of Structural Materials*. ASM International.
- Henderson, D. J. (2010). Response of pierced fixed metal roof cladding to fluctuating wind loads. *Doctoral Thesis*. Townsville: James Cook University.
- Henderson, D. J. (2012). Private discussions.
- Henderson, D., & Ginger, J. D. (2005). Fatigue failure of roof components subjected to wind loading. *Australian Structural Engineering Conference*. Newcastle.
- Henderson, D. J., & Ginger, J. D. (2011). Response of pierced fixed corrugated steel roofing systems subjected to wind loads. *Engineering Structures*, 33:3290-3298.
- Hibbeler, R. C. (2013) *Mechanics of Materials: 9th Edition*. Singapore, Pearson Education South Asia Pte Ltd.
- Hibbit, Karlsson, & Sorensen. (2009). *ABAQUS Example Problems Manual*. Providence: Simulia.
- Hiermaier S. (2007) *Structures Under Crash and Impact: Continuum Mechanics, Discretization and Experimental Characterization*. Springer Science and Business Media.
- Holmes, J. D. (2001). *Wind Loading of Structures*. New York: Taylor and Francis.
- Hosford, W. F. (2009) *Mechanical Behavior of Materials 2nd Edition*. New York: Cambridge University Press.
- Hosford W. F. & Caddell R. M (2011) *Metal Forming: Mechanics and Metallurgy*. Cambridge University Press.
- Innovmetric (2014) PolyWorks Inspector. <http://www.innovmetric.com/en/products/polyworks-inspector>. Accessed 28 October 2014
- Insurance Council of Australia Limited (2015) “Catastrophe events and the community”. Retrieved 17 06, 2015, from <http://www.insurancecouncil.com.au/issue-submissions/issues/catastrophe-events>
- Irwin, G. R. (1957) Analysis of stresses and strains near the end of a crack traversing a plate. *Journal of Applied Mechanics*, 24: 361-364.
- James Cook University. (2010). *Airbox Testing - Cyclone Testing Station*. Retrieved 04 14, 2011, from http://www.jcu.edu.au/cts/facilities/JCUPRD_044740.html
- Jancauskas, E. D., Mahendran, M., & Walker, G. R. (1994). Computer simulation of the fatigue

- behaviour of roof cladding during the passage of a tropical cyclone. *Journal of Wind Engineering and Industrial Aerodynamics*, 51:215-227.
- Jain M., Allin J. & Lloyd D. J. (1999) Fracture limit prediction using ductile fracture criteria for forming of an automotive aluminum sheet. *International Journal of Mechanical Sciences*, 41:1273-1288.
- Koutsoudis A, Vidmar B, Arnaoutoglou F (2013) Performance evaluation of a multi-image 3D reconstruction software on a low-feature artefact. *Journal of Archaeological Science* 40:4450-4456
- Koutsoudis, A, Vidmar B, Ioannakis G, Arnaoutoglou F, Pavlidis G, Chamzas C (2014) Multi-image 3D reconstruction data evaluation. *Journal of Cultural Heritage* 15(1):73-79.
- Kachanov, L. (1986). *Introduction to Continuum Damage Mechanics*. Kluwer Academic Publishers. USA.
- Lee B. H., Keum Y. T. & Wafoner R. H. (2002) “Modeling of the friction caused by lubrication and surface roughness in sheet metal forming”. *Journal of Materials Processing Technology* 130-131:60-63.
- Lee Y. W. (2005) Fracture Prediction in Metal Sheets. Doctoral Thesis. Massachusetts Institute of Technology.
- Lee Y., Barkey M. E. and Kang, H. (2012) *Metal fatigue analysis handbook: Practical problem-solving techniques for computer-aided engineering*. Elsevier.
- Leicester, R. H., & Reardon, G. F. (1976). *Wind damage in Australia: A pictorial review with particular reference to domestic and other low-rise structures*. Victoria, CSIRO Division of Building Research.
- Lemaitre, J. and Chaboche, J. L. *Mechanics of Solid Materials*, Cambridge University Press, 1990.
- Lide, D. (2004) CRC Handbook of Chemistry and Physics, 85th Edition. CRC Press. USA. p14-41
- Liu A. (2005) *Mechanics and Mechanisms of Fracture: An Introduction*. ASM International.
- Lovisa, A.C., Wang, V.Z., Henderson, D.J. and Ginger, J.D. (2012), “A finite element model for pierced fixed, corrugated metal roof cladding subject to upliftwind loads”, *Proceedings of the Australasian Structural Engineering Conference*, Perth, Australia, July 2012.
- Lovisa, A.C. Wang, V.Z., Henderson, D.J. and Ginger, J.D. (2013a), “Wind loading tributaries of corrugated cladding”, *Proceedings of the 8th Asia Pacific Conference on Wind Engineering*, Chennai, India, December 2013.
- Lovisa, A.C. Wang, V.Z., Henderson, D.J. and Ginger, J.D. (2013b) “Development and

- validation of a numerical model for steel roof cladding subject to static uplift loads". *Wind and Structures* 17(5) :495-513.
- Lucas R. M., Al-Bermani F.G.A. & Kitipornchai S., (1997) Modelling of cold-formed purlin-sheeting systems - Part 1: Full Model, *Thin Walled Structures*, 27(3):223-243.
- Lucas R. M., Al-Bermani F.G.A. & Kitipornchai S., (1997) Modelling of cold-formed purlin-sheeting systems - Part 2. Simplified Model, *Thin Walled Structures*, 27(4):263-286.
- Lumann T (2010) Close range photogrammetry for industrial applications. *International Society of Photogrammetry* 65:558-569
- Madayag, A. F. (1969). *Metal fatigue: theory and design*. New York, John Wiley & Sons, Inc.
- Maddox, S. (2003) Comparison of the ASME, BS and CEN fatigue design rules for pressure vessels. *Proceedings of the IMechE seminar, 1st October 2003, London (UK)*
- Mahaarachchi, D. (2003). Behaviour and Design of Profiled Steel Cladding Systems Subject to Pull-through Failures. *Doctoral Thesis*. Brisbane: Queensland University of Technology.
- Mahaarachchi, D., & Mahendran, M. (2000). Pull-through failures of crest fixed steel claddings initiated by transverse splitting. *15th International Specialty Conference on Cold-formed Steel Structures*, (p. 635-646). St. Luis.
- Mahaarachchi, D., & Mahendran, M. (2004). Finite element analysis and design of crest-fixed trapezoidal steel claddings with wide pans subject to pull-through failures. *Engineering Structures*, 1547-1559.
- Mahaarachchi, D., & Mahendran, M. (2009a). A strain criterion for pull-through failures in crest-fixed steel claddings. *Engineering Structures*, 31:498-506.
- Mahaarachchi, D., & Mahendran, M. (2009b). Wind Uplift Strength of trapezoidal steel cladding with closely spaced ribs. *Journal of Wind Engineering and Industrial Aerodynamics*, 97:140-150.
- Mahendran, M. (1989). *Fatigue behaviour of corrugated roofing under cyclic wind loading* TR 35. Townsville: Cyclone Testing Station JCU.
- Mahendran, M. (1990a). Static behaviour of corrugated roofing under simulated wind loading. *Civil Engineering Transactions. I. E. Australia*, CE32(4):212-218.
- Mahendran, M. (1990b). Fatigue behaviour of corrugated roofing under cyclic wind loading. *Civil Engineering Transactions, I. E. Australia*, CE32 (4):219-226.
- Mahendran M (1992) Contrasting behavior of thin steel roof claddings under simulated cyclonic wind loading. *Proceedings of the 11th International Specialty Conference on Cold-Formed Steel Structures*, St. Louis, Missouri, U.S.A, October 20-21.
- Mahendran, M. (1993). Simulation of cyclonic wind forces on roof claddings by random block

- load testing. *Cyclone Testing Station Technical Report No. 38*, James Cook University.
- Mahendran, M. (1994a). Steel Roof Claddings Under Simulated Cyclonic Wind Forces. *Australian Civil Engineering Transactions, I. E. Australia, CE36:1-9*.
- Mahendran, M. (1994b). Behaviour and design of crest-fixed profiled steel roof claddings under wind uplift. *Engineering Structures, 16(5):368-376*.
- Mahendran, M. (1995). Appropriate fatigue loading sequence for roof claddings. *Engineering Structures, 17(7):476-484*.
- Magargee, J., Cao, J., Zhou, R., McHugh, M. and Brink, D. (2011) Characterization of Tensile and Compressive Behavior of Microscale Sheet Metals Using a Transparent Micro-wedge Device, *ASME Journal of Manufacturing Science and Engineering, 133(6)*
- Manson, S. S. (1954) Behaviour of materials under conditions of thermal stress. *National Advisory Commission on Aeronautics: Report 1170*. Cleveland: Lewis Flight Propulsion Laboratory.
- Mattiasson, K., Jergus J. & DuBois, P. (2014) On the prediction of failure in metal sheets with special reference to strain path dependence. *International Journal of Mechanical Science, 88:175-191*.
- McCarthy J (2014) Multi-image photogrammetry as a practical tool for cultural heritage survey and community engagement. *Journal of Archaeological Science, 43:175-185*
- McClintock, F. A. (1963) On the plasticity of the growth of fatigue cracks. *Fracture of Solids, 20, 65-102*, New York (USA).
- Meecham, D., Surry, D., & Davenport, A. G. (1991). The magnitude and distribution of wind-induced pressures on hip and gable roofs. *Journal of Wind Engineering and Industrial Aerodynamics, 38: 257-272*.
- Melbourne, W. H. (1977). Loading cycles for simulation of wind loading. *Proc. Workshop on guidelines for cyclone product testing and evaluation*. Sydney: Experimental Building Station.
- Mendelson, A. (1968). *Plasticity: Theory and application*. New York: The Macmillan Company.
- Milne I., Ritchie, R. O. and Karihaloo B. L. (2003) Cyclic loading and fatigue. *Comprehensive Structural Integrity, 4*.
- Miner, M. A. (1945) Cumulative damage in fatigue, *Journal of Applied Mechanics, 12:159-164*
- Moavenzadeh, F. (1990) *Concise Encyclopaedia of Building and Construction Materials*. MIT Press.
- Mohammadi, S. (2008). *Extended Finite Element Method for Fracture Analysis of Structures*. Victoria: Blackwell Publishing Ltd.

- Morgan, J. W., & Beck, V. R. (1977). Failure of sheet-metal roofing under repeated wind loading. *Civil Engineering Transactions, I.E. Australia*, 1-5.
- NaturalPoint Inc (2013) OptiTrack – MOTIVE – production mocap, simplified. <http://media.naturalpoint.com/optitrack/mediakit/GDC%202013%20Brochure.pdf>. Accessed 18 February 2014
- Osgood, C. C. (1970) *Fatigue Design*. Wiley-Interscience, New York, USA
- Palmgren, A. (1924) Die Lebensdauer von Kugellagern. *Zeitschrift des Vereins Deutscher Ingenieure*, 68:339-341.
- Paris, P. C., Gomez, M. P. & Anderson, W. P. (1961) A rational analytic theory of fatigue. *The Trend in Engineering*, 85:528-534.
- Rogers, C. A., & Hancock, G. J. (1997). Ductility of G550 sheet steels in tension. *Journal of Structural Engineering - ASCE*, 123(12):1586-1594.
- Rooke, D. P., & Cartwright, D. J. (1976). *Compendium of Stress Intensity Factors*. England: The Hillingdon Press.
- Schijve, J. (2009) *Fatigue of Structures and Materials 2nd Edition*. Springer Sciences+Business Media.
- Sharma, R. N., & Richards, P. J. (1999). The influence of Reynolds stresses on roof pressure fluctuations. *Journal of Wind Engineering and Industrial Aerodynamics*, 83:147-157.
- Smith, R. N. (1991). *BASIC fracture mechanics*. Oxford: Butterworth-Heinemann.
- Spranghers K, Vasilakos I, Lecompte D, Sol H, Vantomme J (2012) Full-field deformation measurements of aluminum plates under free air blast loading. *Experimental Mechanics*, 52:1371-1384
- Spranghers K, Vasilakos I, Lecompte D, Sol H, Vantomme J (2013) Numerical simulations and experimental validation of the dynamic response of aluminum plates under free air explosions. *International Journal of Impact Engineering* 54:83-95
- Standards Australia/New Zealand (AS/NZS). (2011). AS/NZS 1170.2: Structural design actions, Part 2: Wind actions. Sydney: SAI Global Limited.
- Standards Australia/New Zealand (AS/NZS). (2007). AS/NZS 1391-2007: Metallic materials – Tensile testing at ambient temperature. Sydney: SAI Global Limited.
- Stathopoulos, T. (1984) Wind loads on low-rise buildings: a review of the state of the art. *Engineering Structures*, 6:119-135
- Stephens, R. Fatemi, A. Stephens, R. & Fuchs O. (2001) *Metal Fatigue in Engineering* 2nd Edition. John Wiley & Sons. New York, USA.
- Stramit. (2009). *Cyclonic Areas Roof and Wall Cladding*, product technical design

- supplement. Stamat Corporation Pty Limited.
- Suresh S. (1991). *Fatigue of materials*. Cambridge Solid State Science Series. Cambridge University Press. Great Britain.
- Suresh Kumar, K. (1999). Modeling of wind-induced pressure fluctuations on roofs of low-rise buildings. *Canadian Journal of Civil Engineering*, 26:453-467.
- Suresh Kumar, K., & Stathopoulos, T. (1998). Fatigue Analysis of roof cladding under simulated wind loading. *Journal of Wind Engineering and Industrial Aerodynamics* 77 & 78:171-183.
- Suresh Kumar, K., & Stathopoulos, T. (1999). Synthesis of non-Gaussian wind pressure time series on low building roofs. *Engineering Structures*, 21:1086-1100.
- The Committee on Fatigue and Fracture Reliability. (1982). Fatigue Reliability: Variable Amplitude Loading. *Journal of the Structural Division*, 47-69.
- The MathWorks, Inc (2012) MATLAB. Natick, Massachusetts, USA.
- Uematsu, Y., & Isyumov, N. (1999). Review of Wind pressures acting on low-rise buildings. *Journal of Wind Engineering and Industrial Aerodynamics*, 82:1-25.
- Visual Computing Lab – ISTI – CNR (2012) Meshlab V1.3.2. <http://meshlab.sourceforge.net/>. Accessed 24 February 2014
- Walker, G. (1975). *Report on Cyclone Tracy - Effects on buildings - Dec 1974*. Australian Department of Housing and Construction.
- Walker, G. R. (1980). A review of the impact of Cyclone Tracy on Australian building regulations and practice. *Civil Engineering Transactions, I.E. Australia*, 100-107.
- Walker, G. R., Minor, J. E., & Marshall, R. D. (1975). The Darwin Cyclone - valuable lessons in structural design. *Civil Engineering - ASCE*, 82-86.
- Walker, G. R., Musulin, R. (2012) “Utilizing catastrophe risk modelling for cost benefit analysis of structural engineering code changes.” *Proceedings of the Australasian Structural Engineering Conference*, Perth, Australia, July 2012.
- Wierzbicki, T., Bao, Y., Lee, Y. & Bai, Y. (2005) Calibration and evaluation of seven fracture models. *International Journal of Mechanical Sciences*, 47:719-743.
- Wirsching, P. H., & Light, C. M. (1980). Fatigue under wide band random stresses. *Journal of the Structural Division*, 1593-1607.
- Wöhler, A (1860) Versuche über die Festigkeit der Eisenbahnwagenachsen. *Zeitschrift für Bauwesen*, 10, English Summary (1867). *Engineering* 4: 160-161
- Wriggers, P. (2008) *Nonlinear Finite Element Methods*. Springer, Berlin.

- Wu C. (2011) VisualSFM: a visual structure from motion system. <http://ccwu.me/vsfm/>. Accessed 24 February 2014
- Xiao Z, Liang J, Yu D, Asundi A (2011) Large field-of-view deformation measurement for transmission tower based on close-range photogrammetry. *Measurement* 44:1705-1712
- Xu, Y. L. (1993). *Wind-Induced Fatigue Loading on Roof Cladding of Low-Rise Buildings*. Townsville: Cyclone Testing Station, James Cook University, Technical Report No.41.
- Xu, Y. L. (1995). Fatigue performance of screw-fastened light-gauge-steel roofing sheets. *Journal of Structural Engineering*, 121(3):389-398.
- Xu, Y. L. (1996). Wind-induced fatigue loading and damage to hip and gable roof claddings. *Journal of Structural Engineering*, 122:1475-1483.
- Xu, Y. L., & Reardon, G. F. (1993). Test of screw fastened profiled roofing sheets subject to simulated wind uplift. *Engineering Structures*, 15(6):423-430.
- Xu, Y. L., & Reardon, G. F. (1998). Variations of wind pressure on hip roofs with roof pitch. *Journal of Wind Engineering and Industrial Aerodynamics*, 73:267-284.
- Xu, Y. L., & Teng, J. D. (1994). Local plastic failure of light gauge steel roofing sheets: Finite element analysis versus experiment. *Journal of Constructional Steel Research*, 30(2):125-150.
- Xu, Y. L., Mehta, K. C., & Reardon, G. F. (1995). Fatigue of metal roof cladding subject to wind loading. Part 1: Fatigue-related characteristics of roof pressures. *Ninth International Conference on Wind Engineering*, New Delhi, India.
- Yoa J. T. P. and Munse W. H. (1961) Low Cycle Fatigue of Metals – Literature Review. First Progress report to the Ship Structure Committee. University of Illinois. Urbana, Illinois.
- Zao K. M & Lee, J. K (2004) Inverse estimation of material properties for sheet metals. *Communications in Numerical Methods in Engineering*, 20:105-118